

Projects in Chaotic Dynamics: Spring 2010

Elizabeth Bradley, Editor

Technical Report CU-CS 1066-10

University of Colorado
Department of Computer Science
Boulder CO 80309-0430 USA

July 2010

Table of Contents

Feasibility of Nonlinear Heart Rate Variability Analysis in Clinical Settings Swamy Ananthanarayan	1
Investigating Baseball Pitch Equations of Motion to Determine “Sensitive” Pitch Parameter Values Ashok Basawapatna	10
An Examination of the Local Dynamics of Computer Performance Gregory Brown	16
A Lorenzian-based Chaotic Encryption Scheme Michael Brunel	23
The Applicability of Compressed Sensing on Nonlinear Dynamic Systems and Chaos Lucas Budman	29
Trajectory Analysis for Manifold Return Transfers for Sun-Earth L1 Libration Point Orbits Bradley Cheetham	36
Propagating the Admissible Region with the Symplectic State Transition Matrix Kohei Fujimoto	42
Rigorously Pursuing Chaos in Time-Series Data: An Algebraic Topological Approach Joshua Garland with Zachary Alexander	56
Are Attractors Attractive? An Analysis of Chaotic and Traditional Photograph Composition Techniques Jeffery Hoehl	76
Low Cost Reconfiguration of Invariant Shape Collinear Coulomb Spacecraft Formations Erik Hogan	84
Analysis of fractal representation of genetic sequences Amrik Sen	93
Spatiotemporal Chaos: Effect of Spatial Smoothing on Bifurcations in a Discrete-Time Chaotic Map Per Sebastian Skardal	99
Are Chaotic Variations ‘Superior’ to Random Variations on a Drum Rhythm? Laura Stiles	115

Feasibility of Nonlinear Heart Rate Variability Analysis in Clinical Settings

Swamy Ananthanarayan

Department of Computer Science

University of Colorado, Boulder

ananthas@colorado.edu

April 2010

Abstract

The measure of heart rate variability (HRV) has become a valuable metric for diagnosing cardiac health. The ECG is the representative signal containing information about the condition of this health metric. Analysis of this highly complex and irregular signal cannot always be addressed through linear statistics. Nonlinear methods are able to describe the processes generated by biological systems in a more effective way. The adoption of these methods in a clinical environment, however, has been difficult and slow. This paper examines the feasibility of using nonlinear analysis methods in such a setting. Given two data sets of a normal patient and a patient with atrial fibrillation (from PhysioNet), we examined the effectiveness of using Poincaré plots, largest Lyapunov exponent, and detrended fluctuation analysis, in differentiating the subjects. All the methods used were able to clearly separate the two data sets. From a clinical perspective, calculating accurate Lyapunov exponents requires an average of 5.5 hours of data, while Poincaré plots and DFA require approximately 100 and 80 minutes, respectively. Both Poincaré plots and DFA would serve well in characterizing a patient relatively quickly, while Lyapunov exponents would be too time intensive. To test our hypothesis, we designed and implemented a simple ECG system that gathered 90 minutes of data from an unclassified subject. A Poincaré and DFA analysis of the data suggested a healthy normal individual.

1 Introduction

It has been observed that the cyclic variations of heart rate plays an important role in the health of an individual. Heart rate variability (HRV), the variation over time of the period between heart beats, is thought to reflect the heart's ability to adapt to changing circumstances. Its variation may contain indicators of current diseases, or warnings about impending cardiac diseases. Physiological signals, however, often vary in a complex and irregular manner making it difficult to analyze them. Since the underlying mechanisms involved in the control of heart rate is mainly nonlinear [4], the application of nonlinear analysis techniques seem appropriate.

One of the controversial topics related to nonlinear science is the dynamical characterization of HRV. While the question as to whether the human heart is chaotic by nature is interesting, it is a question that is unlikely to be resolved very soon. Given the complexity of the human heart, where different subsystems with feedback loops constantly adapt the cardiac system to its physiological needs and requirements, it may very well be that the human heart is chaotic in one instance and stochastic in another. The debate as to its dynamic nature is interesting to the extent that it leads to new insights about health and disease in patients.

Setting aside the difficulties in documenting chaotic dynamics in HRV, the goal of this paper is to examine the feasibility of nonlinear analysis in a clinical setting. Towards that end, it examines several methods such as Poincaré plot analysis, Lyapunov exponents, and detrended fluctuation analysis (DFA) in distinguishing between groups of patients. Most studies of nonlinear techniques on

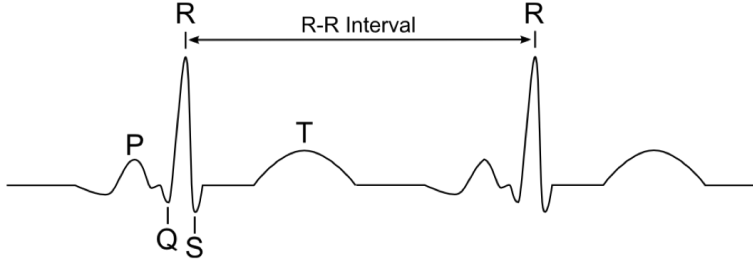


Figure 1: An ECG Example

HRV are based on long-term time series and hence focused on 24-hour ambulatory ECG recordings. We examine using these methods on consecutively smaller data lengths to determine their reliability in HRV classification.

Measuring the electrical impulses of the heart through an ECG is the standard way to study HRV. This paper examines 3 ECG data sets: a healthy subject, a subject with atrial fibrillation, and an unclassified subject. The first two data sets were obtained from PhysioNet, while the third was obtained experimentally through a custom ECG system. The length of time to obtain data from the third subject was informed by the results from the first two data sets. The third subject was then classified based on the analysis of the obtained ECG data.

In the next section, we describe the ECG data used and the RR interval method used in the analysis. Section 3 discusses in detail the nonlinear techniques used in characterizing the signals. The results of the analysis are provided in section 4. Section 5 presents the design and implementation of the custom ECG system followed by an analysis of the data obtained. We finally conclude in section 6.

2 ECG Data and Methods

An ECG measures the electrical impulses of heart activity, and is composed of four components: the p-wave, the QRS complex, and the t-wave (Figure 1). Typically, conditions of the heart are detected by irregular behavior in either the amplitude, duration, or frequency of the smaller waves or QRS complex. While they are valid methods for analysis, they require high resolution data and are affected by noise. Another alternative, which this paper explores, is to focus on the R-peak of the QRS complex, more specifically, the duration between the R spikes. This measure, dubbed the RR interval, is useful in detecting heart beat irregularities. It is robust to noise as it only requires keeping track of the time between major, easily detectable spikes. Given the RR intervals, the heart rate (beats per minute) is given as:

$$HR = 60/R_i \quad (1)$$

This paper analyses three data sets, two of which were obtained from the PhysioNet database of physiologic signals [2]. Each of the two time series from PhysioNet is 24 hours long. The first time series (n1rr) is of a healthy, adult male who is 32 years old. The second time series (a1rr) is of an atrial fibrillation (AF) patient. The sex, and age of the AF patient were not provided. The third data set was obtained experimentally, using a simple, custom ECG system, from a 30 year old adult male with no prior HRV classification (e.g.. normal, AF, cardiac arrhythmia, etc). Informed by our analysis of the two PhysioNet data sets, we gathered 90 minutes of ECG data and then used the data to classify the subject.

3 Nonlinear Methods of Analysis

Nonlinear techniques have been used in a variety of studies to describe complex biological systems in an effective way [1, 3]. The methods employed by this paper to study HRV include, interspike interval embedding, the largest Lyapunov exponent (LLE), Poincaré plot geometry, and detrended fluctuation analysis (DFA). Each is discussed in detail in the subsections below.

3.1 Poincaré Plots

A Poincaré plot analysis portrays the nature of RR interval fluctuations. It is a plot in which each RR interval is plotted as a function of the previous RR interval (RR_n against RR_{n+1}). It is used as a quantitative visual technique where the shape of the plot is used to indicate the degree of heart failure of the subject [10]. The plot provides summary information, as well as detailed beat-to-beat information on the behavior of the heart. It can be analyzed quantitatively by calculating the standard deviations of the distances of the $R - R(i)$ to the lines $y = x$ and $y = -x + (R - R_m)$, where $R - R_m$ is the mean of all the beat-to-beat intervals. The standard deviation of the short-term RR interval is referred to as SD1 (minor axis of the cloud), while the standard deviation of the long-term RR interval is called SD2 (major axis of the cloud). Typically, the ratio SD1/SD2 is used to characterize various cardiac abnormalities. A lower ratio is an indicator of a healthy heart and typically creates a comet or cigar-like plot.

3.2 Interspike Interval Embedding

Often, the first step in nonlinear dynamical analysis is the reconstruction of the phase space. It is used in calculating various measures such as the Lyapunov exponent (Section 3.3). The simplest method for reconstruction is the time-delay method described by Takens [8], where the multidimensional dynamics of the system can be generated from one measurement variable. In order for Takens theorem to hold, the sampling time interval needs to be uniform, which is not the case with RR intervals. If however, we assume that the spikes result from an integrate and fire process, then the $RR_i(s)$ are just an integral of some state variable. This idea, proved by Sauer [7], allows the embedding of RR intervals using usual time delay embedding. The reconstructed and original system attractors are topologically equivalent. For a time series $R - R(n)$, where $n = 1, 2, \dots, N$, the time delay vectors in phase space can be reconstructed as defined by

$$X_n = [RR(n), RR(n + \tau), RR(n + 2\tau), \dots, RR(n + (m - 1)\tau)] \quad (2)$$

where τ is referred to as the delay time and m is the embedding dimension. This paper employed the false nearest neighbors technique in estimating the embedding dimension, and the average mutual information technique in estimating the delay.

3.3 Largest Lyapunov Exponent (LLE)

The largest Lyapunov exponent is a quantitative measure of the sensitivity of the system to initial conditions and gives a measure of predictability. It defines the average rate of divergence of two neighboring trajectories. Even though an m -dimensional system has m Lyapunov exponents, it is often sufficient to compute just the largest Lyapunov exponent. A negative exponent implies that the orbits approach a common fixed point while a zero exponent represents orbits that maintain their relative positions (on a stable attractor). A positive exponent is indicative of orbits that are on a chaotic attractor. Different methods exist for calculating the largest Lyapunov exponent. The method employed by this paper was proposed by Rosenstein et al [6]. It is known to be robust with data length. This method looks for the nearest neighbor of each point in phase space and tracks their separation over a period of time. By plotting the log of the divergence versus time, the LLE is estimated by computing a least-squares fit to the linear region of the resulting curve. The LLE for normal subjects should be lower than patients diagnosed with AF since the variation in RR is much lower (compared to AF).

3.4 Detrended Fluctuation Analysis (DFA)

A time series is generally considered stationary if its mean, standard deviation and higher moments are invariant under time translation. Signals that fail these conditions are considered nonstationary. For such signals, a bounded time series can be integrated and mapped to a self-similar process. A sequence of coin flips, for example, can be mapped using this method to a one-dimensional random walk (a stationary integrated time series). However, using this type of fractal analysis for highly nonstationary signals like heart rate, only makes the nonstationary of the original data even more apparent during the integration procedure.

Detrended fluctuation analysis is used to overcome this complication. This technique, introduced by Peng et al [5], is a modified version of the root-mean-square analysis of a random walk that can be used to quantify the fractal scaling properties of short interval RR interval signals. The general idea behind DFA is to calculate the average amount of fluctuation over bins of different sizes (root mean square deviation between the signal and its trend in each bin) and plot the result as a function of bin size on a log-log scale.

First, the RR time series of length K is integrated using the equation,

$$y(k) = \sum_{i=1}^k [RR(i) - RR_{avg}] \quad (3)$$

where $y(k)$ is the k th value in the integrated series. $RR(i)$ is the i th interbeat interval and RR_{avg} is the average interbeat interval over the entire beat series. The integrated series is then divided in n windows of equal length. In each window, a least squares line representing the trend in that window is fitted to the RR interval data. The y coordinate of the straight line segments are denoted by $y_n(k)$. Finally, the integrated time series is detrended in each window. The root-mean-square fluctuation of the integrated and detrended series is calculated using equation 4.

$$F(n) = \sqrt{1/N \sum_{k=1}^N [y(k) - y_n(k)]^2} \quad (4)$$

This computation is repeated over different window sizes to obtain the relationship between $F(n)$ and the window size n . This relationship can be thought of as the number of beats in a window that is the size of the window of observation. Usually, $F(n)$ will increase with window size. A linear relationship on a log-log graph indicates the presence of self-similarity. The fluctuations in small boxes are related to the fluctuations in large boxes in a power-law fashion. The slope of the line, relating $\log F(n)$ to $\log n$ determines the scaling exponent, α . Fractal like signals result in a scaling exponent value of 1 ($\alpha = 1$). A totally random signal results in a value of 0.5. For a more intuitive understanding, α can be thought of as the “coarseness” of the original time series. The larger the value of α , the smoother the series.

For healthy, normal subjects, the scaling exponent should be closer to 1, indicating fractal-like behavior. For highly varying signals, like patients with atrial fibrillation, the exponent should be very low [9].

4 Results

Using the nonlinear methods discussed above, the two data sets for normal and AF subjects were analyzed. The results focus on the feasibility of using nonlinear approaches in analyzing cardiovascular variability in a clinical setting. If, for example, 24 hours of ECG data is required for a particular nonlinear analysis method, it would be too time intensive to succeed in a clinical environment.

Figure 2 shows the Poincaré plots for both subjects. For the normal subject, the classic cigar shape is clearly visible in the plot. The ratio $SD1/SD2$ for the normal subject is 0.85. In the case of the AF subject, the plot shows a “fan-like” dispersion. The ratio $SD1/SD2$ for the AF subject is 3.02, indicative of an unhealthy heart. This ratio is more in the case of the AF subject due to more

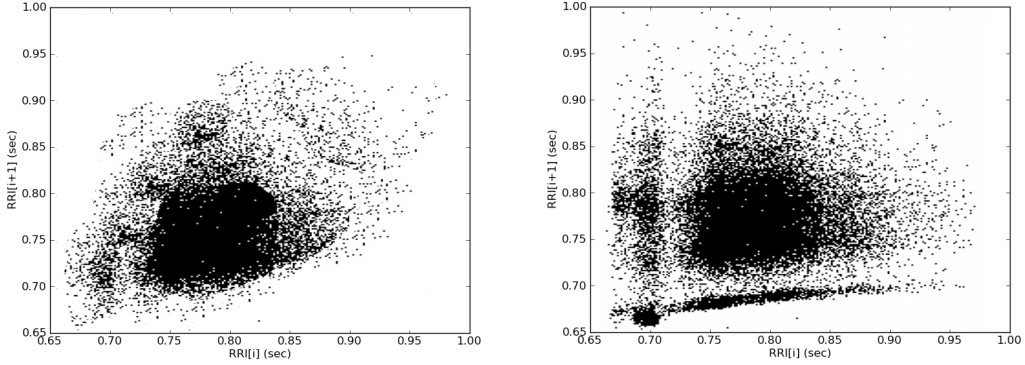


Figure 2: Poincaré plots for normal subject (left) and AF subject (right). The SD1/SD2 ratios are 0.85 and 3.02 respectively.

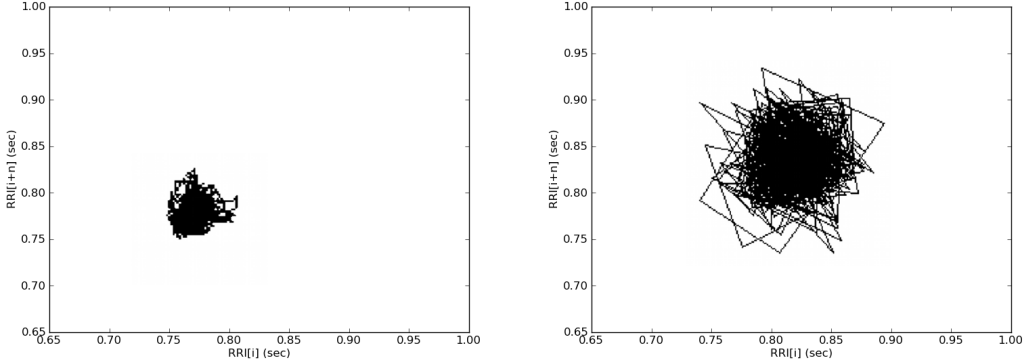


Figure 3: Phase-space plots for normal subject (left, $m = 7, \tau = 2$) and AF subject (right, $m = 8, \tau = 2$).

variation in the RR interval. The Poincaré plots, differentiates the two data sets significantly. To get a clear picture of the plots, approximately 10000 (~ 1.5 hrs) beats were required.

To generate the phase-space plots, Tisean was used to compute the embedding dimension (m) and the delay (τ). The embedding dimension was calculated using false nearest neighbors and the delay was estimated using average mutual information. Figure 3 details the phase-space plots for the two data sets. For the normal subject, the phase-space plot looks like a cluster of points. In the case of atrial fibrillation, heart rate signal records highly erratic variability; this is depicted in the scattering of points in the phase-space plot.

Given a reconstruction of the phase space, the LLEs for the normal and AF subjects were calculated (using Tisean lyap_r). In order to determine the minimum amount of data required for a successful estimation, LLEs were calculated for different time lengths. Table 1 details the results. The LLEs computed from 20 hours of ECG data are the most accurate. Given this baseline, LLEs were then computed for progressively smaller data lengths. For the normal subject, an accurate LLE estimate can be obtained with 5 hours of ECG data; the AF subject required 6 hours. Results show a positive LLE for both data sets, suggesting a chaotic time series. While the LLE characterizes the two subjects well, with the AF subject having a higher LLE than the normal subject (due to higher RR variations), it is too time intensive for a clinical setting.

The last nonlinear method employed to distinguish the two data sets was DFA. Figure 4 shows

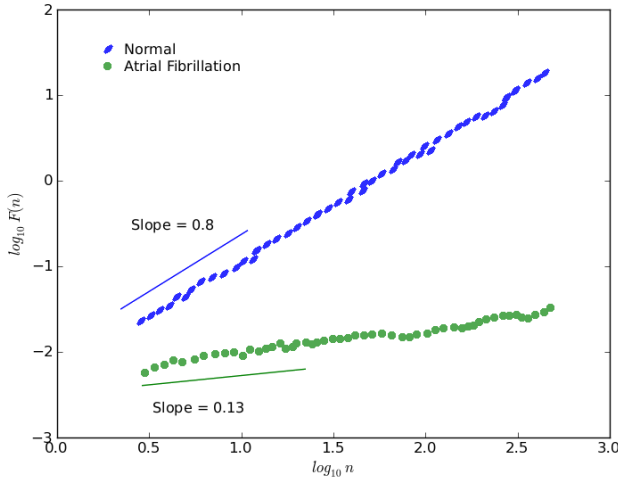


Figure 4: DFA analysis

the results of the analysis. For the normal subject, the fractal scaling (α) exponent is 0.8. In previous studies, healthy subjects revealed a scaling exponent of approximately 1 [9], indicating fractal-like behavior. For highly varying signals, like patients with AF, the scaling exponent is very low. The results support this conclusion with the AF subject having a reduced scaling exponent of 0.13. This method required approximately 8000 beats ($\sim 80\text{min}$), the least amount of data out of the nonlinear methods used.

Table 1: LLEs for various time lengths

	Normal	AF
LLE (10 min)	0.03	0.09
LLE (1 hr)	0.23	0.43
LLE (3 hrs)	0.49	0.35
LLE (5 hrs)	0.53	0.45
LLE (6 hrs)	0.56	0.66
LLE (8 hrs)	0.57	0.64
LLE (20 hrs)	0.55	0.67

5 Experiment and Analysis

Of the nonlinear analysis methods used, Poincaré plot geometry, and DFA required the least amount of data for distinguishing the two subjects. While 1.5 hours of ECG data is still considerable, it is not as prohibitive as a 24 hour requirement. To test these two methods, a simple ECG system was developed and used to gather data from an unclassified subject. The experimental ECG system is by no means perfect, but since the analysis methods described above only require RR intervals, the system only needs to detect the spikes in the signal train and not the finer characteristics (p-wave and t-wave). The simple ECG designed for this experiment is different from many others in that it greatly simplifies the circuitry by eliminating noise reduction components, accomplishing this via software-based data post-processing.

The electrical signals generated by the heart can be detected on the surface of the skin. In theory one should be able to grab two leads of a standard voltmeter and see the voltage change with

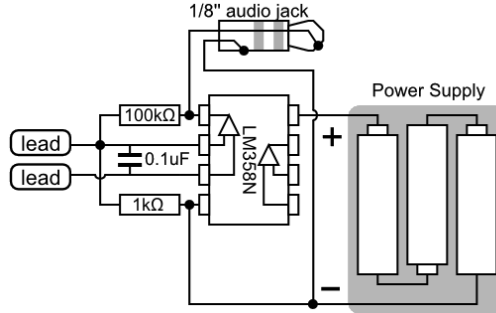


Figure 5: Simple ECG circuit

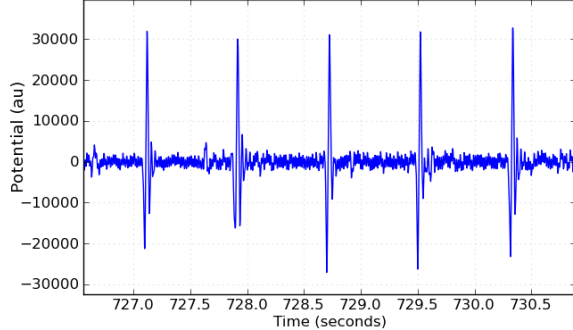


Figure 6: ECG signal of unclassified subject

each heart beat. However, since the fluctuations are rapid and the signal is extremely weak (a few millionths of a volt) by the time it reaches the skin, it is difficult to detect without amplification. A simple way to amplify the electrical difference between two points is via an operational amplifier. The gain on an op-amp is controlled by varying the resistors attached to it. Unfortunately, the amplifier also amplifies radiation from a variety of other electrical sources (computers, cell phones, lights, wiring) which is absorbed by the skin and is measured with the ECG. The traditional method for dealing with noise is complicated analog circuitry. However, since the ECG signal is much slower in comparison to the characteristic, repeating, high-frequency noise, it can be separated using digital signal processing software on the computer. In order to digitize the signal, the analog to digital converter found in the common audio input of a computer sound card can be used.

The circuit diagram of the ECG system is detailed in Figure 5. The 0.1uF capacitor was used to stabilize the signal and reduce high frequency noise. With the circuit output connected to the audio input of the sound card, a sound editor was used to record the ECG data in live mode. Once the data was recorded, it was post processed by applying a lowpass filter at 30Hz. This eliminated most of the electrical noise ($> 30\text{Hz}$), while leaving the ECG intact ($< 15\text{Hz}$). Since, the low pass filter dramatically decreased the potential of the waveform, the volume of the signal was increased. Finally an auto-gain filter was employed to normalize the heart beat potentials.

The ECG signal of the unclassified subject can be seen in Figure 6. It is clear from the trace that even after processing there is still a lot of noise present. While the p-wave and the t-wave are lost in the noise, the R spike is clearly visible and the RR intervals can be calculated. A Poincaré plot of the RR intervals (Figure 7) of the subject seems to suggest a normal, healthy individual. The shape of the plot follows a “cigar-like” pattern and a quantitative analysis of the standard deviations reveals a low SD1/SD2 ratio of 0.77. This classification is confirmed by the DFA analysis, shown in

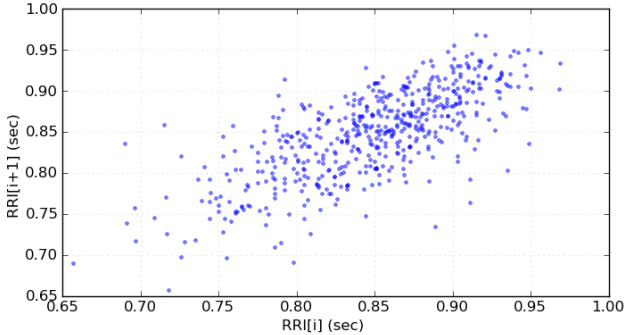


Figure 7: Poincaré plot of unclassified subject

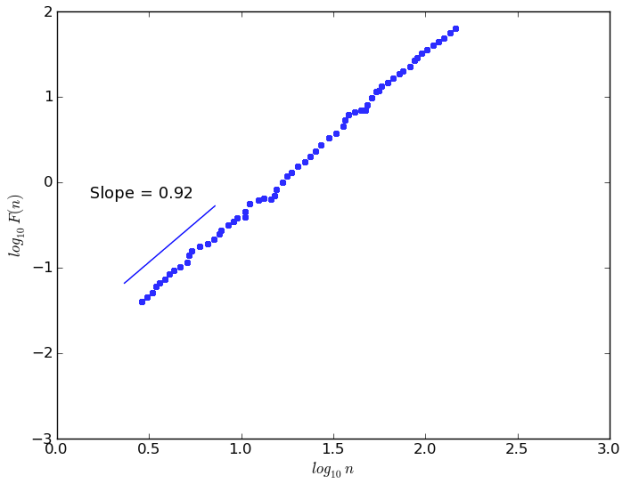


Figure 8: DFA analysis of unclassified subject

Figure 8, where the scaling exponent ($\alpha = 0.92$) is a value close to 1, indicating a healthy subject.

6 Conclusion

Methods from nonlinear dynamics provide valuable information regarding the dynamics and structure of beat-to-beat time series. In this paper, we explored the feasibility of using nonlinear analysis methods in a clinical setting. More specifically, Poincaré plots, LLE, and DFA methods were used in analyzing HRV of two data sets (normal and AF) from PhysioNet. While our analysis allowed us to clearly differentiate the subjects, the data length required varied depending on the method used. Of the three methods used, calculating Lyapunov exponents required the most amount of data, with an average of 5.5 hours of data, while Poincaré plots and DFA required an average of 90 minutes of data. In a clinical setting, both Poincaré plots and DFA would serve well in characterizing a patient, while Lyapunov exponents would be too time intensive. To test our hypothesis, we designed and implemented a simple ECG circuit and gathered 90 minutes of data from an unclassified subject. A Poincaré and DFA analysis of the data suggests a healthy normal individual.

References

- [1] A Babloyantz and A Destexhe. Is the normal heart a periodic oscillator? *Biol Cybern*, 58(3):203–11, 1988.
- [2] A. L. Goldberger, L. A. N. Amaral, L. Glass, J. M. Hausdorff, P. Ch. Ivanov, R. G. Mark, J. E. Mietus, G. B. Moody, C.-K. Peng, and H. E. Stanley. PhysioBank, PhysioToolkit, and PhysioNet: Components of a new research resource for complex physiologic signals. *Circulation*, 101(23):e215–e220, 2000 (June 13). Circulation Electronic Pages: <http://circ.ahajournals.org/cgi/content/full/101/23/e215>.
- [3] Ary L. Goldberger, Luis A. N. Amaral, Jeffrey M. Hausdorff, Plamen Ch. Ivanov, C.-K. Peng, and H. Eugene Stanley. Fractal dynamics in physiology: Alterations with disease and aging. *Proceedings of the National Academy of Sciences of the United States of America*, 99(Suppl 1):2466–2472, 2002.
- [4] H. Kantz, J. Kurths, and G. Mayer-Kress. *Nonlinear Analysis of Physiological Data*. Springer, 1998.
- [5] C.-K. Peng, S. Havlin, H. E. Stanley, and A. L. Goldberger. Quantification of scaling exponents and crossover phenomena in nonstationary heartbeat time series. *Chaos*, 5:82–87, March 1995.
- [6] Michael T. Rosenstein, James J. Collins, Carlo J. De Luca, and Corresponding Michael. A practical method for calculating largest lyapunov exponents from small data sets. *Physica D*, 65:117–134, 1993.
- [7] Tim Sauer. Interspike interval embedding of chaotic signals. *Chaos*, 5(1):127–132, 1995.
- [8] Floris Takens. Detecting strange attractors in turbulence. *Dynamical Systems and Turbulence*, pages 366–381, 1981.
- [9] A. Voss, S. Schulz, R. Schroeder, M. Baumert, and P. Caminal. Methods derived from nonlinear dynamics for analysing heart rate variability. *Royal Society of London Philosophical Transactions Series A*, 367:277–296, January 2009.
- [10] M A Woo, W G Stevenson, D K Moser, R B Trelease, and R M Harper. Patterns of beat-to-beat heart rate variability in advanced heart failure. *Am Heart J*, 123(3):704–10, 1992.

Investigating Baseball Pitch Equations of Motion to Determine ‘Sensitive’ Pitch Parameter Values

Ashok Basawapatna

University of Colorado Boulder

Department of Computer Science Boulder, CO 80303

basawapa@colorado.edu

Chaotic Dynamics Final Project, Professor Elizabeth Bradley

ABSTRACT

When looking at system dynamics, ‘sensitivity’ refers to a small change in initial conditions or parameters yielding a comparatively sizeable change in trajectories over time. In baseball, for example, altering a baseball pitch by inches in both final location and trajectory could be the difference between balls, strikes, pop flies and home runs. This paper investigates how the trajectories of various baseball pitches change due to slight alterations in parameter values and initial conditions for the differential equations that govern the ball’s motion. Once the most sensitive parameter values are discovered, a sensitive pitch is determined from this analysis. Finally, through using major league baseball Pitch f/x data, pitchers who throw sensitive pitches are identified along with the type of actual in-game pitches that tend to be sensitive.

Categories and Subject Descriptors

N/A

General Terms

N/A

Keywords

Chaotic Dynamics, Final Project, Runge Kutta, Baseball Pitch Trajectories, Sensitive Pitches,

1. INTRODUCTION

In baseball the difference between a ball and strike is a matter of inches. Any variable that yields a small change in pitch location cannot only change a given at-bat, but also, the course of a game. Being able to identify the parameters that most effect pitch trajectory and final location, as well as being able to find the degree to which these parameters effect trajectory and pitch location, could be useful in categorizing ‘sensitive pitches’—i.e. pitches wherein a slight change in parameter values or initial conditions yields a greater than normal variation in final ball location and velocity. Such analysis could give insight into the in-game effectiveness of these sensitive pitches as well as how successful pitchers who throw these sensitive pitches are.

In order to do the above analysis we must first better understand the forces that act upon a ball as it flies through the air. For this project, we will specifically be looking at the equations of motion that describe fastball, curveball, slider, and screwball. Figure 1 depicts the spin on these 4 pitches (as thrown by a right handed pitcher) [1].

Previous research covers the analysis of baseball pitch trajectories including spin parameters [5], trajectory tracking [6], and the analysis of specific in-game pitches [7,9]. Specifically, [7] calculated and analyzed the sensitive trajectories of knuckleballs.

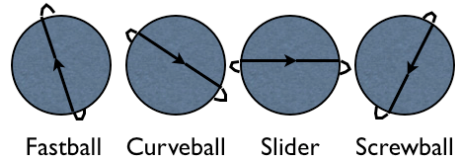


Figure 1: A depiction of the four baseball pitches (for a right handed pitcher), with their respective spins, included in this project

Furthermore, previous Pitch f-x research has looked at automatic pitch classification from Pitch f-x data [4].

As a pitch flies through the air, three factors determine its resulting velocity at each point of its trajectory. First, the ball has an initial velocity due to the force applied by the pitcher throwing the ball towards home plate. Second, air resistance yields a drag force that counteracts the ball’s velocity. Finally, there is a Magnus force due to the spin of the ball. The velocity, drag force and Magnus force are depicted in Figure 2 [2].

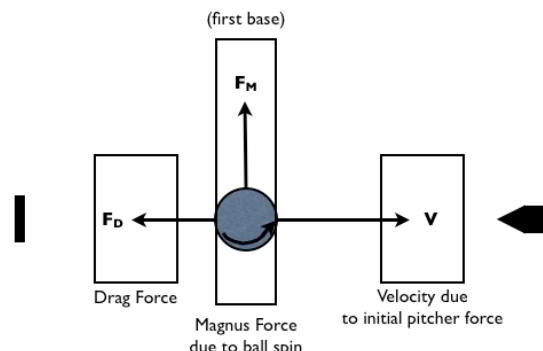


Figure 2: Factors that determine a given pitch’s trajectory: drag force, Magnus force, and velocity due to the pitcher’s initial force

Figure 2 is a top down ‘birds eye view’ perspective; thus, the component of Magnus force pointing towards the first base side originates from the counter-clockwise spin of the baseball around an axis pointing outwards from the page towards the reader (from the perspective in Figure 2). The Magnus force always acts perpendicular to the axis of spin [1]. Figure 3 gives a closer look at parameters that lead to the Magnus force in Figure 2.

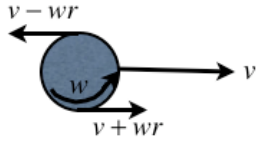


Figure 3: The Magnus force is caused the air on one side of the ball travelling faster than the other side yielding a low pressure system on the slower travelling side and a resulting force in that direction. v is velocity, w is rotation speed and r is ball radius.

Figure 3 depicts the two sides of the ball moving at different velocities. Since air is moving past the ball faster on one side and slower on the other, a low pressure system forms towards the slower (first base side in this case) of the ball resulting in the Magnus force we see in Figure 2. The Magnus force parameters of spin speed and axis of rotation, along with the initial velocity of the ball, are the main system parameters/initial conditions we will be altering to detect sensitive pitches in this paper.

2. METHOD

2.1. The Equations of Motion

The axes we will use for the baseball equations of motion are as follows:

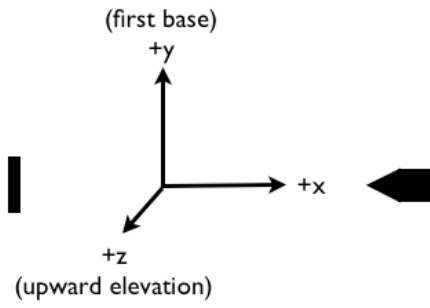


Figure 4: The axes we will be using. $+x$ is towards homeplate, $+y$ is towards first base, and $+z$ points towards the sky

The differential equations of motion we will use for the flight of a pitched baseball are as follows:

$$\begin{aligned}\frac{dx}{dt} &= v_x \\ \frac{dy}{dt} &= v_y \\ \frac{dz}{dt} &= v_z \\ \frac{dv_x}{dt} &= -F(v)v v_x + B w (v_z \sin \phi - v_y \cos \phi) \\ \frac{dv_y}{dt} &= -F(v)v v_y + B w v_x \cos \phi \\ \frac{dv_z}{dt} &= -g - F(v)v v_z - B w v_x \sin \phi\end{aligned}$$

Equation 1: The Differential Equations of Motion for a pitched baseball [2,3].

In Equation 1, v is the speed of the ball, (v_x, v_y, v_z) is the speed in the (x, y, z) direction respectively, w is the speed of rotation, g is the force of gravity, and Φ is the angle between the z -axis and the ball's axis of rotation. B is an approximation constant equal to $4.1e-4$. This approximation constant enables the Magnus terms to be correct; Ideally, the B term would be speed dependent (ie: dependent on drag); however, for the purposes of baseball pitches at speeds from 50-110 mph, this is assumed to be a correct approximation [3]. $F(v)$ is the drag force related to the ball and thus depends on the speed of the ball. $F(v)$ is approximated to be as follows:

$$F(v) = 0.0039 + \frac{0.0058}{1 + \exp\left(\frac{v - v_d}{\Delta}\right)}$$

Equation 2: The approximation of $F(v)$ where v is the speed of the pitch, v_d is 35 m/s and Δ is 5 m/s [2,3]

Finally, the initial condition is assumed to be:

$$\begin{bmatrix} x(0) \\ y(0) \\ z(0) \\ v_x(0) \\ v_y(0) \\ v_z(0) \end{bmatrix} = \begin{bmatrix} 0 \\ 0 \\ 0 \\ v_o \cos(\theta) \\ 0 \\ v_o \sin(\theta) \end{bmatrix}$$

Equation 3: The initial conditions of a baseball pitch that we use for Equation 1.

Where θ is the initial elevation of the ball and v_o is the initial speed. Therefore, all the initial velocity is assumed to be in the x

and z direction with the amount in each direction based on the initial angle of elevation. Thus, the only ball movement in the y direction comes from the Magnus force terms in Equation 1. Also, from Equation 3 we see that the pitch is assumed to start at $(0,0,0)$ regardless of the pitcher's height, release point etc.

It should be noted that Equation 1 only takes into consideration the Magnus force based on the angle between the ball's axis of rotation and the z -axis completely ignoring the Magnus force due to the angle between the ball's axis of rotation and the x or y -axis. [4] actually shows the full equations of motion, including these terms, however, justifies eliminating these terms from the equations of motion saying that the force from this spin is assumed to be small. Another thing to note is that these equations assume that the ball's rate of spin does not change as it travels through the air. In actuality, the rate of spin should decrease as it travels towards the plate.

2.2. Solving the Equations of Motion for Sensitive Parameters

The general method we use to detect sensitive pitches is to take parameters we want to investigate and change them slightly while keeping every other parameter/initial condition constant. For every parameter value, we solve the equations of motion (Equation 1) using fixed step fourth order Rungu Kutta with a timestep of .0001 seconds [1]. After we have obtained all the trajectories that correspond to slight variations of a particular parameter, we go through and compare the ending point (ie: ball's point in space when it crosses home plate and its speed) of each result with the subsequent result (the smallest unit of change in parameter). The adjacent parameter values which exhibit the greatest difference in end point position and velocity are assumed to be the parameter values with the greatest sensitivity. Doing this for each parameter should give us a sensitive pitch profile.

For the purposes of this paper, the values we alter are the speed of rotation (w), the axis of rotation (Φ) as well as the initial conditions: speed (v_o) and initial elevation angle (θ). It should be noted that when altering a particular one of these parameters/initial conditions, we chose arbitrary constant values for the other parameters; it was assumed that the parameter/initial condition we were altering would be sensitive at the same value independent of the values of other parameters/initial conditions. This assumption might not actually be true for every parameter/initial condition we alter. For example, in the trivial case, if we were to set $w=0$, we would not expect that small or large scale changes in Φ would make any difference in pitch trajectory. Time constraints limited the research to just 1 combination-- given more time, ideally, we could go back and do every combination of parameter/initial condition. Though the analysis used in this paper might not return the most sensitive pitch because of the assumption made, it should nevertheless return a sensitive pitch for given parameter/initial condition values used.

Finally, after discovering the sensitive values for every parameter/initial condition, a Pitch f/x profile was made for the pitch having all these sensitive parameter/initial condition values. Then this Pitch f/x profile, with tolerances set on each Pitch f/x parameter, was compared to every pitch thrown in 2009. The tolerances were slowly increased until a size able number of pitches were detected to determine the closest real major league pitch with the sensitivity values described above. The Pitch f/x parameters used for comparison are as follows (note that Pitch f/x uses a different coordinate system-- they swap the x and the y coordinates we use

in Figure 4, so their x is our y etc.): start_speed, end_speed, pfx_x and pfx_z (the furthest deviation that a pitch trajectory has in the x and z direction from the straight line trajectory), (v_{xo}, v_{yo}, v_{zo}) --initial velocity conditions for each component, break_y (break in the y direction), break_angle (horizontal angle of break measured from vertically down with left being positive and right being negative), and spin_rate (speed of spin) [8].

3. RESULTS/DISCUSSION

Each parameter/initial condition was varied based on realistic in-game values one might actually see. These values are as follows.

Rate of spin, w , was altered from 30 rotations per second to 45 rotations per second in increments of 1 rotations per second with $v_o=37.9984$ m/s (~85 mph), $\Phi=0$, and $\theta=0$. The following plot is all the trajectories computed from this calculation:

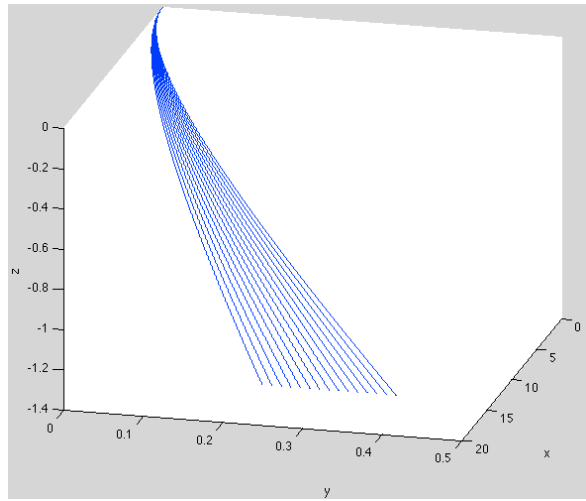


Figure 5: The trajectories obtained by altering w from 30 rps to 45 rps with $v_o=37.9984$ m/s (~85 mph), $\Phi=0$ degrees, and $\theta=0$ degrees.

As w increases, the ball fans out in the y axis which is what we would expect with a $\Phi=0$. Also, as one might expect, the greatest difference happened at $w= 45$ rps. The following graph is the result of the most sensitive w value trajectories plotted together (ie the trajectories that had the greatest difference-- as mentioned above we only looked at parameter and initial condition differences of 1 unit).

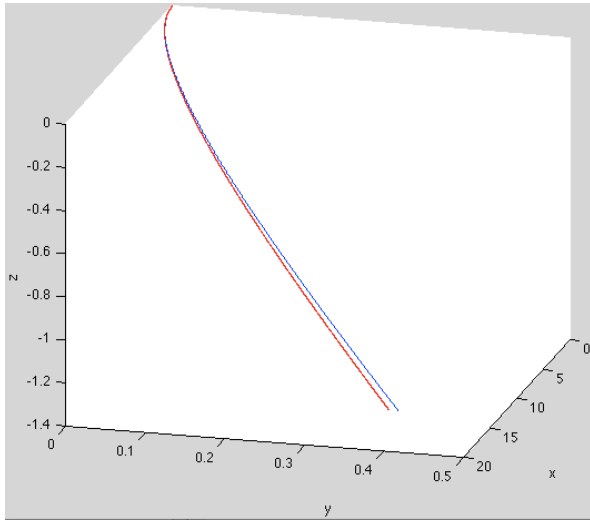


Figure 6: The trajectories obtained with the most sensitive values w equal to 44 and 45 rps with $v_o=37.9984$ m/s (~85 mph), $\Phi=0$ degrees, and $\theta=0$ degrees.

Similarly the axis of rotation, Φ , was altered from 0 to 90 degrees by units of 1 degree (In retrospect it should have been altered from -90 to 90, but assuming symmetry we should get the similar results; this result should correspond to a right hander's curveball) with $w=30$, $v_o=37.9984$ m/s, and $\theta=0$. The following graph is all the Φ trajectories plotted together.

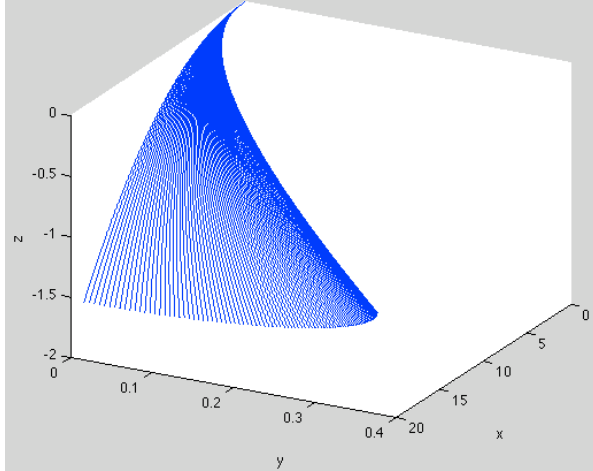


Figure 7: The trajectories obtained by altering Φ from 0 degrees to 90 degrees with $v_o=37.9984$ m/s (~85 mph), $w=30$, and $\theta=0$ degrees.

As one can see, with a low Φ , analogous to the slider pitch in Figure 1, the ball fans out more horizontally and breaks less. With a high Φ the ball breaks more with less horizontal movement. The following graph is the result of the most sensitive Φ values plotted together.

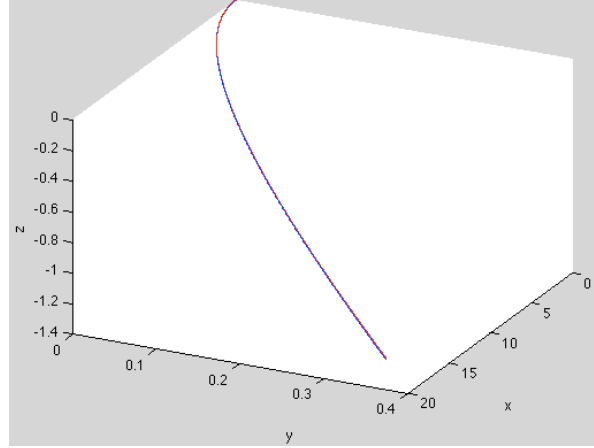


Figure 8: The trajectories obtained with the most sensitive Φ values equal to 7 and 8 degrees with $v_o=37.9984$ m/s (~85 mph), $w=30$, and $\theta=0$ degrees.

In Figure 8 we see that there is very little difference between the two trajectories: one breaks slightly more and one has slightly more horizontal movement.

Initial velocity, v_o , was altered from 36 m/s to 45 m/s (~80 mph to ~100 mph) with $w=30$, $\Phi=0$, and $\theta=0$. The actual change in initial condition vector this represents can be calculated by using Equation 3. The following is a plot of all the trajectories computed from these calculations:

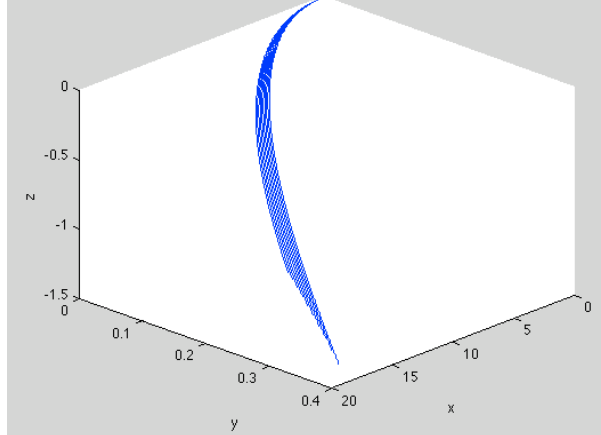


Figure 9: The trajectories obtained by altering v_o from 35 m/s to 45 m/s with $\Phi=0$ degrees, $w=30$, and $\theta=0$ degrees.

For greater velocities, the pitch has less time to break and to curve horizontally. Thus, the faster pitches have a straighter trajectory whereas the slower pitches have more movement (it should be noted that axis orientation was intentionally changed slightly to better depict this phenomenon). The following graph is the result of the most sensitive v_o values plotted together.

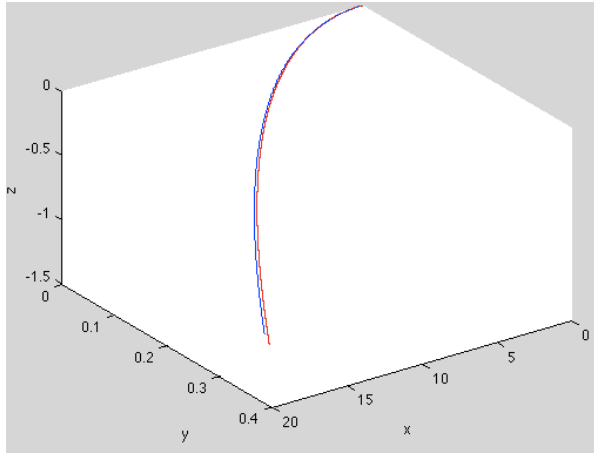


Figure 10: The trajectories obtained with the most sensitive v_o values equal to 39 m/s and 40 m/s (~87.24 mph and ~89.47 mph) with $\Phi = 0$ degrees, $w=30$, and $\theta=0$ degrees.

At the values of v_o equal to 39 m/s and 40 m/s we see that the slower trajectory breaks and moves horizontally noticeably more than the faster trajectory.

Finally, we alter initial elevation, θ , from -2 degrees to 2 degrees in increments of 1 with $w=30$, $\Phi=0$, and $v_o=37.9984$ m/s. Again, one can use Equation 2 to calculate the initial state vector this represents. The following is a plot of all the trajectories computed from these calculations.

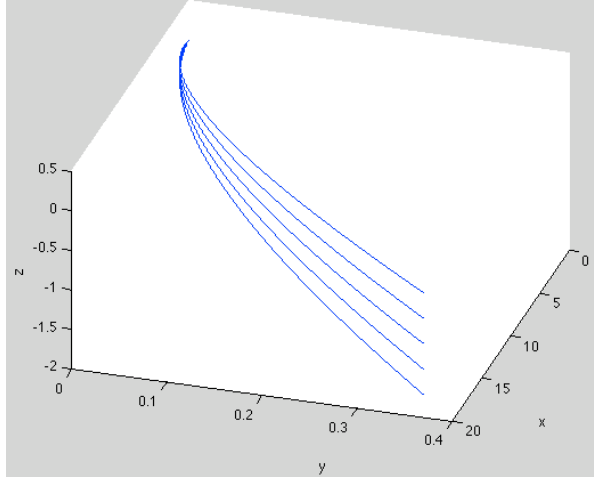


Figure 11: The trajectories obtained by altering θ from -2 to 2 degrees with $\Phi = 0$ degrees, $w=30$ rps, and $v_o=37.9984$ m/s

This is pretty uninteresting; basically throwing a ball at a different initial elevation angle leads to the ball's ending elevation being altered dramatically. One would expect this to be the case; however, without knowing the extent to which this does or does not happen in a game it is hard to justify not analyzing this. For example, over the course of a game, as a pitcher's arm gets tired, one might suspect that the initial angle of elevation might change.

The greatest theta difference was found to be when theta equaled -1 degrees and -2 degrees (since these trajectories are easily distinguishable in Figure 11, I decided not to plot them).

Putting all these trajectory values together we can obtain the most sensitive two pitches. The following is 2 graphs, one of the most sensitive two trajectories with the initial angle, θ , altered (Figure 12), and one of the most sensitive two trajectories with the initial angle not altered (Figure 13).

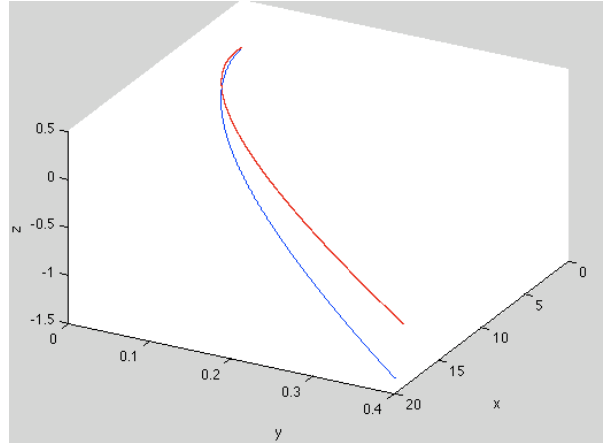


Figure 12: Two trajectories, one with values $(w, \Phi, v_o, \theta) = (45$ rps, 8 degrees, 40 m/s, -2 degrees) and the other with values $(w, \Phi, v_o, \theta) = (44$ rps, 7 degrees, 39 m/s, -1 degrees)

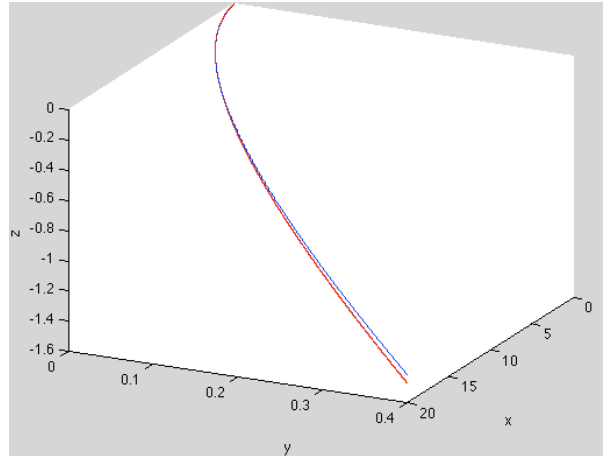


Figure 13: Two trajectories, one with values $(w, \Phi, v_o, \theta) = (45$ rps, 8 degrees, 40 m/s, -1 degrees) and the other with values $(w, \Phi, v_o, \theta) = (44$ rps, 7 degrees, 39 m/s, -1 degrees)

From the above plots we see that our most sensitive pitch, when we take out the change in initial elevation, has a small difference in location with very slight changes in initial/conditions and parameter values. Computing the difference in final state for the pitches in Figure 13, we see that our two pitches have the following differences (in absolute value) when they reach home plate.

$$\begin{bmatrix} x(end) \\ y(end) \\ z(end) \\ v_x(end) \\ v_y(end) \\ v_z(end) \end{bmatrix} = \begin{bmatrix} .00178(m) \\ .000647(m) \\ .0551(m) \\ 1.072(m/s) \\ .0467(m/s) \\ .0664(m/s) \end{bmatrix}$$

Figure 14: The differences in final state, in absolute value, between the two two pitches thrown in Figure 13

With a small change in pitching parameters and initial conditions, the two pitches have slight a change in x velocity and in break (z) when they reach home plate (2.4 mph and 2.16 inches respectively). This small change should be expected based on the minute amount we changed the two pitches. However, a few inches on a breaking ball could be the difference between a ball that gets hit hard and a ground out etc.

The pitches in Figure 12 and 13 are not realistic pitches by any measure. They both refer to a 90 mph curveball which would very rarely, if ever, happen in a game. The range of parameter values used were realistic with respect to that parameter but not necessarily realistic when taken in combination with the other parameter values. Therefore when returning the most sensitive pitch, the pitch returned should not be thought of as an actual pitch, but rather, a combination of sensitive parameters. The trajectories in Figure 12 and 13 give us an idea as to the scale of change we are talking about.

Finally, Pitch f-x data was analyzed to see what type of pitch this would most closely correspond to in baseball. This analysis was done informally, starting each Pitch f-x parameter out with a given tolerance and slowly increasing the tolerances until a sizeable amount of pitches from 2009 were obtained. Pitch f-x can be inaccurate and the tolerance values were somewhat arbitrarily changed among other things. Therefore, these results should be taken more as a proof of concept as to how one might go about transferring this sensitivity analysis to actual in-game pitches and not as infallible conclusions.

The pitch that the above sensitive pitch most consistently corresponded to was a breaking ball. Specifically, in Pitch f-x terms, the pitch usually had approximately the following properties: startSpeed: 80.7 mph, endSpeed: 75.0 mph, vxo: 1.607 ft/s, vyo: -118.285 ft/s, vzo: -3.808 ft/s, pfx_x: 1.293 inches, pfx_z: -4.043 inches, breakLength: 8.0 inches, breakAngle: -14.2 degrees, spinRate: 1078.845 rotations per minute. The pitchers in 2009 who threw this pitch the most were found to be Justin Verlander, Dan Haren, Josh Hammel and Chris Volstadt. All of these pitchers had fairly good 2009 seasons, and with the analysis done thus far, this makes sense because all we have shown is that they all have a pretty significant breaking ball. One might expect a good breaking ball to go hand in hand with success. However, one might also suspect that someone who overly relies on a ‘sensitive pitch’ might possibly miss location leading to more walks and hits as well as more swing through strikes and badly contacted balls because of the deceptive location and velocity of two similar looking pitches. Again, a more formal analysis must be done to see if this is actually the case.

4. CONCLUSIONS

This paper alters various pitch parameters and initial conditions to determine what pitch parameter values are the most sensitive and visualizes these parameters to get a better idea as to how slight changes in these initial conditions/parameters effect the trajectory of a given pitch. Specifically, the most sensitive values corresponding to initial speed, initial elevation, rotation speed, and axis of rotation were found.

Future research should focus on limiting the pitches analyzed to realistic pitches and comparing all these realistic parameter values/initial conditions together to better see the coupling effects, if any, yielding bigger changes in trajectories. Using these realistic pitch trajectories, the Pitch f-x study should be made more formal with tolerance values being changed slightly and in a uniform manner for each parameter. The Pitch f-x study should also be done more in-depth to discover what outcome the sensitive pitch usually had in the real in-game scenario. Finally, it might be interesting to analyze knuckleball equations as those trajectories are actually chaotic meaning small scale variations could yield large scale trajectory differences.

5. REFERENCES

- [1] Adair, R. 1990. *The Physics of Baseball*. Harper and Row, New York, N.Y.
- [2] Fitzpatrick, R. The Physics of Baseball Pitching. Lecture Notes in Phys 329. Updated March 29, 2006. Retrieved March 26, 2010 from University of Texas Austin. <http://farside.ph.utexas.edu/teaching/329/lectures/node41.html>
- [3] Giordano, N. 1997. *Computational Physics*. Prentice-Hall, Upper Saddle River, NJ.
- [4] Nathan, A. Analysis of PITCHf/x Pitched Baseball Trajectories. Department of Physics, University of Illinois, Urbana, IL. December 9, 2007.
- [5] Jinji, Tsutomu, and Sakurai, Shinji. 2006. 'Baseball', Sports Biomechanics, 5: 2, 197 — 214.
- [6] Alaways, L., Mish, S., and Hubbard, M. 2001. "Identification of Release Conditions and Aerodynamic Forces in Pitched Baseball Trajectories." *Journal of Applied Biomechanics*. vol. 17 pp. 63-76.
- [7] Watts, R. and Sawyer, E. 1975. "Aerodynamics of a Knuckleball." *American Journal of Physics*. vol. 43 pp. 960-963.
- [8] Nathan, A. MLB Extended Gameday Pitch Logs. Updated March 8, 2010. Retrieved March 23, 2010 from University of Illinois. <http://webusers.npl.illinois.edu/~a-nathan/pob/tracking.html>
- [9] Watts, R. and Sawyer, E. 1987. "The Lateral Force on a Spinning Sphere: The Aerodynamics of a Curveball." *American Journal of Physics*. vol. 55 pp. 40-44.

An Examination of the Local Dynamics of Computer Performance

Gregory Ichneumon Brown
CSCI 5446: Chaotic Dynamics
University of Colorado at Boulder
browngp@colorado.edu

Abstract—Computer systems are dynamical systems that can be characterized using the tools of nonlinear dynamics. In this paper we examine which nonlinear techniques can be applied to the analysis of computer performance data from real benchmark programs. We find that basic delay coordinate embedding and analysis of unstable periodic orbits provide insights into the dynamics of the system. However, calculations of system invariants such as the largest Lyapunov exponent and correlation dimension of the system are not practical given the limited amount of data in the data sets considered. This limitation seems as if it would be true for many cases when looking at the local dynamics of computer performance for real programs.

I. INTRODUCTION

Computer systems often appear to behave somewhat randomly when someone tries to characterize their performance over time. For instance the number of environment variables defined can cause a dramatic variance in the run time of standard SPEC benchmarks.[3] However, this "randomness" is mostly an artifact of the nonlinear dynamics of the system and its sensitive dependence to seemingly inconsequential aspects of the system's state.

Mytkowicz, Diwan, and Bradley [1] recently characterized computer systems as nonlinear dynamical systems. Their analysis looked at the dynamics of filling matrices in row-major and column-major order on different computer architectures. They found that the same program could behave periodically on one system and chaotically on another system simply due to the different computer architectures involved. They characterized these systems using standard methods for analyzing nonlinear systems: delay coordinate embedding and determining fractal dimension, entropy, and the largest Lyapunov exponent.

However, in order to accurately characterize the system using many of these methods a very large number of samples need to be taken of the system. For real world applications it is generally not possible to run the program longer in order to generate this volume of data. Furthermore, a single program often exhibits different regions of behavior as it transitions from one loop to another and it is not possible to control how long these regions last.

To understand these transitions, we propose thinking of a computer system as moving between a series of attractors based upon how the program perturbs the system. This is much like changing the physics of a double pendulum in a complex way while the pendulum is moving. For some period of time the system is pulled towards some

periodic or chaotic attractor and exhibits periodic or pseudo-periodic behavior. Then when the physics change the system undergoes a bifurcation, follows some transient path, and then settles on a different attractor.

In this paper we look at how some of the nonlinear system analysis techniques can be applied to the local attractors within a time series trace of computer performance metrics. We first look at the problem of applying delay coordinate embedding and present how we found a reliable embedding dimension despite the small amount of data. Then we examine using this embedding to determine the largest Lyapunov exponent, fractal dimension, and entropy for a section of the time series data and we find that it is difficult to use these measurements because of the limited amount of data available. Finally we look at finding local unstable periodic orbits in the time series and hypothesize that this information may provide insight into the relationships between different metrics from the same system.

A. Experimental Data

For performing our analysis we focused on two data sets from Hauswirth, Sweeney, and Diwan's Vertical Profiling experiments. [2] Choosing data that has previously been thoroughly analyzed enables us to examine how different metrics from running the same program relate to one another. These multiple metrics also provide different views into the dynamics of the same system. Additionally this removes the difficult problem of having to rigorously capture new data.

The datasets were generated running two different programs on a PowerPC POWER4 machine with the AIX operating system and Jikes RVM as the Java Virtual Machine. Metrics were sampled from all levels of the system: hardware, operating system, virtual machine, and the application.

The first data set consists of 30 metrics sampled over time while running the JBB benchmark from SPECjbb2000. [4] In this dataset Hauswirth, et al had examined and identified the cause for a gradual increase in the number of instructions per cycle (IPC) metric. In our experiments we focus on comparing the gradual increase in the IPC (referred to as "JBB section 1" throughout the rest of this paper) to the IPC after the gradual increase has settled out ("JBB section 2"). The gradual increase data we look at has a total of 750 samples. Figure 1 shows the region of the IPC time series that corresponds to the gradual increase.

The second data set has 202 metrics captured while running the DB benchmark from SPECjvm98.[5] The anomaly examined in this dataset by Hauswirth, et al was a periodic

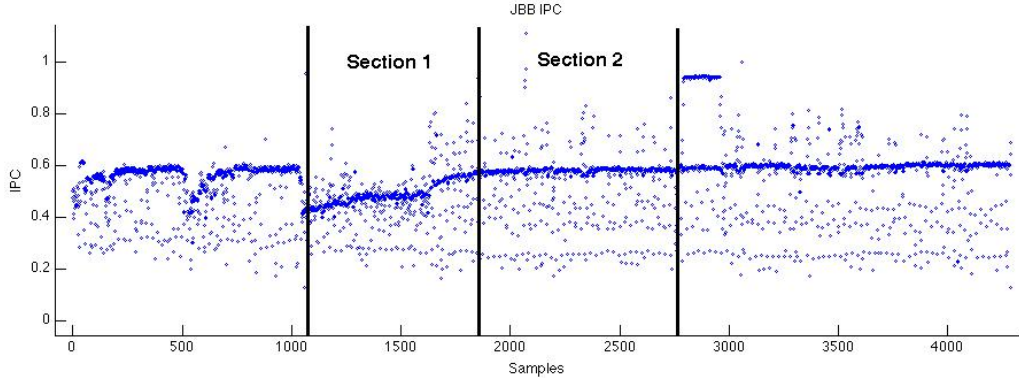


Fig. 1. JBB IPC metric waveform.

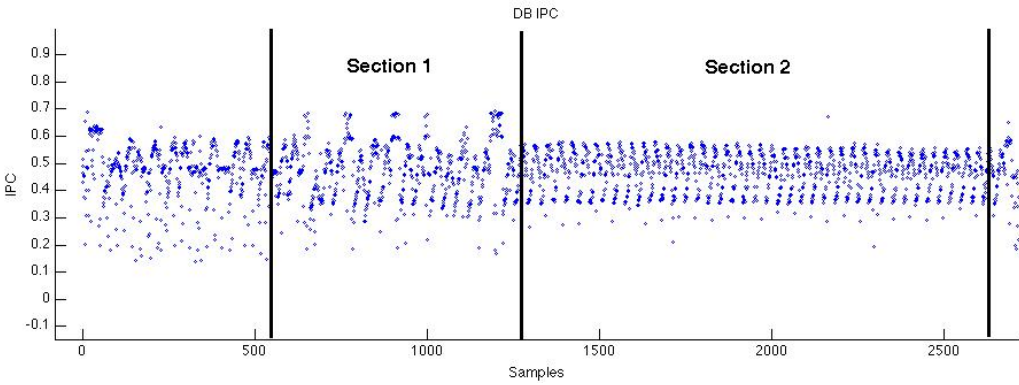


Fig. 2. DB IPC metric waveform.

behavior in the IPC metric. We also focused on this same periodic behavior ("DB section 2") and compared it to previous periodic behavior which had additional irregular patterns in it("DB section 1"). There is a total of 1300 samples showing this periodic behavior. Figure 2 depicts the two regions which we examined.

B. Data Analysis

For most of our data analysis we made use of the functions in the TISEAN [6] package of nonlinear analysis functions. The particular functions we used were:

- *mutual*: Calculate the mutual information between samples.
- *false_nearest*: Varies the embedding dimension and calculates the number of neighbors each point has in the embedded state space.
- *delay*: Embed the dataset with delay coordinate embedding.
- *lyap_k*: Estimates the largest Lyapunov exponent from a dataset.
- *upo*: Find unstable periodic orbits of a particular period.

Since a computer has discrete states that it transitions between rather than being a continuous time system we treated all of our data as a non-linear map between successive states.

II. DELAY COORDINATE EMBEDDING

A common first step in analyzing a time series sampling of a non-linear dynamic system is to use delay coordinate embedding to reconstruct a state space that is topologically equivalent to the original state space.[7] The embedding projects the data into a higher dimension by having each additional dimension represent the sample some time τ later. So in order to complete the embedding a τ and an embedding dimension m must first be determined.

A. Determining τ

For each metric in each data set we determined τ using the standard method of finding the first minimum of the mutual information between all of the samples in the time series.[7] To calculate mutual information we used TISEAN's *mutual* command and then estimated the first minimum as the first point where an increase in τ would cause the mutual information to increase by 0.5%.

This calculation was done for all of the time series within a dataset and τ was chosen to be the median τ from all the time series in each dataset. This resulted in a τ of 2 for JBB and 8 for DB. Figure 3 shows histograms of the τ values from each of the datasets.

Using the same τ across all of the waveforms in a dataset is justified because the samples are being taken at the same

frequency for all of the metrics. Inspection of some of the metrics where τ had been determined to be much larger than the median indicates that the reason for the large τ is that there really was no first minimum in the mutual information between samples, and the minimum detection algorithm was just choosing a minimum based on noise in the mutual information metric. This case usually occurred because the metric in question was showing little to no activity during the program run.

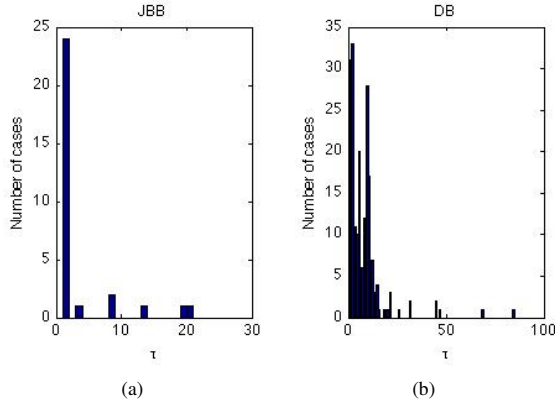


Fig. 3. Histograms of τ for (a) JBB and (b) DB.

B. Determining m

Using the calculated τ value the embedding dimension m was then estimated using the false nearest neighbors method.[8][9] TISEAN's *false_nearest* function indicates how many neighbors a sample has as the embedding dimension increases. For each time series we chose the first m where the false neighbors decreased by less than 0.1%.

Figure 4 shows the distributions of embedding dimensions found for the two datasets. Similar to our calculations of τ we chose an overall embedding dimension $\hat{m} = \text{median}(m) + 1$ as our dimension for all of the time series in that dataset. We added one to the embedding dimension to ensure that the embedded data would fully reflect the dynamics of the system. For both datasets we found and used an embedding dimension of 12.

Interestingly, this embedding dimension is the same one found by Mytkowicz, et al when examining loops filling in matrices on x86 architectures.[1] One would expect that our datasets using the PowerPC POWER4 processor, with a less complicated architecture than the Intel Pentium 4 or Intel Core2 from their work, would exhibit lower dimensional behavior. However, these datasets are also more complicated programs and running on top of a Java virtual machine which may add a few dimensions to the system. A wider investigation on the effective dimension of different computer systems seems appropriate but is outside of the scope of this paper.

C. State Space

Using these calculated m and τ values we embedded the data from JBB sections 1 and 2. Figures 5(a) and 5(b)

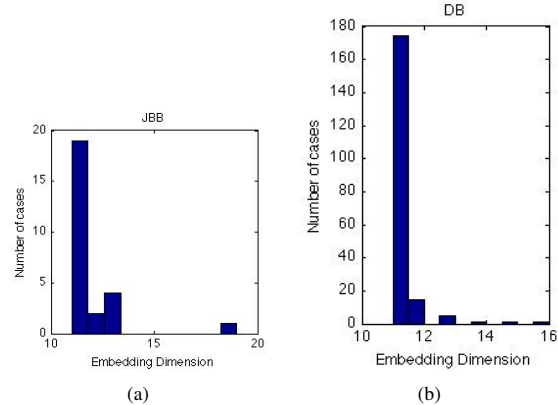


Fig. 4. Histograms of m for (a) JBB and (b) DB.

shows a projection of the embedded data onto the first two dimensions. The embedding for JBB section 2 clearly shows a mostly fixed point with some periodic behavior that can easily be seen to correspond with the slight periodic behavior in that part of the time series. The embedding for JBB section 1 containing the gradual increase shows a similar pattern except that the location of the "fixed point" is moving over time from (0.4,0.4) to (0.6,0.6) as the gradual increase occurs.

Figures 5(c) and 5(d) shows a similar projection of the embedded state space for DB sections 1 and 2. A similar analysis of the state space shows the expected periodicity of section 2. Furthermore the slight decrease in amplitude of the time series data in DB section 2 shows up as the diameter of the projection shrinking over time. The state space for DB section 1 does not exhibit the same regular periodic behavior as section 2, and appears to be more chaotic.

Although these observations about the state space are not terribly surprising when one looks at the time series, it is possible that viewing the data through the prism of an embedded state space trajectory could provide a useful means of examining the time series data. In particular this may be a better representation of the data for use in machine learning techniques since the data points become more separable when they are projected into this higher dimensional space.

III. CALCULATION OF LOCAL INVARIANTS

The number of samples required for effective calculation of the largest Lyapunov exponent (LLE) is a problem still being hotly debated. But even the lowest estimates suggest that to get an accuracy within $\pm 10\%$ for a system with only 3 true dimensions requires 1000 points and increases with at least 3^d as the true dimension d increases. [10] Since the embedding dimension must be greater than twice the true dimension of the system, the computer systems for our datasets clearly have more than 3 dimensions. This indicates that theoretically we have no where near enough data to accurately calculate the LLE.

Nevertheless, it seems worthwhile to consider if there is any information that can be gained from even an inaccurate

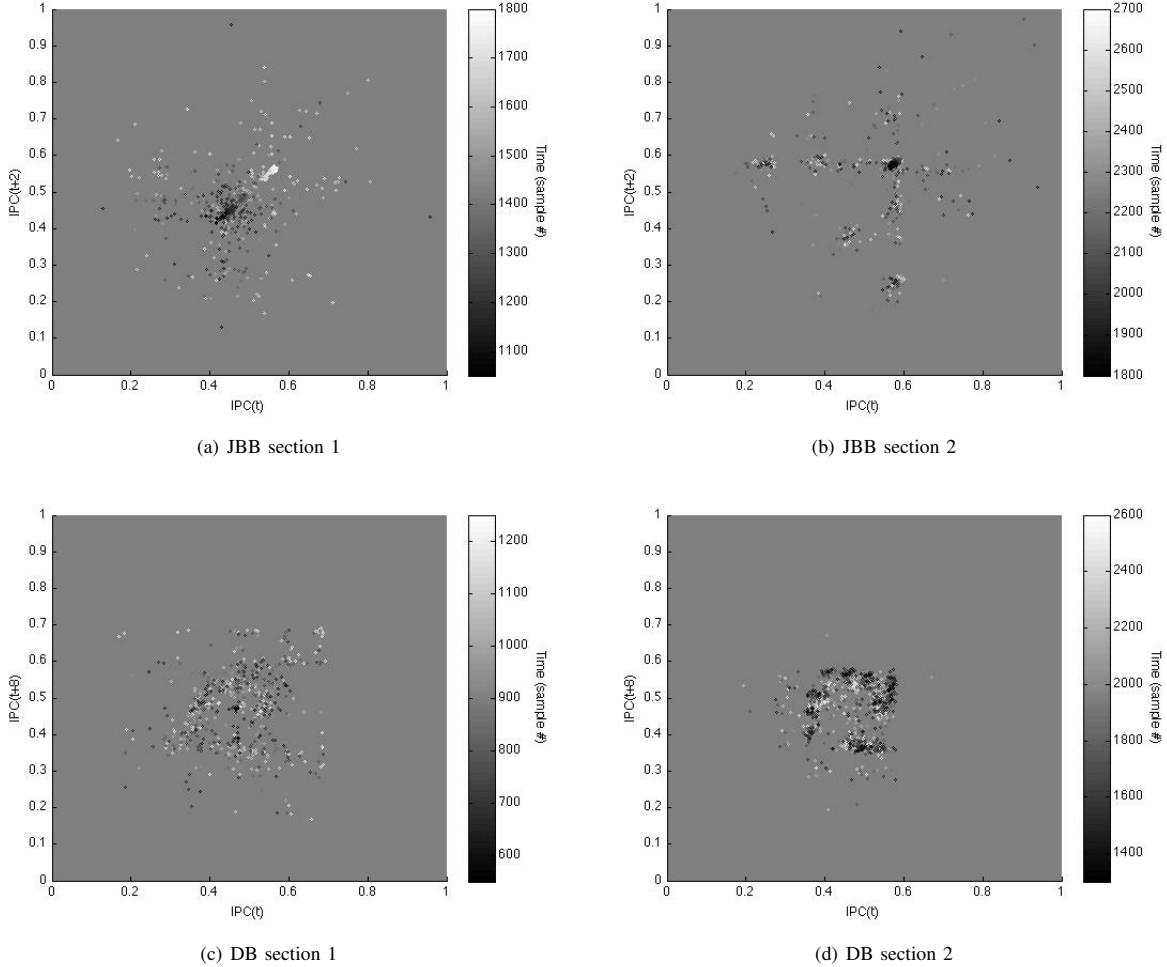


Fig. 5. Embedded State Space projection for (a) JBB section 1, (b) JBB section 2, (c) DB section 1, and (d) DB section 2. The color coding of points corresponds to when in time that point occurred. The color coding makes the gradual increase in JBB section 1 clear as the bulk of the points move towards the upper right as time progresses.

estimation of the largest Lyapunov exponent since it is a good way to characterize the type of an attractor and could give insight into when and how the dynamics change throughout a program run if we could calculate local exponents for multiple windows of the time series.

Using *lyap_k* from TISEAN we calculated the Lyapunov exponents for the four sections in JBB and DB:

- JBB section 1: $\lambda \approx -0.0008$
- JBB section 2: $\lambda \approx -0.0002$
- DB section 1: $\lambda \approx 0.0020$
- DB section 2: $\lambda \approx 0.0010$

Relative to each other these results do match fairly well what we know about these sections of the waveforms. They are all largely periodic which is indicated by lambda being approximately equal to zero. Relative to DB section 2, DB section 1 appears to be more chaotic which is indicated by having a more positive Lyapunov exponent.

However, the process for calculating these values leaves

us with little confidence in them. The output from *lyap_k* requires the user to find a linear scaling region and the slope of that linear region is the LLE. Picking such a scaling region from our outputs was very open to interpretation which leaves us with very little confidence in the final LLE values.

To test these results further we calculated the LLEs corresponding to DB section 2 for all 202 metrics from the DB dataset. In theory since they all come from the same system the LLE should be the same for any of the metrics. The actual results found that the LLE varied from -0.0036 to 0.0106 across the different metrics, and that for 57 of the metrics the LLE could not be determined because there was no visible scaling region in the output of *lyap_k*.

Calculating LLE across all metrics does seem to give a gross approximation of the LLE for the system. However, the wide variation suggests that as anticipated this is not a reliable method of characterizing the system. Based on these results we feel that calculations of the local invariants for the

system are not a practical way to characterize performance data. It could be possible in some cases that the system could be sampled much more quickly thus providing enough data to perform these calculations. However, sampling more quickly will often perturb the dynamics of the running program, thus invalidating the results.

Attempts to calculate the correlation dimension and entropy of the different sections were also not successful. This is an odd result since theoretically calculating the dimension should need quite a bit less data than calculating the LLE. We take this as further confirmation that the local dynamics of real world programs cannot be analyzed using their invariants.

IV. UNSTABLE PERIODIC ORBITS

Since most useful programs consist of some series of loops it makes sense that the periodic behavior in performance metrics would be indicative of what is occurring within the system. One important characteristic of chaotic systems is that they exhibit periodic behavior for brief periods of time before transitioning away to another different period. These unstable periodic orbits (UPOs) can be used to characterize how the system is behaving. For this reason we wanted to explore the relationship between what periods are present in different metrics of the system.

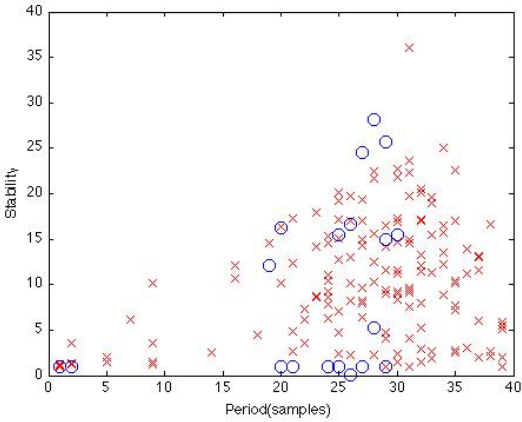


Fig. 6. UPO stability for JBB section 1 (x's) and JBB section 2 (o's) of the IPC metric.

A. Stability of UPOs

Using TISEAN's *upo* function we found the stability of the UPOs in JBB sections 1 and 2 with a period of less than 40 samples.[11] Figure 6 shows the stability of the orbits found for the two sections and which period they occurred at. The *upo* algorithm works by finding patterns that nearly repeat with a particular period in the time series. For this reason section 1 exhibits a much larger number of periods since the IPC is gradually increasing over time and so the UPOs are visiting different regions of state space.

The stability metric which *upo* reports is based on an estimation of the local eigenvalue at that point. These values

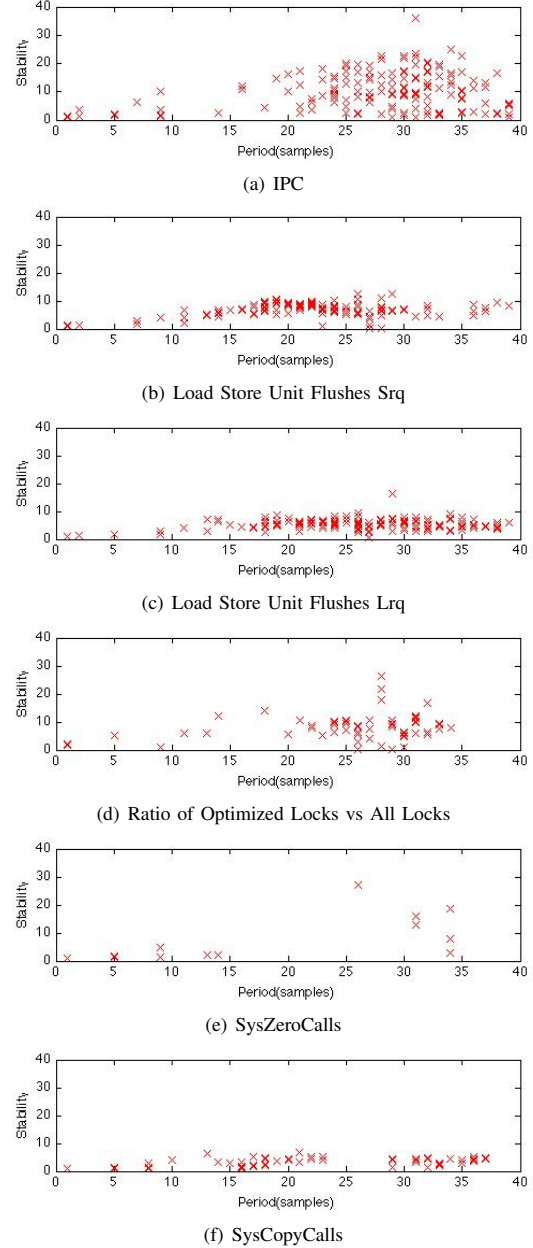


Fig. 7. UPO stability for section 1 of JBB across multiple metrics.

are problematic due to the sparse nature of the data, but the results do suggest that their relative values may be useful. For instance, the obvious dominant periodic pattern throughout the time series is the jump down to around 0.27. This point occurs fairly regularly throughout the entire run of the program and based on inspection of the time series has a period that varies between the mid-twenties and lower thirties. This corresponds with the most stable periods found by *upo*.

To examine how these UPOs appear in other metrics we looked at JBB section 1 for a selected set of metrics. The

resulting periods and their stability are shown in figure 7. Section 1 of the IPC metric has a gradual increase which Hauswirth, et al investigated and created a causality chain for to find the root cause of this performance anomaly. The first step in their causality chain was the Flushes of the Load Store Unit (Figures 7(b) and 7(c)). This then led them to look at the ratio of optimized locks to all locks (Figure 7(d)) as a proxy for how much of the Java code had been optimized over time.

Although it is problematic to draw conclusions from such a small subset of the metrics it seems readily apparent that the UPOs in these three causal metrics appear to be more similar to the UPOs in the IPC metric than the other two metrics that were analyzed. The other two metrics were chosen to be analyzed because based on the authors notes Hauswirth, et al had also considered them as potential causes. Unfortunately due to time constraints on this paper and how long *upo* takes to find UPOs we were not able to run an analysis of all 30 metrics in the JBB dataset.

However, it does seem reasonable that the periods that occur in a metric causing an anomaly would also appear in the anomaly itself. This suggests that an analysis of UPOs may be a useful feature for discriminating between which metrics may indicate the cause of an anomaly. For instance, looking at the percentage of periods that appear in common between two metrics may indicate to what extent they are related. Or the top N most stable periods could be compared.

B. UPOs in State Space

In addition to the stability of the UPO, *upo* outputs a series of points to characterize the path of the orbits it finds. Unfortunately the points in the paths are an average of all the points for that step in the orbit. This averaging corrupts the actual data points such that the path does not correspond to any real points in the data set. Figure 8 shows an orbit of period 28 overlaid onto the embedded state space for JBB section 2. It is expected that the points within a UPO once embedded would overlap directly with the actual data points in the time series. However, as seen in this plot, some of the data points in the orbit do not overlap anywhere near the actual points. This shows how the orbit has been corrupted by the averaging of the data points making this output from *upo* only useful as a rough idea of which points the orbit is visiting. It seems it would be much more useful to have a true trajectory that is representative of the characteristic orbit of a UPO.

V. CONCLUSIONS

In this paper we have examined how some nonlinear dynamics techniques can be used to examine the local dynamics of computer performance of real benchmark programs. The techniques for characterizing the system's invariants (largest Lyapunov exponents, fractal dimension, and entropy) do not appear to be viable methods given the large amount of data needed to accurately estimate these invariants and the small amount of data available for any local region of a program. Additionally, the existing tools for determining unstable

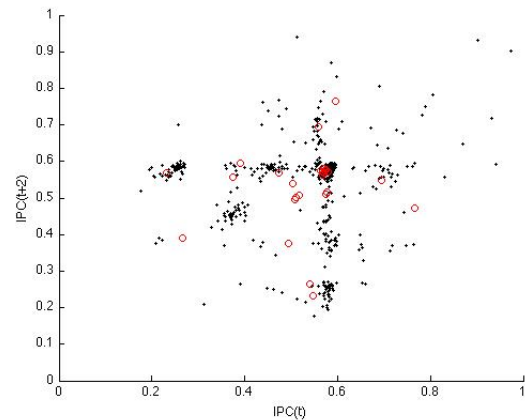


Fig. 8. JBB unstable periodic orbit with period 28. The points in the orbit output by *upo* (circles) does not align with real points from the trajectory (dots).

periodic orbits corrupt the state space of the characteristic orbits they find.

However, some methods do seem to have potential in analyzing computer performance. Delay coordinate embedding provides views of the state space which could be useful in understanding the dynamics of the system. We found that m and τ can be determined by looking at all of the metrics captured from a particular system. This reduces the number of samples needed for any single metric to determine these values. Finding the existence of unstable periodic orbits of local sections of a time series also seems to work well. These orbits also appear to provide a feature for gaining insight into the relationship between different metrics.

VI. FUTURE WORK

Further examination is warranted of how UPOs from different metrics relate to one another. In particular it would be interesting to see if using UPOs as a feature in a machine learning system could help to distinguish between metrics which might be causing a given performance anomaly and those which are not.

Unfortunately *upo* takes a very long time to examine a time series for any particular period, and each period must be examined independently. The time complexity of the algorithm seems to increase with a high polynomial as the period being searched for increases. The authors of the program had actually added a hard-coded limit of 20 for the maximum period which we had to override to examine our datasets. This increasing run time as the period increases prevented us from analyzing the DB dataset because its dominant periods are on the order of 50 to 100 samples.

The characteristic orbits that *upo* outputs for each period it finds are also corrupted by the averaging it does. Not being corrupted, a characteristic orbit might allow comparing orbits of different periods to see how close they are to hitting the same data points. Additionally they might allow comparing orbits that are getting expanded or contracted over time such

as the ones in the JBB gradual increase where some of the points in the orbit are staying mostly the same while other move to new points.

Therefore, for further investigation of the UPOs in computer performance it seems wise to rewrite *upo* to both run faster and produce a characteristic period rather than the mean period which corrupts the orbits actual dynamics. Using this output it would then be interesting to see whether the similarity between the UPOs can be used to discriminate between which metrics may be related to a performance anomaly in another metric.

REFERENCES

- [1] Mytkowicz et al. *Computer systems are dynamical systems*. Chaos: An Interdisciplinary Journal of Nonlinear Science (2009)
- [2] Hauswirth et al. *Vertical profiling: understanding the behavior of object-oriented applications*. Proceedings of the 19th annual ACM SIGPLAN conference on Object-oriented programming, systems, languages, and applications (2004) pp. 251-269
- [3] Mytkowicz et al. *Producing wrong data without doing anything obviously wrong!*. ACM SIGPLAN... (2009)
- [4] Standard performance evaluation corporation. *SPECjbb2000 (java business benchmark)*. <http://www.spec.org/jbb2000>
- [5] Standard performance evaluation corporation. *SPECjbb2000jvm98 benchmarks*. <http://www.spec.org/jvm98>
- [6] R. Hegger, H. Kantz, and T. Schreiber, *Practical implementation of nonlinear time series methods: The TISEAN package*, CHAOS 9, 413 (1999)
- [7] H Kantz and T Schreiber *Nonlinear Time Series Analysis*. Second Edition. Cambridge University Press. (2005)
- [8] Abarbanel and Kennel. *Local false nearest neighbors and dynamical dimensions from observed chaotic data*. Physical Review E (1993)
- [9] Kennel et al. *Determining embedding dimension for phase-space reconstruction using a geometrical construction*. Physical Review A (1992)
- [10] Rosenstein et al. *A practical method for calculating largest Lyapunov exponents from small data sets*. Physica D (1993)
- [11] Schmelcher and Diakonos. *General approach to the localization of unstable periodic orbits in chaotic dynamical systems*. Physical Review E (1998)
- [12] Eckmann and Ruelle. *Fundamental limitations for estimating dimensions and Lyapunov exponents in dynamical systems*. Physica D: Nonlinear Phenomena (1992)

A Lorenzian based chaotic encryption scheme

Michael Brunel

Abstract

In this paper I present a chaotic encryption scheme based upon the Lorenz system. The encryption scheme is a combination of a block and stream cipher.

1. Introduction

Encryption, at its core is, simply transforming one set of data into another set. Civilizations as far back as the ancient Egyptians have used encryption to hide their sensitive data. The fundamental problem with these systems is that they are not overly secure. To achieve security the outputs should be indistinguishable from random. This very naturally leads to utilizing a system that already provides random data. One of the earliest examples of this can be seen in [1]. This early step showed the validity of utilizing an already chaotic primitive to underline an encryption scheme. This work has been followed upon by many people including [2-5].

In this vain I propose a new encryption scheme based on the chaotic regions of the Lorenz system. Utilizing the Lorenz system as an underlying platform, a blocking stream cipher was built around it to encrypt streams of data of arbitrary length. Considerations on the Lorenz system as utilized by an encryption scheme is detailed in the next section. This is followed by the implementation details, some analysis of the system and the data generated and finally some areas of future work.

2. Lorenzian Chaos

While there is no universally accepted definition of what constitutes chaos the following working definition is highly agreed upon [6]:

Chaos is aperiodic long-term behavior in a deterministic system that exhibits sensitive dependence on initial conditions.

1. “Aperiodic long-term behavior” means that there are trajectories that do not settle into either fixed points or predictable orbits.
2. “Deterministic” means that the system can be determined solely from its inputs and knowledge of the system itself. No outside forces, such as noise, factor into the path of the system.
3. “Sensitive dependence on initial conditions” means that nearby trajectories separate exponentially fast.

The Lorenz system is a collection of three Ordinary Differential Equations [7]:

$$\begin{aligned}\frac{dx}{dt} &= \sigma(y - x) \\ \frac{dy}{dt} &= x(\rho - z) - y \\ \frac{dz}{dt} &= xy - \beta z\end{aligned}$$

where σ is called the Prandtl number and ρ is called the Rayleigh number.

For values of ρ over 25 the system becomes a chaotic system as can be seen in Figure 1.

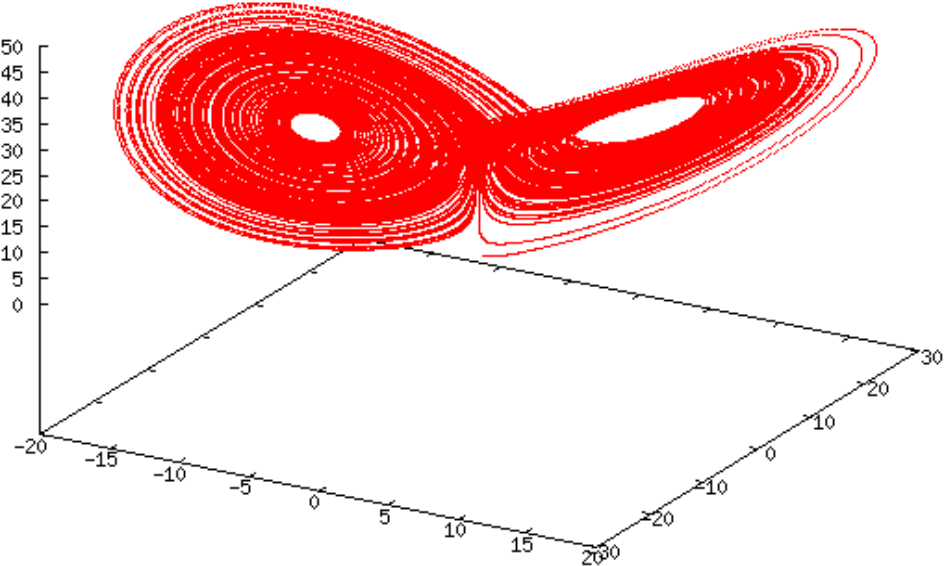


Figure 1: Lorenz system. 150,000 iterations (0,1,1.05) $\sigma = 10$, $\rho=28$ and $\beta = 8/3$

As can be seen in Figure 1, the system does indeed have a chaotic trajectory.

3. Implementation

My system utilizes the Lorenz system in a two step encryption process. Firstly, the plain text file which is to be encrypted is analyzed to determine its size in bytes. This is used as the length of the trajectory needed to be calculated for the Lorenz system. Initial values for the Lorenz system is chosen and a trajectory is generated. This trajectory is then combined with the plain text to make a new file. A second set of initial values are chosen and a second Lorenz trajectory is generated. This is then combined with the text from the previous round. This text is outputted as the encrypted version of the original plain text.

3.1 Initial conditions and the key

The choice of initial conditions for the Lorenz system is very central in determining if the system is chaotic or not. As such, certain bounds have been established on what can be inputted as initial conditions to the Lorenz system. In accordance with the data presented in [6,7] we can ascertain a set of lower bounds on the values of the system.

While all of the variables are used in determining the trajectory of the system, ρ , x , y , and z have the largest impact on this. As such, these are 4 variables that can be set for each run of the Lorenz system.

These 8 variables, 4 from each run, are the concatenated together to form the key of the system.

3.2 Lorenz trajectories

After the trajectory has been generated, the x , y and z coordinates that were generated are converted into their binary form. Then, using binary xor, we combine this with the binary version of the plain text. The second trajectory is combined in a slightly more complicated matter. Each set of coordinates is first converted to binary and xor'ed into a block of the text from the previous round. The binary coordinates are then converted into an unsigned integer value which is then modded by the size file. This gives some new location in the text file, the block in that section is then swapped with the block that we just created. Once the entire trajectory is exhausted we output this new file as the encrypted text.

3.3 Decryption

To decrypt a file, simply provide the encrypted file and the appropriate key. The mechanism for decryption is very similar to that of encryption, except that it is done in reverse. The second step of the encryption process becomes the first step of the decryption process.

4. Data and Analysis

4.1 How random is random

Whenever a system is said to be random, the first question that arises is “is it really random”. Thus, to truly say that a system is random, you must test a systems randomness. Indeed this is an impossible task with a finite set of data from a potentially infinite data set, however with a sufficiently long sample we can be reasonably confident that the given system is indeed random. NIST[8] provides a statistical

package that can be used to determine how random a set of inputs are.

The NIST statistical suite was run on a set of 10 streams, consisting of 1000000 bits each. The streams were generated by encrypting a pdf version of the Perl cookbook. All metrics within the suite were run, however, the Universal metric reported an error that I was unable to resolve in the given time.

From [9] we can determine that an overall pass rate of 88.95% is considered as acceptable for a random number generator. The NIST suit stated that a minimum pass rate for all test preformed was $\approx 89.5607\%$

Analysis of the test data indicates that the BlockFrequency test is the worst performing test, with all others in the upper 90% range. This test compares the frequency of 1's vs 0's in a given block. While this data suggests that my system does indeed equate to random, there is some cause for concern in the poor performance of the BlockFrequency test.

4.2 Speed

Speed is a primary consideration when comparing any new system to that of its predecessor. As such I compared my scheme against AES-256-CBC as provided by the crypt package in Perl. I choose this implementation as a comparison to keep as many variables the same as possible. A comparison of times can be seen in Table 1.

	AES	Lorenz System
1MB	0.013	15.729
2MB	0.022	34.949
5MB	0.045	84.889
10MB	0.102	167.617

Table 1: A comparison of the time needed to encrypt a file. All times in milliseconds

As you can see from Table 1, my code has a linear dependence on the size of the input, which makes it considerably slower than AES. While my RK4 solver is far from optimized I am not confident that an appropriate speed increase can be gained from this alone, and as such it will remain decidedly slower than AES.

4.3 Key space

The key size for my program is 512 bits, which when looking at a straight brute force attack is 2^{512} possible keys. This is well beyond a straight brute force attack, which peak somewhere around 2^{70} . However, during my analysis of this system I noticed some irregularities that may allow an adversary to reduce the key space required to search. Firstly, I do not throw out any part of the transient, as such a sufficiently close guess as to my initial conditions could yield enough data to help narrow down their search space. This can be worked around by throwing out some number of coordinates along the transient. The second thing that I believe could be a problem is the method in which my system chooses its keys, it can be either set by the user, or it uses the Perl rand function to determine a set of initial conditions within the given bounds of chaotic Lorenz. Currently, that includes some very large values for the coordinates and p are possible. I am unsure if a sufficiently high set of values either fails to be chaotic, or takes so long to get to chaos that an attack could be made in that deterministic region.

5. Conclusion

5.1 Future work

Several areas of this project show potential for future work and improvements

5.1.1 Performance

No work was done to compare this algorithm to other algorithms in its fields, or across other fields. There are a vast number of other areas that this system could be used in which merit consideration. Also, there is ample opportunity to fine tune the algorithm within the code itself, especially with currently implemented RK4.

5.1.2 Randomness

With the randomness of this system close to the acceptable limit of random, so work can be done to investigate why this test performs poorly on the BlockFrequency test, as well as its failure to run the Universal test. There is also the potential to alter how the trajectory coordinates are utilized in the combination phases of this code, perhaps using fewer of the more static bits.

5.1.3 Key space

While a straight brute force attack is unfeasible, as noted in section 4.3, some other more clever attacks based on near trajectory approaches are potentially possible. An investigation of the feasibility of these attacks, and similar exploits based on the inherent properties of a chaotic system could be investigated.

- [1] J. Fridrich, "Image encryption based on chaotic maps," in Proceedings of the IEEE International Conference on Systems, Man and Cybernetics, vol. 2, pp. 1105–1110, 1997
- [2] G. Chen, Y. Mao, and C. K. Chui, "A symmetric image encryption scheme based on 3D chaotic cat maps," *Chaos, Solitons & Fractals*, vol. 21, no. 3, pp. 749–761, 2004.
- [3] Y. Mao, G. Chen, and S. Lian, "A novel fast image encryption scheme based on 3D chaotic baker maps," *International Journal of Bifurcation and Chaos*, vol. 14, no. 10, pp. 3613–3624, 2004.
- [4] Z.-H. Guan, F. Huang, and W. Guan, "Chaos-based image encryption algorithm," *Physics Letters A*, vol. 346, no. 1–3, pp. 153–157, 2005.
- [5] A. N. Pisarchik and M. Zanin, "Image encryption with chaotically coupled chaotic maps," *Physica D*, vol. 237, no. 20, pp. 2638–2648, 2008.
- [6] Steven Strogatz. *Nonlinear Dynamics and Chaos: With Applications to Physics, Biology, Chemistry and Engineering*. Perseus Books Group, 1 edition, pp. 323-324, 2001.
- [7] Edward Lorenz. *Journal of the atmospheric sciences; deterministic non periodic flow*. 20(2):130-141, 1963.
- [8] Andrew Rukhin, Juan Soto, James Nechvatal, Miles Smid, Elaine Barker, Stefan Leigh, Mark Lewonen, Mark Vangel, David Banks, Alan Heckert, James Dray, and San Vo. *A Statistical Test Suite for Random and Pseudorandom Number Generators for Cryptographic Applications*. National Institute of Standards and Technology, August 2008.
- [9] Charmaine Kenny. *Random number generators: An evaluation and comparison of random.org and some commonly used generators*. Technical report, The Distributed Systems Group, Computer Science Department, Trinity College Dublin, 2005.

The Applicability of Compressed Sensing on Non-Linear Dynamic Systems & Chaos

Lucas Budman

Abstract

This paper investigates the applicability of Compressed Sensing, a new technique for signal acquisition and compression, on non-linear dynamic systems and chaos. Compressed Sensing theory asserts that signals can be “sensed” and recovered with far fewer samples or data points than traditional methods specify. Most of the Compressed Sensing research to date has focused on linear signal acquisition and the Fourier domain. To investigate Compressed Sensing’s applicability on non-linear dynamic systems, we study a Lorenz system in two states. First, we investigate a fixed-point Lorenz attractor. We show that our Compressed Sensing technique is able to weakly capture the dynamics of the system using only 29% of the original signal. Second, we investigate a chaotic Lorenz attractor (strange attractor). We show that our Compressed Sensing technique is able to capture the dynamics of the chaotic attractor using 60% of the original signal.

I. Introduction

The Nyquist rate asserts that a signal must be sampled at least twice the maximum frequency presented in the signal. However, recent research in signal recovery techniques has shown that one can recover certain signals with far fewer samples using the theory of Compressed Sensing. We know that the Nyquist theorem is based upon linear assumptions and is not applicable to non-linear dynamic systems. The question becomes – “Is Compressed Sensing applicable to non-linear dynamic systems?”

In this paper, we investigate the applicability of Compressed Sensing on non-linear dynamic systems and chaos. We present a Compressed Sensing technique for compressed data acquisition of non-linear time-series signals. This technique utilizes the theory of Compressed Sensing and the discrete wavelet transform. We utilize two different Lorenz systems to test our technique and present results on our findings.

In specific applications, this technique might enable more accurate control signal acquisition and possibly better time-series predictive techniques through signal resolution enhancement.

II. Compressed Sensing

Compressed Sensing is a new technique for signal acquisition and compression. Compressed Sensing systems allow robust data acquisition to occur with far fewer samples/measurements ($M \ll N$) than expected by standard theories. These systems measure signals by a linear dimensionality reduction process as follows [1]:

$$y = \Phi x \quad (1)$$

where Φ is an $M \times N$ measurement matrix and x , the signal to be measured, has a sparse representation $x = \Psi\alpha$ in some basis. The signal equation is typically expressed as $x = \Psi\alpha$ where Ψ is an $N \times N$ orthonormal basis matrix.

This linear dimensionality reduction produces an underdetermined linear system of equations that can be recovered using the linear program:

$$\min \|x^*\|_1 \text{ subject to } \Phi x^* = \Phi x \quad (2)$$

The theory relies on two central tenants, a K-sparse signal and incoherent sampling. The signal must be sparse or nearly sparse in a convenient basis. This is referred to as K-sparse where K represents the number of non-zero entries in α . Said another way, K-sparse represents the number of active components in α . The number of measurements necessary to accurately reproduce or in some cases exactly reproduce a signal is directly related to K . The measurement basis Φ must also be incoherent or exhibit low coherence to the representation basis Ψ . The coherence between the measurement basis Φ and the orthonormal representation basis Ψ is defined as [1,2]:

$$\mu(\Phi, \Psi) = \sqrt{n} \cdot \max_{1 \leq k, j \leq n} |\langle \varphi_k, \psi_j \rangle|. \quad (3)$$

where φ and ψ represent the components of the two bases. It follows from equation 3, above, that $\mu \in [1, \sqrt{n}]$. The system has maximum incoherence when $\mu \approx 1$. The number of measurements necessary to accurately recover a signal is also directly proportional to the incoherence of the bases. This relationship is defined as [1, 2]:

$$m \geq C \cdot \mu^2(\Phi, \Psi) \cdot S \cdot \log n \quad (4)$$

where m is the number of measures, C is a positive constant, μ is the coherence measure defined above, S is the K value or sparsity, and n is the signal length.

From equations 3 and 4, it can be shown with overwhelming probability that a signal can be accurately reconstructed with [3,4]:

$$M \gtrsim K \cdot \log N \quad (5)$$

measures M, where K is the sparsity value, and N is the length of the signal. This inequality is derived with the assumption that $\mu = 1$, i.e. there exists an incoherent relationship between the measurement basis Φ and the orthonormal representation basis Ψ .

Using a Gaussian random measurement basis with mean 0 and variance $1/m$, the probability of coherence between the measurement basis Φ and the orthonormal representation basis Ψ is extremely low, almost zero. This represents a “near-optimal” sensing strategy that has a high probability of incoherence [3,4]. Given this fact, the research presented in this paper is centered around a Compressed Sensing process that utilizes a Gaussian random measurement basis with mean 0 and variance $1/m$.

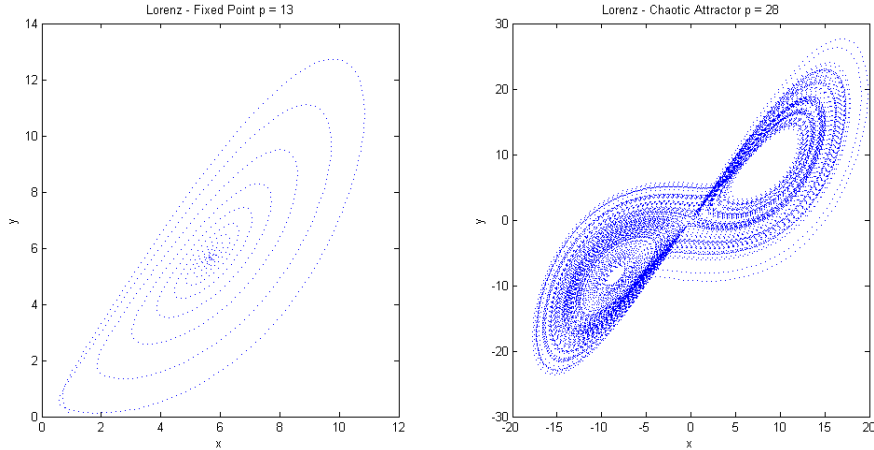
III. Lorenz System

The Lorenz system, a three-dimensional dynamic system, is utilized to study the applicability of Compressed Sensing on non-linear dynamic systems and chaos. The system is defined by the following system of ordinary differential equations (ODE):

$$\begin{aligned} \frac{dx}{dt} &= \sigma(y - x) \\ \frac{dy}{dt} &= x(\rho - z) - y \\ \frac{dz}{dt} &= xy - \beta z \end{aligned} \tag{6}$$

This system has been selected for this study for three primary reasons: 1). It is a fairly simple system, 2). It has been well-studied 3). It is a chaotic system under certain initial conditions. The third criterion above is important, because this research investigates not only non-linear systems but also non-linear systems that are chaotic.

In this research, we utilize two different Lorenz systems. These two different systems are defined by their initial conditions. The first system is a fixed-point attractor (see figure 1). It is defined by the initial conditions: $\sigma = 10$, $\beta = 8/3$, $\rho = 13$, $x = 1$, $y = 0$, $z = 0$. The second Lorenz oscillator is a chaotic system that exhibits a strange attractor (see figure 2). It is defined by the initial conditions: $\sigma = 10$, $\beta = 8/3$, $\rho = 28$, $x = 1$, $y = 0$, $z = 0$. The only difference between these two systems is the initial condition ρ , but the dynamics of the two systems are wildly different.



Figures 1, 2: Figure 1 depicts a Lorenz system with $\rho = 13$. This is a fixed-point attractor. Figure 2 – depicts a Lorenz system with $\rho = 28$. This is a chaotic attractor (strange attractor).

To approximate the Lorenz ODE system, we utilize a fixed time step Runge-Kutta (RK) integrator. Specifically, we utilize the fourth-order method; simply referred to as RK4. It is important to note that a fixed time-step integrator is used for this research. Later in the paper, we present calculated values of the largest Lyapunov exponents. To calculate these values, we employ the TISEAN time-series analysis package and the *lyap_r* method. This method uses the algorithm of Rosenstein *et al* [12]. The Rosenstein algorithm first embeds the time-series signal using delay coordinate embedding. For delay coordinate embedding to work properly, a stable fixed time period signal is required.

We use a fixed time step of 0.01 (h) to integrate the Lorenz system. To investigate the dynamics of the wavelet transform, the system is integrated for 165 seconds. This produces 16,500 data points. The first 116 points of data are discarded. These points are considered the transients. The data set is then reduced in size to 16,384 points. To investigate the dynamics of Compressed Sensing, the signal is then shortened to 8,192 points. Points 8,193 to 16,384 are dropped from the data set. This is necessary to make the problem tractable in both the memory and computational domains.

It is important to note that the system sizes are chosen for a couple of reasons. First, the wavelet transform that is utilized in this research requires a signal that is a power of two. Second, a relatively small data set allows the problem to be computationally tractable. This is important during the signal recovery phase. Finally, the signal is long enough to exhibit the non-linear dynamics that are under investigation.

For all time-series analysis presented in this paper, we utilized the x component of the generated data set. We did not investigate any differences

between the x, y, and z components of the systems. This investigation is unnecessary, as the x component should fully incorporate the dynamics of the underlying system.

IV. Wavelet Transform

The first tenant of Compressed Sensing is that the signal to be measured must be sparse in some basis. Compressed Sensing does not specify the basis that must be used. It instead just assumes that there exists a sparse basis. It is up to the implementer to determine the appropriate basis.

In the case of non-linear dynamic systems determining the proper basis is a hard problem. Typically, Compressed Sensing investigates signals in the Fourier Domain using Discrete Fourier Transforms (DFT). DFT is not applicable to the non-linear, non-stationary time-series signals that are investigated here [10]. The Fourier transform is dependent on linear and stationary assumptions.

To over come the limitation of Fourier transforms, recent research in non-linear data analysis has shown that wavelet transforms can capture the time-frequency characteristics of non-linear dynamic systems [11]. The wavelet transform is defined as the following:

$$[W_\psi f](a, b) = \frac{1}{\sqrt{|a|}} \int_{-\infty}^{\infty} \overline{\psi\left(\frac{x-b}{a}\right)} f(x) dx \quad (7)$$

where a is a scale parameter and ψ is an orthonormal wavelet.

For the wavelet transform to be applicable to the Compressed Sensing problem, it must be shown that the transform produces a K-sparse basis for the system and that the transform maintains the dynamics of the system. In this research, K-sparse is defined as the number of values, K, above or below a threshold value. The threshold value in theory should be zero, but because of machine accuracy and other error conditions, K is defined as a threshold.

To investigate whether the wavelet basis is sparse, we first transformed the two Lorenz time-series signals ($p=13$ and $p=28$) using Matlab and the WaveLab library [13]. We utilized a Coiflet wavelet transform with the following parameters: par (a parameter related to the support and vanishing moments of the wavelets) = 3, coarsest Level = 4. Figure 3 and 4 provide a visual representation of the two sparse domains, Lorenz $p=13$ and $p=28$. The fixed-point system is very sparse as expected by its dynamics. It spirals in towards its fix-point and then remains at its fix-point. The chaotic system on the other hand is not as sparse. Visual it looks fairly sparse but there are a lot of small non-zero terms in the data set that are not visible in figure 4.

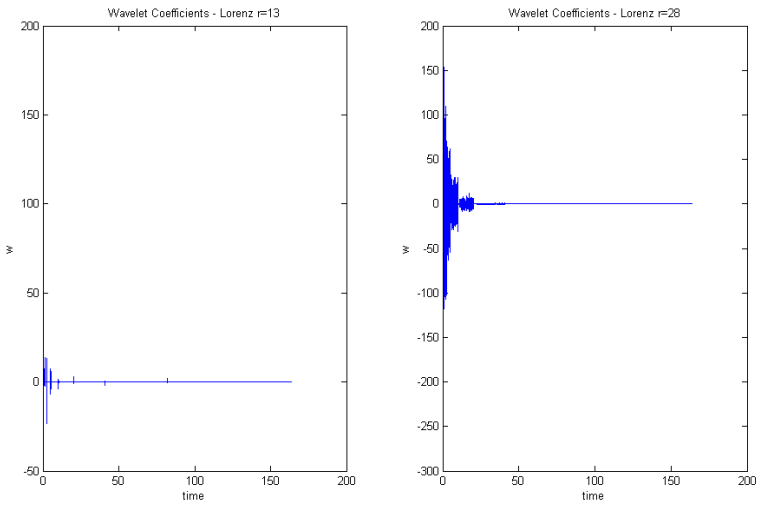
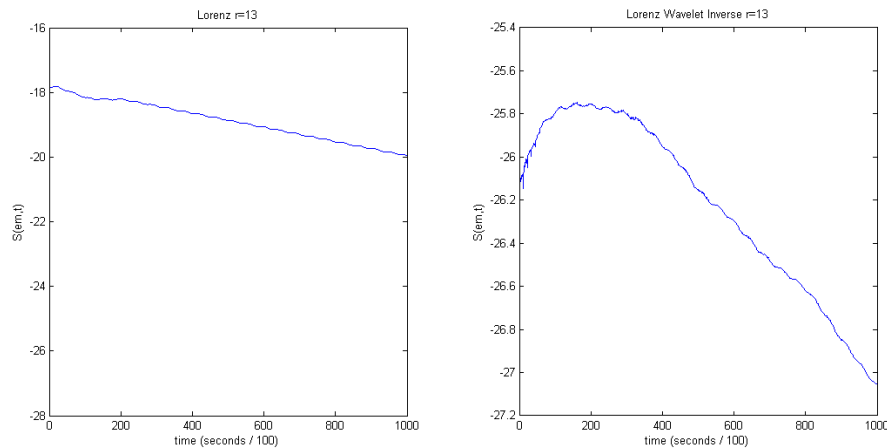


Figure 3, 4: Figure 3 plots the wavelet coefficients over time for Lorenz ($p=13$). Figure 4 plots the wavelet coefficients over time for Lorenz ($p=28$).

To explore whether the wavelet transform maintains the dynamics of the system, we first analyzed the effects of the transform on the fixed-point attractor Lorenz system. We performed a wavelet transform on the x component time-series data for the Lorenz system ($p=13$) followed by an inverse wavelet transform. The wavelet transform followed by the inverse should, at least in theory, give us back the original system or in this case the original time-series data. Next, we analyzed the dynamics of the original signal by computing the Lyapunov exponent, λ_1 . We performed the same calculation for the wavelet signal.



Figures 5, 6: Figure 5 plots the average divergence over time for the Lorenz System ($p=13$). Figure 6 plots the average divergence over time for the Lorenz System ($p=13$) after a wavelet / wavelet Inverse transform.

Figure 5 plots the average divergence over time for the Lorenz system with $\rho=13$. Figure 6 plots the average divergence over time for the Lorenz System with $\rho=13$ after a wavelet transform and an inverse wavelet transform. We computed both plots utilizing the TISEAN *lyap_r* tool. The slope of the linear region of these plots indicates the largest Lyapunov exponent, λ_1 . The slope of the normal Lorenz system is $\lambda_1 = -0.22$ seconds, while the slope of the wavelet system is $\lambda_1 = -0.18$ seconds. The scaling region used for both slope calculations is between time = 400 to 1000. The dynamics of the system are not perfectly preserved by the wavelet transform. The Lyapunov exponents are close, but the plots are dissimilar. To further investigate the wavelet effects, we calculated the Euclidean distance of the residuals and plotted the residuals over time (see figure 7). The Euclidean norm of the residuals is $\|\varepsilon\|_2 = 2.2586e-8$. The actual difference between the expected value and the predicted value (wavelet transform) is very small, but large enough to affect the underlying dynamics of the system.

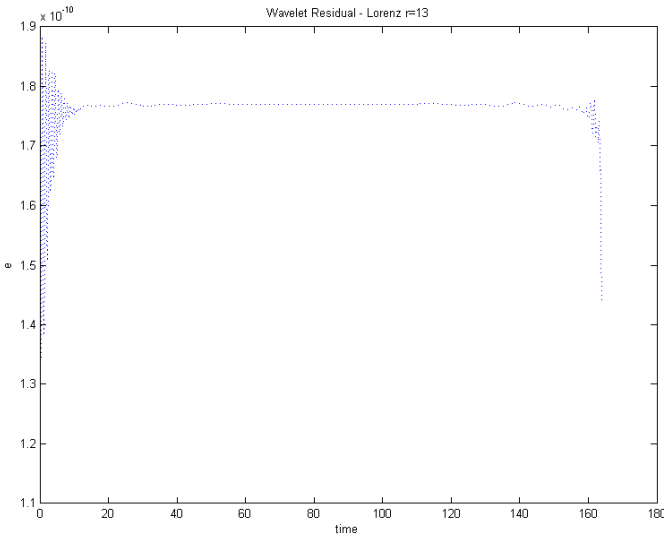


Figure 7: Plots the residuals over time for the wavelet transform.

To further analyze the impact that the wavelet transform has on the dynamics of the Lorenz attractor, we next performed the same analysis for the chaotic attractor, $\rho=28$. Figures 8 plots the average divergence over time for the Lorenz System with $\rho=28$. Figure 9 plots the average divergence over time for the Lorenz System with $\rho=28$ after a wavelet transform and an inverse wavelet transform. The slope of the normal Lorenz system and the wavelet inverted system are both $\lambda_1 = 0.84$. The scaling region used for both slope calculations is between time = 0 to 400.

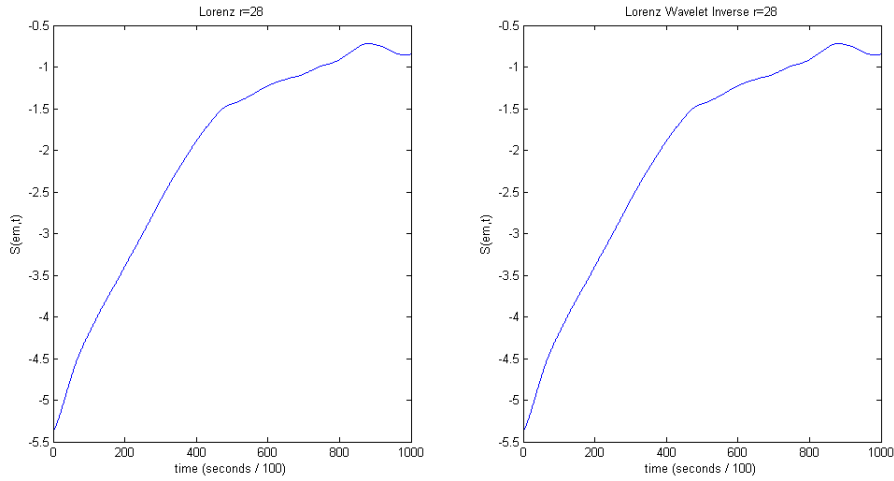


Figure 8, 9: Figure 8 plots the average divergence over time for the Lorenz System ($\rho=28$). Figure 9 plots the average divergence over time for the Lorenz System ($\rho=28$) after a wavelet / wavelet Inverse transform.

The dynamics of the system are properly preserved by the wavelet transform. The Euclidean norm of the residuals is $\|\varepsilon\|_2 = 1.4998e-8$. Figure 10 plots the residuals over time for the chaotic Lorenz system.

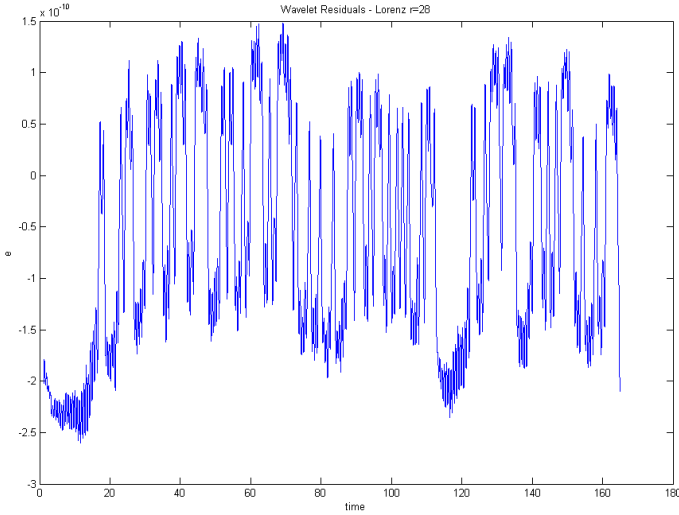


Figure 10: Plots the residuals over time for the wavelet transform.

V. The Impact of Compressed Sensing On A Fixed-Point Attractor

To investigate the effects of Compressed Sensing on a dynamic system, we first investigated the effects it has on a Lorenz fixed-point attractor. The fixed-point

attractor was selected for several reasons. First, it represents a fairly simple non-linear dynamic flow model. Second, it is inherently sparse. The attractor spirals in towards a fixed-point and once it reaches the fixed-point it stays at that point. Finally, the Lorenz system has been thoroughly researched and studied.

A. Method

We integrated the Lorenz system with initial conditions $\sigma = 10$, $\beta = 8/3$, $\rho = 13$, $x = 1$, $y = 0$, $z = 0$ (see Lorenz section for details). This produced a data set of 8,192 (N) points over a period of ~ 82 seconds. Utilizing WaveLab [13] and a Coiflet wavelet transform, we then transformed the x-variable time-series data into its corresponding wavelet coefficients.

To decide on the number of points to randomly sample, we employed a K-sparse threshold of $1e-5$. This threshold yielded a K-sparse basis with $K = 616$ (the number of active / non-zero components of the signal). With this threshold value, we calculated $M = 2,411$ (the number of data points to randomly sample) utilizing equation 5 above.

Next, we generated an $M \times N$ Gaussian random measurement matrix Φ using Matlab's `randn` function. Using Matlab's `ortho` function, we produced an orthonormal basis for the Gaussian random measurement matrix. Using the measurement matrix we randomly "sensed" 2,411 points out of the 8,192 wavelet coefficients of the signal (equation 1). These 2,411 points formed the measurement signal. Using the measurement signal, we then computed the minimum energy solution:

$$x_0 = \Phi b \quad (8)$$

where x_0 is the initial guess, Φ is the measurement matrix, and b is the sensed signal.

In order to recover or reconstruct an estimate of the original signal y , we must find a solution to the linear optimization problem described in equation 2. The goal is to find a solution to the underdetermined l_1 -minimization problem (equation 2). To solve this linear program, we leveraged the L1-Magic convex program library [6]. L1-Magic implements several different optimization routines. For this research, we leveraged the basis pursuit method. This method is implemented using the interior point algorithm for convex optimization. We used the following tuning parameters for the basis pursuit algorithm: duality gap = $1e-3$, maximum number of primal-dual iterations = 20, tolerance for conjugate gradients = $1e-8$, maximum number of conjugate gradients iterations = 10,000.

B. Dynamics

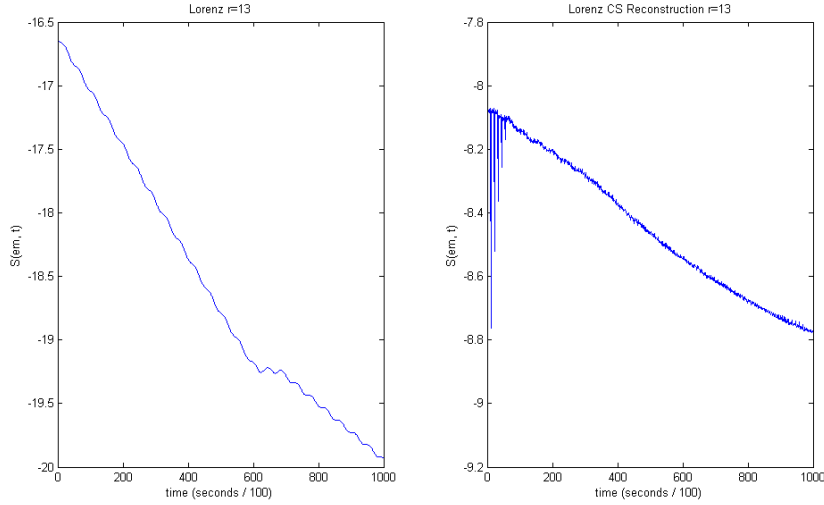


Figure 11, 12: Figure 11 plots the average divergence over time for the fixed-point Lorenz System ($\rho=13$). Figure 12 plots the average divergence over time for the Compressed Sensing reconstructed fixed-point Lorenz System ($\rho=13$).

To explore the effects that Compressed Sensing has on the dynamics of the fixed-point Lorenz system, we calculated the largest Lyapunov exponent λ_1 for the original signal (x-axis time-series) and the Compressed Sensing reconstructed signal. We calculated the Lyapunov exponent using TISEAN's *lyap_r* command. We used an embedding dimension of 6, which represents twice the Euclidean dimension of the system. We selected a time delay of 11, which has been suggested as an optimal delay for the Lorenz system [15]. Figure 11 and 12 plot the average divergence over time for the two systems. The slope of the linear region of these plots indicates the largest Lyapunov exponent, λ_1 . The slope of the original Lorenz signal is $\lambda_1 = -0.44$ seconds, while the slope of the reconstructed signal is $\lambda_1 = -0.08$ seconds. The scaling region used for both slope calculations is between time = 100 to 600. The dynamics of the system are not perfectly preserved by the Compressed Sensing embedding. The Lyapunov exponents are close, but the plots are dissimilar. The reconstructed plot exhibits a fair amount of noise. This is especially visible in the region between 0 and 100.

To further investigate the Compressed Sensing effects, we calculated the Euclidean distance of the residuals (predicted vs. theoretical values). The Euclidean norm of the residuals is $\|\varepsilon\|_2 = 0.0596$. The actual difference between the expected value and the predicted value (Compressed Sensing reconstruction) is not large, but enough to affect the underlying dynamics of the system.

C. Discussion

As noted in the methods section above, we measured 2,411 random points from the Lorenz time-series data set. This comes out to be roughly 29% of the data.

Using this reduced dataset, we were able to reconstruct the time-series signal fairly accurately. We measured an L2 norm of the residuals of just 0.0596. When looking at a plot of the original signal vs. the reconstructed signal, it is very hard to tell the difference between the two systems. In fact, no comparison plots are included in this paper because the plots would add very little value. You cannot tell the difference between the original signal and the Compressed Sensing reconstructed signal.

When we investigated the Lyapunov exponent, a dynamical invariant, a slightly different picture emerged. The calculated value of the largest Lyapunov exponent for the recovered signal did not closely match the calculated value of the original signal. This indicates that the reconstructed signal does not possess the same dynamics as the original signal. Both Lyapunov exponents are small negative values. This indicates that both systems are contracting, i.e. heading towards a fixed point.

As noted above in the Wavelet section, the wavelet transform changed the dynamics of the fixed-point Lorenz attractor. In contrast, the chaotic attractor was not affected by this transform. Given this information, it is likely that the reconstructed fixed-point attractor's dynamics is at least in part affected by the wavelet transform.

We also investigated the effect of increasing the measurement signal size. We doubled the measurement size from 2,411 to 4,822 and then re-ran the process of sensing and reconstructing. Interestingly, doubling the signal size caused very little change in the dynamics. With the longer signal, the calculated largest Lyapunov exponent was $\lambda_1 = -0.11$ seconds.

VI. The Impact of Compressed Sensing On A Chaotic Attractor

To continue our analysis on the effects of Compressed Sensing on a dynamic system, we next investigated the effects it has on a Lorenz chaotic attractor (strange attractor). Again this system was chosen for many of the same reasons stated above in the fixed-point section. In addition, we wanted to investigate if a chaotic system could be sensed, compressed, and recovered using the Compressed Sensing method.

A. Method

We followed almost exactly the same procedure as used above for the fixed-point attractor. The only difference was that we employed a K-sparse threshold of 1e-1. This was required because the wavelet basis of the chaotic attractor had a large number of small non-zero active components. This threshold yielded a K-Sparse basis of $K = 1,273$ (the number of active / non-zero components of the signal). With this threshold value, we estimated $M = 4,982$ (the number of data points to randomly sample) using equation 5 above.

B. Dynamics

To further explore the effects that Compressed Sensing has on the dynamics of the Lorenz system, we examined the Lorenz chaotic attractor. We calculated the largest Lyapunov exponent λ_1 for the original signal (x-axis time-series) and the Compressed Sensing reconstructed signal. Again, we calculated the Lyapunov exponent using TISEAN's *lyap_r* command. We used an embedding dimension of 6, which represents twice the Euclidean dimension of the system. We selected a time delay of 11, which has been suggested as an optimal delay for the Lorenz system [15]. Figure 13 and 14 plot the average divergence over time for the two systems. The slope of the linear region of these plots indicates the largest Lyapunov exponent, λ_1 . The slope of the original Lorenz signal is $\lambda_1 = 0.84$ seconds, while the slope of the reconstructed signal is $\lambda_1 = 0.79$ seconds. The scaling region used for both slope calculations is between time = 0 to 400. The dynamics of the system are fairly well preserved by the Compressed Sensing embedding. The Lyapunov exponents are very close and the plots are just slightly different.

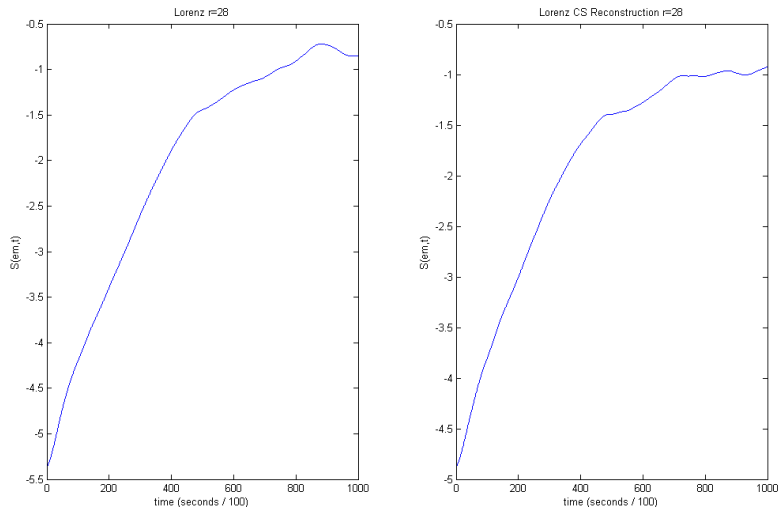


Figure 13, 14: Figure 13 plots the average divergence over time for the fixed-point Lorenz System ($\rho=13$). Figure 14 plots the average divergence over time for the Compressed Sensing reconstructed fixed-point Lorenz System ($\rho=13$).

To further investigate the Compressed Sensing effects, we calculated the Euclidean distance of the residuals (predicted vs. theoretical values). The Euclidean norm of the residuals is $\|\varepsilon\|_2 = 1.3923$. The actual difference between the expected value and the predicted value (Compressed Sensing reconstruction) is not large, but bigger than the fixed-point residuals.

C. Discussion

In contrast to the fixed-point attractor, the chaotic attractor required a larger measurement data set. For the chaotic attractor, we randomly measured 4,982 points, which is roughly 60% of the data. As expected, the chaotic attractor is not as sparse in the wavelet basis as the fixed-point attractor. Using this larger data set, we measured an L2 norm of the residuals of 1.3923. This is significantly higher than the measured value for the fixed-point Lorenz system. Again, when looking at a plot of the original signal vs. the reconstructed signal, it is very hard to tell the difference between the two systems.

The calculated values of the largest Lyapunov exponent between the original and reconstructed signal did not change much. We calculated a value of $\lambda_1 = 0.84$ for the original and $\lambda_1 = 0.79$ for the reconstructed signal. Both values are positive indicating that the system is indeed chaotic and expanding in at least one dimension.

VII. Conclusion

In this paper, we proposed a new technique for compressing non-linear dynamic time-series data. We showed that both a chaotic and a fixed-point Lorenz attractor can be sensed, compressed, and recovered using our technique. In addition, we presented findings that indicate our technique maintains the dynamics of the chaotic attractor. We measured the largest Lyapunov exponent, a dynamical invariant, of both the original chaotic attractor and the recovered signal. We found very little change between the two measured values. These measurements provide strong indication that our Compressed Sensing framework properly maintains the dynamics of the Lorenz chaotic attractor. However, our current mechanism failed to maintain the dynamics of the fixed-point attractor. We measured fairly different Lyapunov exponent values for the original fixed-point attractor and the recovered signal. This indicates that the dynamics are not properly maintained by our technique for the Lorenz fixed-point attractor.

While these results validate the applicability of Compressed Sensing on certain non-linear dynamic systems, they also raise new questions and new areas of research. We found in our research that Coiflet wavelet transforms maintain the dynamics of a chaotic attractor but failed to do so for a fixed-point attractor. Further, we discovered that signal length did little to improve the dynamics of the fixed-point attractor. In the end, we believe that Compressed Sensing is applicable to non-linear dynamic systems and chaos.

REFERENCES

- [1] E.J. Candès, "Compressive Sampling," in Proc. International Congress of Mathematicians, vol. 3, Madrid, Spain, 2006, pp. 1433-1452

- [2] E.J. Candès, Michael B. Wakin, "An Introduction To Compressive Sampling," IEEE Signal Processing, vol. 25, no. 2, pp. 21-30, March 2008
- [3] D. Donoho, "Compressed Sensing," IEEE Trans. Information Theory, vol. 52, no. 4, pp. 1289-1306, April 2006
- [4] E.J. Candès, T. Tao, "Near Optimal Signal Recovery From Random Projections: Universal Encoding Strategy?," IEEE Trans. Information Theory, vol. 52, no. 12, pp. 5406-5425, December 2006
- [5] R. Berinde, P. Indyk, "Sparse Recovery Using Sparse Random Matrices," available at <http://people.csail.mit.edu/indyk/report.pdf>
- [6] E.J. Candès, J. Romberg, "l1-MAGIC: Recovery of Sparse Signals via Convex Programming," 2005, available at <http://www.acm.caltech.edu/l1magic>
- [7] Rice University DSP Group, Compressed Sensing Resources, available at <http://www.dsp.ece.rice.edu/cs>
- [8] M. F. Duarte, R. G. Baraniuk, "Spectral Compressive Sensing," available at <http://www.math.princeton.edu/~mduarte/images/SCS-TSP.pdf>
- [9] R. G. Baraniuk, M. B. Wakin, "Random Projections of Smooth Manifolds," Foundations of Computational Mathematics, vol. 9, no. 1, pp. 51-77, February 2009
- [10] N.E. Huang, Z. Shen, S.R. Long, M.C. Wu, H.H. Shih, Q. Zheng, N.C. Yen, C.C. Tung, H.H. Lu, "The Empirical Mode Decomposition and the Hilbert Spectrum for Nonlinear and Non-stationary Time Series Analysis," Proceedings of Royal Society of London, 454, pp. 903-995, 1998
- [11] T.L. Kijewski-Correa, A. Kareem, "Time-Frequency Characterization of Non Linear Dynamical Systems," 9th ASCE Specialty Conference on Probabilistic Mechanics and Structural Reliability
- [12] M. T. Rosenstein, J. J. Collins, C. J. D. Luca, "A practical method for calculating largest Lyapunov exponents from small data sets," Physica D, 65, 117, 1993
- [13] WaveLab 850, available at <http://www-stat.stanford.edu/~wavelab/>
- [14] S. Mallat, "A Wavelet Tour of Signal Processing," Academic Press, 1998
- [15] M. T. Rosenstein, J. J. Collins, C. J. De Luca, "A practical method for calculating largest Lyapunov exponents from small data sets," 1992

TRAJECTORY ANALYSIS FOR MANIFOLD RETURN TRANSFERS FROM SUN-EARTH L1 LIBRATION POINT ORBITS

Bradley W. Cheetham*

Orbits within the unstable equilibrium regions of the Sun-Earth three-body system have been the focus of much past research. It is common to investigate transfers to these regions and trajectories to remain in these regions. Returning to Earth, on the other hand, is a less well studied concept. While the Genesis mission returned to the Earth directly, no mission has returned to orbit the Earth. This work will examine transfers from this region back to Earth orbits of varying altitude and inclination. Potential future applications could involve scientific missions, reduced cost orbital plane changes, or stealth orbit transfers.

INTRODUCTION

Libration points in the Sun-Earth system have been used as staging grounds for scientific missions for decades. These missions generally are sent to the Sun-Earth regime and maintain orbits to achieve scientific objectives. The first of these missions was the International Sun-Earth Explorer-3 (ISEE-3) in 1978 which traveled to the Sun-Earth L₁ point and after its nominal mission demonstrated the ability to transfer within the Sun-Earth system efficiently utilizing perturbations from multiple bodies. More recently Parker and Lo proposed using the dynamics of libration point orbits (LPOs) to enable efficient transfers to the Moon.¹ Current work is investigating the use of libration point orbits as staging grounds for operationally responsive space² and for improving the efficiency of transfers between orbits of varying inclination and altitudes.³

Under the assumptions of the Circular Restricted Three-Body Problem (CRTBP) five stationary solutions, referred to as libration points, exist.⁴ Libration points are equilibrium points in a three-body system where the gravitational forces and centripetal accelerations are equal. The five libration points, also referred to as Lagrange points, are shown in Figure 1 where the primary is the Sun and the secondary is considered to be the Earth-Moon system centered at the systems barycenter. Naming convention here will refer to the points with the prefix L_# to denote a libration point. Extensive research has identified numerous families of periodic and quasi-periodic orbits about the libration points.^{5,6,7} For purposes of this study, one family was selected and orbits were generated for reference. It is important to note that different families may not exhibit consistent behavior due to the nature of the chaotic environment within which they exist. Thus all conclusions derived from this initial work are only to be considered applicable to the orbital regime evaluated; it is not yet possible to extend these conclusions to universal application.

*Graduate Research Assistant, Colorado Center for Astrodynamics Research, University of Colorado, Boulder, Colorado 80309.

For this research the focus will be on using L_1 initial orbits. While several missions have flown to and maintained orbits about this LPO in the Sun-Earth system, to date no spacecraft or mission has returned from this LPO to an Earth orbit.

To demonstrate the accessible altitudes for transfers from LPOs about the Sun-Earth L_1 point, Poincare maps will be the primary tool used. These maps will be constructed in three-dimensional space to show the location of the periapsis crossing for each orbit. Similar work has been done by Nakamiya et al⁸ and Villac and Scheeres⁹ investigating transfers in the Hill Three-Body Model. The work performed here will build upon the concepts and initial understandings developed by both Nakamiya and Villac and expand upon this work by evaluating the transfers in the CRTBP and specifically by investigating these transfers in exclusively the Sun-Earth system.

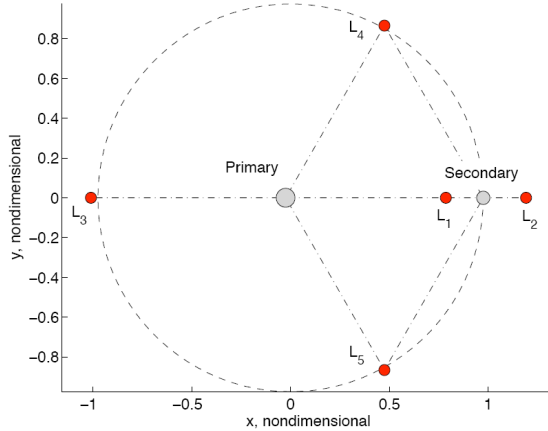


Figure 1. Libration Points in a generic Three-Body System.

FORMULATION

LPOs in this paper are modeled under the equations of motion of the Circular Restricted Three-Body Problem (CRTBP). The CRTBP model assumes that there exist two massive bodies, a primary and a secondary, and a third body (i.e. a spacecraft) which is assumed to have negligible mass compared to the other two bodies. The orbits of both the primary and secondary are assumed to be circular about their combined center of mass, which is referred to as the barycenter of the system. The reference frame for three-body analysis is centered on this barycenter and rotates with the same angular velocity as the two primaries.

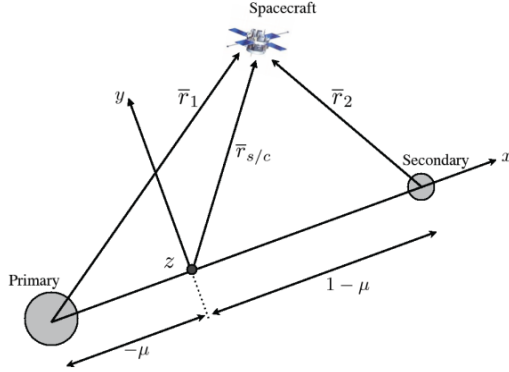


Figure 2. Three Body Problem Formulation.

As seen in Figure 2, the x -axis is defined as the line extending from the origin through the secondary. The z -axis extends in the direction of the angular momentum of the system and the y -axis completes the right-hand coordinate frame. The system is also normalized by the mass parameter μ , defined in Equation 1,

$$\mu = \frac{m_2}{m_1 + m_2}, \quad (1)$$

where m_1 and m_2 are masses of the primary and secondary, respectively.

The equations of motion governing the movement of the third body are:

$$\ddot{x} = 2\dot{y} + x - \frac{1-\mu}{r_1^3}(x + \mu) - \frac{\mu}{r_2^3}(x - 1 + \mu) \quad (2)$$

$$\ddot{y} = -2\dot{x} + y - \frac{1-\mu}{r_1^3}y - \frac{\mu}{r_2^3}y \quad (3)$$

$$\ddot{z} = -\frac{1-\mu}{r_1^3}z - \frac{\mu}{r_2^3}z. \quad (4)$$

The reader is directed to Szebehely for a further explanation of the equations of motion.¹⁰

The distances from the barycenter to the primary and secondary, respectively, may be found as

$$r_1 = \sqrt{(x + \mu)^2 + y^2 + z^2} \quad (5)$$

$$r_2 = \sqrt{(x - 1 + \mu)^2 + y^2 + z^2} \quad (6)$$

The equations of motion shown in Equations 2-4 allow for the existence of an integral of motion in the rotating frame. The integral of motion is known as the Jacobi constant, C , and is given by Equation 7.

$$C = 2U - V^2 \quad (7)$$

$$U = \frac{1}{2}(x^2 + y^2) + \frac{1-\mu}{r_1} + \frac{\mu}{r_2} \quad (8)$$

$$V = \sqrt{\dot{x}^2 + \dot{y}^2 + \dot{z}^2} \quad (9)$$

IMPLEMENTATION

The non-linear dynamics of the CRTBP cause the creation of orbits to be a non-trivial endeavor. Due to the chaotic nature of the region, initial conditions are extremely important and even slight variations of position or velocity can result in completely different behavior. The generation of initial conditions for periodic orbits in this region requires a two step process.

The first step for generating these orbits utilized a third order Richardson-Cary analytical expansion to generate an orbit from which initial conditions are derived.^{11,12} The non-dimensional parameter and the libration point region (L_1) were held constant while the Z-amplitude was varied from a dimensional value equivalent of 0 to 1.4 million kilometers. This process was used to generate a representative set of 5000 initial conditions for periodic orbits.

These 5000 initial conditions as generated by the Richardson-Cary routine were then further refined using a single-shooter algorithm. The single shooting-shooting algorithm used here takes advantage of the symmetry of a LPO and integrates the initial conditions forward in time to the point at which they cross the x-z plane. It then varies the values of the initial conditions using the state transition matrix until the trajectory crosses the plane perpendicularly. The tolerance enforced on this constraint determines the extent to which the orbit will exhibit periodic tendencies.¹³

This single-shooter algorithm was implemented and, in conjunction with a variable step Runge-Kutta 7/8 integration scheme, used to refine the initial conditions as generated from the Richardson-Cary step previously. After running the single-shooter over all the initial conditions, those trajectories that converged within tolerances were saved for later use. A sample of these orbits is shown below in Figure 3 in the rotating reference frame.

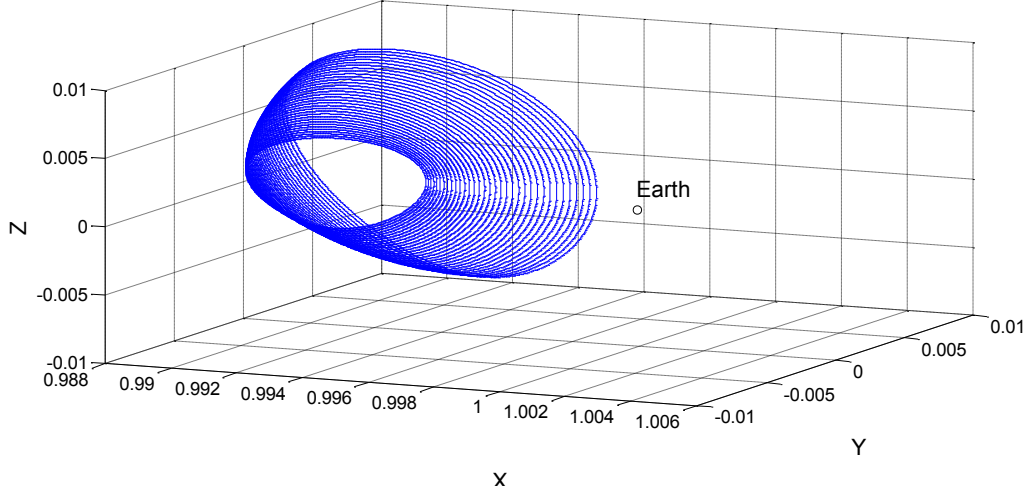


Figure 3. Sample set of LPOs generated for study (non-dimensional units).

After generation of the initial LPOs in the Sun-Earth L_1 region was complete the next step in the analysis of return trajectories was to develop a scheme to generate invariant manifolds which depart the LPO and approach the Earth. The key data this study sought was the accessibility of Earth orbits from these LPOs using manifolds with varied departure time (of the orbit) and varied initial orbits.

In order to generate these invariant manifolds the Monodromy matrix, which is the state transition matrix propagated for one orbital period, is used to determine the stable and unstable directions. These directions correspond to the eigenvectors of the Monodromy matrix. At the desired point of departure from the orbit, a small (on the order of 1×10^{-5} to 1×10^{-6}) non-dimensional perturbation to the position and velocity is added or subtracted from the state in the unstable direction. Depending on the sign of this contribution the manifold will either depart the LPO and approach the secondary body or it will depart away from the secondary body. This behavior is not consistent between orbits and thus a positive perturbation on one LPO may exhibit the opposite behavior of another LPO with the same perturbation. The reader is directed to Parker and Chua for more detailed explanation of how to generate stable/unstable invariant manifolds.¹⁴ Within this implementation a code is used to account for computational errors in the calculation of the eigenvalues which was developed by Russell.¹⁵ As an example of the manifolds generated for this study Figure 4 shows the unstable manifolds, in red, of an orbit with the manifolds approaching the secondary as time moves forward.

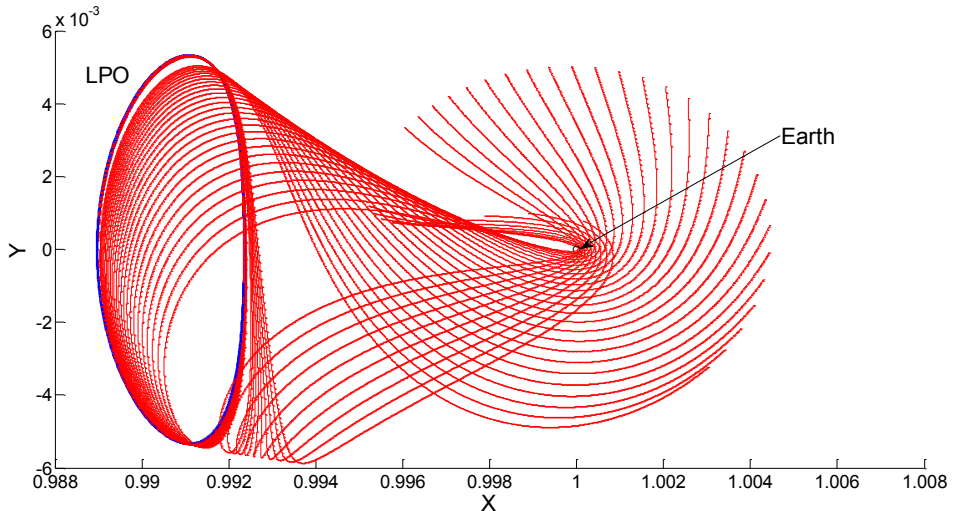


Figure 3. Invariant manifolds departing towards Earth (non-dimensional units).

With the ability to create manifolds the last step in developing the tools for this study was to create a code to find how close each manifold passes to the Earth. This seemingly trivial evaluation proved to be a challenge. After multiple approaches were attempted and several discussions with subject matter experts, a less-than-optimal yet effective scheme was devised. The challenge stems from two major considerations. First a generic code which tracks the trajectory until the distance to the Earth grows, or in other words when the sign of the difference between successive points changes, and determines this to be periapsis is ineffective. Due to the asymptotic departure from the LPO, after perturbation the trajectory can seemingly approach and depart with respect to the Earth several times. Secondly due to the step size of the variable step integrator, as the trajec-

trajectory approaches the Earth there is no guarantee that an integration point will be placed at the location of periapsis.

To address this challenge a script was developed which looks at the entire unstable invariant manifold trajectory and calculates the smallest distance to Earth along that trajectory. Using this as a starting point, unless this point lies at the end of the trajectory in which case it is discarded, the script backs up 5 integration steps and integrates forward using a much smaller fixed time-step integrator. This procedure is iterated until the periapsis is found to within a pre-specified tolerance. In evaluating this script several checks are required including a check for planetary impact, a check that the perturbation has caused the manifold to approach the secondary, and a check to make sure the iteration does not continue infinitely. An example of both the need for this script as well as its implementation, Figure 4 shows several manifolds propagated and the subsequent points (thick parts of the trajectories) solved for using the periapsis code.

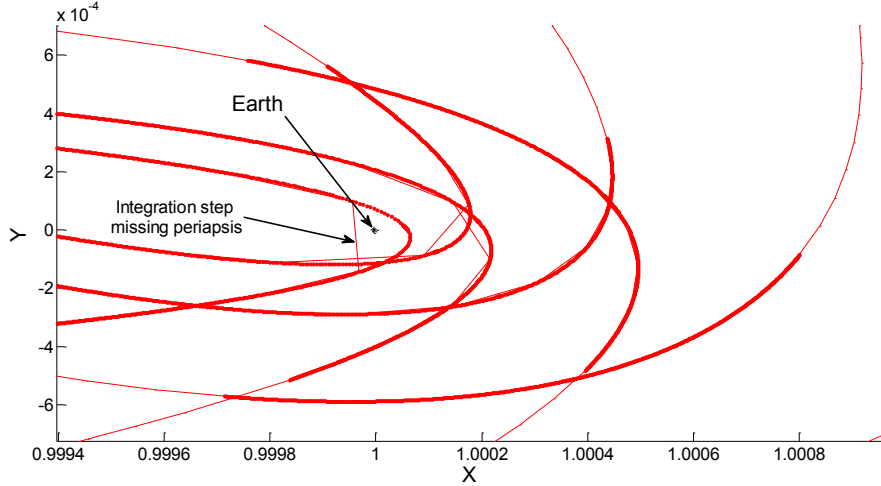


Figure 4. Periapsis code solving for closest Earth approach (non-dimensional units).

RESULTS

Using the tools described in the previous section, analysis was done on the Earth return accessibility behaviors of multiple LPOs. The results shown here are representative of an extensive opportunity for future study.

Generating and propagating manifolds for an entire orbit with reasonable fidelity is a computationally intensive task. Thus the first analysis that was performed was to see if there were specific ranges along LPOs within which manifolds were more likely to have a close, and thus useful, approach of Earth. To evaluate this tendency of an orbit several LPOs were selected from the group generated for analysis and examined. It is very important to note that all conclusions derived from these orbits are applicable only to this family or group of orbits. There are numerous factors which influence these results. In addition to the family of orbits, the size of the perturbation applied to the LPO at the desired point of departure plays a very significant role in the relationship between departure point and Earth approach distance. As this perturbation decreases, the manifold more closely models a realistic trajectory. The trade-off, however, is that the smaller

the perturbation is, the longer the trajectory takes to depart the libration point region and consequently more computational resources are needed to run over multiple manifolds.

Results were generated for four different LPOs. These LPOs are shown in Figure 5 and are labeled A, B, C, and D. This identification will be used in subsequent plots and text to refer to each orbit.

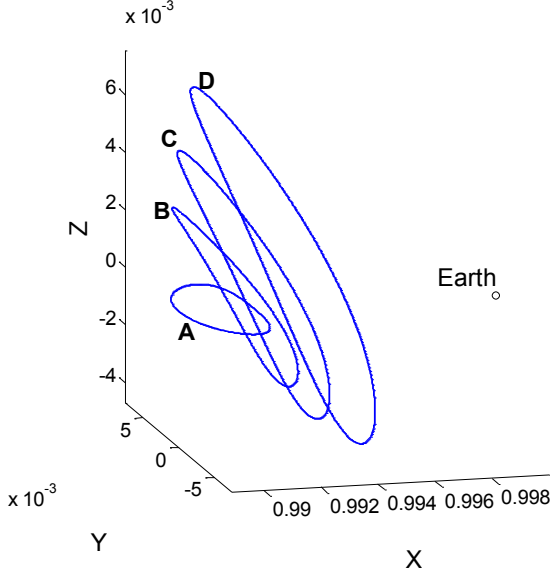


Figure 4. Evaluated representative LPOs (non-dimensional units).

As shown in Equation 7 a Jacobi constant can be calculated for each orbit in the CRTBP. This value is constant over the entire orbit and can only be changed by forces external to the system. The Jacobi values for each of the orbits A-D is shown in Figure 5.

Orbit Designation	Jacobi Value
A	3.00083727793964
B	3.00076187145967
C	3.00066900380081
D	3.00053477198624

Figure 5. Value of Jacobi constant for each representative LPO.

It can be observed from Figure 5 that for this orbit family, the larger the z-amplitude (out of plane), the lower the value of the Jacobi constant.

The figures below will demonstrate the behavior of these four orbits with a perturbation of 5×10^{-5} . The behavior of the departure location along the LPO is directly affected by this perturba-

tion size. Thus the results observed are valid for only this family of orbits with this specific perturbation.

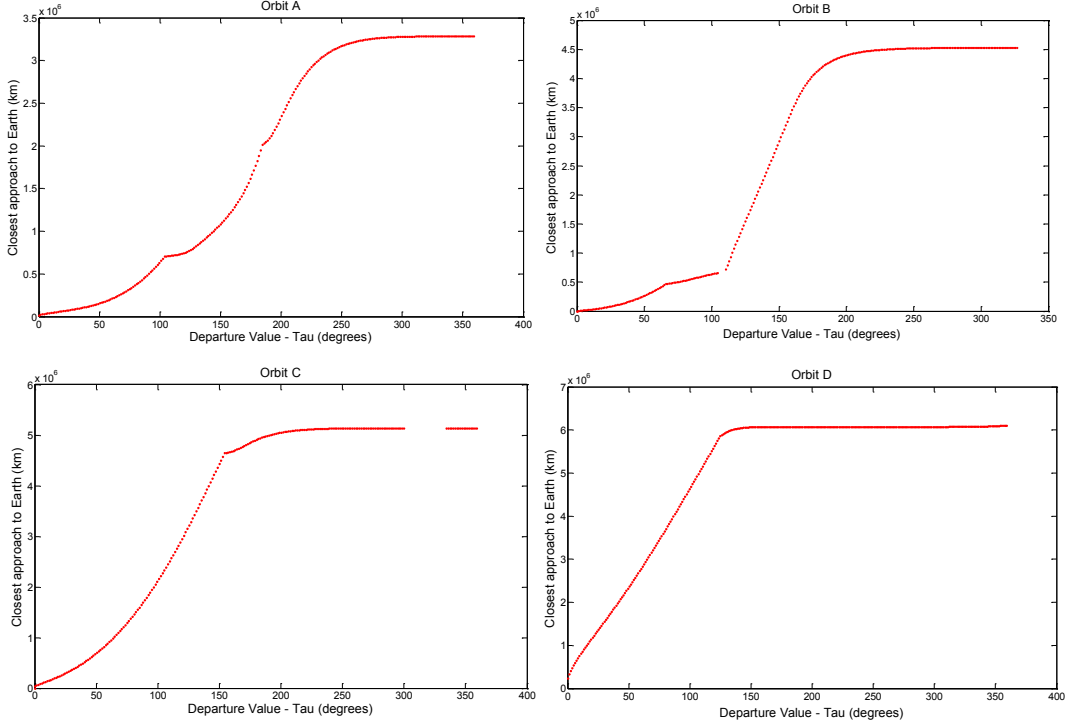


Figure 6. Closest approach versus departure location on LPO.

Figure 6 clearly shows a trend over all of the orbits that there are certain departure windows along the LPO which provide closer approaches to the Earth. These trajectories, under the formulation used for this paper, appear to approach Earth when they depart within the range of 0-45 degrees. Thus for future implementation, this proves there are ‘sweet spots’ which only need to be evaluated with manifolds and once these are determined, code can be streamlined to only evaluate these areas of the orbit. It is apparent from the plot for orbit D in Figure 6 that it does not approach very close to the Earth and has a very small window within which manifolds come even close a usable return Earth orbit. Similar data to this is possible from such plots over a larger range of orbits with a higher fidelity of evaluation.

The following plots Figures 7-10 show the three dimensional Poincare plot for the four orbits identified previously. One plot, to the left, shows a general plot of the location at which the trajectory approaches closest to the Earth for all departures. The second figure, to the right, shows where the trajectories approach close to a usable Earth orbit. For reference, the radius of geostationary orbits is 4.2164×10^4 km.

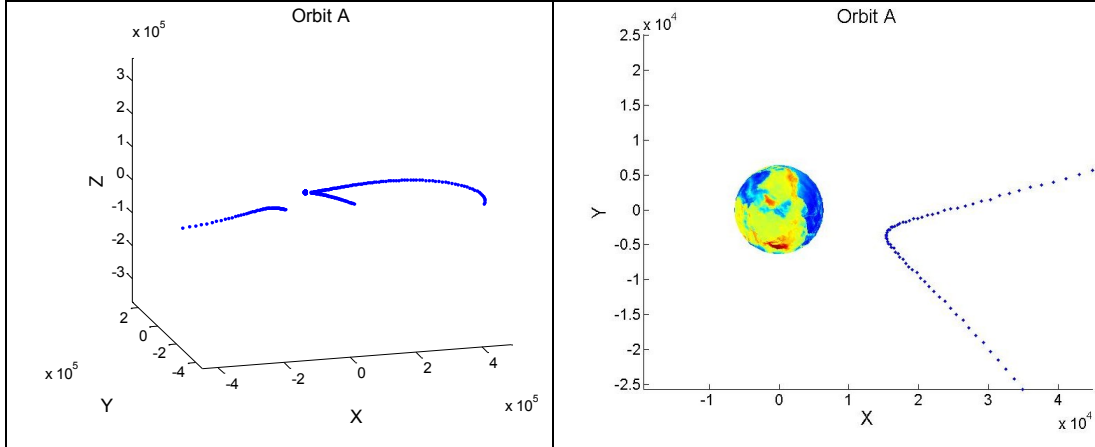


Figure 7. Poincaré maps of closest Earth approach for LPO A.

Figure 7 shows the plots for closest approach of orbit A which is an entirely in-plane LPO. This is commonly referred to as a Lyapunov orbit when there is no out of plane component for the orbit. Just as the orbit itself is in-plane, initial conditions originating in this LPO result in in-plane manifolds and in-plane Earth approaches. The discontinuity of the plot on the left is caused by propagation time. All manifolds are propagated for the same length of time, although some pass by the Earth sooner than others. Thus it is possible with this implementation to be detecting the second periapsis if it is closer than the first. The plot on the right is zoomed in and shows how the orbits approach closer to the Earth. In this case it is observed that manifolds from LPO A approach the Earth at a distance that is within the range of mid-Earth orbits (MEOs) and Geostationary orbits (GEOs).

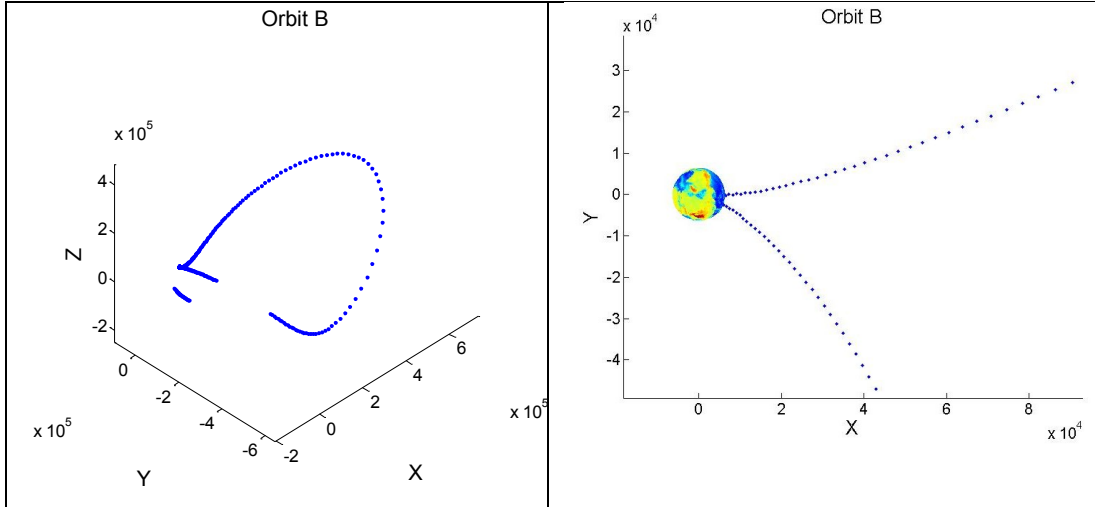


Figure 8. Poincaré maps of closest Earth approach for LPO B.

Demonstrating the behavior of manifolds originating on LPO B, Figure 8 shows that overall the manifolds behave differently than in Figure 7 and in this case cover close approaches from low Earth orbit (LEO) out to GEO. This accessibility would likely result in further study of this orbit.

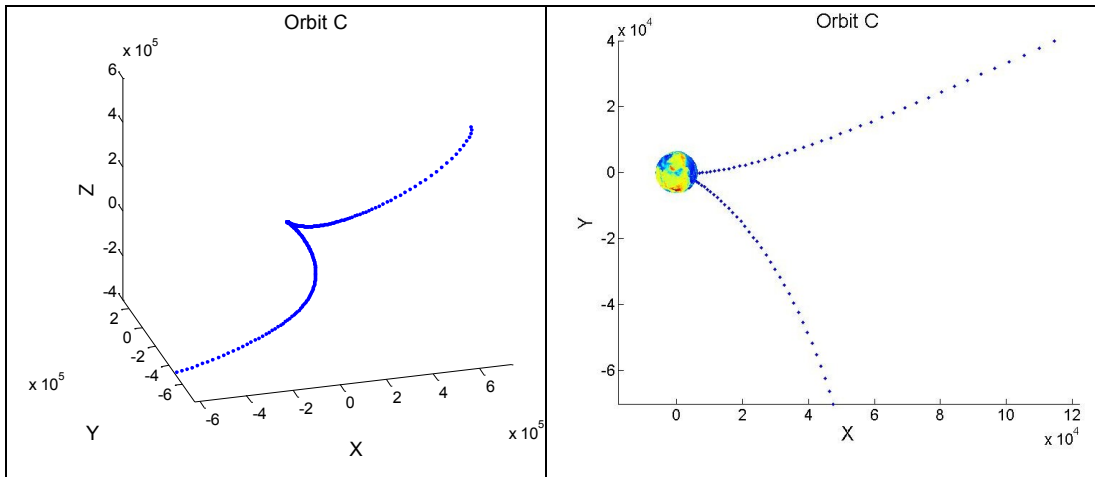


Figure 9. Poincare maps of closest Earth approach for LPO B.

Demonstrated in Figure 9, LPO C behaves differently in a global sense with a much wider range of approach distances. This orbit again approaches Earth from LEO to GEO making it an interesting target of future study.

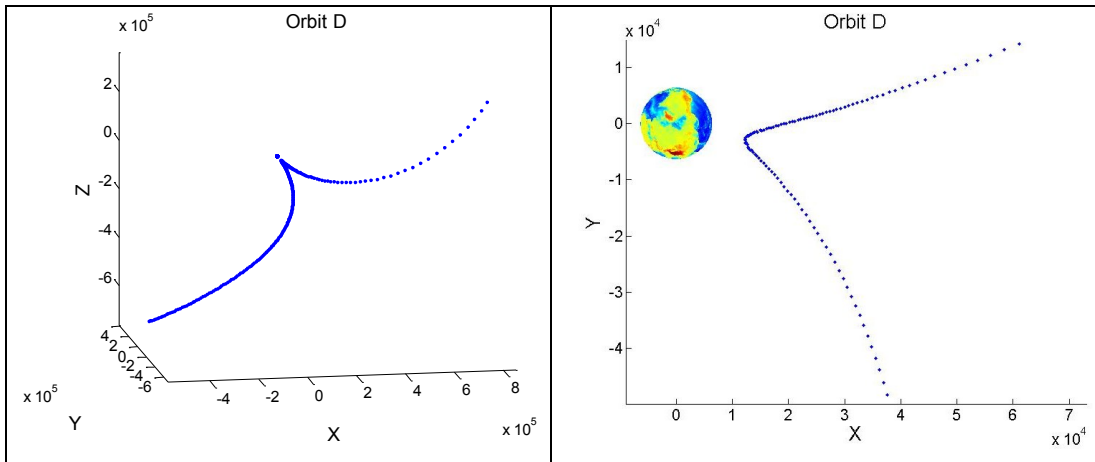


Figure 10. Poincare maps of closest Earth approach for LPO D.

The final figure demonstrating these results, Figure 10, demonstrates that orbit D does have similar accessibility to orbit A which approaches Earth from MEO to GEO.

FUTURE RESEARCH

As stated previously, the work done here serves as the foundation for extensive subsequent study. Future development in this area is likely to include a more effective Earth-approach code which will likely be developed within the integration scheme itself. Another area for exploration would be to validate the results seen here for various other LPO families. Evaluation of the affect of perturbation size on manifold Earth-approach behavior would also be beneficial.

Additionally effort will be spent to develop an evaluation scheme to study the inclination access of these manifolds. Such an inclination scheme will need to utilize the velocity vector at Earth approach and determine what inclination orbit this trajectory would enter if an in-track burn were performed in the negative-velocity direction.

Finally, the near-term culmination of this work will be to implement a looping script which will be able to evaluate the Earth approach distance and inclination for a broad range of LPOs and thus provide an ability to evaluate the appropriate LPO which will generate a desired manifold to orbits with specified altitude and inclination.

CONCLUSION

The chaotic nature of these non-linear orbits was observed clearly in the vast variation of manifold behaviors based on changing initial conditions along a single orbit. Patterns were found demonstrating that within the orbits studied there are certain specific regions along an LPO from which initial conditions propagate to advantageous Earth approaches. Simultaneously it was observed that some orbits have limited Earth orbit accessibility. These conclusions demonstrate that the specific initial conditions, as expected, drive the accessibility of Earth orbits from LPOs.

This work has demonstrated that there is sufficient evidence of the benefits that would arise from investigating this behavior with increased rigor and fidelity. As expected, these manifolds are symmetric to those used to leave Earth for LPO transfers. However, transfers from high Earth orbits have not been studied at length and may in fact be the target altitude and inclinations which such a transfer is advantageous for.

ACKNOWLEDGMENTS

Dr. Kate Davis for assistance with concept and code development as well as graphical support for figures.

Dr. Elizabeth Bradley for generous instruction and enlightenment to the beauty of chaos.

REFERENCES

- [1] Parker, J. S. and M. W. Lo, "Shoot the Moon 3D" Paper AAS 05-383, AAS/AIAA Astrodynamics Specialist Conference, Lake Tahoe, California, August 7-11, 2005.
- [2] Cheetham, B. W., K. E. Davis, and G. H. Born, "Initial Study of ORS Libration Point Utilization and Associated Guidance and Navigation Challenges," Paper AAS 10-093, AAS Guidance and Control Conference, Breckenridge, Colorado, February 6-10, 2010.
- [3] Davis, K. E., and R. Anderson, "Preliminary Study of Geosynchronous Orbit Transfers from Low Earth Orbit Using Invariant Manifolds" George H. Born Symposium. May 2010. (in progress)
- [4] Szebehely, V., "Theory of Orbits: The Restricted Problem of Three Bodies." New York: Academic Press, 1967.
- [5] Broucke, R. A., "Periodic Orbits in the Restricted Three-Body Problem with Earth-Moon Masses," Tech. Rep. 32-1168, Jet Propulsion Laboratory, Cal. Tech., 1968.
- [6] Breakwell, J. V. and J. V. Brown, "The Halo Family of 3-Dimensional Periodic Orbits in the Earth-Moon Restricted 3-Body Problem," Celestial Mechanics, Vol. 20, November 1979, pp. 389–404.
- [7] Hénon, M., "New Families of Periodic Orbits in Hill's Problem of Three Bodies," Celestial Mech. & Dynamical Astr., Vol. 85, 2003, pp. 223–246.
- [8] Nakamiya, M., Scheeres, D. J., Yamakawa, H., and Yoshikawa, M., "Analysis of Capture Trajectories into Periodic Orbits About Libration Points," Journal of Guidance, Control, and Dynamics, Vol. 31(5), 2008, pp 1344-1350.
- [9] Villac, B. F., and Scheeres, D. J., "Escaping Trajectories in the Hill Three-Body Problem and Applications," Journal of Guidance, Control, and Dynamics, Vol. 26(2), 2003, pp 224-232.
- [10] Szebehely, V., Theory of Orbits: The Restricted Problem of Three Bodies, Academic Press, New York, 1967.
- [11] Richardson, D. L. and N. D. Cary, "A Uniformly Valid Solution for Motion of the Interior Libration Point for the Perturbed Elliptic-Restricted Problem," in AIAA/AAS Astrodynamics Specialist Conference, Number AIAA 75-021, AIAA/AAS, July 1975.
- [12] Richardson, D. L., "Analytical Construction of Periodic Orbits about the Collinear Points," Celestial Mechanics, Volume 22, 1980, pp. 241–253.
- [13] Howell, K. C., "Three-Dimensional, Periodic, 'Halo' Orbits," Celest. Mech. Volume 32(1), 1984, pp. 53-71.
- [14] Parker, T. S. and L. O. Chua, Practical Numerical Algorithms for Chaotic Systems, Springer-Verlag, New York, 1989.
- [15] Russell, R. P., "Global Search for Planar and Three-Dimensional Periodic Orbits near Europa," Journal of the Astronautical Sciences, Volume 54(2), 2006, pp. 199–226.

Propagating the Admissible Region with the Symplectic State Transition Matrix

Kohei Fujimoto
CSCI 5446 Spring 2010

April 30, 2010

Abstract

Situational awareness of Earth-orbiting particles such as active satellites and space debris is highly important for future human activities in space. The intersection of multiple admissible regions can be used to correlate optical observations as well as give an initial state estimate. The current algorithm, however, uses Keplerian dynamics, which is often an insufficient model for long term propagation. In this paper, I discuss results obtained with a symplectic integrator and its linear counterpart, the symplectic state transition matrix. The new dynamics causes interactions of admissible regions that had not been observed with Keplerian dynamics to appear.

1 Introduction

Situational awareness of Earth-orbiting particles such as active satellites and space debris is highly important for future human activities in space. Presently, over 300,000 particles have been estimated to exist, and over 80,000 observations are made per day [1]. Observations are made either by radar or optical sensors. Determining the state of some Earth-orbiting object based on one optical observation is an underdetermined problem, since usually the range and range-rate of the object remain unknown. Furthermore, it is generally uncertain whether two arbitrary optical observations are of the same object. This is the crux of the too short arc (TSA) correlation problem [2][3].

Fujimoto and Scheeres are currently investigating a correlation technique that uses an uncertainty region of the observed objects state, or the admissible region, that is defined based on some physical constraints of the possible orbits [4]. The admissible region is a 2-dimensional submanifold embedded in a 6-dimensional state space. The intersection of multiple admissible regions can be used to correlate optical observations as well as give an initial state estimate. Furthermore, the propagation of the admissible region over time can be linearized locally to speed up computation. In our current algorithm, however, we only use Keplerian dynamics for the propagation, which does not capture the dynamical effects of a gravitational field of an oblate Earth or of third-bodies.

In this paper, I discuss an updated correlation algorithm that utilizes a symplectic integrator and its linear counterpart, the symplectic state transition matrix (SSTM), which allowed me to incorporate orbit perturbations due to the J_2 term of the Earth's gravity potential. I first define the admissible region in detail as well as introduce the necessary dynamics / dynamical systems concepts (Section 2). Next, I outline the symplectic integration methods I implemented: the 4th order Gauss collocation method, and the 4th order SSTM (Section 3) [5][6]. With these tools, I simulate observing objects in a GPS, Molniya, and GEO orbit 3 times each over the span of 100 hours (Section 4). The manifolds propagated by the symplectic integrator began to deviate from the Keplerian solution significantly for observations separated by 100+ hours, and the intersection region changed as a result. The symplectic propagator ultimately improved initial state estimates compared to Keplerian dynamics.

2 Background

In this section, I explain how the admissible region concept can be used to correlate optical observations and give an initial orbit estimate. I also introduce the basics of symplecticity and linearized dynamics.

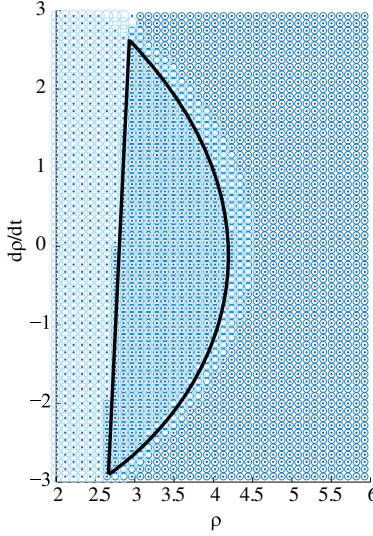


Figure 1: An admissible region for $\mathfrak{X} = (\alpha, \delta, \dot{\alpha}, \dot{\delta}, \Theta, \Phi) = (2.064 \text{ rad}, -0.2378 \text{ rad}, 0.5072 \text{ rad/hr}, 0.0654 \text{ rad/hr}, 4.8 \text{ rad}, 0.1 \text{ rad})$. The different shadings represent the different regions which satisfy each criterion in set C ; thus, the admissible region is where all types of shading overlap, or the region outlined by the black line.

2.1 The Admissible Region

For optical-only observations, which are usually made for objects in medium Earth orbit (MEO) and geostationary orbit (GEO), only the angles and angular rates of the track can be determined [7][8]. That is, the range and range rate remains largely unconstrained, except for a few physical restrictions which can be used to constrain their values. Thus, each track can be mathematically expressed in terms of an *attributable vector* \mathfrak{X} at epoch t of the observation [3]:

$$\mathfrak{X} = (\alpha, \delta, \dot{\alpha}, \dot{\delta}) \in [-\pi, \pi] \times (-\pi/2, \pi/2) \times \mathbb{R}^2, \quad (1)$$

where α is the right ascension and δ is the declination of the observed object. For a more complete description of the track, I append the longitude $\Theta \in [-\pi, \pi]$ and latitude $\Phi \in (\pi/2, \pi/2)$ of the observation as observation parameters.

For any \mathfrak{X} , I can take different values of range and range-rate $(\rho, \dot{\rho})$ to complete the topocentric coordinates of the particle and thus obtain different physical orbits. However, not all of these orbits are relevant for any given application. For instance, we may not be interested in objects that escape Earth orbit a couple of hours after observation. Rather, a closed region of the $(\rho, \dot{\rho})$ plane can be defined such that all of the physically relevant orbits are contained within the interior of this region. I define this region as the *admissible region* $F_{\mathfrak{X}}(t)$ [2]. A set of criteria C defining the admissible region has been proposed by Marsukin, et al.:

$$C = \bigcap_{i=1}^4 C_i, \quad (2)$$

and

$$C_1 = \{(\rho, \dot{\rho}) : E \leq 0\} \quad C_2 = \{(\rho, \dot{\rho}) : 2 \leq \rho \leq 20\} \quad (3)$$

$$C_3 = \{(\rho, \dot{\rho}) : 1.03 \leq r_p\} \quad C_4 = \{(\rho, \dot{\rho}) : r_a \leq 25\}, \quad (4)$$

where E is the specific geocentric energy of the debris particle, and r_p and r_a are the perigee and apogee altitudes, respectively. Units of length are in Earth radii. Figure 1 is an example of an admissible region.

Suppose we have multiple admissible regions $F_{\mathfrak{X}_1}(t_1), F_{\mathfrak{X}_2}(t_2), \dots, F_{\mathfrak{X}_n}(t_n)$ each based on uncorrelated optical tracks at different times. To determine whether these observations are correlated, I map their respective admissible regions

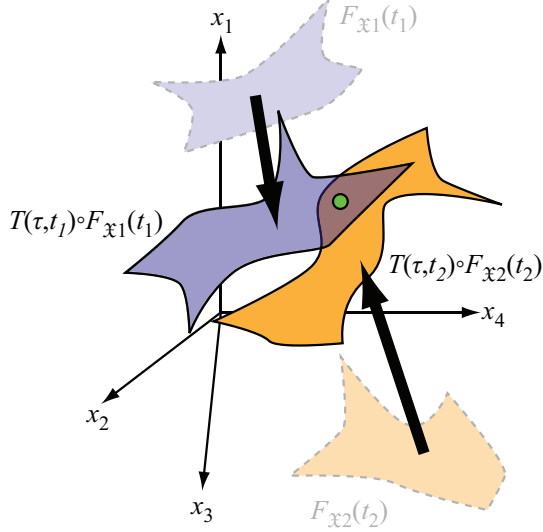


Figure 2: Map T evolves admissible regions $F_{x1}(t_1)$ (blue) and $F_{x2}(t_2)$ [orange] from two separate observations to a common epoch τ . The intersection point [green] is where the observed object most likely exists in state space.

to a common state space and propagate them to a common epoch time τ with some transformation $T(\tau, t_i)$, where $i = 1, 2, \dots, n$. In this paper, I use the Poincaré orbit element space, which are non-singular canonical orbit variables [9]:

$$\begin{aligned} l &= \Omega + \omega + M & \Omega &= \sqrt{\mu a} \\ g &= \sqrt{2\Omega(1 - \sqrt{1 - e^2})} \cos(\omega + \Omega) & \mathfrak{G} &= -g \tan(\omega + \Omega) \\ h &= \sqrt{2\Omega \sqrt{1 - e^2} (1 - \cos i)} \cos \Omega & \mathfrak{H} &= -h \tan \Omega, \end{aligned} \quad (5)$$

where μ is the standard gravitational parameter. We expect that if the observations are related, then their admissible region maps $T(\tau, t_i) \circ F_{x_i}(t_i)$ would intersect at the same state space coordinate as the observed object. Furthermore, since T is invertible and continuous, each $T(\tau, t_i) \circ F_{x_i}(t_i)$ are 2-dimensional manifolds embedded in 6-dimensional space. As a consequence, the probability that any 2 admissible region maps intersect randomly is 0 [10]. Figure 2 is a graphical representation of the algorithm.

In the current algorithm, T is a Keplerian propagator that simply adjusts the mean anomaly by:

$$\Delta M = \sqrt{\frac{\mu}{a^3}} \Delta t, \quad (6)$$

where Δt is the propagation time. Although simple, requiring just one propagation time step, a Keplerian propagator assumes the object is affected only by gravity from a perfectly spherical Earth. In reality, the Earth has very complex features on its surface that change the gravity potential function. Gravity from third bodies such as the sun and the moon also pull on the object, among many other perturbing forces. Therefore, Keplerian dynamics is only a good approximation for, at best, $\sim 10^0$ hours prior and after an observation. If we are to propagate objects for longer periods of time, we need to incorporate a better force model.

2.2 Symplecticity

Symplecticity is an important characteristic of Hamiltonian flow [5][11]. Let us define symplecticity by first considering a 2-dimensional state space $p-q$ spanned by vectors $\xi = (\xi_p, \xi_q)^T$ and $\eta = (\eta_p, \eta_q)^T$. Then, we say that a linear

map $A : \mathbb{R}^2 \rightarrow \mathbb{R}^2$ is *symplectic* if:

$$\det[(\xi \quad \eta)] = \det[(A\xi \quad A\eta)]. \quad (7)$$

The determinant for 2-space is the oriented area between ξ and η , so a symplectic map in 2-space preserves area. For a general $2d$ -dimensional map $A : \mathbb{R}^{2d} \rightarrow \mathbb{R}^{2d}$, we define the conserved quantity as the sum of determinants over p_i - q_i space for all $i = 1, 2, \dots, d$:

$$\sum_{i=1}^d \det[(\xi_i \quad \eta_i)] = \sum_{i=1}^d \det[(A'\xi_i \quad A'\eta_i)], \quad (8)$$

where $\xi_i = (\xi_{pi}, \xi_{qi})^T$, $\eta_i = (\eta_{pi}, \eta_{qi})^T$, and $A' : \mathbb{R}^2 \rightarrow \mathbb{R}^2$ such that $A'\xi$ is equal to the p_i - q_i components of $A\xi$, and so on. Therefore, the sum of the areas between ξ_i and η_i in each p_i - q_i space is conserved. We simplify (7) and (8) as:

$$A^T \begin{pmatrix} 0 & I \\ -I & 0 \end{pmatrix} A = A^T J A = J, \quad (9)$$

where I is the identity matrix. For non-linear continuously differentiable flows $\varphi(\mathbf{p}, \mathbf{q})$, each point on the map is locally approximated by a linear map through its Jacobian $\partial\varphi/\partial(\mathbf{p}, \mathbf{q})$. We thus define a flow to be symplectic if:

$$\left(\frac{\partial\varphi}{\partial(\mathbf{p}, \mathbf{q})} \right)^T J \left(\frac{\partial\varphi}{\partial(\mathbf{p}, \mathbf{q})} \right) = J \quad (10)$$

is true at every point on the flow.

A *symplectic numerical integrator* is a numerical integration scheme set up so that it preserves a flow's symplecticity. That is:

$$\left(\frac{\partial(\mathbf{p}_{n+1}, \mathbf{q}_{n+1})}{\partial(\mathbf{p}_n, \mathbf{q}_n)} \right)^T J \left(\frac{\partial(\mathbf{p}_{n+1}, \mathbf{q}_{n+1})}{\partial(\mathbf{p}_n, \mathbf{q}_n)} \right) = J, \quad (11)$$

where n indicates the current integration step. It has been shown that integration methods that preserve quadratic first integrals such as angular momentum and energy are symplectic [12]. The great advantage to applying symplectic methods to Hamiltonian systems instead of, say, standard Runge-Kutta integration, is that it rigorously obeys conservation laws and preserves the “structure” of the system. As a consequence, we expect an increase in integration accuracy.

2.3 Linearized Dynamics

Suppose we have some dynamical system described by the following differential equation:

$$\dot{\mathbf{x}} = f(t, \mathbf{x}). \quad (12)$$

By taking a Taylor series expansion about some reference point \mathbf{x}_0 and dropping higher order terms, we linearize the dynamics about this point:

$$\dot{\mathbf{x}}_0 + \delta\dot{\mathbf{x}} = \frac{\partial f}{\partial \mathbf{x}_0}(\mathbf{x}_0 + \delta\mathbf{x}) \Leftrightarrow \delta\dot{\mathbf{x}} = \frac{\partial f}{\partial \mathbf{x}_0}\delta\mathbf{x}. \quad (13)$$

Instead of solving (13) to find $\delta\mathbf{x}$ at a later time, we'd like to define a matrix Φ such that:

$$\delta\mathbf{x}(t) = \Phi(t, t_0)\delta\mathbf{x}_0 \quad (14)$$

called the *state transition matrix* (STM). From the definition,

$$\dot{\Phi} = \frac{\partial f}{\partial \mathbf{x}_0}\Phi. \quad (15)$$

To solve for the STM of a system, typically one would numerically integrate (15) simultaneously with (13) using initial conditions $\Phi = I$.

The symplectic integrator explained in Section 2.2 can only propagate points in time. The aim of this paper, however, is to propagate admissible regions, which are 2-dimensional manifolds. I can take a large number of sample points on the manifold and propagate them non-linearly using a symplectic integrator, but this process often becomes a bottleneck for the correlation algorithm. It is more efficient to take a smaller subset of sample points and use these as reference points to linearly propagate small planar regions in state space. Computation times reduce from on the order of days to tens of minutes while still retaining density distribution to within $\sim 5\%$ over the entire manifold [4].

3 Method

In this section, I outline the symplectic numerical integrator (Gauss collocation) and the SSTM that I implemented for this project

3.1 Gauss Collocation Method

The Gauss collocation method is a type of symplectic integrator. In a general collocation integration method, given initial conditions \mathbf{x}_0 at time t_0 for a system $\dot{\mathbf{x}} = f(t, \mathbf{x})$, the flow is approximated as some polynomial $u(t)$ of decree s such that 1. $u(t_0) = \mathbf{x}_0$ and 2. the time derivative of u matches f at s distinct points [5]. That is:

$$\begin{cases} u(t_0) = \mathbf{x}_0 \\ \dot{u}(t_0 + c_i h) = f(t_0 + c_i h, u(t_0 + c_i h)), \end{cases} \quad (16)$$

where $i = 1, 2, \dots, s$, c_i 's are constants specified by the method and integration order, and h is the integration time step. In the Gauss method, the c_i 's are the zeros of the s -th shifted Legendre polynomial. The equations can be reformulated in the Runge-Kutta form [13]:

$$\begin{cases} k_1 = f \left[t_0 + \left(\frac{1}{2} - \frac{\sqrt{3}}{6} \right) h, \mathbf{x}_0 + \left\{ \frac{1}{4} k_1 + \left(\frac{1}{4} - \frac{\sqrt{3}}{6} \right) k_2 \right\} h \right] \\ k_2 = f \left[t_0 + \left(\frac{1}{2} + \frac{\sqrt{3}}{6} \right) h, \mathbf{x}_0 + \left\{ \left(\frac{1}{4} + \frac{\sqrt{3}}{6} \right) k_1 + \frac{1}{4} k_2 \right\} h \right] \\ \mathbf{x}_1 = \mathbf{x}_0 + \frac{1}{2} (k_1 + k_2) h \end{cases} \quad (17)$$

Note that k_1 depends on both k_1 and k_2 , and the same is true for k_2 . Therefore, the Gauss collocation method is an *implicit integrator*. One computationally efficient way to solve for the k parameters is to use a Newton-Raphson iteration. If we let $\mathbf{K}_n = (k_{1n}, k_{2n})^T$ be the n -th guess for the k parameters,

$$\frac{\partial f}{\partial \mathbf{x}_0} \Big|_{\mathbf{K}_n} (\mathbf{K}_{n+1} - \mathbf{K}_n) = - \left(\left[\begin{array}{c} f \left[t_0 + \left(1/2 - \sqrt{3}/6 \right) h, \mathbf{x}_0 + \left\{ 1/4 k_{1n} + \left(1/4 - \sqrt{3}/6 \right) k_{2n} \right\} h \right] \\ f \left[t_0 + \left(1/2 + \sqrt{3}/6 \right) h, \mathbf{x}_0 + \left\{ \left(1/4 + \sqrt{3}/6 \right) k_{1n} + 1/4 k_{2n} \right\} h \right] \end{array} \right] - \mathbf{F}_n \right) = -\mathbf{F}_n \quad (18)$$

$$\Leftrightarrow \mathbf{K}_{n+1} = \mathbf{K}_n - \frac{\partial f}{\partial \mathbf{x}_0} \Big|_{\mathbf{K}_n}^{-1} \mathbf{F}_n. \quad (19)$$

$\partial f / \partial \mathbf{x}_0|_{\mathbf{K}=0}$ is a good enough approximation for $\partial f / \partial \mathbf{x}_0|_{\mathbf{K}_n}$ in most cases.

Figure 3 shows a comparison between the integration accuracy of a 4th order Gauss collocation integrator and a constant step 4th order Runge-Kutta integrator written for a class assignment [14]. Figure 4 is a comparison of the change in energy over time. We see that the Runge-Kutta solution loses energy, and thus the numerical dynamics force the orbit to spiral inwards.

3.2 Symplectic State Transition Matrix

Instead of integrating (15) with a symplectic numerical integrator to solve for the STM, we can take advantage of the discretized dynamics and find some set of matrices \mathcal{F}_n such that:

$$\Phi(t, t_0) = \mathcal{F}_n \circ \mathcal{F}_{n-1} \circ \cdots \circ \mathcal{F}_1 \circ \Phi(t_0, t_0), \quad (20)$$

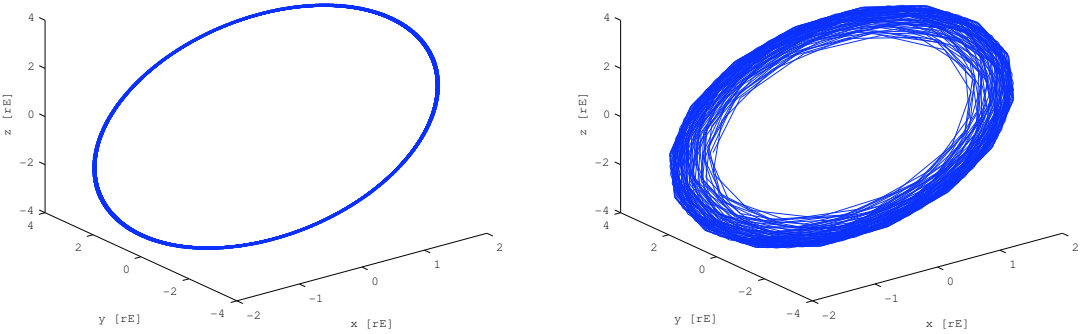


Figure 3: Orbit of a GPS satellite propagated 700 hours with 1000 time steps using a symplectic (left) and Runge-Kutta (right) integrator. Point-mass gravity potential was used for this example.

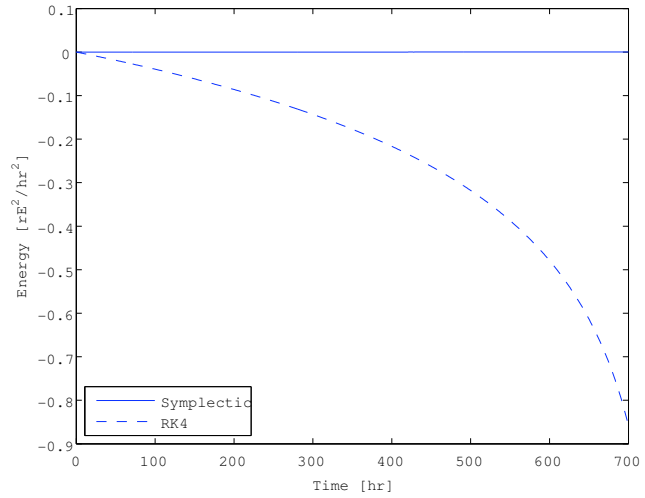


Figure 4: A comparison of the change in specific total energy for the example in Figure 3.

where n is the number of integration steps and $\Phi(t_0, t_0) = \mathbf{I}$ [6]. The discretized Hamiltonian dynamics are:

$$\mathbf{q}_{n+1} = \mathbf{q}_n + h\mathbf{p}_n - \alpha h^2 \frac{\partial U_n}{\partial \mathbf{q}_n} \quad (21)$$

$$\mathbf{p}_{n+1} = \mathbf{p}_n - \alpha h \frac{\partial U_n}{\partial \mathbf{q}_n} - (1 - \alpha)h \frac{\partial U_{n+1}}{\partial \mathbf{q}_{n+1}}, \quad (22)$$

where \mathbf{q} is the general coordinate, \mathbf{p} is the general momentum, U is the potential function, h is the integration timestep, and α is parameter that dictates the integration “direction”: $\alpha = 0$ corresponds to backward Euler, $\alpha = 1$ to forward Euler, and $\alpha = 1/2$ to midpoint rule. Then,

$$\begin{pmatrix} \delta \mathbf{q}_{n+1} \\ \delta \mathbf{p}_{n+1} \end{pmatrix} = \mathcal{F}_n \begin{pmatrix} \delta \mathbf{q}_n \\ \delta \mathbf{p}_n \end{pmatrix}, \quad (23)$$

where

$$\mathcal{F}_n = \begin{pmatrix} \mathbf{I} - \alpha h^2 (\partial^2 U_n / \partial \mathbf{q}_n^2) & h \mathbf{I} \\ -\alpha h (\partial^2 U_n / \partial \mathbf{q}_n^2) - (1 - \alpha)h (\partial^2 U_{n+1} / \partial \mathbf{q}_{n+1}^2) (\mathbf{I} - \alpha h^2 (\partial^2 U_n / \partial \mathbf{q}_n^2)) & \mathbf{I} - (1 - \alpha)h^2 (\partial^2 U_{n+1} / \partial \mathbf{q}_{n+1}^2) \end{pmatrix}. \quad (24)$$

This formulation is 1st order and is symplectic (i.e. $\Phi^T J \Phi = J$) only for $\alpha = 0$ or 1 . For a 2nd order accuracy, we combine two integration steps:

$$\begin{pmatrix} \delta \mathbf{q}_{n+1} \\ \delta \mathbf{p}_{n+1} \end{pmatrix} = \mathcal{F}_{n+1/2}(\alpha = 1) \circ \mathcal{F}_{n+1/2}(\alpha = 0) \begin{pmatrix} \delta \mathbf{q}_n \\ \delta \mathbf{p}_n \end{pmatrix} = \mathcal{F}'_n \begin{pmatrix} \delta \mathbf{q}_n \\ \delta \mathbf{p}_n \end{pmatrix} \quad (25)$$

$$\Leftrightarrow \mathcal{F}'_n = \begin{pmatrix} \mathbf{I} - h^2/2 \cdot (\partial^2 U_{n+1/2} / \partial \mathbf{q}_{n+1/2}^2) & h \left\{ \mathbf{I} - h^2/4 \cdot (\partial^2 U_{n+1/2} / \partial \mathbf{q}_{n+1/2}^2) \right\} \\ -h \cdot (\partial^2 U_{n+1/2} / \partial \mathbf{q}_{n+1/2}^2) & \mathbf{I} - h^2/2 \cdot (\partial^2 U_{n+1/2} / \partial \mathbf{q}_{n+1/2}^2), \end{pmatrix} \quad (26)$$

where $n + 1/2$ is a half integration step of $h/2$ between n and $n + 1$. For even higher order accuracy, we employ a technique called fractal decomposition, which is based on Lie group theory [15]:

$$\begin{pmatrix} \delta \mathbf{q}_{n+1} \\ \delta \mathbf{p}_{n+1} \end{pmatrix} = \mathfrak{F}_n \begin{pmatrix} \delta \mathbf{q}_n \\ \delta \mathbf{p}_n \end{pmatrix}, \quad (27)$$

where

$$\mathfrak{F}_n(h, t) = \mathcal{F}'_n(s_3 h, t + (1 - s_3)h) \circ \mathcal{F}'_n(s_3 h, t + (1 - 2s_3)h) \circ \mathcal{F}'_n((1 - 4s_3)h, t + 2s_3 h) \circ \mathcal{F}'_n(s_3 h, t + s_3 h) \circ \mathcal{F}'_n(s_3 h, t) \quad (28)$$

and $s_3 = 1/(4 - \sqrt[3]{4})$.

4 Results

I simulated observing the following objects 3 times each over 100 hours:

GPS ($a, e, i, \Omega, \omega, M$) = (3.9994 r_E , 0.0006, 1.1284 rad, 4.9148 rad, 4.2128 rad, 2.9461 rad)

Molniya (4.1472 r_E , 0.5529, 1.2347 rad, 5.5811 rad, 2.4137 rad, 4.8996 rad)

GEO (6.6102 r_E , 0.0003, 0.0002 rad, 3.1274 rad, 2.3294 rad, 5.7226 rad),

where a is the semi-major axis, e is the eccentricity, i is the inclination, Ω is the longitude of the ascending node, ω is the argument of periaxis, and M is the mean anomaly of the object. These values are actual spacecraft data taken from the TLE catalog [16]. The first observation is made at time 0, the second at ~ 50 hours, and the third ~ 100 hours. Since we are most interested in how the new dynamics and integration scheme affects the propagation of the manifolds, I assume that we have knowledge regarding which object each observation was of.

I model the dynamics of the observed objects with the following gravitational potential:

$$U = \frac{\mu}{r} \left\{ 1 - J_2 \left(\frac{R_E}{r} \right)^2 \left(\frac{3}{2} \sin^2 \varphi - \frac{1}{2} \right) \right\}, \quad (29)$$

where r is the radial distance of the debris object from the Earth's center of mass, J_2 is the oblateness term of the spherical harmonics decomposition of the Earth's shape, R_E is the radius of the Earth, and $\varphi = z/r$ is the latitude of the debris object [9]. We expect secular perturbations in (Ω, ω, M) , and smaller periodic perturbations in all orbital elements. Note that any conservative perturbation force can be added to the potential function, including third-body effects, higher order harmonics of the Earth's surface, and solar radiation pressure. For this project, I chose to implement only the J_2 term because it is the largest perturbation force for objects in MEO and GEO by at least an order of magnitude, and due to project time constraints [17].

For each observation, I take a 0.01×0.01 sized subset of the admissible region in the $\rho\dot{\rho}$ space that includes the true state of the observed object and map it to Poincaré orbit element space. I then propagate the subsets backwards in time to the epoch of the first observation for that object using 1. Keplerian motion and 2. symplectic numerical integration as described in Section 3 with the potential in (29). Similar to Hsu's method of locating attractors, we determine where the manifold lies in 6-space by discretizing the space into $100 \times 314 \times 49 \times 30 \times 10 \times 10 = 4.6158 \times 10^9$ discretization units, or "bins," and recording whether the non-linearly mapped reference points on the manifold or their local linear approximations lie in each bin [18]. The number of bins in each coordinate direction was chosen such that the bins were hypercubes with equal sides. Instead of searching for exact intersections of admissible regions, I look for bins where subregions of multiple admissible regions exist; i.e. when the two manifolds *overlap*. Since it is extremely difficult to depict a 6-dimensional space on 2-dimensional paper, we project the Poincaré space onto 3 2-dimensional planes using their symplectic coordinate-conjugate momentum pairs; i.e. $\mathfrak{L}-\mathfrak{l}$, $\mathfrak{G}-\mathfrak{g}$, and $\mathfrak{H}-\mathfrak{h}$ [7].

4.1 GPS

Figure 5 shows the propagated admissible regions for all 3 observations. The observations were made at time 0, 58.7 hours, and 100 hours. As time passes, the manifold is stretched in the \mathfrak{l} direction, which is a measure of the angular position of the spacecraft on the orbit. \mathfrak{l} is modulo 2π , so as a consequence, the manifold gets "shredded" in the $\mathfrak{L}-\mathfrak{l}$ plane [7]. The most notable difference between the symplectic and Keplerian integration schemes is in the $\mathfrak{H}-\mathfrak{h}$ plane, which is expected since these are equivalent to Ω in the classical orbit elements, and J_2 perturbs Ω the most. We see that as time passes, the admissible region map propagated by Keplerian dynamics drifts away from the true spacecraft state. At 100 hours, the Keplerian propagator has accumulated so much error that the map no longer includes the true state. On the other hand, the map propagated by the symplectic integrator includes the true state all 3 times. The symplectic integrator allows us to implement a better force model with good numerical accuracy.

Figure 6 shows the the observations at time 0 and 100 hours run through the correlation algorithm explained in Section 2.1. For both propagation schemes, the admissible regions overlap over a small region ($\sim 10^0$ bins), so the algorithm correctly correlates the two observations. However, since the admissible region map from Keplerian dynamics does not include the true state, neither does the overlap region. Therefore, the accuracy of the initial state estimate from the Keplerian dynamics is poor. Conversely, the overlap region for the manifolds propagated with the symplectic integrator does include the true state, so accuracy is improved in this case.

4.2 Molniya

Molniya orbits were often used by the Soviet Union during the cold war for its communication satellites [9]. Accurate integration of Molniya orbits in a reasonable timeframe proved to be difficult due to its high speed at its periapsis compared to the two other objects (7.2359 km/s versus 3.9530 km/s for GPS, 3.0748 km/s for GEO). That is, small time steps are required to completely capture the dynamics of the object near periapsis, thus increasing the number of total time steps. With the MATLAB implementation I wrote for this paper, propagation of the admissible region subspace by 108 hours using 2000 time steps required 30+ hours on a dual-core Xeon server. This setting, however, only achieves ~ 0.1 Earth radius accuracy in the position, as seen in Figure 7. The integration error is large enough to push objects into the wrong discretization bins in state space.

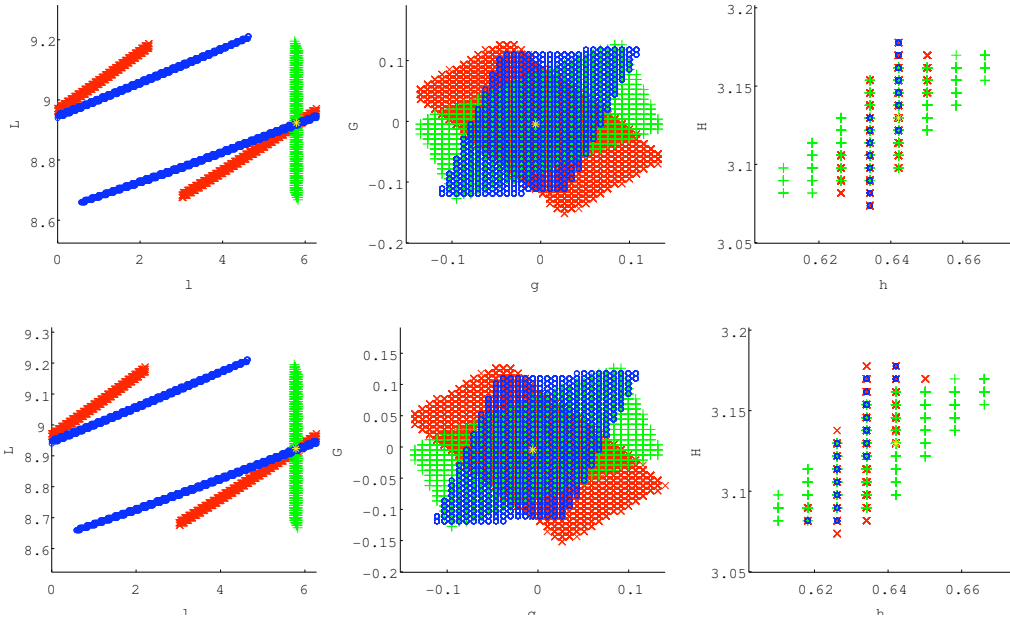


Figure 5: Admissible regions from time 0 (green), 58.7 hours (red), and 100 hours (blue) propagated back to time 0 using a symplectic (top) and Keplerian (bottom) propagator for observations of a GPS satellite. The manifolds have been projected onto the Ω - l (left), G - g (mid), and H - h (right) planes. Each symbol is a discretization bin that includes the respective manifold. The actual coordinate of the object's state is indicated by the yellow x.

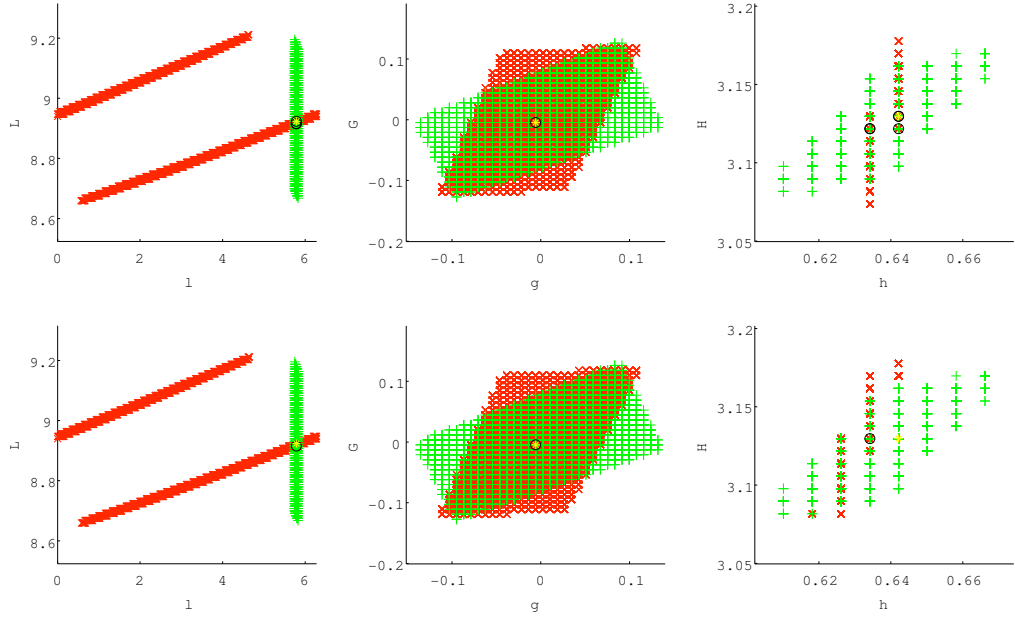


Figure 6: Correlation process for observations at time 0 (green) and 100 (red) hours using a symplectic (top) and Keplerian (bottom) propagator for a GPS satellite. The overlap region is indicated in black, and the actual coordinate of the object's state by the yellow x. The Keplerian propagator fails to include the true state in the Ω -I and \mathfrak{H} - \mathfrak{h} planes.

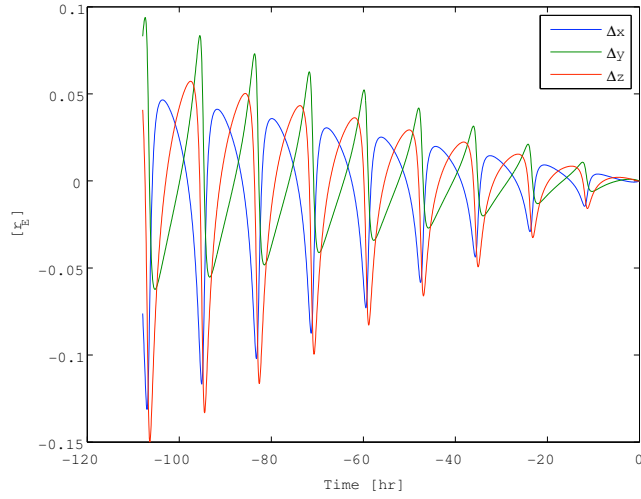


Figure 7: Position error of backward propagation of an object in Molniya orbit for a 4th order Gauss collocation integrator using 2000 time steps over 100 hours. The “true” orbit was calculated with a 4th order constant step Runge-Kutta method with 10000 time steps.

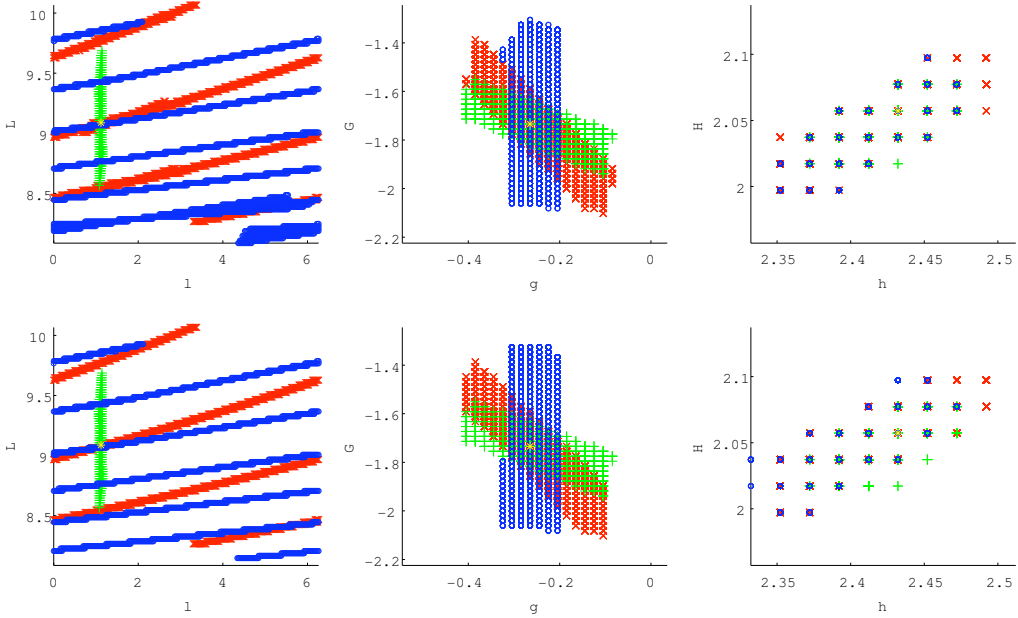


Figure 8: Admissible regions from time 0 (green), 60 hours (red), and 108 hours (blue) propagated back to time 0 using a symplectic (top) and Keplerian (bottom) propagator for observations of a Molniya satellite.

With the above caveat in mind, Figure 8 shows the propagated admissible regions for all 3 observations. The observations were made at time 0, 60 hours, and 108 hours. The manifolds propagated by 108 hours with the two methods are visibly different in all projection planes. The manifold propagated by the symplectic integrator has irregular lumps after 108 hours for $\Omega \sim 8$. This behavior is likely numerical dynamics, since generally the lower Ω is for an object, the higher its velocity at periapsis. Unlike the GPS case, the true state is included in all admissible region maps for both the symplectic and Keplerian integrators.

Figure 9 shows the the observations at time 0 and 108 hours run through the correlation algorithm. Again, the algorithm correctly correlates the observations for both propagation schemes. Neither overlapping region, however, includes the true state due to numerical dynamics for the symplectic propagator and poor force modeling for the Keplerian propagator. This example illustrates that no matter how accurate my force model may be and no matter how strictly my integrator conserves energy, I may still obtain poor state estimation results from a lack of time steps. A variable step symplectic integrator should be implemented for practical use, and desirably, the results should constantly be corroborated with those from another integration scheme, or those using different time steps.

4.3 GEO

Figure 10 shows the propagated admissible regions for all 3 observations. The observations were made at time 0, 50 hours, and 100 hours. Secular perturbation due to the J_2 term increases as the orbit's semi-major axis decreases and as the inclination increases. GEO objects are in circular, zero-inclination orbit with a larger semi-major axis than the previous two orbit types, so we expect the difference between the symplectic and Keplerian propagation to be the smallest of the three examples. Indeed, even after propagating for 100 hours, the it is difficult to visually discern the difference between the manifolds maps from the symplectic integrator and that from Keplerian dynamics. The manifolds, nevertheless, do move around in state space even though the satellite will appear to be fixed in the night sky (hence its name, “geostationary orbit.”)

Figure 11 shows the the observations at time 0 and 100 hours run through the correlation algorithm. Again, the

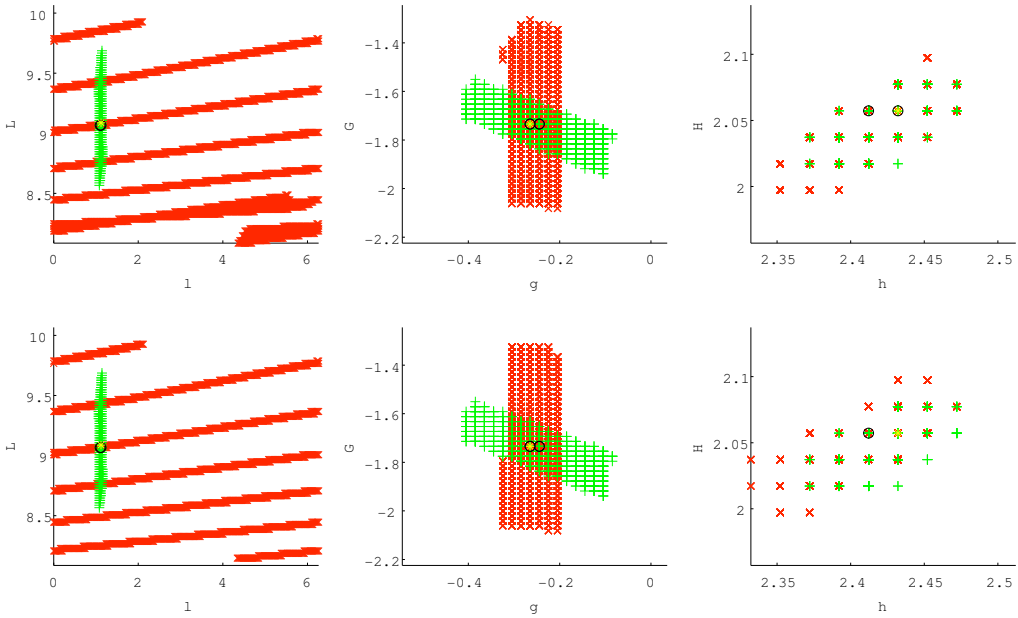


Figure 9: Correlation process for observations at time 0 (green) and 108 (red) hours using a symplectic (top) and Keplerian (bottom) propagator for a Molniya satellite. The overlap region is indicated in black. Both propagators fail to include the true state in the \mathfrak{L} - I plane, and the Keplerian propagator further fails in the \mathfrak{H} - h plane.

algorithm correctly correlates the observations for both propagation schemes. Furthermore, the overlap region calculated with the symplectic propagator includes the true object state. Surprisingly, the overlap region from Keplerian dynamics failed to do so. Even for objects as high in altitude and low in inclination as GEO, the Keplerian propagator accumulated enough error over 100 hours to push the true state out of the overlap region. I conclude that a point-mass dynamics model is simply insufficient for accurate state estimation, and thus Keplerian dynamics is not recommended for propagating objects for over $\sim 10^1$ hours.

5 Conclusions

In this paper, I discussed symplectic propagation of admissible regions in state space to incorporate better force models with high numerical accuracy. A Gauss collocation method and the symplectic state transition matrix were implemented. For the three examples I investigated – GPS, Molniya, and GEO objects – I found that although a Keplerian propagator was enough to correlate optical observations, the symplectic integrator produced better initial state estimates especially for propagation times on the order of 10^2 hours. Future work would be to propagate the entire admissible region rather than a subset, and to incorporate more perturbation terms in the force model.

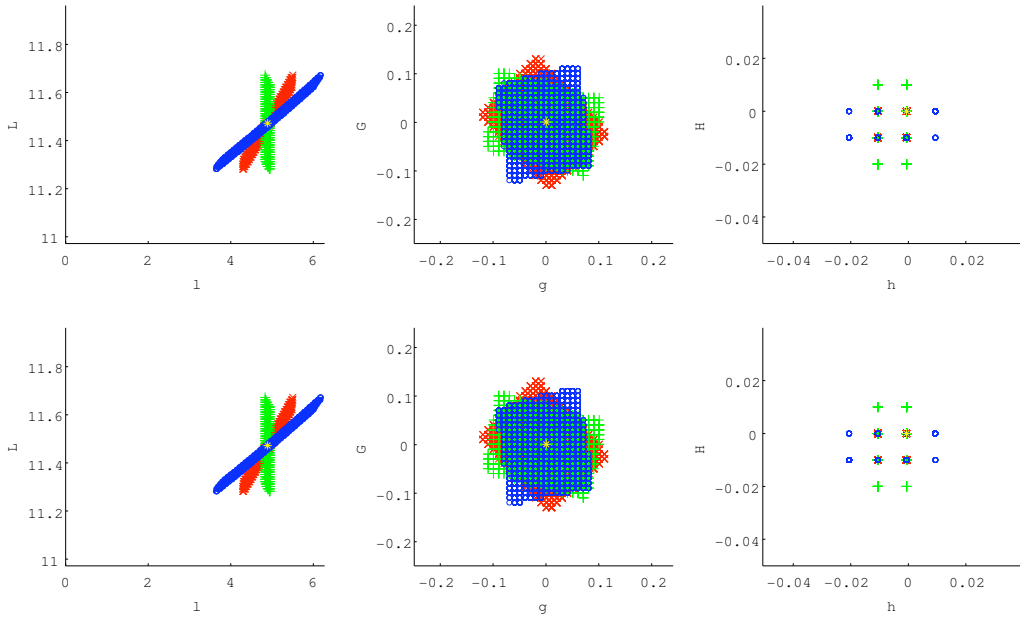


Figure 10: Admissible regions from time 0 (green), 50 hours (red), and 100 hours (blue) propagated back to time 0 using a symplectic (top) and Keplerian (bottom) propagator for observations of a GEO satellite.

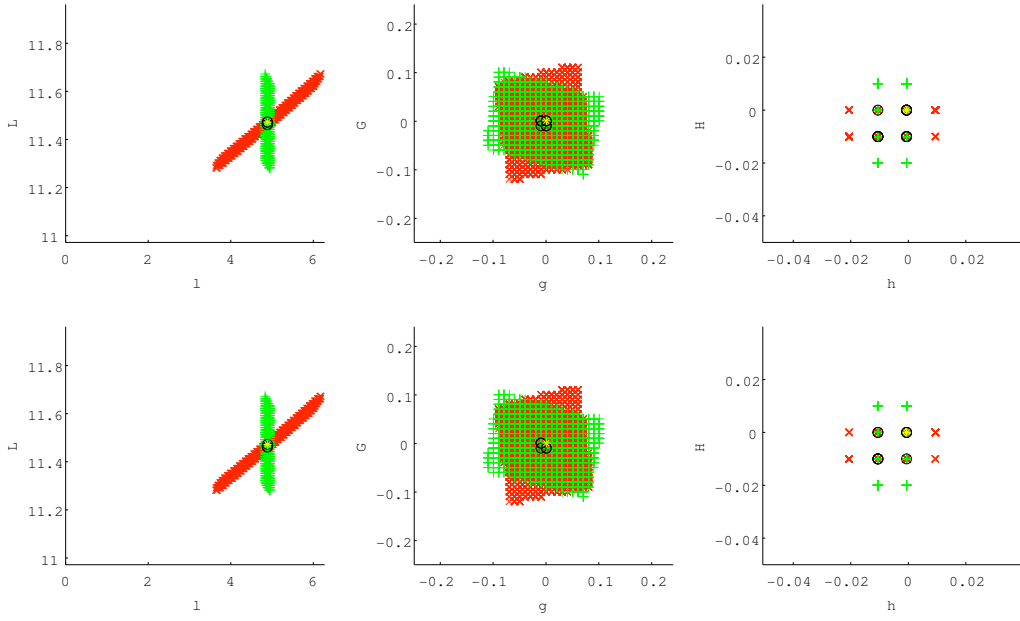


Figure 11: Correlation process for observations at time 0 (green) and 100 (red) hours using a symplectic (top) and Keplerian (bottom) propagator for a GEO satellite. The overlap region is indicated in black. The Keplerian propagator fails to include the true state in the g - g plane.

References

- [1] Rossi, A. The earth orbiting space debris. *Serb. Astron. J.*, (170):112 (2005).
- [2] Milani, A., Gronchi, G., Vitturi, M., and Knežević, Z. Orbit determination with very short arcs. i admissible regions. *Celest Mech Dyn Astr*, 90:5785 (2004).
- [3] Tommei, G., Milani, A., and Rossi, A. Orbit determination of space debris: admissible regions. *Celest Mech Dyn Astr*, 97:289304 (2007)
- [4] Fujimoto, K., and Scheeres, D. J. Correlation of Optical Observations of Earth-Orbiting Objects by Means of Probability Distributions. Accepted to the *2010 AIAA/AAS Astrodynamics Specialist Conference* (2010).
- [5] Hairer, E., Lubich, C., Wanner, G. *Geometric Numerical Integration: Structure-Preserving Algorithms for Ordinary Differential Equations*. Springer-Verlag, Berlin, Germany. (2002).
- [6] Tsuda, Y., and Scheeres, D. J. Computation and Applications of an Orbital Dynamics Symplectic State Transition Matrix. *Journal of Guidance, Control, and Dynamics*, 32(4): 1111-1123 (2009).
- [7] Maruskin, J. M., Scheeres, D. J., and Alfriend, K. T. Correlation of optical observations of objects in earth orbit. *Journal of Guidance, Control and Dynamics*, 32(1):194209 (2009).
- [8] Fujimoto, K., Maruskin, J. M., and Scheeres, D. J. Circular and zero-inclination solutions for optical observations of Earth-orbiting objects. *Celest Mech Dyn Astr*, 106:157182 (2010).
- [9] Vallado, D. *Fundamentals of Astrodynamics and Applications*. Microcosm Press, Portland (2007).
- [10] Carter, J. S. *How Surfaces Intersect in Space: An introduction to topology*. World Scientific, Singapore, second edition (1995).
- [11] Poincaré, H. *Les Méthodes Nouvelles de la Mécanique Céleste*. Gauthier-Villars, Paris (1892,1893).
- [12] Bochev, P. B., and Scovel, C. On quadratic invariants and symplectic structure. *BIT* 34:337-345 (1994).
- [13] Hammer, P. C., and Hollingsowrth, J. W. Trapezoidal methods of approximating solutions of differential equations, *MTAC* 9:92-96 (1955).
- [14] Bradley, E. *Chaotic Dynamics CSCI 4446/5446 Spring 2010: Problem Set 4*. (2010). Retrieved from <http://www.cs.colorado.edu/~lizb/chaos/ps4.pdf> on April 30, 2010.
- [15] Suzuki, M. Fractal Decomposition of Exponential Operators with Applications to Many-Body Theories and Monte Carlo Simulation. *Physics Letters A*, 146(6):319323 (1990).
- [16] Satellite situation report. Report, HQ AFSPC/XOCS.
- [17] Calais, E. *Satellite Orbits* (presentation). Retrieved from http://web.ics.purdue.edu/~ecalais/teaching/geodesy/Satellite_orbits.pdf on April 29, 2010.
- [18] Hsu, C. *Cell-to-Cell Mapping*. Springer-Verlag (1987).

Rigorously Pursuing Chaos in Time Series Data: An Algebraic Topological Approach

Joshua Garland* Zach Alexander †

1 Introduction

Rigorously proving that a dynamical system exhibits chaos numerically is a particularly fascinating aspect of numerical dynamics. During this semester we examined several different properties of a dynamical system which are usually *signatures* of chaos but not sufficient evidence to prove a system is in fact chaotic. The closest we were able to come to numerical proof of chaos was by studying the Lyapunov exponent and the capacity dimension of the Lorenz attractor. Both of these methods are unsatisfactory in a rigorous sense. Neither provide concrete proof of a system's chaotic nature, due in part to their vast dependence on parameter values. Mischaikow outlines an alternative to these in [4] and [6]. In [4] Mischaikow's outlines an algorithm to compute a lower bound on the topological entropy of a system, positive entropy being a sufficient condition for chaos! In [6] Mishaikow *et al.* rigorously explains the theory behind this algorithm using aspects of both Algebraic Topology and Conley Index Theory.

Mischaikow's approach is fascinating in that it beautifully couples Chaos, Computer Science and Mathematical theory. By personally coding these algorithms, I hope to gain a better understanding of the theory explained in [6]. My project will aim to: First, implement these algorithms and second, explore as much of the background theory as time allows.

While I implement [4], which is intended for experimental data, Zach Alexander will do independent analysis of this system, but from a flow perspective using GAIO. When we both finish our analysis we will compare our results. Even with a poor delay coordinate embedding we hope to preserve the topological structure of the attractor. Hence, if I conclude that the system exhibits a positive entropy then Zach should as well. Much of the literature states that similar techniques work with flows but most papers are oriented around maps, a direct comparison between experimental and flow data does not directly appear in the literature as far as Zach and myself can tell.

Remark: Zach and I do not expect to obtain the same entropy because while there is at least a homeomorphism between our attractors and the entropy is preserved under such a conjugacy map, we are only able to compute a lower bound. Since Zach is using the equations while I am embedding it would not at all be surprising if one of us computes a tighter lower bound on the entropy.

In addition to this flow comparison, I will compare the results of this algorithm with the results found in [10] by Sarah Day, a PhD student of Mischaikow. In [10] an alternative

*University of Colorado at Boulder, Department of Applied Mathematics.

†Collaborator from University of Colorado at Boulder, Department of Applied Mathematics.

algorithm is rigorously outlined to analyze topological entropy of a system defined with a map. She then uses this algorithm to rigorously prove a lower bound on the entropy of the Hénon map. I would like to use the code I generate based on [4] on the Hénon map and see how the two outputs compare.

2 Theory¹

The following section will aim to provide the reader with an elementary introduction to the theory which governs the algorithm [4]. It is not intended to be a complete overview of any of the subjects, just a basic introduction.

2.1 Symbolics Dynamics and Topological Entropy

Define T to be the $m \times m$ ($m \geq 2$) matrix with entries $t_{ij} \in \mathbb{Z}_2$. The symbol space corresponding to T is: [10]:

$$\Sigma_T := \{S = (s_0 s_1 \dots) | t_{s_k s_{k+1}} = 1 \forall k\}$$

We can think of the symbol space, Σ_T , as the set of words which can be generated by T through transition. We think of Σ_T in this way because T represents all allowable transitions between symbols in our symbolic dynamical system. We also need to define $\sigma_T : \Sigma_T \rightarrow \Sigma_T$ as $\sigma_T(s) := s'$, where $s'_i = s_{i+1}$. [10] That is σ_T is a continuous map on our symbol space which takes collections of symbols to collections of symbols interior to words. We refer to the framework (Σ_T, σ_T) as a *subshift of finite type*. This name emphasizes that we have a finite number of symbols, m . That is we have a finite number of characters in our “symbolic alphabet” and only a subset of the set of all words generated by these m characters is allowed by the matrix T which governs allowable symbol transitions. The finite type also emphasizes that all words can be defined using a *finite* matrix T . Furthermore, the set of forbidden words is finite. Moreover, with an appropriate choice of metric on Σ_T our shift map $\sigma_T : \Sigma_T \rightarrow \Sigma_T$ is in fact a dynamical system [10].

The reason that dynamics defined by *subshift of finite type* are of interest is that objects which can be difficult to identify such as fixed points and periodic orbits are easily obtained utilizing (Σ_T, σ_T) . For example to find a period n orbit, we would just need to find the word s^* such that $s^* = (s_0 s_1 \dots) \in \Sigma_T$ such that $s_{i+n} = s_i \forall i \in \mathbb{N}$. Since important aspects of dynamical systems are easily identifiable using (Σ_T, σ_T) it would seem that this technique, would allow almost trivial analysis of dynamical systems and their landscapes. Unfortunately this isn’t quite the case, most dynamical systems cannot be expressed in terms of symbolic dynamics with subshifts of finite type. Fortunately, there are now methods which exist to represent a general non-hamiltonian dynamical system by symbolic dynamics through a special *topological conjugacy* or a less restrictive *topological semi-conjugacy*. [10].

Definition 1. A continuous map $\rho : X \rightarrow Y$ is a topological semi-conjugacy between $f : X \rightarrow X$ and $g : Y \rightarrow Y$ if $\rho \circ f = g \circ \rho$ and ρ is surjective. If in addition ρ is injective, then ρ is a topological conjugacy .[10]

The reason we are interested in such mappings is that several properties of dynamical systems are invariant to topological (semi-)conjugacy. In particular properties such as periodic

¹Much of this section will follow the theoretical development in [10, 2, 1] and is included to provide background theory to explain the algorithm. For a more rigorous discussion see [10, 2, 1, 6, 3]

orbits and topological entropy are preserved under the actions of ρ . Thus if we can generate a conjugacy map between a general dynamical system, and a finite subshift dynamical system, we can analyze properties using the finesse of the symbolic dynamics, without being restricted to dynamics defined by subshift dynamics.

The property we are particularly interested in is a dynamical systems *topological entropy*, h_{top} , which is a measure of the complexity of a given system. A map f for which $h_{top}(f) > 0$ is said to be chaotic, and if, $h_{top}(f) > h_{top}(g)$ then we say f is ‘more chaotic’ than g . The Bowen’s definition of topological entropy is as follows[10]:

Definition 2. Let $f : X \rightarrow X$ be a continuous map. A set $W \subset X$ is called (n, ϵ, f) -separated if for any two different points $x, y \in W$ there is an integer j with $0 \leq j < n$ so that the distance between $f^j(x)$ and $f^j(y)$ is greater than ϵ . Let $s(n, \epsilon, f)$ be the maximum cardinality of any (n, ϵ, f) -separated set. The topological entropy of f is the number

$$h_{top}(f) = \lim_{\epsilon \rightarrow 0} \limsup_{n \rightarrow \infty} \frac{\log(s(n, \epsilon, f))}{n}$$

While in theory this definition makes sense, computationally calculating this quantity is quite challenging. However, the dynamics defined by subshift of finite type gives a very nice computational way of rigorously calculating this quantity. Thus if we can define a topological semi-conjugacy between our dynamical system and some symbolic system, we can calculate the original systems topological entropy which is invariant to the actions of conjugacy mappings.

Theorem 1. Let T be a symbol transition matrix and let $\sigma_T : \Sigma_T \rightarrow \Sigma_T$ be the associated subshift of finite type. Then $h_{top}(\sigma_T) = \log(sp(T))$ where $sp(T)$ is the spectral radius of T .

Unfortunately most systems are not defined as a subshift and linking a system to a conjugate subshift system is challenging. The algorithm we implement uses *Conley index theory* to build a subshift system with the *itinerary function* serving as the semi-conjugacy between the two systems[10]. The following two theorems are the brunt of what validates this algorithm theoretically and are taken from [10].

Definition 3. Suppose $N \subset X$ may be decomposed into $m < \infty$ disjoint, closed subsets ($N = \cap_{i=1,\dots,m} N_i$). Let S be the maximal invariant set in N (i.e. S is the largest set such that $S \subset N$ and $f(S) = S$). Then $f^j(S) \subset N \forall j = 0, 1, \dots$. Finally, let T be the $m \times m$ symbol transition matrix given by

$$t_{ij} = \begin{cases} 1 & : (S \cap N_j) \cap N_i \neq \emptyset \\ 0 & : \text{otherwise} \end{cases}$$

The itinerary function $\rho : S \rightarrow \Sigma_T$ is given by $\rho(x) = s_0 s_1 \dots$, where $s_j = i$ for $f^j(x) \in N_i$.

Using the itinerary map as our semi-conjugacy mapping we can obtain a lower bound on the topological entropy of our system in the following way.

Theorem 2. Suppose that the itinerary function ρ is a semi-conjugacy from $f : S \rightarrow S$ to $\sigma_T : \Sigma_T \rightarrow \Sigma_T$ for some $S \subset X$ and subshift of finite type (σ_T, Σ_T) with symbol transition matrix T . Then

$$h_{top}(f) \geq \log(sp(T)) = h_{top}(\sigma_T)$$

where $sp(T)$ is the spectral radius of T .

That is the spectral radius of the Transition matrix for which our system is semi-conjugate to will be a lower bound on the entropy of our system. A positive lower bound will allow us to conclude our original system is chaotic, whereas a zero lower bound will not allow us to conclude anything about our system and is considered a trivial entropy. Before describing the algorithm implementation one more theoretical digression is necessary.

2.2 Basic Conley Index Theory and Homology²

A fundamental aspect of Mischaikow's *et .al* algorithm [4] is to construct an isolating neighborhood of the original dynamical system. An isolating neighborhood, N , is a strict subset of the system image which *strictly* contains one of the dynamical systems invariant sets, $\text{inv}(N)$. Unlike an invariant set, trajectories can leave an isolating neighborhood but they must do so through what is called the (isolating neighborhood) exit set, which we will call L . Two crucial concepts behind the isolating neighborhood is that the isolating neighborhood is compact and its exit set, L , has a non trivial intersection with ∂N . This tells us the following: not only is the invariant set strictly contained in the interior of N but also that points in the set $K = N \setminus L$ are unable to leave N . We are not however interested in the structure of the isolating neighborhood, which is computable, but we are interested in the isolated invariant neighborhood.[4] To deal with this theoretical discrepancy the algorithm relies on the usage of Conley Index Theory. First we must understand the idea of an *index pair*.

Definition 4. [4] Given an isolating neighborhood N of f , a pair of compact sets (K, L) with $L \subset K \subset N$ is called an index pair if the following properties are satisfied:

1. If $x \in K$ and $f(x) \in N$ then $f(x) \in K$.
2. If $x \in L$ and $f(x) \in N$ then $f(x) \in L$.
3. If $x \in K$ and $f(x) \notin N$, then $x \in L$
4. The maximal invariant set contained in N is a subset of the interior of $K \setminus L$.

According to [4] the importance of an index pair is that the index pair that the homology groups $H_*(N/L)$ and a homology map $F_* : H_*(N/L) \rightarrow H_*(N/L)$ induced by \mathcal{F} are invariants of the maximal invariant set contained in N . Furthermore, if under a change in the dynamics, N remains an isolating neighborhood, the homology group and map do not change. To utilize index pairs to recover the structure of the invariant sets we return to [10]. Before defining the conley index we must have the following definition:

Definition 5. Two group homomorphisms $\phi : G \rightarrow G$ and $\psi : G' \rightarrow G'$ on abelian groups G and G' are shift equivalent if there exists group homomorphisms $r : G \rightarrow G$ and $s : G' \rightarrow G'$ and a constant $m \in \mathbb{N}$ (referred to as the 'lag') such that

$$r \circ \phi = \psi \circ r, \quad s \circ \psi = \phi \circ s, \quad r \circ s = \psi^m, \quad \text{and } s \circ r = \phi^m.$$

The shift equivalence class of ϕ , denoted $[\phi]_s$, is the set of all homomorphisms ψ such that ψ is shift equivalent to ϕ .

²This section is loosely based around [6], however much of the notation and definitions are borrowed from [10], [2].

Definition 6. Let $P = (P_1, P_0)$ be an index pair for isolated invariant set $S = \text{Inv}(\overline{P_1 \setminus P_0})$ and let $f_{P_*} : H_*(P_1, P_0) \rightarrow H_*(P_1, P_0)$ be the map induced by the relative homology groups $H_*(P_1, P_0)$ from the map f_P . The Conley index of S is the shift equivalence class of f_{P_*}

$$\text{Con}(S, f) := [f_{P_*}]_s$$

While this definition is precise, a less rigorous definition can be used for the purposes of this algorithm.

Definition 7. If (K, L) is an index pair of $\text{Inv}(N)$, then the Conley Index of $\text{Inv}(N)$ is defined to be the homotopy type of the quotient space N/L .

Some very nice properties of the Conley Index can be summarized in the following way.

Proposition 3. The Conley index is an index of isolating neighborhoods that satisfy:

1. If N and M are isolating neighborhoods such that $\text{inv}(N) = \text{inv}(M)$ then the Conley Index $(N) = \text{Conley Index}(M)$.
2. If $\text{Conley Index}(N)$ is non trivial that is not equal to zero then the $\text{inv}(N) \neq \emptyset$.
3. If N is an isolating neighborhood for a continuous family of dynamical systems ϕ_λ , $\lambda \in [0, 1]$ then $\text{Conley Index}(N, \phi_0) = \text{Conley Index}(N, \phi_1)$.

The third is important because it guarantees that the Conley Index is invariant to small perturbations in the dynamical system. Since this project will be oriented around delay coordinate embedded data it will inevitably possess small perturbations resultant from both RK4 error, embedding error and fixed point error. This property allows us to utilize the Conley Index with very little concern for it varying from the true dynamical systems index.

Thus, using the index pair (K, L) we need to construct the quotient space K/L . Within this topological subspace we think of each point in the exit set L as a single point in the quotient space. To visually understand this see Figure 1.³ With this Figure think of K as the blue and L as the red. The final image is the quotient space K/L . This allows us to construct a set of manifolds whose surface is the isolating neighborhood of the invariant set with the exiting set compressed to a single point. From this we can compute the homology group of the quotient space $H_*(K/L)$. Where the elements of $H_*(K/L)$ are the homotopy equivalence classes of closed curves lying on the surface of the quotient space. To visualize homotopy classes observe Figure 2⁴, we consider two curves in this space of the same *homotopy class* or *homotopy equivalent* if one can be continually deformed into another. So $[\gamma_1] \equiv [\gamma_2] \equiv [\gamma_3] \equiv [\gamma_4]$ are all homotopy equivalent but none of these are equivalent to $[\gamma_5]$ since this curve cannot be continually deformed to the others due to the hole in space.

Since $[\gamma_4]$ is homotopy equivalent to a single point, this class will be the identity of our homology group. For each element of $H_*(N/L)$ we receive a copy of \mathbb{Z} . More precisely, if the index pair consists of disjoint sets $(N_j, L)_{j=1}^J$ then our homology group $H_*(N/L)$ will be the free group isomorphic to $\mathbb{Z}^J := \{(z_1, \dots, z_J) | z_1, \dots, z_J \in \mathbb{Z}\}$. For example again consider Figure 1, then the order of $H_*(N/L)$ would be 2 and thus $H_*(N/L) \cong \mathbb{Z} \oplus \mathbb{Z} := \{(z_1, z_2) | z_1, z_2 \in \mathbb{Z}\}$.

Once we have constructed $H_*(N/L)$ we can construct from the multivalued map a transition matrix $T : H_*(N/L) \rightarrow H_*(N/L)$ which forms a subshift of finite type on $H_*(N/L)$. Using the itinerary map as our semi-conjugacy mapping we can obtain a lower bound on the topological entropy of our system by Theorem 2.

³Illustration by D. Y. Garland

⁴Illustration by D. Y. Garland

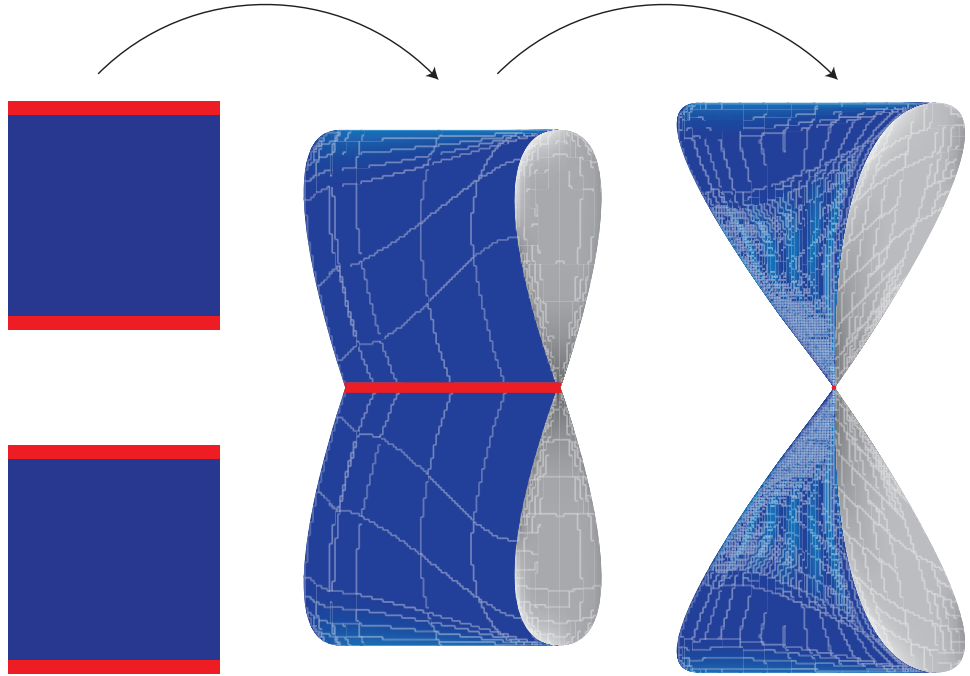


Figure 1: Topological Quotient Space

2.3 The System

In order to investigate this algorithm I will be using a known chaotic system from [11], in particular:

$$\begin{aligned}\dot{x} &= -2y \\ \dot{y} &= x + z^2 \\ \dot{z} &= 1 + y - 2z\end{aligned}$$

I will not however, be directly using the governing equations. Instead, using fourth/fifth order Runge Kutta (Matlabs ode45) I integrated the system and then used an embedding program to generate several embeddings by varying both τ and m . A boast of this algorithm is that it can recover topological quantities of a data set even if the embedding dimension is low or if τ is chosen poorly. In light of this I choose an embedding which looked very poor compared to the original system and used this as the dynamical system. An example of the final bad embedding can be seen in Figure 4. The final step in obtaining the “experimental data” is to take a Poincaré section of this data. While several Poincaré sections were taken and analyzed, the Poincaré section in Figure 5 was the primary data being analyzed.

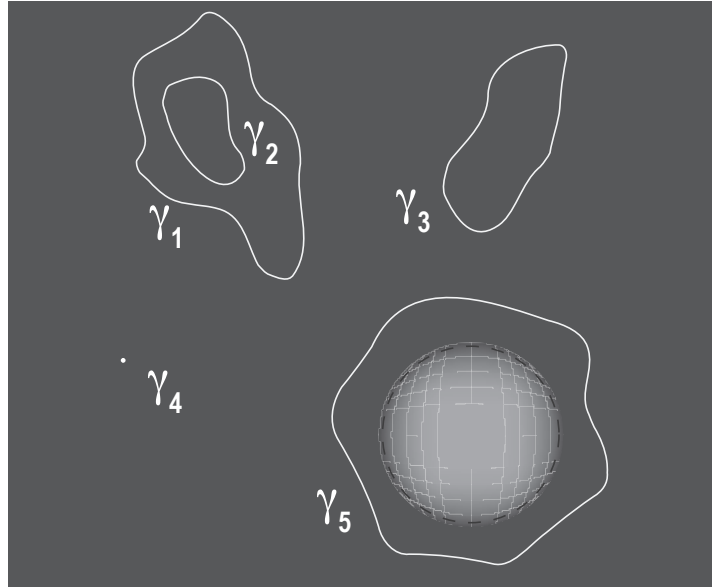


Figure 2: Homotopy Classes

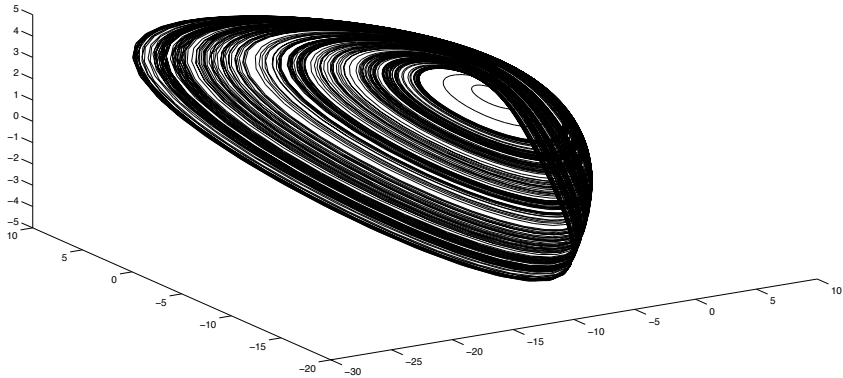


Figure 3: The original system.

Before deciding on this system I considered the following properties: Lyapunov Exponent, Capacity Dimension and the ratio of dominant to recessive Lyapunov exponents. We also wanted a system which would be very difficult to prove was chaotic by traditional means, i.e. calculation of fractal dimension and the Lyapunov exponent. In general a low dimensional delay coordinate embedding will be most successful if the dominant Lyapunov exponent is quite small and positive and the majority of the other exponents are large and negative.

The Lyapunov spectrum of this system is $\{0.076, 0, -2.076\}$ [11]. Notice the dominant Lyapunov exponent is very small and positive. Standard algorithms which are intended to analyze experimental time series data can have up to a 10% error in the calculation of the dominant Lyapunov exponent.[12] This particular system would be exceptionally difficult to

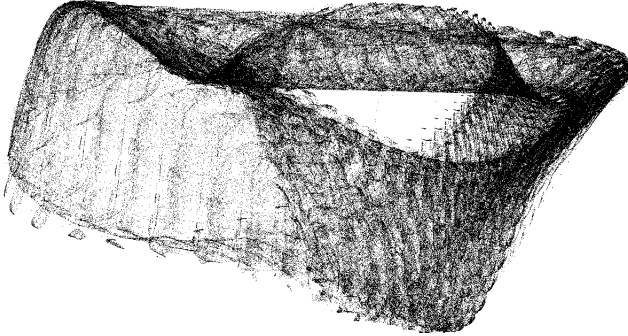


Figure 4: Embedded system.

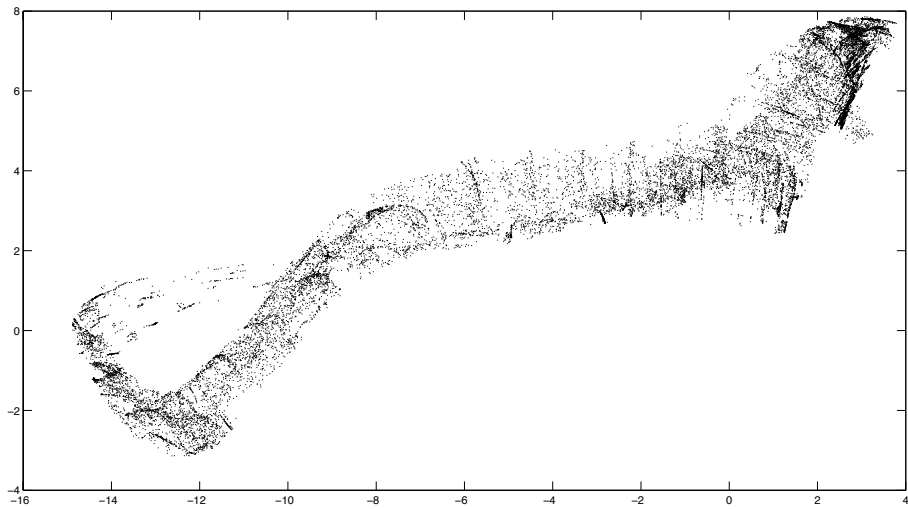


Figure 5: Poincaré Section of the bad embedding.

conclude chaos based on the Lyapunov exponent as 10% fluctuation could quite easily have this system result in a negative Lyapunov exponent! Moreover, the large negative Lyapunov exponent should allow very successful low dimensional embeddings. Furthermore, this system has a non-integer capacity dimension, 2.037 [11] which is a nice signature of chaos but not necessary as can be seen with Sprott's simple chaotic system [11]. For these reasons this system should be a great candidate for this algorithm.

3 Computational Aspects

My implementatoin of [4] will construct a multivalued map, \mathcal{F} , and a collection of cubes which act as an isolating neighborhood N of an invariant set under the influence of \mathcal{F} . Lastly it will construct an index pair for \mathcal{F} .

The final stage of [4], namely the calculation of the transition matrix and itinerary function,

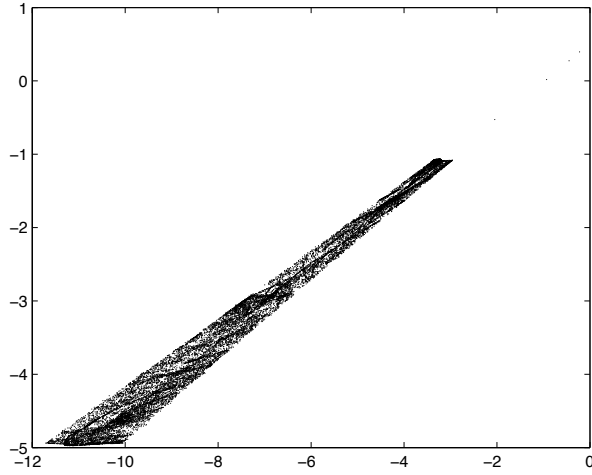


Figure 6: Zach’s Poincaré section of the original system.

will be accomplished with CHomP, a free software library developed by Mischaikow *et al.*

3.1 Algorithm Implementation

The Multivalued Map The multivalued map can be thought of as a symbolic encoding of the original dynamical system. We would like \mathcal{F} to be coarser than the original map f while preserving the basic properties of the original system. This in part helps mitigate error propagation due to delay coordinate and experimental error. As described in [4], to define

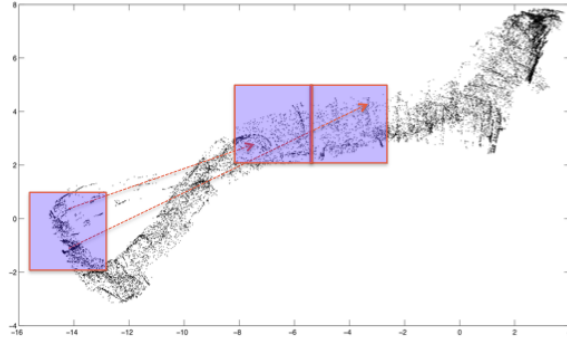


Figure 7: Visual example of the map creation process.

\mathcal{F} we first define the image and range of \mathcal{F} . To do this we divide our phase space into a grid of squares with side lengths ϵ . We then define \mathcal{G} to be the set of squares which contain experimental data points and Y , to be the region of phase space which is determined by \mathcal{G} . The next step is to define a dynamical system on Y , this dynamical system will be a multivalued map called $\mathcal{F} : \mathcal{G} \rightrightarrows \mathcal{G}$, which takes grid squares to grid squares.

This task was accomplished by placing a grid over the experimental data using a similar mapping used traditionally to calculate the capacity dimension. This collection of grid squares will act as the domain of \mathcal{F} . We now need to construct the preimage and imaging sets of \mathcal{F} constraining our space to the original systems image. That is, we need both $\mathcal{G}|_{\mathcal{F}}$ and $Y = \mathcal{G}|_{\mathcal{F}(G)}$ such that: if $g \in G$ then $f(g) \in \mathcal{F}(G) \forall g \in \mathcal{G}$ where f is the original flow.

So we must construct $\mathcal{G}|_{\mathcal{F}} = \{G' | \mathcal{F}(G) = G'\}$ for each $G \in \mathcal{G}\}$ and its image. To accomplish this we take each experimental data point, $g \in G$ for all $G \in \mathcal{G}$, and map each g forward one step in time (See Figure 7).

We then record all possible image squares of G in a cell array (See Figure 8). Each index in the cell array represents a grid element G and the cell array as a whole represents \mathcal{G} . Each cell is a matrix containing the image of a particular G under \mathcal{F} for which that index corresponds. So cells which are nonempty in the cell array represent $\mathcal{G}|_{\mathcal{F}}$ and the corresponding cells represent each of their images in \mathcal{F} . Notice that each grid square G can map to many grid squares, this is why the map is referred to as a multivalued map and NOT a function. While it seems this is the map we are looking for we are not quite done. Defined as above, \mathcal{F} does not quite preserve the dynamics of the original system.

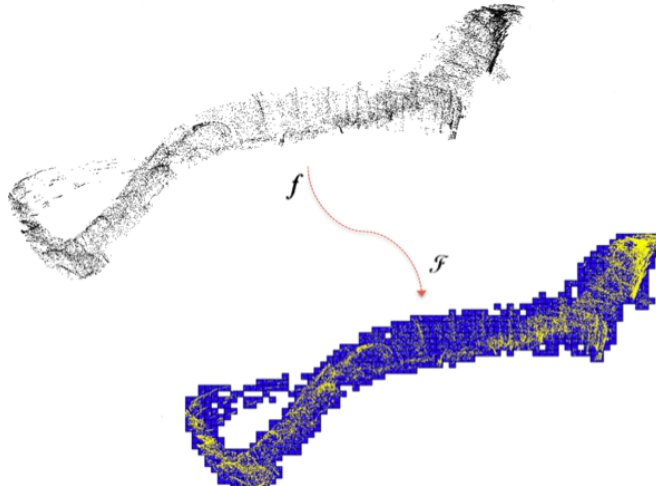


Figure 8: Visual representation of transition from f to \mathcal{F}

Before using \mathcal{F} three issues must be resolved: (1) we must guarantee that we preserve the original mapping (i.e. if $g \in G$ then $f(g) \in \mathcal{F}(G) \forall g \in \mathcal{G}$ where f is the original flow) by eliminating images which have trivial intersections, (2) the “four square” problem, and lastly (3) guarantee that Y does not exceed the image of the original image set, up to ϵ -resolution.

First, we make sure the mapping is preserved. Observe this might not be the case if the image squares are disjoint. To solve this problem for each G we use $\mathcal{F}(G)$ to construct the smallest rectangle containing $\mathcal{F}(G)$ and take all squares in this rectangle to be the new $\mathcal{F}(G)$. This solves the disjoint image problem.

The next issue to resolve is the “four square” image problem described in [4]. The simplest statement of this problem, is if four squares lie next to each other, the image of the four squares must have an intersection which is nontrivial. The reason being is that if a point lies on the boundary, or worse, the central corner of the four grid squares, it must be mapped interior to the image of these four squares. At first this seemed trivial and superfluous, and was ignored

for a long time. However, it turns out to my surprise that experimental data very frequently violates this property and this turned out to be an extremely important property for \mathcal{F} to satisfy. Not satisfying this property seemed to manifest itself when \mathcal{F} was being verified to be acyclic. Violating this four square problem seemed to almost directly impact the maps acyclicity. We will consider this later when we discuss CHomP in the results section of this paper.

The solution to this problem is given in [4]: “For each grid point, look at the images of the four grid squares which meet at that point. If they do not intersect, increases each image by the set of all squares which intersect the set representing it.” Similar language to this is used in [10] when talking about a sets combinatorial neighborhood. Thus to fix this problem we extend each image square by its combinatorial neighborhood until the image of four squares has a nontrivial intersection, and finally updating \mathcal{F} to reflect this increase in image.

The final problem arises from the additional images being added. Essentially we must ensure that the dynamical system defined on Y is no larger than the original system. To do this we simply intersect each image with the dynamical system, that is we take $\mathcal{G}|_{\mathcal{F}}$ and intersect it with Y so that $\forall G \in \mathcal{G} \quad \mathcal{F}(G) = \mathcal{F}(G) \cap Y$. This last step ensures that the dynamical system defined on Y is no larger than the original system. That is no image squares are generated if they do not contain an original experimental data point. We then translate the cell array \mathcal{F} into a text file formatted as prescribed by [8] to be used by CHomP.

Isolating Neighborhood To construct the isolating neighborhoods we utilize both \mathcal{F} and \mathcal{F}^{-1} repetitively, where $\mathcal{F}^{-1}(C) := \{G \in \mathcal{G} | \mathcal{F}(G) \cap C \neq \emptyset\}$ [4], until we no longer have any change in the image set. To start this we guess a strict subset of $\mathcal{G} \cap Y$ which we call C_0 . This is the first approximation to the isolating neighborhood, the only restriction which is placed on the guess is that it is a strict subset of $\mathcal{G} \cap Y$. We then define $C_1 = C_0 \cap \mathcal{F}(C_0) \cap \mathcal{F}^{-1}(C_0)$. That is we move each $G \in C_0$ forward in time and backwards in time one step. The second step in this procedure is to “remove a component of C_1 which touches the boundary of C_0 relative to Y ”.[4] After removing any such $G \in C_1$ we check if $C_0 = C_1$. We continue this process until $C_i = C_{i+1}$ for some i . Once the algorithm has converged in this sense we define C_{i+1} to be our isolating neighborhood N .

Index Pairs Now that we have an isolating neighborhood N we can produce an index pair for \mathcal{F} . Let L consist of the elements of $\mathcal{F}(C_{i+1})$ which touch ∂C_{i+1} relative to Y , this will constitute the exit set L . We then define $K = C_{i+1} \cup L$, then (K, L) is an index pair for \mathcal{F} . We must now calculate $H_*(K, L)$ and the corresponding map on homology T , which will act as our itinerary function and semi-conjugacy between these new subshift of finite type dynamics namely $H_*(K, L)$ and our original system. For this computation we will rely on CHomP. With these inputs I can use *homcubes* from the CHomP library in order to calculate the topological entropy of the system.

4 Challenges and Results

4.1 Challenges

With [4] coded I thought I would be able to investigate several different variations on this dynamical system. In fact I thought it would be quite easy to analyze any time series, experimental data or dynamical system with this algorithm as long as it primarily acted as a map. Unfortunately, the fact of the matter is that two awkward sentences in [4] make this algorithm ambiguous at two crucial moments. On top of this *homcubes* is quite sensitive to what it accepts as input. In particular, besides theoretical considerations made in [4]

additional computational and theoretical restrictions are placed on \mathcal{F} by *homcubes* such as acyclicity⁵.

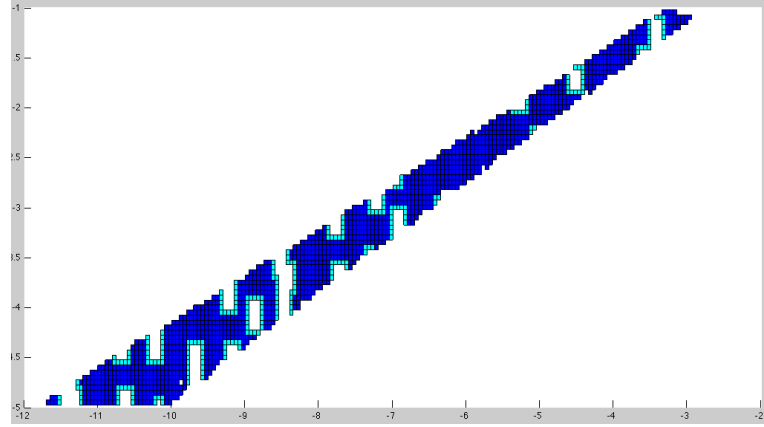


Figure 9: An index pair generated by this software which looks correct, but produced very bad output with CHomP.

$H_0 = 0$	The map induced in homology by the inclusion: Dim 0: 0	The composition of F and the inverse of the map induced by the inclusion: Dim 0: 0
$H_1 = \mathbb{Z}_{2^{19}}$		
The map induced in homology is as follows:		
Dim 0: 0		
Dim 1: $f(x1) = y17$	Dim 1: $i(x1) = y2 + y8$	Dim 1: $i(x1) = x9$
$f(x2) = 0$	$i(x2) = y6$	$i(x2) = x4$
$f(x3) = 0$	$i(x3) = y14$	$i(x3) = x17$
$f(x4) = y6$	$i(x4) = y2$	$i(x4) = x5$
$f(x5) = 0$	$i(x5) = y4$	$i(x5) = x13 + x15$
$f(x6) = y3 + y16$	$i(x6) = y1$	$i(x6) = x2$
$f(x7) = 0$	$i(x7) = y10$	$i(x7) = x16$
$f(x8) = 0$	$i(x8) = y10 + y11 + y15$	$i(x8) = x1 + x4$
$f(x9) = 0$	$i(x9) = y17$	$i(x9) = x11$
$f(x10) = 0$	$i(x10) = y16$	$i(x10) = x7$
$f(x11) = 0$	$i(x11) = y9$	$i(x11) = x7 + x8 + x19$
$f(x12) = y10 + y11 + y12$	$i(x12) = y19$	$i(x12) = x18$
$f(x13) = y10$	$i(x13) = y5 + y13$	$i(x13) = x15$
$f(x14) = 0$	$i(x14) = y8 + y13 + y18$	$i(x14) = x3$
$f(x15) = y16$	$i(x15) = y13$	$i(x15) = x19$
$f(x16) = y7 + y19$	$i(x16) = y7$	$i(x16) = x10$
$f(x17) = 0$	$i(x17) = y3$	$i(x17) = x9$
$f(x18) = y13$	$i(x18) = y12$	$i(x18) = x1 + x4 + x14 + x15$
$f(x19) = 0$	$i(x19) = y15$	$i(x19) = x12$

Figure 10: The resulting output from CHomP for 9. Observe the high dimensional Homology group.

Furthermore, actually finding an isolating neighborhood for a dynamical system is far less trivial than originally believed based on [4]. Mischaikow presents the calculation of a semi-conjugacy between the subshift of finite type namely $H_*(K, L)$ and the original system as a completely trivial action which is almost an afterthought of [4]. Calculating this semi-conjugacy however seems to be a fundamental challenge in this process which I now see

⁵We say that a cubical (combinatorial multivalue) map $\mathcal{F} : \mathcal{X} \rightarrow \mathcal{Y}$ is acyclic if for every set of cubes $\mathcal{R} \subset \mathcal{X}$ such that $\cap \mathcal{R} \neq \emptyset$, the set $|\mathcal{F}(\mathcal{R})|$ is acyclic.[8].

after coding this algorithm from scratch. Constructing a valid isolating neighborhood and generating a map which satisfy acyclicity in order to use CHomP were by far the most time consuming computational aspects of this project.

The Isolating Neighborhood algorithm as stated in [4] begins by guessing a proper subset of $\mathcal{G}|_{\mathcal{F}}$ and then iterating in the way described in section 3.1. The challenge of this however is finding an isolating neighborhood which can then be translated into an index pair which satisfies all the requirements listed in section 2.2. The issue is that the isolating neighborhood and the index pair act similarly but, have several theoretical restrictions which deviate them just enough that finding an index pair becomes extremely challenging.

For example, if you choose your initial guess to be too large, say only 50 cubes are removed from the image, then using [4] you almost get immediate convergence. This makes sense theoretically because if you consider the majority of $\mathcal{G}|_{\mathcal{F}}$ minus some small number of cubes it would make sense that this is a compact cover of several invariant sets. The problem is this usually results in a trivial homology group since the quotient space N/L will have no holes. This trivial homomorphism almost always results in a zero entropy which does not allow us to make any conclusions about the chaos of the given system. If you take the other extreme and take a very small guess as the initial guess the probability of this being a cover of a disconnected invariant set is almost zero, and so the algorithm almost always results in $K = \emptyset$ which results in a trivial itinerary mapping and nothing can be said about the chaos of the original system. Even when the algorithm does converge, many times taking (K, L) as an index pair for \mathcal{F} would result in a violation of acyclicity which would cause *homcubes* to crash.

This guess and check method suggested in [4] seems highly inefficient. With hundreds of guesses and checks made with the Sprott Poincaré section, Sprott flow and Hénon data not a single index pair was found by this algorithm. It seems that a huge amount of luck is needed in the guessing process. For this reason it seems a more systematic approach is needed such as the methods described in [1, 2, 10]. This will be discussed further in the future works section.

4.2 Sprott Poincaré Section Compared with Sprott Flow

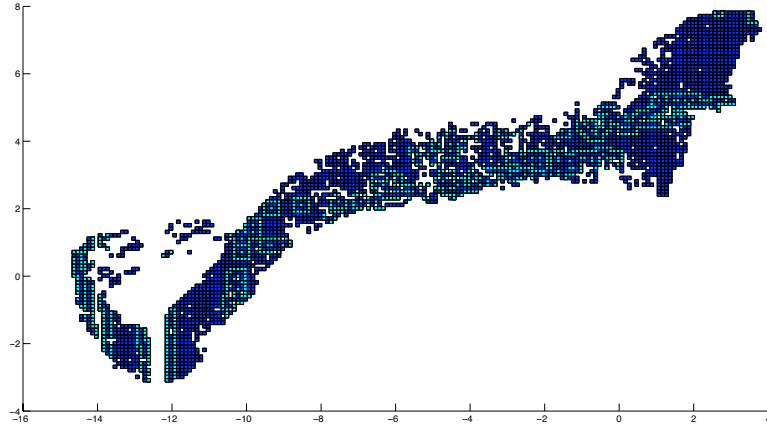


Figure 11: Resulting index pair from a large original guess. Only about 50 cubes removed.

Due to the challenges in finding an index pair I was not able to calculate a lower bound on the topological entropy for the Poincaré section. For similar reasons Zach was also unable to calculate a lower bound on entropy for his system. Thus, no direct comparisons could be made between the Flow and embedded data, which was very disappointing.

On several occasions we got results from *homcubes*. However, in each case as we analyzed the output, implications were that the output was unreliable. Such reasons were: extremely high dimensional homology groups for low dimensional quotient spaces, nonzero traces of inclusion maps, trivial mappings, inclusion maps which did not agree with the transition matrices etc. For these reasons we were not at all confident in the results we received and did not think comparing them was in any way helpful or legitimate. Several examples of neighborhoods and corresponding index pairs can be seen in the following figures. None of these however resulted in positive entropy.

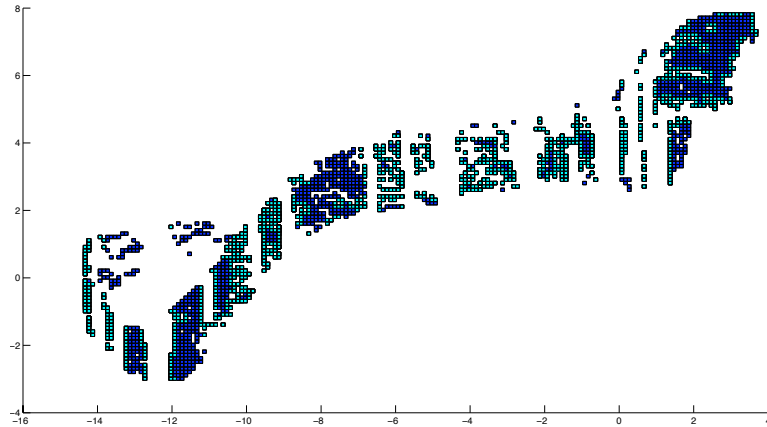


Figure 12: Resulting index pair from a medium original guess. Several hundred cubes removed

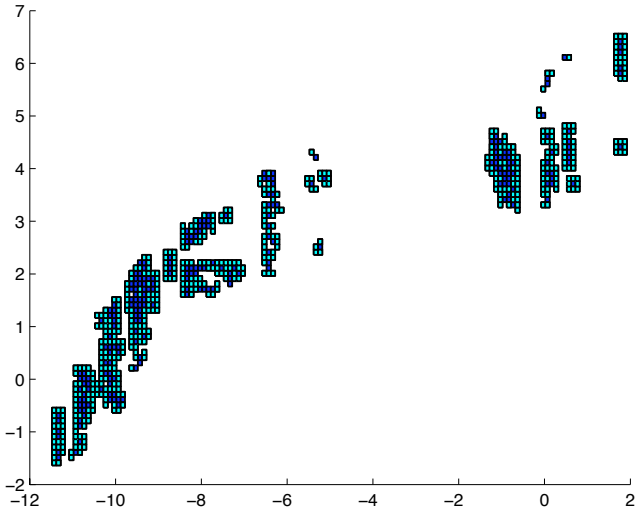


Figure 13: Resulting index pair from a very small original guess. Almost all cubes removed.

4.3 Hénon Results

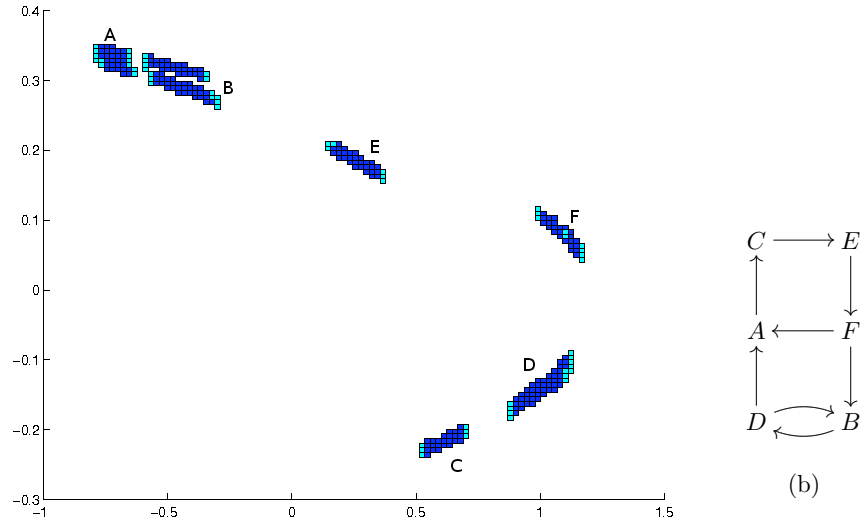


Figure 14: Isolating Neighborhood with Commuting Diagram from [10].

As a way of trying to better understand [4] I considered other similar algorithms in hopes of understanding the fundamental problem better. The most helpful and promising algorithm I investigated was found in the dissertation of Sarah Day and was published in [10] and added to in [1]. What initially intrigued me was that this particular paper had very explicit

explanations which were backed up by theoretical considerations and proofs. Moreover, this paper simply uses the Hénon map and as such is easily reproducible. With [4] the results are produced by data recorded from a magneto-elastic ribbon. The data they used however is nowhere to be found which makes testing the algorithm and reproducing the results almost impossible. My initial aim was to use my code on this map and see if my results would be similar to [10]. After scrutinizing [1, 2, 10] it also occurred to me that while the algorithm in [10] was intended for the analysis of maps it would also serve quite nicely for the analysis of time series data through Poincaré sections.

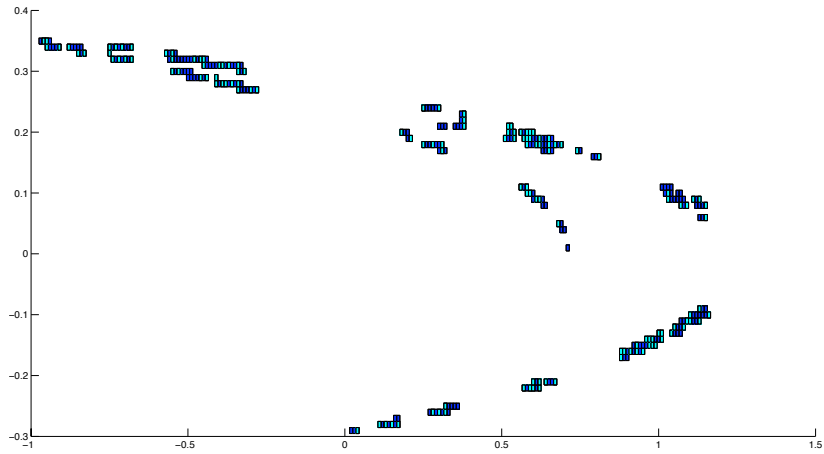


Figure 15: A similar isolating neighborhood as that found in [10]

Figures 14 and 15 illustrate that my algorithm was able to compute isolating neighborhoods very similar to those found in [10]. The main difference is the interval arithmetic being used in her implementation. In addition, she also uses graph theory on the symbolic transition matrix in order to automate the construction of an isolating neighborhood.

Figures 16-17 demonstrate one of the methods implemented in [10] to locate an isolating neighborhood. The basic idea is that particular cubes are “blown out” or folded and then the resulting set is cut down to an isolating neighborhood by the PRL algorithm. The important feature to notice about these pictures are where the bands of empty space occur. These will relate to holes in the Topological quotient space which will directly effect the homology group being formed for the subshift of finite type.

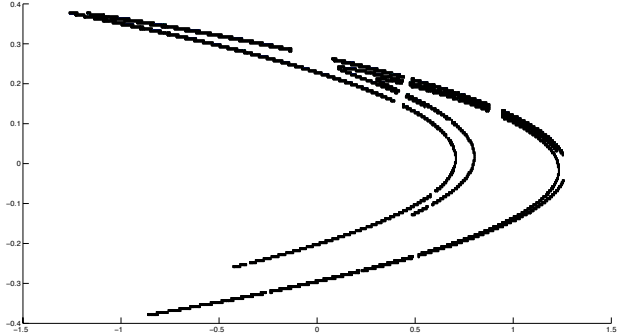


Figure 16: My resultant index pair from the “Blowout” method using a depth 5 blowout

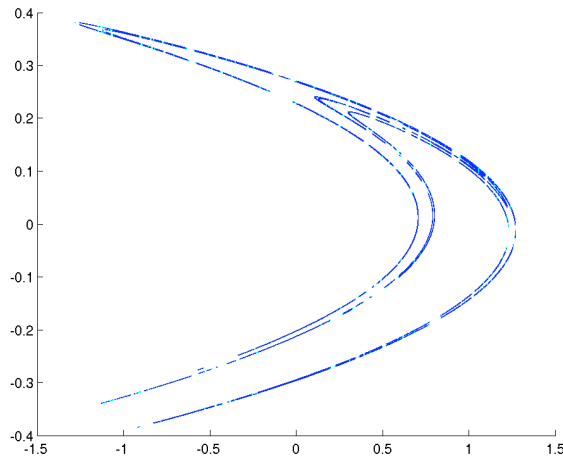


Figure 17: Sarah’s resultant index pair from the “Blowout” method from [10].

When I inserted the above index pairs and associated map into *homcubes* I received either a trivial homology or a violation of acyclicity warning. This was further evidence to me that I should consider an alternative algorithm because it does not seem the PRL consistently produces maps which allow transition to subshift of finite type.

5 Further Work and Conclusions

Investigating the work of Mischaikow *et. al* was an incredible learning experience. Not only did I gain knowledge in Chaotic systems but in Algebraic Topology, and Conley Index Theory. In addition I gained valuable experience in the act of algorithm deciphering. Moreover [4] provided a great springboard into this vast subject matter.

In the near future I hope to create an algorithm based on the best from each of the algorithms I studied. Each had strengths and weaknesses and it would seem that a compilation of these algorithms would be quite strong. For example in [10] a great Isolating Neighborhood algorithm is outlined which utilizes graph theory to find cycles and fixed points with respect

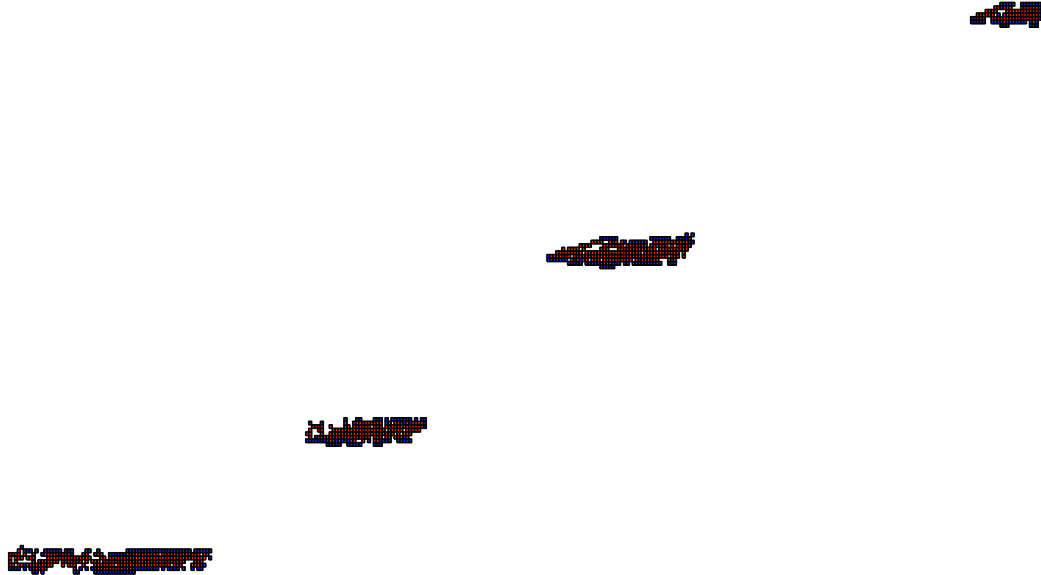


Figure 18: An index pair generated by Zach using the Cycle method described in [10].

<pre> H_0 = 0 H_1 = Z^4 Computing the homology of Y over the ring of integers... Reducing D_2: 8 + 0 reductions made. Reducing D_1: H_0 = 0 H_1 = Z^4 The map induced in homology is as follows: Dim 0: 0 Dim 1: f(x1) = y2 f(x2) = -y4 f(x3) = y1 f(x4) = -y3 The map induced in homology by the inclusion: Dim 0: 0 Dim 1: i(x1) = -y3 i(x2) = y1 i(x3) = y2 i(x4) = y4 </pre>	<p>The inverse of the map induced by the inclusion:</p> <pre> Dim 0: 0 Dim 1: I(y1) = x2 I(y2) = x3 I(y3) = -x1 I(y4) = x4 </pre> <p>The composition of F and the inverse of the map induced by the inclusion:</p> <pre> Dim 0: 0 Dim 1: F(x1) = x3 F(x2) = -x4 F(x3) = x2 F(x4) = x1 </pre>
--	--

Figure 19: Output of CHomP illustrating a 4 cycle in the Index Pair shown in Figure 18

to \mathcal{F} . These cycles are then connected using Dijkstra as an initial “region of interesting dynamics”. This region of interest is then used as an initial guess for a set to grow into an Isolating Neighborhood. For the multivalued map, the PRL algorithm [4] seems the most promising as it was originally developed with time series analysis in mind. For the index pair

I would return to Mischaikow, but not [4], in his book he provides a very nice algorithm for this computation. Preliminary results suggest this approach will be quite useful. In fact, Zach was able to rigorously prove the existence of a 4 cycle, the Index Pair and output can be seen in Figure 18. In addition, with this collection of tools I was able to verify fixed points and 2 cycles for the Hénon map.

References

- [1] S. Day, O. Junge, and K. Mischaikow. A rigorous numerical method for the global analysis of infinite dimensional discrete dynamical systems. *World Scientific, Singapore*, pages 157–162, 2005.
- [2] S. Day O. Junge and K. Mischaikow. A rigorous numerical method for the global analysis of infinite dimensional discrete dynamical systems. *SIAM Dynamical Systems*, 3:117–160, 2008.
- [3] M Mrozek A.Symczak K. Mischaikow and J. Reiss. From Time Series to Symbolic Dynamics: An Algebraic Topological Approach. December 1997.
- [4] K. Mischaikow, M. Mrozek, Instytut Informatyki, J. Reiss, and A. Szymczak. Construction of symbolic dynamics from experimental time series. *Rev. Let*, 82:1144–1147, 1998.
- [5] Konstantin Mischaikow. The conley index theory: A brief introduction. 1998.
- [6] T Kacynski Konstantin Mischaikow and M Mrozek. Computing homology. *Homology, Homotopy and Applications*, 5(2):233–256, 2003.
- [7] James R. Munkres. *Topology*. Prentice Hall, Reading, Massachusetts, second edition, 2000.
- [8] Paweł Pilarczyk. Homology map computation with the chomp software. 2007.
- [9] Joseph J. Rotman. *An Introduction to Algebraic Topology*. Springer, New York, NY, 1988.
- [10] R. Frongillo S. Day and R. Trevino. Algorithms for rigorous entropy bounds and symbolic dynamics. *SIAM Journal on Applied Dynamical Systems*, 7(4):1477–1506, 2008.
- [11] J. C. Sprott. Some simple chaotic flows. *Physical Review E*, 50(2):342–351, 1994.
- [12] Alan Wolf, Jack B. Swift, Harry L. Swinney, and John A. Vastano. Determining lyapunov exponents from a time series. *Physica*, pages 285–317, 1985.
- [13] Afra J. Zomorodian. *Topology for Computing*. Cambridge University Press, New York, NY, 2005.

Are Attractors Attractive?

An Analysis of Chaotic and Traditional Photograph Composition Techniques

Jeffery Hoehl

University of Colorado at Boulder
Department of Computer Science
Boulder, Colorado

jeffery.hoehl@colorado.edu

ABSTRACT

There is an intrinsic linking between beauty, nature, and mathematics that has been thoroughly analyzed but is still not fully understood. This paper discusses some of the previous research and background of how aesthetic beauty relates to mathematics and natural patterns. A study is conducted and discussed wherein photographic composition techniques based on mathematical patterns were tested for aesthetic preference. It was determined that composition techniques based on the Rössler chaotic formula do significantly better than traditional techniques for influencing photographic composition.

Categories and Subject Descriptors

G.1.7 [Numerical Analysis]: Ordinary Differential Equations – chaotic systems

General Terms

Experimentation, Human Factors, Theory.

Keywords

Chaotic Dynamics, photography, composition, aesthetics of mathematics.

1. INTRODUCTION

1.1 The Visual System

The connections between beauty, nature, and mathematics are often experienced on a daily basis and routinely implied in conversations ranging from friendly banter to scientific discourse. It is well-known that simple mathematical patterns can be found throughout nature and form very attractive aesthetics. For instance, the Fibonacci sequence can be seen in the patterns of a sunflower's seeds and the shape of pinecones, and much of Mandelbrot's inspiration for fractal research resided in describing the forms of mountains, clouds, and rivers [Mandelbrot 1989]. The relationship between mathematical equations, nature, and our understanding of beauty seems to be intrinsically linked. Mathematical symmetry, repetition, and size ratios are all generally found to be aesthetically pleasing, even in a "raw" visual representation [Mandelbrot 1989]. Yet surprisingly little is known about what connections actually exist between these concepts and exactly how they operate; a deeper understanding of why patterns and images of natural life are so appealing is generally lacking.

Although there appears to be significant knowledge gaps into why human nature has an appreciation for mathematical patterns and the natural environment, it is not a result from a lack of trying. Quite the contrary, mathematicians, cognitive scientists, evolutionary psychologists, and artists, amongst many others,

have all addressed the issue and although much has been discovered, much still remains to be discovered. As expected, nearly all disciplines confirm intuitions that the natural environment is aesthetically pleasing and patterns are liked, but the complexity of how this occurs is quite unexpected. For instance, visual pattern recognition was once thought to be a strictly higher-level cognitive process but more recent research has found that "not only does information from lower-level processing influence higher levels, but higher-level processing, involving stored knowledge, can guide lower-level perception in tasks such as segmentation" [Mitchell 2008]. In other words, our visual systems are not unidirectional; what we perceive can influence what we think and what we think can influence what we perceive. This effect can propagate to nearly all levels of cognitive processing: "[Rob] Goldstone reported on experimental results that indicated that even the most abstract of tasks—mathematical reasoning—is affected by visual input, such as the layout of the problem on the page" [Mitchell 2008].

The key to the visual system is not the layering alone, but rather the "ability to fluidly integrate the different levels that provide the major source of visual understanding in humans and other animals" [Mitchell 2008]. In fact, this fluid integration is so capable that "while modern computer vision systems have impressive performance in some specific domains, there are no systems able to recognize instances of visual categories or understand the contents of visual scenes with anywhere near the generality and robustness of human perception" [Mitchell 2008]. The visual system is incredibly resilient as well and a "search of complex visual displays for single features can take place in parallel with relatively little effect of the number of distractors" [Posner 1990]. Not only is the human visual system fast, but it is not easily distracted.

1.2 Art from Math

The interaction between cognitive layers can help to explain why humans are attracted to certain patterns and by extension certain mathematical images and art forms. The fluid interaction of information between the low-level perceptual layers of the brain and the higher-level interpretation layers of the brain could be led to create harmonious or discordant flows. Visual images that have a combination of both simple patterns as well as more complex meaning can be considered more aesthetically pleasing than those that simply have basic repeating patterns. In essence, activating more of the cognitive pipeline can be a potential measure for determining aesthetics. Although this idea is conjecture, it is supported by Mandelbrot's exploration and discovery of a new art form, fractal geometry, and Ned Kahn's observations on aesthetics: "Your mind is working on a lot of levels. You're

processing this visual information, and you're recognizing patterns, some so subtle you probably can't describe what you're seeing, but on some level aesthetically... there's an indication that there is an order in there" [Walker 1999].

In Mandelbrot's description of fractals, he mentions that "the inputs are typically so extraordinarily simple as to look positively simple-minded. The outputs, to the contrary, can be spectacularly complex" [Mandelbrot 1989]. In essence, this plays quite well to the configuration of the visual system, a vast combination of interactions between simple and complex systems. As such, one would expect that fractals would be visually attractive which is exactly what he found: "most surprisingly and without any prodding, this new geometric language has given rise to a new form of art" [Mandelbrot 1989]. In fact, he attributes their inherent beauty to the very survival of the field of fractals: "the beauty of a flower is useful – even indispensable – to the survival of its species. Similarly, it was the attractiveness of the fractal images that first brought them to the attention of many colleagues and then of a wide world" [Mandelbrot 1989].

The research into fractals is also interesting in its applications to modeling nature. As Mandelbrot investigated the ability of fractals to model mountain ranges he found that "when the representation of nature by fractal is perceived as successful, it also tends to be perceived as beautiful. Unquestionably, the fractal 'forgeries' of mountains and clouds are examples of representational art" [Mandelbrot 1989]. If fractals are to be taken as an indication, then portions of the beauty of nature lie in the interaction between simple and complex patterns and portions of the beauty of art lie in its ability to represent the natural world.

1.3 Math from Art

Just as art and beauty arise out of mathematically-based approaches, there are examples of math being found in art-based endeavors. Dan Rockmore writes about the field of "stylometry" which derives mathematical models of artists and styles from artistic works [2007]. Notably, Richard Taylor has provided the work of Jackson Pollock and discovered that "the 'chaos' for which one critic famously denounced Pollock's work in the 1950s is something that Taylor saw quite literally as the mathematics of fractal geometry" [Rockmore 2007]. Regularity can be found by examining the different color layers of Pollock's paintings and calculating the fractal dimension therein. As Rockmore insightfully notes, however: "it's significant that Taylor found a

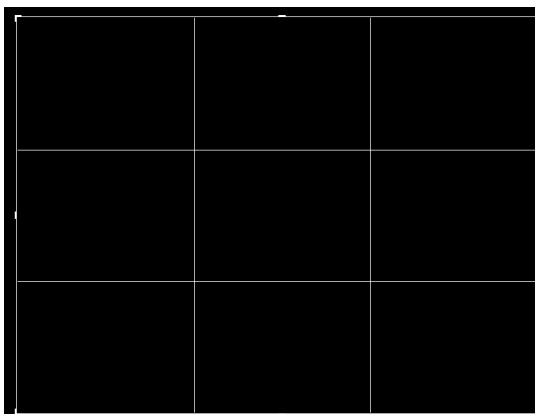


Figure 1: Rule of Thirds

digital signature for Pollock. But what might be even more significant is that the art world paid attention to it, for this shows the art/science boundaries are continuing to become fuzzier and fuzzier" [2007]. Thus, not only are there intrinsic links between math, art, and nature, but as those links are discovered they are becoming increasingly useful in pragmatic ways.

1.4 Implications for Photography

The connection between the low and high level processing of visual information and aesthetics can also be seen in the field of photography. It has been discovered that the most influential factor in the appeal of a photograph was its composition compared to other factors such as colorfulness, portrayal of babies, visibility of faces, sharpness, quality of image, etc [Savakis 2000]. In other words, the geometric layout of items in a photograph has the most influence on its aesthetics over all other factors. Again this plays into the relationship between lower-level and higher-level cognitive process interactions. The individual shapes, patterns, and images in a photograph can quickly be perceived and interpreted by the visual system, but there is likely another interplay appearing with the composition of the shapes and patterns and their relationships to one another. The effects of composition not only have effects on the aesthetic value, but also on the memory impact of an image. It has been found that "focusing on the layout is more important than focusing on the objects for remembering a given scene" [Mitchell 2008]. Overall, the *relationship* between objects in photographs tends to have more value than the objects themselves.

Generally speaking, there are no rigid rules for creating compositions in photograph [Savakis 2000]. However, photographers have developed several techniques and heuristics for creating appealing composition in two-dimensional photographs. The most common composition heuristic by far is the "rule of thirds." With this composition, major focal points of the photograph are placed approximately one-third inward from the borders of the image. In other words, two horizontal lines can be constructed and put on top of an image, one-third of the way from the top and bottom of the total image height. Similarly, two vertical lines can be constructed and put one-third of the way from the left and right of the total image width. These four lines will create four intersection points which are the suggested focal points of the image, Figures 1 and 2.

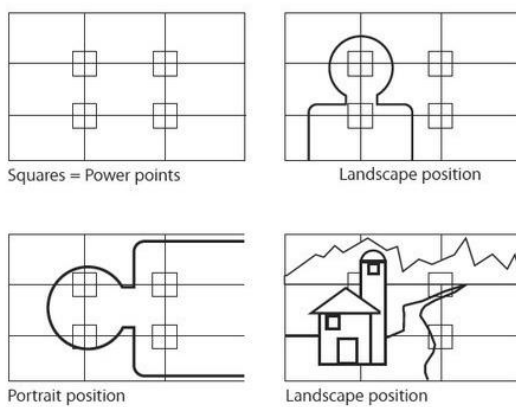


Figure 2: Rule of Thirds Composition [Jones 2010]

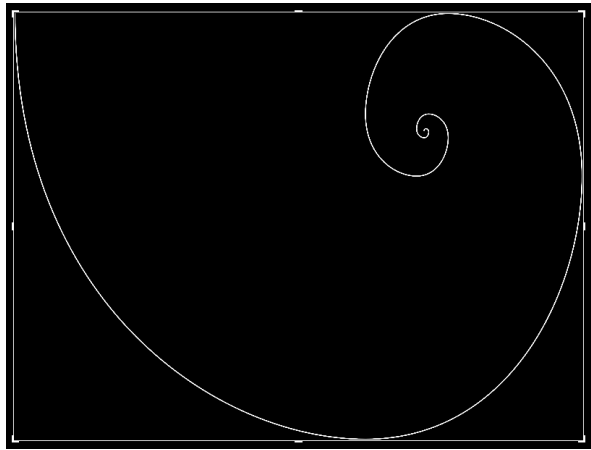


Figure 3: Golden Spiral

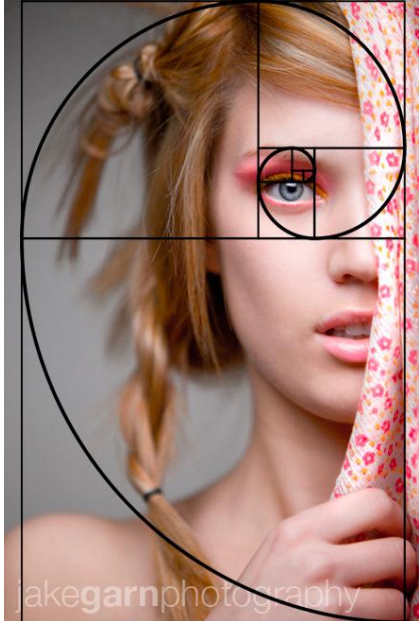


Figure 4: Golden Spiral Example [Garn 2010]

Another compositional heuristics that is widespread amongst photographers is the use of the golden spiral, Figure 3. The golden spiral is created by decreasing the radius of a spiral in proportion to the golden ratio. Focal points of an image should then be placed along the path or near the center of the spiral as shown in Figure 4.

In both the rule of thirds and the golden spiral, the layout and focal points of objects in a photograph are based on their relative ratios to each other. Thus the composition has little mathematical basis other than the value of the ratio and has, in Mandelbrot's terms, no representational value. The two compositional patterns do have the effect of moving focal areas away from the center of the image. This is largely their main function as photographs with

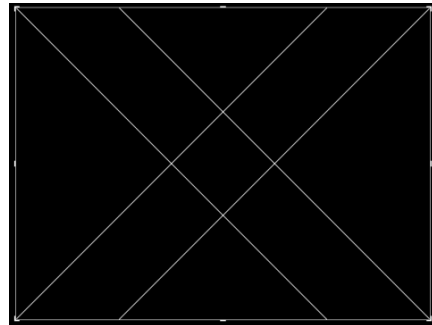


Figure 5: Diagonals Composition

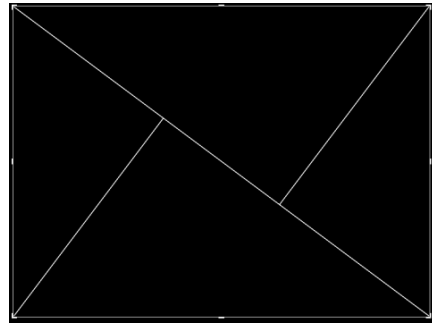


Figure 6: Triangles Composition

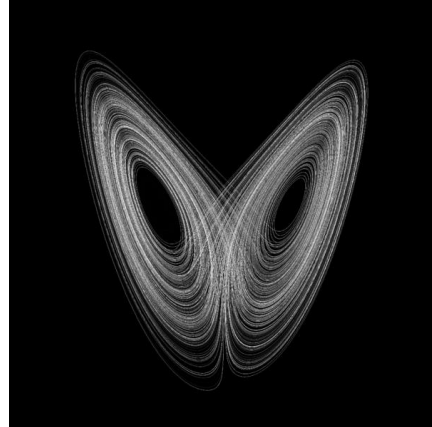


Figure 7: Lorenz Composition

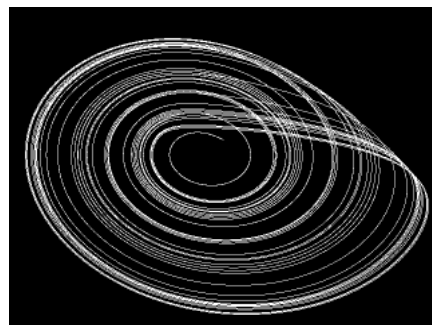


Figure 8: Rössler Composition [Bradley 2010]

perfectly centered subjects tend to feel static and unbalanced. Similarly, photographs with strong contrast, such as a horizon line, cut across the center or middle of the image tend to be less liked than those with contrast areas off-center.

The most common technique for creating photographs with the rule of thirds or the golden spiral composition is to crop and adjust photographs in post-production editing. Many graphics packages will allow users to overlay the composition guides over photographs and crop or distort a photo to match the guides. Other, less-common, overlays can also be used including one focused on diagonal lines, Figure 5, and one on triangles, Figure 6. Yet all of the common overlay techniques are based on ratios of the distance between objects and have no representational value.

An obvious question thus arises. If simple, ratio-based compositions can improve the aesthetic value of a photograph, can other methods based on other mathematical principles be used to provide aesthetic improvements as well? Specifically, can chaotic dynamics be used to create new overlays to guide the compositions of photographs and how would these compositions compare to the traditional ones? Overlays based on chaotic dynamics could have the potential advantage of being based on observed patterns and shapes, rather than ratio values, and thus might be more cognitively interesting than existing composition techniques. The interplay between simple patterns and complex patterns would be heightened. Additionally, the chaotic dynamics based compositions could be rooted in systems that have representational value much like Mandelbrot's fractals. If patterns that are based on natural phenomena are used, one would expect a higher level of aestheticism to result.

2. METHODOLOGY

2.1 General Setup

Just as a survival mechanism exists for fractals and beauty for a set to become more popular, a similar natural selection can be seen with chaotic dynamics equations [Mandelbrot 1989]. In particular, two of the most popular dynamical systems to be studied are the Lorenz and Rössler systems [Lorenz 1963, Rössler 1976]. Projections and models of the two systems have distinct patterns that are visually interesting and captivating. The two systems are widely discussed in chaotic dynamics literature and appear in several introductory texts on the topic. As such, they provide ideal candidates for testing as potential composition guides in comparison to two of the most common traditional guides, the rule of thirds and the golden spiral.

This study evaluated the relative aesthetic value of the four composition layouts by creating an online user survey that compared the chaotic compositions against the traditional ones. The results were used to determine if any significant benefit or detriment could be found by using the new composition styles.

2.2 Image Set Selection

This study examined the comparisons by first gathering representative photographs that exhibit compositions reflective of each desired composition heuristic. Photographs that are exemplars of the rule of thirds and golden spiral were collected as well as images that resemble layouts similar to the Lorenz and Rössler systems. The images were chosen from a gallery of curated photographs from an online photography community, 1x.com [1x 2010]. The curation process for the site ensures that images meet a minimum threshold for image quality, style,

content, and technique. By using a gallery that is vetted in this manner, those same variables are controlled for in the user judgment process. Images of lower quality or of offensive content are not present and are thus controlled for. Additionally, preferences between images were further controlled by only evaluating photographs that ranked in the top 200 most popular images of all time on the site. This ensured that both the site curators as well as the site's community population both agreed upon all images of being the highest caliber and quality. As such, judgments made in this study's survey should not show effects from basic subjective quality measures.

Evaluations of over 200 photographs were made and an initial filtering of images was based on subject matter and content of images. Images that were simply portraits, single subject, contained strong religious symbols, contained offensive images, contained adult content, or contained common phobias (i.e. snakes, spiders, etc.) were removed from the test set to further control for selection bias. The threshold for filtering was essentially determined to ensure composition was an influencer for photo selection rather than being completely outweighed by one of the common confounding variables. By filtering the dataset, a collection of approximately 120 photographs remained that were similar in quality, content, style, and popularity yet had compositional variability.

2.3 Image Classification

Although overlays and guides can be used to assist in manipulating photographs to fit a compositional pattern, detecting the use of a composition pattern is much more difficult: "although general guidelines for photographic composition have been

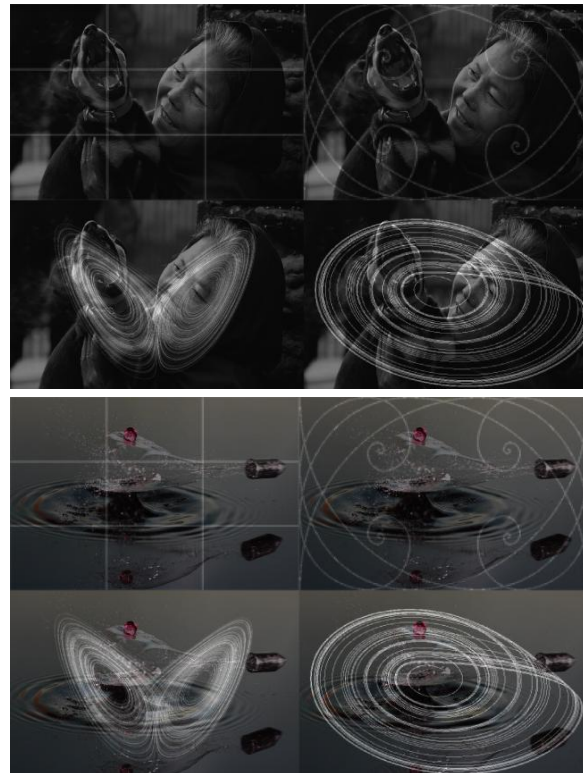


Figure 9: Screenshots of Image Classifier [Limawhisky 2010, Augsteijn 2010]

established, there is no work to date for automatic determination of a picture's composition" [Savakis 2000]. As such, a custom classification tool had to be created to streamline and assist with the human judgment of photographs to determine if an underlying composition heuristic was present. Specifically, a tool was created that projected the four composition overlays (Figures 1, 3, 7, and 8) of interest onto four repetitions of a photograph to allow a human judge to determine the best fit of composition. The tool allowed for the manipulation of the overlays to ensure accurate classification. For instance, the golden spiral overlay was rotated and translated in various directions to ensure that all variations of the golden spiral could be correctly detected. The tool also handled various image aspect ratios by scaling the composition overlays to correctly match the aspect ratio of the underlying image. In some instances, this could lead to distortion, but generally the scaling was minimal and distortion negligible ensuring a good wellness of fit. A sample of the classification tool's interface can be seen in Figure 9.

The image classification process involved viewing each image with the composition overlays and determining which of five categories it best fit in: Lorenz, Rössler, Thirds, Golden Spiral, or No Good Fit. The classification program would appropriately rename and categorize each image based on the judgments made. Once the initial classification of all the photographs was made, the 10 images that fit each classification most strongly were used for the final survey. This process was essentially a continual reiteration of the first classification pass but with successively stricter thresholds until only the 10 most fitting images in each composition category remained. The final test set consisted of 40 images, 10 each of the four composition categories.

2.4 Survey Configuration

A web-based application was created to conduct the survey. This allowed for the convenience and flexibility of participants to take as much time as they needed, take as many iterations of the survey as they desired, and to expand the participant pool. The application was created in PHP and presented results using HTML/CSS to allow for the broadest support of participant access as possible.

The web application presented a set of twenty pairs of photographs to participants, Figure 10. In each pairing, one photograph with a traditional composition style and one photograph with a chaotic composition style were presented. Users were asked to select the photograph in each pair they preferred based on aesthetics only, without knowing what the differentiating factor was. The paired photographs, their column

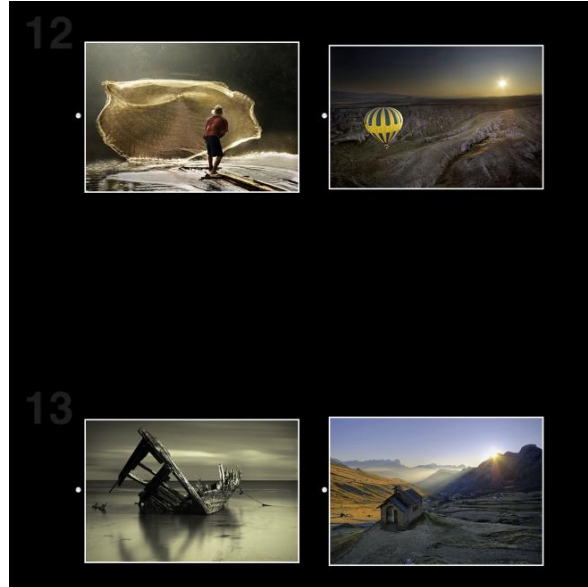


Figure 10: Online Survey for Photo Judgment [Arment 2010, Rudomina 2010, Smart 2010, Strahinjic 2010]

position, and their ordering on the page were all randomized to ensure ordering effects were not present. The pairs of photographs were randomized to prevent effects of one image being clearly favored to an alternate photograph. By randomizing all pairings, the composition effects should become more prevalent and generally favorable images will have less of a statistical impact. After twenty pairings, the user could opt to submit their results at which point the data was saved and available for analysis. The participants were thanked for their participation but were not prevented from retaking the survey multiple times.

2.5 Participants

The participants involved in the study were initially a convenience sample of the students taking Spring 2010 Chaotic Dynamics course at the University of Colorado at Boulder. However, the participants were encouraged to use their social networks to recruit additional participants. As such, an ad-hoc social graph of participants was created. The major participant groups included

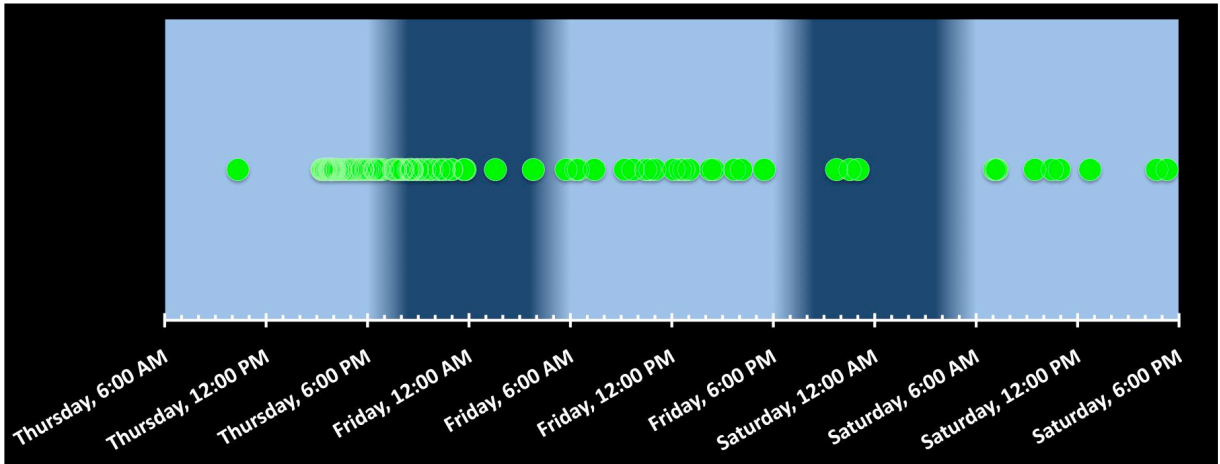


Figure 11: Timeline of Survey Submissions

the course students themselves, previous students of the course over the past five years contacted through an email list, and social connections through those individuals.

3. RESULTS

3.1 Summary Statistics

In total 122 survey sessions were taken with 2,353 pairs of photographs rated. Seven sessions only rated 19 pairings, one sessions only rated 17 pairings, and 4 sessions had zero or one rating. The latter 4 sessions were likely participants that were simply attempting to see what the survey was about and what the application did but did not want to actually participate. Those ratings were removed from analysis as outliers for individual-based statistics.

The effects of the social networking and broadcasting of the survey seemed to have a dramatic effect as well. Not only was the total number of sessions much higher than the number of class members, but only 25% of survey sessions originated from the University of Colorado at Boulder campus network. This includes users taking the survey from the main campus, campus housing, or through the VPN network.

The survey submissions over time were generally as one would expect as seen in Figure 11. The vast majority of users responded immediately after receiving a personal invitation or email as seen by the majority of submissions from Thursday near 3pm through Thursday evening and nearly all surveys coming in by Saturday evening. There were obvious drop-offs at night and in the early morning with resurgence occurring during the daytime. One particular gap exists between early Friday evening and late Friday evening. This could result from people returning home and taking the survey after being out on a Friday night or from users in different time zones completing the survey during daylight hours. For instance, several submissions originated from Japanese users. Very few submissions were received after Saturday evening and they were discarded as outliers due to pragmatic needs to process data.

3.2 Chaotic versus Traditional Composition

As shown in Table 1, the number of votes for chaotic compositions, 1186, is only slightly higher than that for traditional compositions, 1167. Using a two-tail χ^2 -test with $\alpha=0.05$, we can

Table 1: Combined Votes by Chaotic or Traditional Composition

Traditional	1167	49.6%
Chaotic	1186	50.4%

Table 2: Votes by Composition Style

Thirds	590	25%
Golden Spiral	577	25%
Rössler	662	28%
Lorenz	524	22%
Total	2353	100%

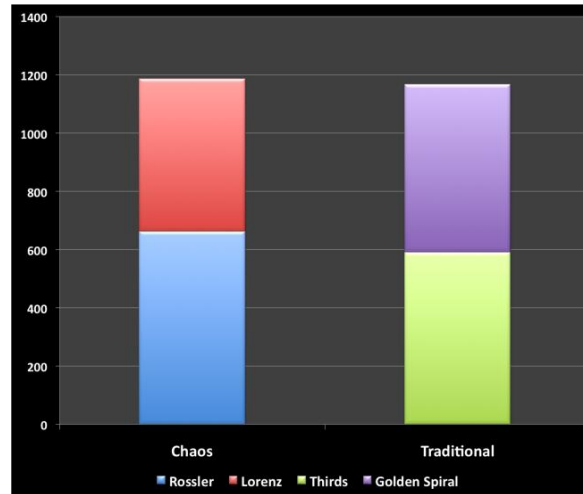


Figure 12: Combined Votes for Composition Styles

calculate $\chi^2=0.153$ which is not statistically significant ($\chi^2<0.001$ or $\chi^2>5.024$ needed for significance). The variation between the chaotic and traditional compositions is not greater than what we could account for based on chance and random choice. In other words, we cannot attribute user preferences to the photographs based solely on whether it used a chaotic or traditional composition approach.

However, if we analyze the data based on the individual type of composition style in the same manner, two-tail χ^2 -test with $\alpha=0.05$, we obtain $\chi^2=16.484$ which is statistically significant ($\chi^2<0.216$ or $\chi^2>9.348$ needed for significance). Thus, there does seem to be an effect where the composition type is affecting user preference. A quick look at Table 2 indicates that both the rule of thirds and the golden spiral are nearly exactly at chance rates. However, the Rössler composition style is higher than chance at 28% and the Lorenz composition style is lower than chance at 22%. An effect seems to be present that the Rössler composition is indeed preferred by users while the Lorenz composition is disliked by users. Since these are both chaotic-based compositions, their results cancel each other out at a high-level but differences do exist between them. This combining effect can be seen in Figure 12. Interestingly, both of the traditional, and most common compositions, are at chance rates.

In both the former, collapsed, and the latter, independent cases, it is important to note that the proportions of choice are still closely related. This is important in that it signifies that none of the composition styles were particularly unviable as an alternative. Although the Lorenz composition was statistically chosen less than chance, it was still picked 22% of the time. In the big picture, this would still indicate a viable choice to use if one were determining how to compose a photograph. Although it does not do as well as the others, it is still a potential candidate for compositional use. The same is true of the other three composition styles. Although Rössler was chosen more often than the traditional compositions, they are all still quite competitive with each other.

3.3 Individual Effects

Although the previous analysis indicates the results of the survey across the population of participants, it does little to explain the effects of the individuals and the preferences each survey

Table 3: Individual Preferences for Composition

Individuals Preferring Chaos	54	46%
Individuals Preferring Traditional	45	38%
Individuals with No Preference	19	16%

Table 4: Individual Preferences for Composition by Type

Individuals Preferring Thirds	27	23%
Individuals Preferring Golden Spiral	16	14%
Individuals Preferring Rössler	35	30%
Individuals Preferring Lorenz	12	10%

participant had.

At the individual level, one can determine whether a particular survey participant preferred chaotic compositions, traditional compositions, or had no preference. In doing so, one can calculate the results in Table 3 indicating the number of participants that chose chaotic compositions more often than traditional, vice versa, or at the same rate. With a two-tail χ^2 -test at $\alpha=0.05$, we obtain $\chi^2=3.746$ which is not statistically significant (using 2 degrees of freedom comparing only preferences for chaos and traditional compositions with no expectation of a lack of preference). However, one can observe a difference if a one-tail χ^2 -test with $\alpha=0.10$ is used. There seems to be a difference that more individuals prefer chaotic compositions overall but the confidence is slightly lower.

Looking at Table 4 one can notice very interesting result in individual preferences for composition types. The Rössler and rules of thirds compositions are quite dominate amongst individual preferences and is significant with a two-tail χ^2 -test at $\alpha=0.05$, obtaining $\chi^2=17.797$ ($\chi^2<0.216$ or $\chi^2>9.348$ needed for significance). Thus, more individuals seem to prefer the rule of

Table 5: Most Winning and Least Winning Images

Picture	Win Count	Composition
T_18606	80	Thirds
R_14369	79	Rössler
R_31933	78	Rössler
R_32531	78	Rössler
T_26147	77	Thirds
...
T_32134	39	Thirds
L_32529	36	Lorenz
L_31943	34	Lorenz
T_14346	31	Thirds
L_32522	25	Lorenz

thirds and the Rössler composition types than individuals that prefer the golden spiral or the Lorenz compositions. This can also be seen in Figures 13 and 14 relating the number of chaotic and traditional choices made to the number of individuals doing so. The chaotic composition histogram is slightly left-skewed while the traditional composition histogram is slightly right-skewed.

3.4 Image Effects

An analysis of the images that were chosen more often than others reveals a consistent, linear spread between the most popular images and the least popular. However, an analysis of the most winning and least winning images, Table 5, reveals trends previously exposed in the analysis. Amongst the top five most winning images, three are based on the Rössler and amongst the top five least winning images, three are based on Lorenz. The rule of thirds compositions are well spread throughout the list and the golden spiral images are generally centered about the middle. As a general descriptive rule, the Rössler compositions won the most, the Lorenz compositions won the least, the rule of thirds had the highest standard deviation, and the golden spiral the least.

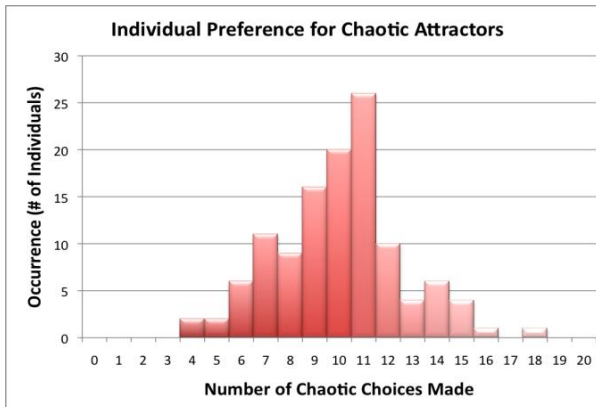


Figure 13: Individual Preference for Chaotic Composition Histogram

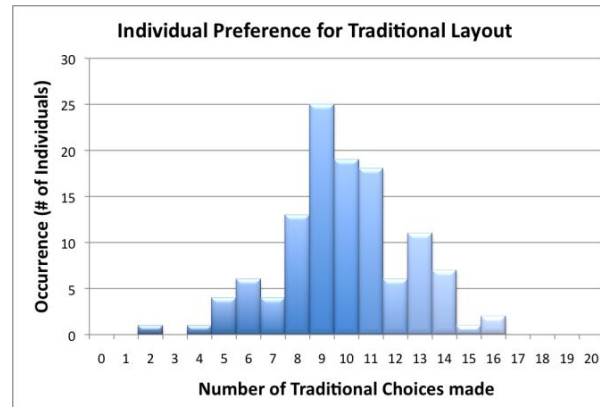


Figure 14: Individual Preference for Traditional Composition Histogram

4. CONCLUSION AND FUTURE WORK

This study evaluated the notion that visualizations of mathematical formulae are often inherently beautiful and visually appealing. It was determined that although chaotic attractors as composition guides are not necessarily an improvement across the board when compared to traditional composition guides, they are not a step backwards either. When split apart between the rule of thirds, golden spiral, Lorenz, and Rössler compositions, the Rössler composition clearly performs better overall. Thus, a solid recommendation can be made that using the Rössler attractor as a composition guide can result in aesthetically pleasing photographs. This finding is particularly interesting because it conflicts with commonly taught practice.

In general, the rule of thirds and the golden spiral are taught as successful alternatives to an inclination of new photographers to focus subjects in the center of a frame. Yet the Rössler composition guide is closely related to that behavior but with a focal point slightly off in one corner. Perhaps a successful learning technique could be to not only use the Rössler composition guide as a successful technique, but one that would take very little modification from early photographers' natural inclinations. As such, the Rössler composition style can be implemented as a great learning tool.

Another explanation of the Rössler compositions possible success is the rise of online social networks and shared social media. The survey participants have been exposed to more amateur and peer photography than what has been historically possible and thus the "bulls-eye" pattern of composition may be more familiar to the participants. A future study could control for familiarity of amateur photography to enthusiast or professional photography to determine this effect.

The success of the Rössler composition, and the non-failure of the Lorenz composition, suggest that there are likely many more opportunities for new composition guides. The focus on traditional compositions may be stifling creativity and the field of chaotic dynamics seems well poised to offer suggestions for new ideas and forms in composition techniques. One can even imagine situating objects based on the three-dimensional forms of chaotic dynamic formulas in three-dimensional space and then taking the two-dimensional photograph from that configuration. Thus, there seem to be many opportunities for both immediate pragmatic gains for photographers as well as future study for other improvements in aesthetic design and thought.

5. ACKNOWLEDGMENTS

My appreciation goes out to all of the students in the Spring 2010 Chaotic Dynamics class for their participation and feedback in this study. The same goes out to all of the participants who provided survey data and especially Dr. Bradley for providing assistance in gathering participants.

6. REFERENCES

- [1] 1x.com. 2010. <http://www.1x.com>. Last Accessed: April 30, 2010.
 - [2] Lorenz, E. N. 1963. Deterministic Nonperiodic Flow. *Journal of the Atmospheric Sciences*, 20:130-141.
 - [3] Mandelbrot, B. 1989. Fractals and an art for the sake of science. In *SIGGRAPH 89 Art Show Catalog - Computer Art in Context* (Boston, Massachusetts, United States, July 31 - August 04, 1989). M. Resch, Ed. SIGGRAPH '89. ACM, New York, NY, 21-24.
 - [4] Mitchell, M. 2008. Visual Understanding. *Santa Fe Institute Bulletin*, Spring 2008, 51-54.
 - [5] Posner, M. I., and Petersen, S. E. 1990. The Attention System of the Human Brain. *Annual Review of Neuroscience*, 13:25-42.
 - [6] Rockmore, D. 2007. The Numbers of Our Nature: Is There a Math of Style? *Santa Fe Institute Bulletin*, Winter 2007, 10-17.
 - [7] Rössler, O.E. 1976. An Equation for Continuous Chaos. *Phys. Lett.* 57A:397-398.
 - [8] Savakis, A., Etz, S. P., Loui, A. C.. 2000. Evaluation of image appeal in consumer photography. In *Proceedings of Human Vision and Electronic Imaging*.
 - [9] Walker, H. 1999. Discovering Patterns – The Interface Between Art and Science. *Santa Fe Institute Bulletin*, Fall 1999, 9-14.
- ## 7. IMAGE ATTRIBUTIONS
- [1] Arment, A. 2010. Sengkol's Fisherman. <http://1x.com/photo/32273/>. Last Accessed: April 30, 2010.
 - [2] Augsteijn, L. 2010. Shot of a drop shot. <http://1x.com/photos/popular/ever/25887/>. Last Accessed: April 30, 2010.
 - [3] Bradley, L. 2010. Strange Attractors. <http://www.stsci.edu/~lbradley/seminar/attractors.html>. Last Accessed: April 30, 2010.
 - [4] Garn, J. 2010. The Tremendously Lazy Rule of Thirds. <http://jakegarn.com/the-rule-of-thirds>. Last Accessed: April 30, 2010.
 - [5] Jones, B. 2010. Helpful Photography Cheat Sheets to Make Your Life Easier. <http://www.thephotoargus.com/resources/helpful-photography-cheat-sheets-to-make-you-life-easier>. Last Accessed: April 30, 2010
 - [6] Limawhisky, 2010. Best friend. <http://1x.com/photo/32522/>. Last Accessed: April 30, 2010.
 - [7] Rudomina, R. 2010. Flight at dawn. <http://1x.com/photo/32023/>. Last Accessed: April 30, 2010.
 - [8] Smart, M. 2010. The court of heaven “A galley’s last stand”. <http://1x.com/photo/17445/>. Last Accessed: April 30, 2010.
 - [9] Strahinjic, R. 2010. Morning. <http://1x.com/photo/18606/>. Last Accessed: April 30, 2010.

Low Cost Reconfiguration of Invariant Shape Collinear Coulomb Spacecraft Formations

Erik Hogan*

University of Colorado, Boulder, CO 80303

This paper investigates the stability of circular three-craft invariant shape Coulomb formations, with the goal of investigating potential reconfigurations using hyperbolic manifolds. The system is expressed in a novel rotating frame so that a circular invariant shape solution corresponds to a single point in state space. After identifying a case where multiple shapes exist for constant charge levels, a linearization of the equations of motion are done about the equilibria. The eigenvalues of the linearized system are used to perform a stability analysis for each of the invariant shapes. It is found that one equilibrium exhibits marginally stable behavior while the other is a hyperbolic point. The stable and unstable manifolds are examined for the hyperbolic equilibrium. For the case examined here a reconfiguration using hyperbolic manifolds is not possible, but the results suggest that more studies are needed.

I. Introduction

CLOSE formation flying of spacecraft presents many exciting possibilities, with applications ranging from advanced weather monitoring to high resolution earth imaging and astronomy applications. The ability to concentrate a large number of scientific instruments within a group of satellites separated by tens of meters would be a major step forward over the limited space provided by a single satellite. A further advantage of using a satellite formation results from the fact that not all of the satellites need to be launched simultaneously. This means that an advanced complex of scientific instrumentation could be pieced together gradually over time. Because the satellite formation would not need to be connected by rigid structure, a large savings in mass would occur over a large complex like the International Space Station. With the high cost of sending objects into orbit, any reduction in mass would result in a significant reduction in cost. This would make space-based science missions more economical, allowing for a larger number of studies to be conducted. One potential application where close formation flights would be particularly useful is the field of interferometry. In fact, such formations have been proposed for the Terrestrial Planet Finder Interferometer concept currently under study by NASA.^{1,2}

Many instruments used to conduct space based research can be very sensitive to interference caused by free floating particles. When considering close formation flight of a small cluster of satellites, this can be a very serious problem if traditional propellant-type thrusters are used to maintain the formation. In such close proximity, it is almost guaranteed that the propellant mass ejected by a thruster on one satellite will come into contact with other satellites and possibly interfere with the delicate instrumentation onboard. One way to circumvent this problem is to use electrostatic forces to control the formation.^{3,4} By charging individual spacecraft, attractive and repulsive forces are created which can be used to control a close formation at distances up to tens of meters. This method of propulsion essentially requires no propellant, meaning there will be no ejected particles to interfere with other craft in the formation. Furthermore, it is also very efficient, requiring power levels on the order of Watts.⁵ Such a propulsion method would require active charge control, which has already been demonstrated on the SCATHA and ATS missions.^{6,7,8}

For the current study, we consider three-craft collinear invariant shape Coulomb formations in deep space.⁹ Plasma effects will be ignored, as large Debye lengths are assumed. Furthermore, only electrostatic forces will be considered, as external forces (gravity, solar radiation pressure, etc.) are assumed to be nonexistent. The charge levels on the three craft will be set at constant, but not necessarily equal, values. With such a configuration, it has been hypothesized

*Graduate Student, University of Colorado

that a situation may exist where two invariant shape solutions are possible for the same charge levels.⁹ The goal of the current study is to confirm that this hypothesis is valid, and study the stability of the resulting invariant shape solutions. For a case where two invariant shapes result for the same charge levels, we would like to ascertain whether or not a reconfiguration might be possible using hyperbolic manifolds in state space. That is, can we slightly perturb one invariant shape such that the natural dynamics of the system will cause a reconfiguration into another? Such a reconfiguration would be beneficial, as it would require minimal energy input. From a mission design standpoint, the two invariant shapes could be used to perform different tasks. Transferring between the two on a manifold would be inexpensive compared to more direct methods, and could extend the life of the formation.

II. Background

A. Hamiltonian Treatment

When considering the intercraft forces between charged craft, it is appropriate to treat the craft as point charges for a reasonable approximation.¹⁰ Using this assumption, a Coulomb formation may be treated as a conservative Hamiltonian system, so long as the charge levels on the craft are held constant. In the collinear invariant shape formation, the charge levels on the craft are maintained at a constant level. To determine the Hamiltonian form for the formation, expressions for the potential and kinetic energy are needed. If we define the generalized momentum term, \vec{p}_i , as

$$\vec{p}_i = m_i \dot{\vec{r}}_i,$$

where m_i is the mass of craft i , the total formation kinetic energy can be expressed as

$$T = \sum_1^3 \frac{\vec{p}_i \cdot \vec{p}_i}{2m_i}. \quad (1)$$

Noting that the potential energy between two craft is¹⁰

$$V = k_c \frac{c_1 c_2}{r},$$

where k_c is the Coulomb constant, c_1 and c_2 are the charges on craft 1 and 2, and r is the distance between the craft, the total system potential energy can be expressed as

$$V = k_c \left(\frac{c_1 c_2}{r_{12}} + \frac{c_1 c_3}{r_{13}} + \frac{c_2 c_3}{r_{23}} \right). \quad (2)$$

With both of these quantities defined, the system Hamiltonian is expressed as

$$H = T + V. \quad (3)$$

To determine the system dynamics, we define the position of each spacecraft to be the generalized coordinates, \vec{q}_i . Pairing the conjugate momenta, \vec{p}_i , with their corresponding \vec{q}_i , the system dynamics are determined by

$$\begin{aligned} \dot{\vec{p}}_i &= -\frac{\partial H}{\partial \vec{q}_i} \\ \dot{\vec{q}}_i &= -\frac{\partial H}{\partial \vec{p}_i}. \end{aligned}$$

For any craft i in the formation, the Hamiltonian equations lead to

$$m_i \ddot{\vec{r}}_i = \sum_{j=1, j \neq i}^3 k_c \frac{c_1 c_2}{r_{ji}^2} \hat{\mathbf{e}}_{ji}, \quad (4)$$

where $\hat{\mathbf{e}}_{ji}$ is the unit vector from craft j to craft i . This form is identical to the system dynamics when non-constant charges are present. The difference is that in such a case energy will no longer be conserved, which is due to the fact that power is required to change the charge levels on the craft.

B. Invariant Shape Formation

Hussein et. al⁹ lays the groundwork for determining invariant shape Coulomb formations. It is important to recognize that invariant shape does not mean fixed shape. That is, the formation geometry at some time t_i does not necessarily have to match that at some other time, t_j . To better define the meaning of invariant shape, consider a collinear configuration of craft, as shown in Fig. 1. If we define a parameter, χ , as

$$\chi = \frac{r_{23}}{r_{21}}, \quad (5)$$

then an invariant shape formation is one where χ is constant for all time. The individual separation distances can change with time, so long as the ratio of one to the other remains unchanged. It is apparent that due to separation distances being positive quantities, χ will be positive. In a collinear invariant shape formation, the craft will orbit about the formation center of mass on Keplerian trajectories. The trajectories may be circular, elliptic, parabolic, or hyperbolic. These trajectories will evolve such that the craft are collinear for all time.

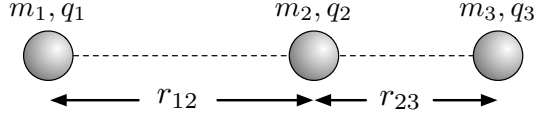


Figure 1: Collinear invariant shape Coulomb formation

In order to maintain this collinear invariant shape, the craft must be charged appropriately depending on the value of χ . Given a set of charges, the appropriate value of χ can be determined by satisfying the quintic equation⁹

$$0 = -w_2 w_3 (m_2 + m_3) - w_2 w_3 (2m_2 + 3m_3) \chi + [w_1 m_1 (w_2 - w_3) - w_2 w_3 (m_2 + 3m_3)] \chi^2 + [w_1 w_2 (3m_1 + m_2) + w_3 m_3 (w_1 - w_2)] \chi^3 + w_1 w_2 (3m_1 + 2m_2) \chi^4 + w_1 w_2 (m_1 + m_2) \chi^5,$$

where $w_i = c_i/m_i$. Considering only the case where all three craft are of equal mass, the above quintic equation can be reduced to the form

$$0 = -2 - 5\chi + (\delta - \sigma - 4)\chi^2 + (4\delta + \sigma - 1)\chi^3 + 5\delta\chi^4 + 2\delta\chi^5, \quad (6)$$

where $\delta = c_1/c_3$ and $\sigma = c_1/c_2$. It is apparent that the coefficients in Eq. 6 are dependent only on the craft charges. Depending on the values of these charges, it may be possible to find multiple positive χ values which satisfy the equation. Indeed, this was predicted by Hussein et. al,⁹ though no particular cases were found. It turns out, however, that a multitude of cases do in fact exist where two χ values satisfy Eq. 6 for a given δ and σ . Consider, for example, setting $\delta = -0.05$ and $\sigma = 7$. Solving for the roots of Eq. 6 yields two positive values: $\chi = 3.2508, 4.3283$. This is but one example out of many that will yield such a result.

Having identified that multiple invariant shape solutions exist for a constant set of charges, we would like to know if a reconfiguration may be possible using hyperbolic manifolds that connect one invariant shape to another. In essence, we are looking for a heteroclinic orbit to connect one invariant shape solution to another. Typically, the Coulomb formation dynamics are expressed in an inertial frame with the center of mass at the origin. The problem with such a configuration is that the only true “equilibrium” parameter which remains constant for an invariant shape is χ . That is, if you put the system in an invariant shape configuration, χ will remain constant for all time but the state variables $(\vec{r}_1, \dot{\vec{r}}_1, \dots, \vec{r}_3, \dot{\vec{r}}_3)$ will be time varying. This makes performing a standard linearization about an invariant shape equilibrium impossible. What is needed is a way to express the system dynamics in a manner such that an invariant shape solution corresponds to a single point in state space. The solution to this problem is obtained by expressing the dynamics in a rotating coordinate frame.

III. 3-Body Dynamics

A. Rotating Coordinate Frame

To determine the stability of the equilibria of the collinear invariant shape Coulomb formation, we will derive the system dynamics in a rotating coordinate frame, \mathcal{B} , defined by the orthogonal unit vectors

$$\mathcal{B} : \left\{ \hat{\mathbf{b}}_1, \hat{\mathbf{b}}_2, \hat{\mathbf{b}}_3 \right\}.$$

The \mathcal{B} frame is aligned such that craft 1 is confined to the $\hat{\mathbf{b}}_1$ axis for all time, while craft 2 and 3 are free to move about in the $\hat{\mathbf{b}}_1$ - $\hat{\mathbf{b}}_2$ plane. The origin of the \mathcal{B} frame is aligned with the center of mass of the formation, and the frame rotates about this point as craft 1 moves around the center of mass. This configuration is depicted in Figure 2. The angular velocity of the \mathcal{B} frame relative to the inertial frame, \mathcal{N} , is expressed as

$$\omega_{\mathcal{B}/\mathcal{N}} = \dot{\theta}\hat{\mathbf{b}}_3.$$

The kinematic equations for craft 1 in \mathcal{B} frame components are

$$\vec{r}_1 = x_1\hat{\mathbf{b}}_1 \quad (7)$$

$$\dot{\vec{r}}_1 = \dot{x}_1\hat{\mathbf{b}}_1 + \dot{\theta}x_1\hat{\mathbf{b}}_2 \quad (8)$$

$$\ddot{\vec{r}}_1 = (\ddot{x}_1 - x_1\dot{\theta}^2)\hat{\mathbf{b}}_1 + (x_1\ddot{\theta} + 2\dot{\theta}\dot{x}_1)\hat{\mathbf{b}}_2. \quad (9)$$

The kinematic equations for craft two and three in \mathcal{B} frame components are

$$\vec{r}_i = x_i\hat{\mathbf{b}}_1 + y_i\hat{\mathbf{b}}_2 \quad (10)$$

$$\dot{\vec{r}}_i = (\dot{x}_i - y_i\dot{\theta})\hat{\mathbf{b}}_1 + (\dot{y}_i + x_i\dot{\theta})\hat{\mathbf{b}}_2 \quad (11)$$

$$\ddot{\vec{r}}_i = (\ddot{x}_i - x_i\dot{\theta}^2 - y_i\ddot{\theta} - 2\dot{y}_i\dot{\theta})\hat{\mathbf{b}}_1 + (\ddot{y}_i - y_i\dot{\theta}^2 + x_i\ddot{\theta} + 2\dot{\theta}\dot{x}_i)\hat{\mathbf{b}}_2. \quad (12)$$

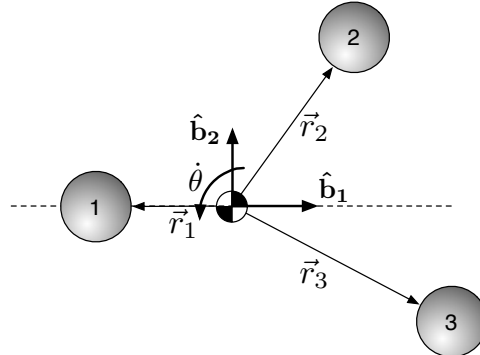


Figure 2: The rotating \mathcal{B} frame.

Returning to Eq. 4, the equation describing the dynamics of a craft in the formation, we can determine the state equations in the \mathcal{B} frame. Beginning with craft 1, we obtain

$$\ddot{x}_1 = \frac{k_c c_1}{m_1} \left(c_2 \frac{x_1 - x_2}{r_{12}^3} + c_3 \frac{x_1 - x_3}{r_{13}^3} \right) + x_1\dot{\theta}^2 \quad (13)$$

$$\ddot{\theta} = -\frac{k_c c_1}{m_1 x_1} \left(c_2 \frac{y_2}{r_{12}^3} + c_3 \frac{y_3}{r_{13}^3} \right) + \frac{2\dot{\theta}\dot{x}_1}{x_1}. \quad (14)$$

Applying Eq. 4 to craft 2 and 3, we obtain

$$\ddot{x}_2 = \frac{k_c c_2}{m_2} \left(c_1 \frac{x_2 - x_1}{r_{12}^3} + c_3 \frac{x_2 - x_3}{r_{23}^3} \right) + x_2\dot{\theta}^2 + y_2\ddot{\theta} + 2\dot{y}_2\dot{\theta} \quad (15)$$

$$\ddot{y}_2 = \frac{k_c c_2}{m_2} \left(c_1 \frac{y_2}{r_{12}^3} + c_3 \frac{y_2 - y_3}{r_{23}^3} \right) + y_2\dot{\theta}^2 - x_2\ddot{\theta} - 2\dot{x}_2\dot{\theta} \quad (16)$$

$$\ddot{x}_3 = \frac{k_c c_3}{m_3} \left(c_1 \frac{x_3 - x_1}{r_{13}^3} + c_2 \frac{x_3 - x_2}{r_{23}^3} \right) + x_3\dot{\theta}^2 + y_3\ddot{\theta} + 2\dot{y}_3\dot{\theta} \quad (17)$$

$$\ddot{y}_3 = \frac{k_c c_3}{m_3} \left(c_1 \frac{y_3}{r_{13}^3} + c_2 \frac{y_3 - y_2}{r_{23}^3} \right) + y_3\dot{\theta}^2 - x_3\ddot{\theta} - 2\dot{x}_3\dot{\theta}. \quad (18)$$

Contained in Eqs. 13-18, then, are the dynamics of the Coulomb formation expressed in the \mathcal{B} frame. Note that these equations imply an 11-dimensional state space, described by the state variables

$$\vec{X} = [x_1, \dot{x}_1, x_2, \dot{x}_2, y_2, \dot{y}_2, x_3, \dot{x}_3, y_3, \dot{y}_3, \dot{\theta}].$$

The advantage of using the \mathcal{B} frame is that a particular class of invariant shape solutions correspond to a single point in state space. If we consider only the case where the craft orbit about the formation center of mass on circular trajectories, the invariant shape satisfies a dynamic equilibrium such that $\ddot{\vec{X}} = \vec{0}$. In order for this to be true, $\dot{x}_1 = \dot{x}_2 = \dot{x}_3 = \dot{y}_2 = \dot{y}_3 = 0$. Furthermore, all craft must lie on the $\hat{\mathbf{b}}_1$ axis so that $y_2 = y_3 = 0$. To maintain the equilibrium, the craft must be positioned at finite x_i values such that the centripetal forces acting along the $\hat{\mathbf{b}}_1$ axis precisely balance with the Coulomb forces acting on the craft. When this happens, $\dot{\theta}$ will be constant and the craft will maintain a circular invariant shape. The state variables all take on constant values, corresponding to a single point in state space. Thus, we have derived the dynamics in such a way that we can use linearization to analyze the stability of a circular invariant shape solution.

B. System Constraints

As noted above, Eqs. 13-18 imply an 11-dimensional state space. There are a few important constraints, however, which can be used to reduce this state space dimension. First, consider the fact that the Coulomb forces are internal to the system. That is, the force from craft i on craft j is exactly equal and opposite of the force from craft j on craft i . If these electrostatic forces are the only forces acting on or within the system, the center of mass is inertial due to the fact that

$$M\ddot{\vec{R}}_c = \sum \vec{F}_{ext} = 0.$$

As a result, we can always establish initial conditions which will maintain the center of mass at the origin of \mathcal{B} for all time. Doing this yields four constraint equations for the system,

$$0 = m_1\vec{r}_1 + m_2\vec{r}_2 + m_3\vec{r}_3 \quad (19)$$

$$0 = m_1\dot{\vec{r}}_1 + m_2\dot{\vec{r}}_2 + m_3\dot{\vec{r}}_3. \quad (20)$$

This means that at any point in time, if we know the positions and velocities of craft 1 and 2, we can compute the position and velocity of craft 3. This is significant because it allows for a reduction in state space to exclude x_3, \dot{x}_3, y_3 and \dot{y}_3 .

Similarly, we can reduce the state space even further by considering angular momentum. Recalling that when only Coulomb forces are acting within a formation no external forces or torques are present, we can conclude that the formation angular momentum is constant because

$$\dot{\vec{H}} = \vec{L} = 0.$$

Note that due to all craft motion being contained in the $\hat{\mathbf{b}}_1 - \hat{\mathbf{b}}_2$ plane, the angular momentum will always be aligned with the $\hat{\mathbf{b}}_3$ axis. If we denote the initial angular momentum as \vec{H}_0 , it naturally follows that at any time, t ,

$$\vec{H}_0 = \sum_{i=1}^3 \vec{r}_i(t) \times m_i \dot{\vec{r}}_i(t) \quad (21)$$

By expressing \vec{r}_i and $\dot{\vec{r}}_i$ in \mathcal{B} frame components, we can explicitly solve for the angular rate $\dot{\theta}$ at any point in time knowing the initial angular momentum. Contained in Eqs. 19-21, then, are five constraints which can be used to reduce the state space from eleven dimensions to six. The reduced state space can thus be described by the state variables

$$\vec{X}^* = [x_1, \dot{x}_1, x_2, \dot{x}_2, y_2, \dot{y}_2].$$

C. Equation Linearization

To determine stability properties of a circular invariant shape solution, a linearization of Eqs. 13-16 is done about a dynamic equilibrium, \vec{X}_e^* . Using a first order Taylor series approximation, the linearized dynamics are expressed as

$$\dot{\vec{X}}^* = \left[\frac{\partial \dot{\vec{X}}^*}{\partial \vec{X}^*} \right]_{\vec{X}_e^*} \delta \vec{X}^*, \quad (22)$$

where δ is used to signify small perturbations about the equilibrium point. The Jacobian matrix $\left[\frac{\partial \dot{\vec{X}}^*}{\partial \vec{X}^*} \right]$ is evaluated at the equilibrium point, \vec{X}_e^* , and the eigenvalues of this matrix are computed. These eigenvalues yield insight into the stability properties of the invariant shape solution. Should it be found that an invariant shape solution is a saddle point, the eigenvectors of the Jacobian matrix can be used to slightly perturb the initial conditions to examine the behavior of the stable and unstable manifolds. Seeing how these manifolds evolve with time will yield insight into whether or not it is possible to connect two invariant shape solutions using the natural dynamics of the system.

IV. Analysis of a Multiple Invariant Shape Case

Returning again to the example case mentioned above, with $\delta = -0.05$ and $\sigma = 7$, an analysis will be performed to determine whether or not a reconfiguration is possible using connecting manifolds. To determine the charge levels for each craft, c_1 is arbitrarily set at $10\mu\text{C}$, and the other two charges are computed using δ and σ . Recall that two invariant shape solutions were obtained using Eq. 6: $\chi = 3.2508, 4.3283$. In order to examine the stability of these invariant shape solutions, we first need to determine the equilibrium point in state space, which requires initial conditions. The invariant shape solution places no requirement on the actual separation distances; it only requires that the ratio remain constant for all time. Thus, we are free to choose one of the separation distances. In this case, we will choose the distance between craft 1 and 2, denoted as x_{12} . As described above, a circular invariant shape solution confines all craft to the $\hat{\mathbf{b}}_1$ axis, with zero initial velocity. We only need to find the x coordinates for each craft, and the angular rotation of the \mathcal{B} frame that will yield a dynamic equilibrium. Consider arbitrarily placing craft 1 at the origin $(0,0)$ in the \mathcal{B} frame. Note that for this development, we have not yet aligned the origin with the formation center of mass. With craft 1 as the rightmost craft in the formation, craft 2 and 3 would be located at $\vec{r}_2 = -x_{12}\hat{\mathbf{b}}_1$ and $\vec{r}_3 = -(1 + \chi)x_{12}\hat{\mathbf{b}}_1$. Using the positions of the three craft, the center of mass of the formation is computed as

$$\vec{R}_c = -\frac{x_{12}(2 + \chi)}{3}\hat{\mathbf{b}}_1. \quad (23)$$

To enforce the requirement that the origin of \mathcal{B} be aligned with the center of mass, we compute the compliant craft locations using

$$\begin{aligned} \vec{r}_1 &= -\vec{R}_c \\ \vec{r}_2 &= -x_{12}\hat{\mathbf{b}}_1 - \vec{R}_c \\ \vec{r}_3 &= -(1 + \chi)x_{12}\hat{\mathbf{b}}_1 - \vec{R}_c. \end{aligned}$$

Thus, given a desired separation distance, x_{12} , we can immediately determine the equilibrium location of the craft in the \mathcal{B} frame as

$$\vec{r}_1 = \frac{(2 + \chi)x_{12}}{3}\hat{\mathbf{b}}_1 \quad (24)$$

$$\vec{r}_2 = \frac{(\chi - 1)x_{12}}{3}\hat{\mathbf{b}}_1 \quad (25)$$

$$\vec{r}_3 = -\frac{(1 + 2\chi)x_{12}}{3}\hat{\mathbf{b}}_1. \quad (26)$$

To determine the angular rate, $\dot{\theta}$, of the formation we introduce an alternate form of the dynamics derived by Hussein et. al.⁹ The equations of motion for a single craft in an invariant shape formation can be expressed as

$$\ddot{r}_i = -\frac{\mu_i}{r_i^3}\vec{r}_i. \quad (27)$$

Using this form, the angular rate of a circular invariant shape formation can be determined by

$$\dot{\theta} = \sqrt{\frac{\mu_i}{r_i^3}}. \quad (28)$$

For the case where all craft are of mass m , the parameter μ is determined for craft 1 as

$$\mu_1 = -\frac{(2 + \chi)^2 k_c c_1}{9m} \left[c_2 + \frac{c_3}{(1 + \chi)^2} \right]. \quad (29)$$

We can then combine Eqs. 28 and 29 to determine the necessary value of $\dot{\theta}$ to maintain an invariant shape formation. Recall that while $\dot{\theta}$ does not appear explicitly in the state variables, it is necessary in order to determine the initial angular momentum of the system. This angular momentum value will be constant for all time. This introduces an important requirement when establishing initial conditions for the invariant shape solutions. It is mandatory that both invariant shape equilibria be configured such that they have the same angular momenta. If they do not, they are different dynamical systems occupying an entirely different state space. It would be impossible for the invariant shape solutions to connect along manifolds. To ensure this constraint is met, the initial conditions are set for one invariant shape formation. The angular momentum resulting from this configuration is used to determine the initial conditions for the other invariant shape solution. For a circular invariant shape solution, the angular momentum of the formation is

$$\vec{H} = m\dot{\theta}(r_1^2 + r_2^2 + r_3^2) \hat{b}_3. \quad (30)$$

In order to determine the necessary initial conditions, Newton-Raphson iteration can be used on Eq. 30 to find the appropriate value for x_{12} that will yield the required momentum.

Using the above procedure, the equilibrium conditions were determined for the two invariant shape solutions under consideration. The results are summarized in Table 1. Only the six state variables and the angular momenta are presented, to correspond with the reduced state space. The position and velocity of craft 3 can be computed using the center of mass constraint. Likewise, $\dot{\theta}$ can be computed using the angular momentum. Having determined the state-space equilibrium point, we can proceed to a stability analysis using the linearized equations of motion.

χ	x_1 (m)	\dot{x}_1 (m/s)	x_2 (m)	\dot{x}_2 (m/s)	y_2 (m)	\dot{y}_2 (m/s)	H_0 (kg m ² /s)
3.2508	44.616	0	19.125	0	0	0	350.972
4.3283	42.188	0	22.188	0	0	0	350.972

Table 1: Equilibrium conditions for circular invariant shapes

Considering first the case where $\chi = 3.2508$, the Jacobian matrix in Eq. 22 is computed using the parameter values outlined in Table 1. The resulting six eigenvalues of this matrix, presented in Table 2, consist of three complex conjugate pairs with 0 real parts. This implies that small perturbations will cause the craft to oscillate about the equilibrium configuration. Indeed, this behavior is observed when the system is perturbed slightly from the equilibrium, as seen in Fig. 3. Unfortunately, the results of this linearization do not necessarily yield a true picture of the stability of the invariant shape. While it appears to be marginally stable, it is entirely possible that nonlinear terms in the dynamics could cause the perturbation to grow slowly with time, ultimately resulting in instability and large scale divergence from the invariant shape equilibrium. It is clear, however, that this particular configuration is not a saddle point with stable and unstable manifolds. Thus, we cannot exploit a manifold to potentially reconfigure the craft to another equilibrium.

χ	Eigenvalues
3.2508	$\pm 7.687i \times 10^{-4}, \pm 5.467i \times 10^{-4}, \pm 2.966i \times 10^{-4}$
4.3283	$\pm 9.747i \times 10^{-4}, \pm 5.470i \times 10^{-4}, \pm 0.3284$

Table 2: Eigenvalues of Jacobian matrices for the invariant shape solutions

Considering next the case where $\chi = 4.3283$, the Jacobian matrix is re-calculated with the parameter values in Table 1. The six eigenvalues of this matrix, shown in Table 2, consist of two complex conjugate pairs with zero real parts, and two real numbers, one positive and one negative. The appearance of the real number eigenvalues means that this invariant shape solution is a saddle point. Small perturbations will deviate from the equilibrium due to the instability. In this case, unlike before, stable and unstable manifolds do exist. While there is little hope of a reconfiguration using these manifolds, it is still of interest to examine what they look like. The stable manifold was computed by slightly perturbing the system along this manifold and integrating backwards in time. Likewise, the system was also perturbed slightly along the stable manifold and integrated forward in time. The resulting craft trajectories in the orbit plane are presented in Fig. 4. Interestingly, it appears that the two manifolds are almost mirror images of each other, reflected across the \hat{b}_1 axis. The main difference is the speed of the craft. The craft on the

unstable manifold travel much farther in the same amount of time as those on the stable manifold. This results in more oscillations for the craft on the unstable manifold than those on the stable manifold. It is clear, however, that the stable manifold does not originate at another invariant shape solution, and the unstable manifold does not connect to another invariant shape solution.

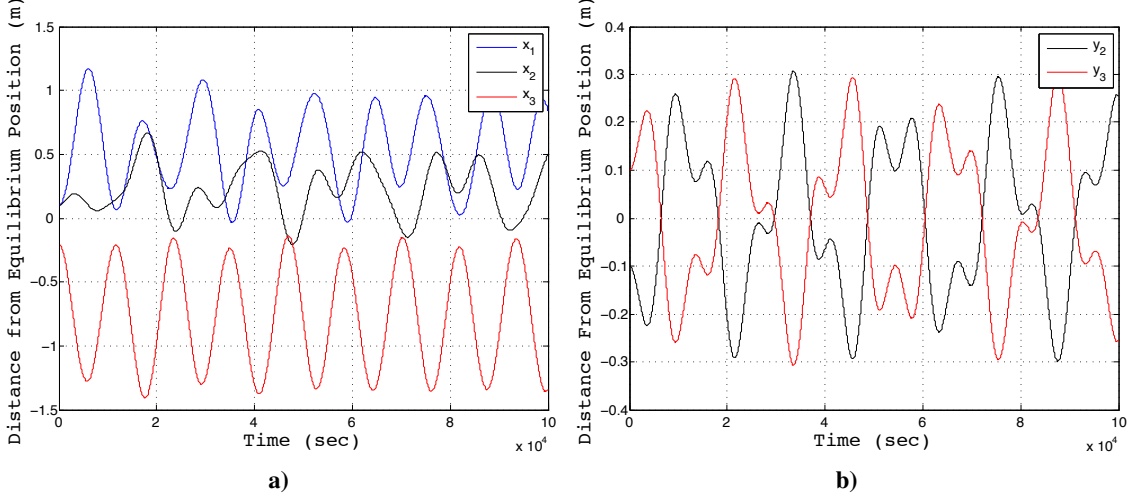


Figure 3: Time evolution of a) x and b) y coordinates after a small perturbation for the $\chi = 3.2508$ circular invariant shape.

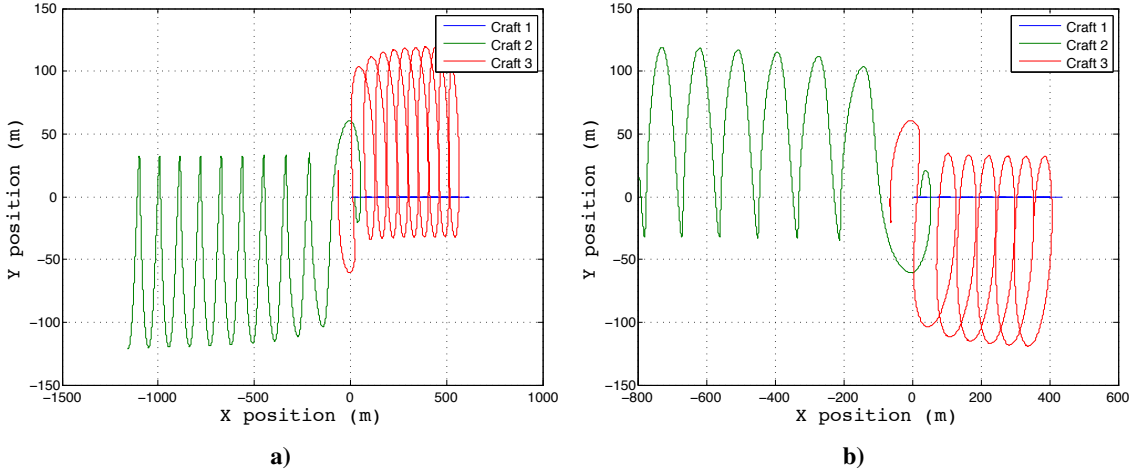


Figure 4: Craft trajectories on a) stable and b) unstable manifolds for the $\chi = 4.3282$ invariant shape.

V. Conclusion

We have examined a case where multiple invariant shape solutions exist for a constant set of charges. Using the rotating \mathcal{B} frame, the circular invariant shape solution is reduced to a single point in a six dimensional state space. The two different equilibria are found to have different stability properties. For the $\chi = 3.2508$ shape, we see marginally stable-like behavior. Small perturbations tend cause oscillations about the equilibrium state. It is unclear, however, whether or not these oscillations will grow into instability if given enough time. On the other hand, the $\chi = 4.3283$ shape is found to be a saddle point equilibrium. The unstable and stable manifolds of this invariant shape appear to originate very far from the center of mass of the formation. While a reconfiguration along a hyperbolic manifold is the goal of the stability analysis, it is not possible for this case. The conclusion we can draw, however, is that different

invariant shape solutions can have different stability properties. This is an important result, as it implies we may find a case where two invariant shape solutions for the same system could both be hyperbolic points with a connecting heteroclinic orbit in state-space. Thus far, the results have been inconclusive regarding such a reconfiguration, but it is hypothesized that such a case does exist. What remains to be done is a large search of the invariant shape solution space in an attempt to find a case with multiple hyperbolic equilibria. The development outlined here has provided the necessary tools for analyzing the stability of invariant shape solutions and will be useful in further studies.

References

- ¹Lawson, P. R. and Dooley, J. A., "Technology Plan for the Terrestrial Planet Finder Interferometer," Tech. Rep. JPL Publication 05-5, NASA Jet Propulsion Lab, June 2005.
- ²Lawson, P. R., Lay, O., Johnston, K. J., and Beichman, C. A., "Terrestrial Planet Finder Interferometer Science Working Group," Tech. Rep. JPL Publication 07-1, NASA Jet Propulsion Lab, March 2007.
- ³King, L. B., Parker, G. G., Deshmukh, S., and Chong, J.-H., "Spacecraft Formation-flying using Inter-vehicle Coulomb Forces," Tech. rep., NASA/NIAC, available online at <http://www.niac.usra.edu> under "Funded Studies.", January 2002.
- ⁴King, L. B., Parker, G. G., Deshmukh, S., and Chong, J.-H., "Study of Interspacecraft Coulomb Forces and Implications for Formation Flying," *AIAA Journal of Propulsion and Power*, Vol. 19, No. 3, 2003, pp. 497–505.
- ⁵Schaub, H., Parker, G. G., and King, L. B., "Challenges and Prospects of Coulomb Spacecraft Formation Control," *Journal of the Astronautical Sciences*, Vol. 52, No. 1-2, 2004, pp. 169–193.
- ⁶Mullen, E. G., Gussenoven, M. S., and Hardy, D. A., "SCATHA Survey of High-Voltage Spacecraft Charging in Sunlight," *Journal of the Geophysical Sciences*, Vol. 91, 1986, pp. 1074–1090.
- ⁷Garrett, H. B., Schwank, D. C., and DeFrost, S. E., "A Statistical Analysis of the Low Energy Geosynchronous Plasma Environment. -I Protons," *Planetary Space Science*, Vol. 29, 1981b, pp. 1045–1060.
- ⁸Garrett, H. B., Schwank, D. C., and DeFrost, S. E., "A Statistical Analysis of the Low Energy Geosynchronous Plasma Environment. -I Electrons," *Planetary Space Science*, Vol. 29, 1981a, pp. 1021–1044.
- ⁹Hussein, I. I. and Schaub, H., "Invariant Shape Solutions of the Spinning Three Craft Coulomb Tether Problem," *Journal of Celestial Mechanics and Dynamical Astronomy*, Vol. 96, No. 2, 2006, pp. 137–157.
- ¹⁰Hussein, I. I. and Schaub, H., "Stability and Control of Relative Equilibria for the Three-Spacecraft Coulomb Tether Problem," *Acta Astronautica*, Vol. 65, No. 5-6, 2009, pp. 738–754.

Analysis of fractal representation of genetic sequences

Amrik Sen

Department of Applied Mathematics
University of Colorado, Boulder
Boulder, CO 80309
Amrik.Sen@Colorado.edu

1 Introduction

One of the problems of interest to biologists is to determine patterns in genetic sequences that have no current explanation [Ber]. In fact experimental observation pertaining to the presence of excess oligonucleotides of some type over the expected number for random sequences can be taken as evidence for this functional significance [Sol] and hence reveal dependencies between bases that form the skeleton of any nucleic acid. Knowledge of these dependencies may be extremely useful while constructing probabilistic bounds for occurrence of a family of motifs in a gene sequence [SL]. In this paper, we employ a variant of the *chaos game representation* algorithm first coined by Barnsley [Bar] to graphically represent a typical random gene sequence. Analysis of this fractal representation enables us to answer questions like: (1) What is the probability of occurrence of a motif with a particular type of trailing subsequence, in a random sequence of fixed length ? (2) What is the conditional probability of finding a particular base given the occurrence of a certain subsequence ? In this paper, we also propose a new fractal characterization of another object of interest to probabilists , labelled Ψ_n , which denotes the number of times a rare motif may occur in a random sequence of given length, n . In spirit, this is equivalent to what is known as the *occupancy problem* in Markov process where mathematicians are concerned about the type of distribution of Ψ_n [Erh]. For biologists, a mathematical characterization of Ψ_n provides information about chances of random occurrence of mutants.

The rest of the paper is organized as follows. Section(2) introduces the chaos game algorithm and the variant employed for representing genetic sequence. In section(2.1) we provide some experimental results (plots) of this algorithm when applied to real gene sequences. In section (2.2), we propose how information may be extracted from these pictorial representations and quantified in terms of probability of occurrences of a certain class of events (subsequences). In section (3.1), we state some relevant definitions and theorems which we use to characterize Ψ_n in section (3.2). Finally, in section (4) we conclude with a brief summary and scope for future work.

2 The *chaos game* (CG) algorithm

In figure(1) we see the structure of a typical double stranded DNA. In most traditional approaches, like the one in [Ken], the occurrence of the nucleotide bases is assumed to be independent, i.e. $Pr(X_i = g|X_{i-1} = c) = Pr(X_i = g) = p_g$ and so on. Here, X_i denotes a random variable at the i^{th} instant of the random sequence of length, n ; X_i may be either one of a, c, g or t . However, this assumption about independence is far from the truth, as we will see shortly.

The chaos game is an algorithm which enables one to produce fractal structures in an iterative manner. Formally, it belongs to the more general class of linear iterative function system. The basic steps of the algorithm are as follows [Jef]:

- Locate three initial points in a plane such that they are not collinear.
- Label one of the vertices with the numerals 1 and 2, the second vertex with the numerals 3 and 4, and the third vertex with the numerals 5 and 6.
- Pick a random initial starting point in the plane.
- Roll a six-sided die, the number rolled on the die picks out the corresponding vertex of the triangle.
- Place a mark halfway between the current point and the indicated vertex.
- Continue the above procedure.

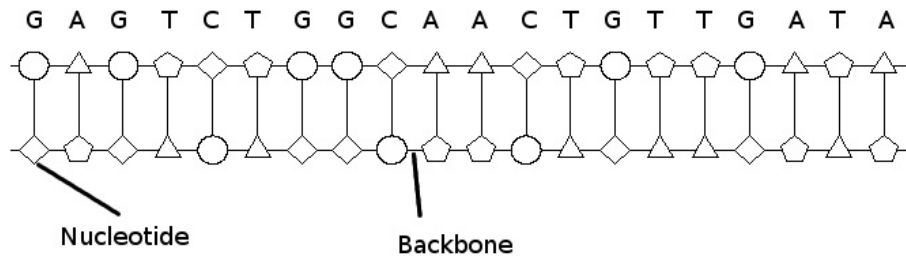


Figure 1: A typical double stranded DNA sequence.

The algorithm produces the well known *Sierpinski triangle* with 3 initial points; however with 5,6 or 7 initial points, the chaos game code produces a pentagon within a pentagon, a hexagon within a hexagon, a heptagon within a heptagon respectively. The case with 4 initial points is quite different though. In fact with 4 initial points, the space (square) gets filled up uniformly and randomly with dots. Thus we see that the patterns produced depend heavily on the initial number of vertices, hence the name *chaos game*.

It may be important to note that the picture produced by the chaos game is known as the *attractor*. A more formal treatment of the chaos game in terms of iterated function systems may be found in [Edg] but has been omitted from discussion in this paper.

In this paper, we employ the chaos game algorithm with some modification to reveal certain patterns in genetic sequences. We refer to figure(2). We start by assigning the tags corresponding to each of the bases in a DNA sequence (i.e. *a*, *c*, *g* and *t*) to the four vertex of a square. We take the center of the square as the starting point of our algorithm and read the genetic sequence character by character, each time placing a dot half way between the current point and the vertex corresponding to the character being read out from the sequence and continue the process until we have read the entire sequence. A few initial instances of this algorithm is shown in figure(2).

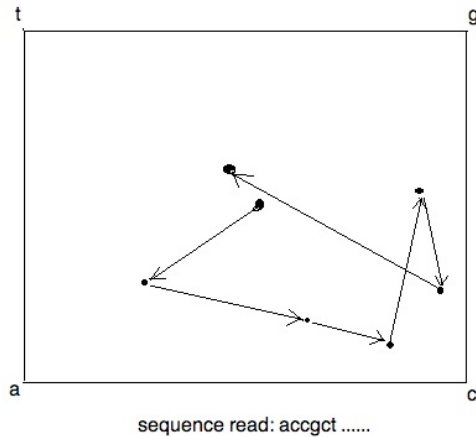


Figure 2: modified chaos game algorithm

2.1 CGR on experimental sequences

If the sequence being read were to be truly random with independent occurrence of the nucleotide base, we would expect absence of any interesting pattern(s). To ascertain our claim, we generated a random sequence comprised of characters from the alphabet, $\mathcal{A} = \{a, c, g, t\}$ by using *Matlab*'s pseudo random generator, `randi()` and obtained the picture shown in figure(3). Clearly, we see that the space within the square was uniformly and randomly filled with dots, thereby implying the lack of any inherent dependencies in the occurrence of the bases.

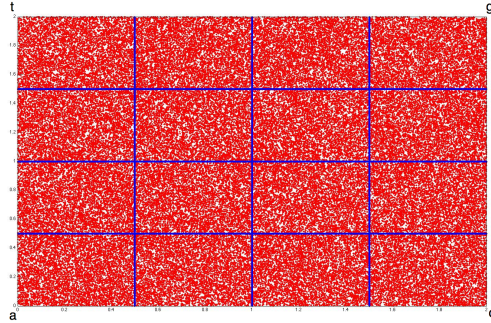


Figure 3: Chaos game representation of a truly random sequence.

Now, we use the gene database from the National Center for Biotechnology Information to test the CGR code on some real gene sequences. The results are shown in the figures in this section. A few interesting features of

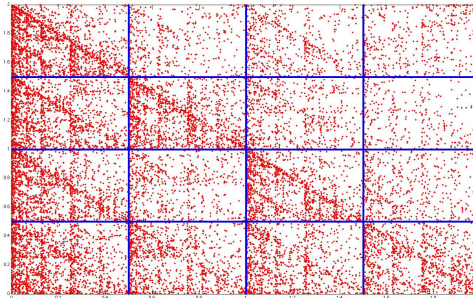


Figure 4: CGR of mitochondrial RNA sequence from Atlantic Hagfish.

the above representation produced by the CG algorithm are noted as below.

- neighboring points on the CGR are not close by in the actual sequence.
- subsequences ending with a common *trailing sequence* are mapped to their respective sub-quadrant as shown in figure(6).
- evidence of fractal nature of the plots imply presence of dependence in occurrence of the bases.
- figure(6) reveals regions of sparsity, for eg. the *cg* sub-quadrant; this implies that the likelihood of a *g* occurring after an occurrence of *c* is less likely in comparative terms. Similar arguments may be made for other subsequences.
- The features/patterns observed in the human DNA have also been found in the DNA sequences of vertebrates and those of certain viruses like HIV.

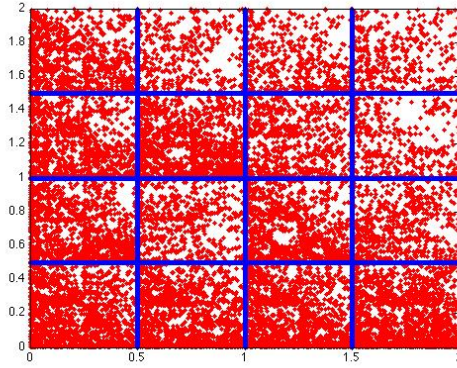


Figure 5: CGR of mitochondrial RNA sequence from Homo Sapiens Neanderthalensis.

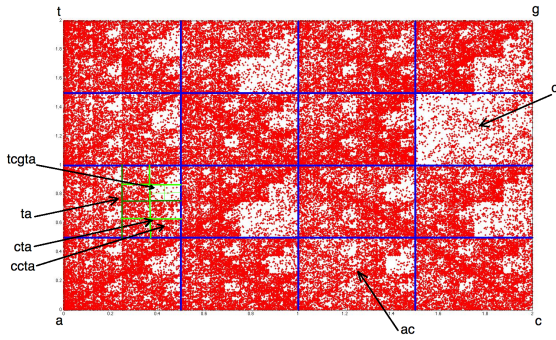


Figure 6: CGR of human DNA extracted from clone cell.

2.2 Probabilistic assertions about the occurrence of motifs

While [Jef] did report similar results, he relied on visual characterization of the patterns found in CGRs. In fact it was noted by [Jef] that a more mathematical and measure theoretic approach would be an extremely useful direction of future research. In the light of the above statement by [Jef], we make a novel attempt in that direction. It may be useful to note that the following information may be quantified using the CGR,

- $Pr(\text{occurrence of a subsequence}) = \frac{\text{no. of dots in the corresponding sub-quadrant}}{\text{total no. of dots in the plane}}$
- In a Markov chain model of the genetic sequence, i.e. if $\{X_i\}_{i \geq 0}$ is a Markov process with finite state space $\{a, c, g, t\}$, the *joint distribution* of the chain (as an example) is computed as follows [Fu]:

$$Pr(X_n = g, X_{n-1} = c, \dots, X_1 = g, X_0 = t) = Pr(X_n = g | X_{n-1} = c) \dots Pr(X_1 = g | X_0 = t) Pr(X_0 = t)$$

Clearly, the terms in the right hand side can be easily derived from the CGR of the sequence, for eg. $Pr(X_n = g | X_{n-1} = c) = \frac{\text{no. of dots in the cg sub-quadrant}}{\text{no. of dots in the c sub-quadrant}}$. The above is with respect to a first order Markov model. For higher order Markov models, it should be clear that the above arguments can be extended by looking at subsequence lengths of 3 or more and their respective sub-quadrants.

- One interesting aspect of the CGR pointed out earlier is the fact that points close in the sense of the Euclidean norm in the CGR plane may be far apart in the sequence space. An alternative measure in the CGR space may be to use the *Hausdorff* measure. In this regard, it may be useful to point out the strong similarities between the CGR of the RNA sequence from the Atlantic Hagfish and the *Sierpinski gasket*; and therefore we can estimate the Hausdorff dimension of the CGR of the RNA from the Hagfish to be about $\frac{\log 3}{\log 2} = 1.58$ which is numerically verified by using the box-counting algorithm from problem set 10. [Jia] also provide tight bounds on the estimates of the Hausdorff measure of such fractal sets.

3 Fractal characterization of Ψ_n

Recall that Ψ_n denotes the number of times a particular type of rare motif may occur in a random sequence of length, n . The cumulative distribution of Ψ_n defined here as $Pr(\sum_{m \geq 0} \Psi_n^{(m)} \leq c)$ is of immense interest to probabilists; however the nature of the rare events does not enable one to compute this explicitly and hence many like [Erh] have proposed approximate distributions with error bounds. Here, we propose a novel fractal characterization of Ψ_n in terms of a set whose elements are described based on $\sum_{m \geq 0} \Psi_n^{(m)} \leq c$ in some limiting sense stated shortly below. Such results have recently been of much interest in the context of random walks.

3.1 Fractal geometry in a probability space, $(\Omega, \mathcal{F}, \mu)[DT]$

Definition: A subset $A \subset \Omega$ is said to be a *fractal* with respect to a measure (probability measure) μ over Ω if $\mu(A) = 0$ and $dim_\mu(A) = Dim_\mu(A) = \text{constant}$. Here, $dim(\cdot)$ is the Hausdorff dimension and $Dim(\cdot)$ is the packing dimension as described in [DT].

Clearly, our knowledge about the *Cantor* set being a fractal satisfies this definition because the lebesgue measure, $\lambda(A) = 0$ and $dim_\lambda(A) = Dim_\lambda(A) = \frac{\log 2}{\log 3}$. It may also be useful to recall the equivalence of the lebesgue measure over the unit real line and the probability measure over Ω [Qu].

In the same spirit, we state the following theorem.

Theorem [Bill][DT]: For $\omega \in \Omega$, let $u_n(\omega) = \{\omega_0 : X_i(\omega_0) = X_i(\omega); i = 1, 2, \dots, n\}$ and let $A = \{\omega : X_k(\omega) = a_k; k = 1, \dots, n\} \subset \Omega$ s.t. $\mu(A) = 0$ for some n , then $\exists \nu(A) = p(a_1, \dots, a_n)$ s.t. $\nu(u_n(\omega)) \leq \mu(u_n(\omega))^c \forall \omega \in \Omega$ and $c > 0$ constant.
Also, for some $M_0 \subset \{\omega : \lim_{n \rightarrow \infty} \frac{\log \nu(u_n(\omega))}{\log \mu(u_n(\omega))} = c\}$, if $\nu(M_0) > 0$; then M_0 is a *fractal* and $dim_\mu(M_0) = Dim_\mu(M_0) = c$.

3.2 Characterization of Ψ_n

Let Z_i denote a finite length query subsequence (or motif) and S_0 be the *rarely* occurring target motif of the same length. $\Psi_n := \sum_{i \geq 1} [Z_i \in S_0] \equiv \sum_{i \geq 1} I_i$; where I_i has success probability p_{S_0} . Here, $[.]$ refers to the *indicator* function.

The *strong law of large numbers* implies $\frac{1}{m} \sum_{m \geq 1} \Psi_n^{(m)} \rightarrow np_{S_0}$ as $m \rightarrow \infty$, n fixed. Next we define, $A := \{\omega : \frac{1}{m} \sum_{m \geq 1} \Psi_n^{(m)}(\omega) \not\rightarrow np_{S_0}\}$ and $B_c := \{\omega : \lim_{m \rightarrow \infty} \frac{1}{m} \sum_{m \geq 1} \Psi_n^{(m)}(\omega) \leq c \in [0, np_{S_0})\}$. Clearly, $B_c \subset A$; $Pr(B_c) = 0$. Hence, using the theorem above we have a new measure ν s.t. $\nu(B_c) > 0$, $dim_\mu(B_c) = f(c)$ and B_c is a *fractal*.

It must be pointed out here that while the theorem above is only an existence statement of the new measure ν , no general construction of such a measure has been reported in the literature; however some example specific constructions have been proposed for ν by [Bill].

4 Conclusion

In this paper, we have presented a fractal representation of genetic sequence via the modified CGR algorithm and have thereby shown the inherent dependencies amongst the nucleotide bases. We have made an attempt to extend the visual features of the CGR to more probabilistic and measure theoretic assertions about the same. We have also proposed a novel fractal based characterization of Ψ_n which was defined as the number of times a rare motif may be seen in a random gene sequence. Future work may include extending this characterization and establishing a stronger mathematical relation between the fractal characterization and the recent works on approximating probability distribution for Ψ_n . A comparative study of the CGR based representation of genes and other graphical representations of genes may also be very interesting.

References

- [Ber] Berthelsen, Cheryl L et. al., *Global fractal dimension of human DNA sequences treated as pseudorandom walks*, Physical Review A, (Vol. 45, Number 12), 1992.
- [Sol] Solov'yev, Victor V., *Fractal graphical representation and analysis of DNA and protein sequences*, BioSystems, 30 (1993) 137-160, ©Elsevier Scientific Publishers Ireland Ltd.
- [SL] Sen, A. and Lladser, M., *On some Chen-Stein like bounds for probability of finding a family of motifs in a random genetic sequence*, (manuscript in preparation).
- [Bar] Barnsley, M., *Fractals Everywhere*, 1988, ©Morgan Kauffmann.
- [Erh] Erhardsson, T., *Compound Poisson approximation for Markov chains using Stein's method*, The Ann. of Prob., 1999, Vol 27, No 1.
- [Ken] Kennedy, R., *Calculating RNA motif probabilities and recognizing patterns in sequence data*, Honor's thesis, 2009, Univ. of Colorado, Boulder.
- [Jef] Jeffrey, Joel H., *Chaos game representation of gene structure*, Nucleic Acid Research, Vol. 18, No. 8, p: 2163-2170, ©1990 Oxford University Press.
- [Edg] Edgar, G., *Measure, Topology and Fractal Geometry*, 2nd edition, 2007, ©Springer.
- [Fu] Fu, J. et al., *Distribution Theory of Runs and Patterns and Its Applications*, 2003, ©World Scientific Press.
- [Jia] Jia, B., *Bounds of Hausdorff measure of the Sierpinski gasket*, J. Math. Anal. Appl., 330 (2007), 1016-1024.
- [DT] Dai, C. and Taylor, S.J., *Defining fractals in a probability space*, Illinois J. Math., 1994, Vol 38, No. 3.
- [Qu] Qu, C.Q. et al., *Hausdorff measure of homogeneous Cantor set*, Acta Mathematica Sinica, 2001, Vol 17, No. 1, 15-20.
- [Bill] Billingsley, P. *Hausdorff dimension in probability theory II*, Illinois J. Math., 1961, Vol 5, 291-298.

Spatiotemporal Chaos: Effect of Spatial Smoothing on Bifurcations in a Discrete-Time Chaotic Map

Chaotic Dynamics

Per Sebastian Skardal

(Dated: Due April 30)

I. INTRODUCTION

Many problems that arise in either physics, chemistry, or biology are spatiotemporal in nature. That is they evolve according to both spatial and dynamic effects. In general spatiotemporal dynamics problems are difficult to solve and there is little general theory about the behavior of solutions. This paper will explore the spatiotemporal dynamics of a system inspired by previous and current research with my advisor Professor Juan G. Restrepo. The system will be a set of integrodifference equations that is applicable to cardiac dynamics. The system is discrete in time and continuous in space.

Because the system is discrete in time several quantities are analytically solvable. This will both ease some of the reliance on numerical simulation and yield some analytical results. The model is biologically relevant in a certain parameter range that does not induce chaotic behavior, but I will explore more extreme parameter choices that do. The goals of this paper are mathematical rather than biological. I will not connect results back to biology, but rather explore spatiotemporal dynamics in a more complicated regime for a more academic purpose.

A. Other work in spatiotemporal dynamics

The two most generic ways to add spatial dependence to a dynamical system utilize either spatial derivatives or spatial integrals. Thus, coupling these with either differential or difference equations (in time) can lead to many possibilities in modelling spatiotemporal behavior. Coupling spatial derivatives with time derivatives yields systems of partial differential equations, which are for instance applicable to some reaction-diffusion systems¹ and fluid flow problems. Coupling spatial integrals with time derivatives yields systems of integro-differential equations, which can model populations of coupled oscillators²⁻⁴. Both spatial derivatives and integrals can be coupled with discrete-time maps as well, which can model cardiac behavior⁵.

The case in which spatial integrals are combined with discrete-time maps remain a less popular choice to model phenomena. However, some interesting examples exist. In 1986 Kot and Schaffer⁶ studied a handful of integrodifference equations used to model the dispersal of organisms in ecology. As is usually the case in biological models, several simplifying assumptions were made, for instance the homogeneity of the environment. The main goal of the paper, however, was to spark interest in specifically integro-difference equations.

In 1998 Venkataramani and Ott⁷ used integrodifference equations to explore temporal period doubling in a spatiotemporal system. Specifically the application was in the pattern formation in vibrated sand. Their system consisted of a discrete-time map that was then analyzed in the Fourier domain.

B. Inspiration: cardiac dynamics

The system in this paper is one that models the behavior of *cardiac alternans*. In heart tissue the two most important quantities are the trans-membrane voltage V and the intracellular calcium concentration $[Ca^{2+}]_i$. A normal, healthy heart displays perfectly periodic signals (with periodicity one) for both the voltage and calcium concentration. That is, if T is the period of stimulation, then $V(t) = V(t + T)$ and $[Ca^{2+}]_i(t) = [Ca^{2+}]_i(t + T)$ for any time t . If the voltage and calcium signals lose this periodicity, however, several kinds of cardiac arrhythmia can occur.

Cardiac alternans is defined as an alternating pattern of the voltage and calcium signals in which the signals become period two. The easiest way to visualize this transition is through the action potential duration (APD) and peak calcium (\widehat{Ca}) quantities. The action potential duration at a beat n (APD_n) is defined as the time that it takes a cell to repolarize after a stimulus at that beat and the peak calcium at a beat n (\widehat{Ca}_n) is defined as the local maximum of the calcium signal during that beat. A heuristic of these measurements is given in figure 1(a).

In terms of these measurements, cardiac alternans becomes an alternating large-small-large-small pattern of the discrete-time quantities APD_n and \widehat{Ca}_n . Healthy cardiac function displays period *one* behavior and cardiac alternans

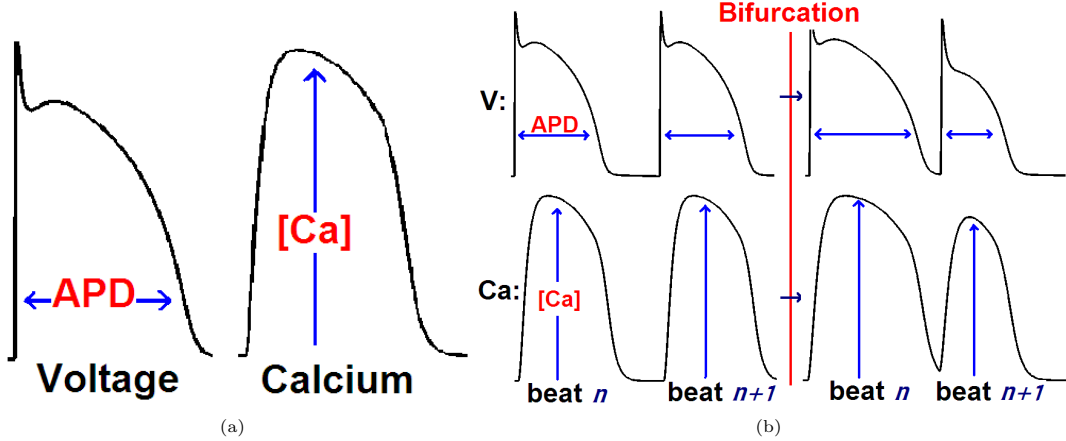


FIG. 1: The measurements of APD_n and \widehat{Ca}_n (a). Period-doubling bifurcation: the transition from normal cardiac behavior to alternans(b).

displays period *two* behavior, which suggests that this transition is a period-doubling bifurcation. In fact, in 1984 Guevara et. al.⁸ showed that this is true. A heuristic of this period-doubling bifurcation is shown in figure 1(b).

Cardiac alternans can appear in a two ways. First, the alternans in voltage and calcium can be *positively* coupled. This means that a large (small) action potential corresponds to a large (small) calcium signal at the same beat. In other words, APD_n will be large (small) when \widehat{Ca}_n is large (small). Voltage and calcium can also be *negatively* coupled. This means that a large (small) action potential corresponds to small (large) calcium signal at the same beat. In other words, APD_n will be large (small) when \widehat{Ca}_n is small (large).

Furthermore, cardiac alternans can be induced by either voltage or calcium. Because of the way that voltage affects the calcium concentration, voltage-induced alternans are always positively coupled. However, when alternans are calcium-induced, the coupling can be either positive or negative. This complication follows from the complexity of the different calcium currents flowing in and out of the cell.

The effects of voltage-induced alternans has been the topic of several papers (for example by Karma^{5,9}) and are relatively well understood. However, the effect of calcium-induced alternans remains for the most part unexplored and poorly understood. This was the inspiration of our model of cardiac behavior. That is, the goal is to induce calcium alternans in a system where calcium and voltage are coupled together on some spatial domain.

C. The governing equations

Keeping in mind that we wish to model some sort of period-doubling behavior, we introduce the following discrete-time map

$$c_{n+1} = -rc_n + c_n^3, \quad \text{for } r \geq 0. \quad (1)$$

Not unlike the logistic map, this map has both cascades of period-doubling bifurcations as well as banded chaotic regions in parameter space. The reason we have chosen this map is because of the symmetry of periodic solutions around $c = 0$, which will make some analytical solutions attainable. Later analysis of this map will show a (stable) period-one solution for $0 \leq r \leq 1$, period-two solutions for $1 \leq r \leq 2$, and so on.

The fact that periodic solutions (and chaotic sequences) will be in the range $[-2, 2]$ may raise some issues in so far as the modelling of actual calcium levels in the heart. However in the regime of period-one and -two solutions, the map above is conjugate to the actual values of \widehat{Ca} both for a healthy heart and one with alternans. Formally this means that by some (continuous) change of coordinates we can map steady-state solutions c^* of equation (1) to more realistic values for \widehat{Ca} seen experimentally.

However, to fully explore the effects of alternans, we must couple calcium to voltage, even if the alternans are not voltage driven. First, we will introduce a few coupling parameters that describe the interaction between calcium and voltage alternans. Second, we will introduce a spatial integral kernel in the voltage equation to model the diffusion of

voltage across the domain. The equations are the following:

$$\begin{aligned} c_{n+1}(x) &= -rc_n(x) + c_n^3(x) + \alpha a_n(x), \\ a_{n+1}(x) &= \int G(x, x') [\beta a_n(x') + \gamma c_{n+1}(x')] dx'. \end{aligned} \quad (2)$$

Here $c_n(x)$ and $a_n(x)$ represent the value of the calcium and voltage alternans, respectively, at a point x in the spatial domain, r is our “bifurcation” parameter and is a measure of how strong the calcium alternans are, α , β , and γ are coupling parameters, and $G(x, x')$ is the diffusive integral kernel. α represents voltage-to-calcium coupling, which is always positive, so $\alpha < 0$, γ represents calcium-to-voltage coupling, which can be positive or negative, so γ can have either sign, and β represents the perpetuation of voltage alternans, so $\beta < 0$. All three coupling parameters are taken to be less than one in magnitude to prevent divergence of solutions. In our computations we choose $G(x, x') = G(x, x', \sigma^2)$ to be Gaussian with standard deviation σ^2 ($G(x, x', \sigma^2) = \frac{1}{\sqrt{2\pi\sigma^2}} e^{-\frac{(x-x')^2}{2\sigma^2}}$). In our simulations we will take $\sigma = 1$. The spatial domain will be one dimensional.

There are three main topics of interest as to the solutions to this map. First, we will explore how steady-state solutions to this system *coarsen*. By coarsen, we mean how the domain separates into different *in-phase* regions. An example of this is the plot in figure 2(a), which depicts period-two steady-state solutions for different r values given random initial conditions (red is small r , blue is large r). Second, we will explore the effects the coupling parameters have on bifurcations. Since the bifurcation is driven by the map in equation (1), we expect the bifurcations of the system (2) to be similar. Finally, we will explore the competition between the bifurcation parameter r and the diffusion kernel G . A large r value will tend to polarize solutions and the integral kernel will be a smoothing operator.

II. PRE-ANALYSIS

A. Classifying coarsening

How we choose to characterize the coarsening of calcium alternans is essential to the problem. If we start from random initial conditions, the domain will separate into different in-phase regions each time, depending on local averages of the initial data. Thus, no unique solution can be found for random initial conditions. Instead, we will calculate the values of steady-state periodic solutions of $c(x)$ for x near the boundaries of different in-phase regions and in the middle of such in-phase regions that are “far-away” from such boundaries. An analytical expression for $c(x)$ is difficult to obtain and depends on the kernel $G(x, x')$, so these two quantities will be the basis of our analysis of coarsening.

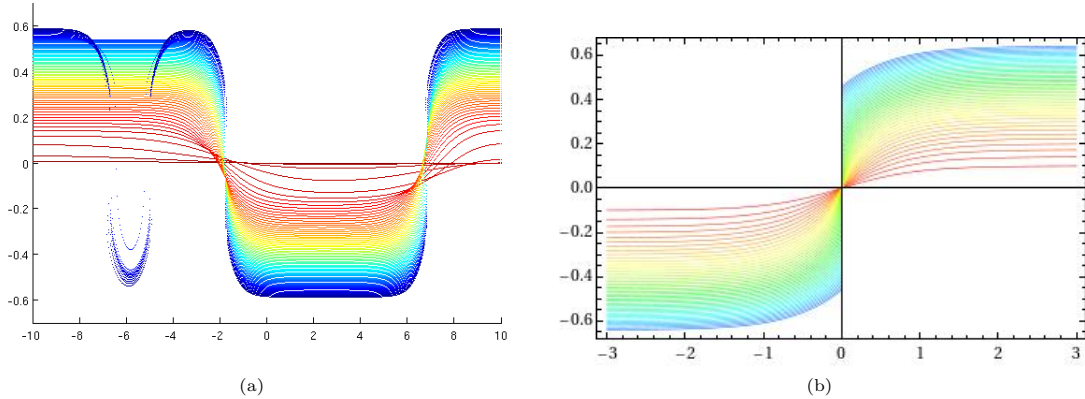


FIG. 2: Solutions to the system in equation (3). Coarsening of in-phase regions given random initial conditions (a), and analytical solutions for the step-initial conditions in equation (4) (b). r values range from 0.75 (red) to 1.1 (blue). The horizontal axis is space (x) and the vertical axis is the value $c(x)$.

Calculating these two quantities for random initial conditions is also problematic. We could run simulations and use numerical results, but this raises other issues. Instead of starting with random initial conditions, we can start with

so-called “step” initial conditions defined as

$$c_0(x) = \epsilon \cdot \text{sgn}(x),$$

for some non-zero constant k , which will give exactly two different in-phase regions with a boundary at $x = 0$. Thus, we can liken the quantities $\lim_{x \rightarrow 0^\pm} c(x)$ and $\lim_{x \rightarrow \pm\infty} c(x)$ to the values of $c(x)$ for x near boundaries and far away from boundaries, respectively. The analytical period-two steady-state solution for $c(x)$ with step initial conditions is plotted in figure 2(b) for different r (red is small r , blue is large r). I.e. we will use the time series of $\lim_{x \rightarrow 0^\pm} c(x)$ and $\lim_{x \rightarrow \pm\infty} c(x)$ to characterize the dynamics of the system.

The standard deviation or width of the kernel $G(x, x')$ won’t affect either of the values $\lim_{x \rightarrow 0^\pm} c(x)$ or $\lim_{x \rightarrow \pm\infty} c(x)$, but rather the shape of $c(x)$ in between. In the step initial condition case, the width of G (in our case σ^2) will affect how fast $c(x)$ converges to $\lim_{x \rightarrow \pm\infty} c(x)$ as x moves away from zero. It’s straight-forward to see that if G is wide the convergence will be slower and if G is narrow then it will be faster. In the case of random initial conditions the width of G will also define a minimum width of a coarsened region. Because of the smoothing operator no steady-state coarsened region with width less than the width of G can exist.

In order to predict behavior for higher-order bifurcation and chaos, we will first solve the system for r in the period-two regime. We can calculate all the quantities of interest analytically because of the map’s symmetry.

B. Analysis of the uncoupled calcium map

Since all bifurcations and chaos will be driven by the map given in equation (1) a thorough analysis of this map is useful. The bifurcation diagram of this map is given in figure 3, and it clearly shows period-doubling bifurcations as well as banded chaos and islands of stability.

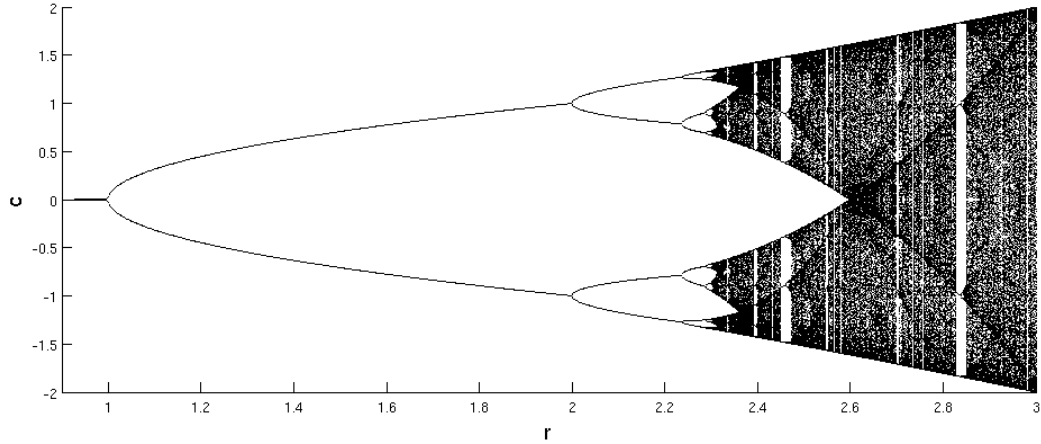


FIG. 3: Bifurcation diagram for the map in equation (1).

Up to a certain point, we can compute the (stable) periodic solutions c and the bifurcation values r_c in the following way. For period p solutions, compute the intersections of the p^{th} -return map $c_{n+1} = f^p(c_n; r)$ with $c_{n+1} = c_n$ (as a function of r), which gives period- p solutions (both stable and unstable). Then we can compute (over successive parameter ranges of r) which of these solutions have a derivative less than one in magnitude. Since this map is clearly period-doubling, we look for period-one solutions, then period-two, then period-four, and so on. The results of such analysis for periods one, two and four are given in the following table:

period of stable solutions	Steady-state $c(r)$	Range of r
one	$c(r) = 0$	$r \in [0, 1]$
two	$c(r) = \pm\sqrt{r-1}$	$r \in [1, 2]$
four	$c(r) = \pm\frac{\sqrt{r \pm \sqrt{r^2-4}}}{\sqrt{2}}$	$r \in [2, \sqrt{5}]$
eight

Thus, period-doubling bifurcations happen at $r_c = 1, 2, \sqrt{5}, \dots$. Just after $r = \sqrt{5}$ stable solutions become period-eight, but become difficult to obtain analytically. As with most maps that display period-doubling behavior, there is an infinite number of period-doubling cascades and for some r sequences become chaotic. Investigation of the connection between period-doubling cascades and chaos in such maps is an active area of research studied by many such as Sander and Yorke¹⁰.

C. Period-two steady-state solutions

Since the bifurcation is driven by a symmetric equation, we can assume that if $c^*(x)$ is a periodic steady-state solution, then so is $-c^*(x)$. To ease notation, define

$$c_{\pm\infty} = \lim_{x \rightarrow \pm\infty} c(x), \quad c_{0\pm} = \lim_{x \rightarrow 0^\pm} c(x),$$

to be the quantities discussed above. Furthermore, let $r_{c,\infty}$ and $r_{c,0}$ be the critical r values for which bifurcation happens as $x \rightarrow \pm\infty$ and $x \rightarrow 0^\pm$. We will consider solution for the cases $\beta = 0$ and $-1 < \beta < 0$. In general the period-two case can be solved for both, but at higher order periods we will need to set $\beta = 0$ to solve analytically.

1. $\beta = 0$:

In this case, plugging in for $a_n(x)$ gives

$$c_{n+1}(x) = -rc_n(x) + c_n^3(x) + \eta \int G(x, x', \sigma^2) c(x') dx',$$

where $\eta = \alpha\gamma$. In order to compute $c_{\pm\infty}$ and $c_{0\pm}$, note that $\lim_{x \rightarrow \pm\infty} \int G(x, x', \sigma^2) c(x') dx' = c_{\pm\infty}$ and $\lim_{x \rightarrow 0^\pm} \int G(x, x', \sigma^2) c(x') dx' = 0$. (This is easy to see from figure 2(b).) Also, since solutions are period-two and symmetric about zero, we have that $c_{n+1}(x) = -c_n(x)$. Therefore,

$$\begin{aligned} -c_{\pm\infty} &= -rc_{\pm\infty} + c_{\pm\infty}^3 + \eta c_{\pm\infty}, & -c_{0\pm} &= -rc_{0\pm} + c_{0\pm}^3, \\ \Rightarrow c_{\pm\infty} &= \pm\sqrt{1-r-\eta}, & c_{0\pm} &= \sqrt{r-1}. \end{aligned}$$

Thus, we have that

$$c_{\pm\infty} = \begin{cases} 0 & \text{if } r \leq 1 + \eta \\ \pm\sqrt{r-1-\eta} & \text{if } r \geq 1 + \eta \end{cases}, \quad \text{and} \quad c_{0\pm} = \begin{cases} 0 & \text{if } r \leq 1 \\ \pm\sqrt{r-1} & \text{if } r \geq 1 \end{cases},$$

and the critical bifurcation points are

$$r_{c,\infty} = 1 + \eta, \quad \text{and} \quad r_{c,0} = 1.$$

2. $-1 < \beta < 0$:

When $\beta \neq 0$ the voltage term doesn't die out immediately. Nonetheless, repeatedly plugging in for $a_{n-i}(x)$ gives

$$c_{n+1}(x) = -rc_n(x) + c_n^3(x) + \eta \sum_{k=1}^{\infty} \underbrace{\beta^{k-1} \int \dots \int}_{k} \left[\prod_{j=1}^k G(x^{(j-1)}, x^{(j)}, \sigma^2) \right] c_{n-k+1}(x^{(k)}) dx^{(k)} \dots dx^{(1)}.$$

Using Fubini's theorem¹¹ to interchange the order of integration and some Gaussian distribution tricks, this gives

$$c_{n+1}(x) = -rc_n(x) + c_n^3(x) + \eta \int \tilde{G}(x, x', \sigma^2) c_{n-k+1}(x') dx',$$

where

$$\tilde{G}(x, x', \sigma^2) = \sum_{k=1}^{\infty} |\beta|^{k-1} G(x, x', k\sigma^2).$$

So as not to break up the flow of this paper I've included the computation of $\tilde{G}(x, x', \sigma^2)$ in the appendix.

Again we use the symmetry of period-two solutions and $\lim_{x \rightarrow \pm\infty} \int G(x, x', \sigma^2) c(x') dx' = c_{\pm\infty}$ and $\lim_{x \rightarrow 0^\pm} \int G(x, x', \sigma^2) c(x') dx' = 0$ to get that

$$\begin{aligned} -c_{\pm\infty} &= -rc_{\pm\infty} + c_{\pm\infty}^3 + \frac{\eta}{1+\beta} c_{\pm\infty}, & -c_{0^\pm} &= -rc_{0^\pm} + c_{0^\pm}^3, \\ c_{\pm\infty} &= \pm \sqrt{1 - r - \frac{\eta}{1+\beta}}, & c_{0^\pm} &= \sqrt{r-1}. \end{aligned}$$

Thus, we have that

$$c_{\pm\infty} = \begin{cases} 0 & \text{if } r \leq 1 + \eta \\ \pm \sqrt{r-1 - \frac{\eta}{1+\beta}} & \text{if } r \geq 1 + \eta \end{cases}, \quad \text{and} \quad c_{0^\pm} = \begin{cases} 0 & \text{if } r \leq 1 \\ \pm \sqrt{r-1} & \text{if } r \geq 1 \end{cases},$$

and the critical bifurcation points are

$$r_{c,\infty} = 1 + \frac{\eta}{1+\beta}, \quad \text{and} \quad r_{c,0} = 1.$$

Note that the solutions for $-1 < \beta < 0$ extend to the $\beta = 0$ case.

In just the period-two case we already see the presence of the competition between r and the smoothing integral. The function $c(x)$ becomes discontinuous for $r > r_{c,0}$. Thus, depending on the sign of η we get different behaviors. If $\eta < 0$ then we have three ranges $(0, r_{c,\infty})$, $(r_{c,\infty}, r_{c,0})$, and $(r_{c,0}, \dots)$ where steady-state $c(x)$ is identically zero, bifurcation has happened *away* from boundaries but $c(x)$ is still continuous, and bifurcation has occurred at $x = 0$ and $c(x)$ is discontinuous at the boundaries, respectively. If $\eta > 0$, however then three ranges are $(0, r_{c,0})$, $(r_{c,0}, r_{c,\infty})$, and $(r_{c,\infty}, \dots)$ where steady-state $c(x)$ is identically zero, bifurcation has happened *at* from boundaries (thus $c(x)$ is discontinuous at the boundaries) but $c_{\pm\infty} = 0$, and $c(x)$ is discontinuous and nowhere zero, respectively.

This difference in bifurcation near and away from boundaries raises several questions. Does this difference in bifurcations transcend to high-order periodic solutions? What do the bifurcation diagrams for $c_{\pm\infty}$ and c_{0^\pm} look like (perhaps they are just shifted left or right by $\frac{\eta}{1+\beta}$)? Finally, is it possible for *just one* of either $c_{\pm\infty}$ or c_{0^\pm} to be chaotic?

III. HIGHER-ORDER PERIODICITY AND CHAOS

A. Analytic results

Despite higher-order periodic solutions being not applicable to cardiac behavior, it's still interesting to explore what happens for larger r values (similar to the Lorenz system). For analytic analysis we will consider $\beta = 0$. Again we use

$$c_{n+1}(x) = -rc_n(x) + c_n^3(x) + \eta \int G(x, x', \sigma^2) c(x') dx',$$

and the fact that $\lim_{x \rightarrow \pm\infty} \int G(x, x', \sigma^2) c(x') dx' = c_{\pm\infty}$. For $c_{\pm\infty}$ we get the map

$$c_{n+1, \pm\infty} = -\rho c_{n, \pm\infty} + c_{n, \pm\infty},$$

where $\rho = r - \eta$. Thus, the bifurcation diagram for $c_{\pm\infty}$ will be the same as for the map in equation (1) (see figure 3), but shifted by η . In terms of r , we summarize the low-order periodic solutions as follows:

period of stable solutions	Steady-state $c_{\pm\infty}(r)$	Range of r
one	$c_{\pm\infty}(r) = 0$	$r \in [\eta, 1 + \eta]$
two	$c_{\pm\infty}(r) = \pm \sqrt{r - \eta - 1}$	$r \in [1 + \eta, 2 + \eta]$
four	$c_{\pm\infty}(r) = \pm \frac{\sqrt{r-\eta} \pm \sqrt{(r-\eta)^2 - 4}}{\sqrt{2}}$	$r \in [2 + \eta, \sqrt{5} + \eta]$
eight

which matches up with the period-two analysis above.

The same sort of analysis does not work for $c_{0\pm}$. Solutions are still periodic around $c_{0\pm} = 0$, but since the periodicity is greater than 2, then in general $c_{n+1,0\pm} \neq -c_{n,0\pm}$. Instead, the map becomes

$$c_{n+1,0\pm} = -rc_{n,0\pm} + c_{n,0\pm}^3 + \eta\xi_n, \quad \text{where} \quad \xi_n = \int G(0, x', \sigma^2) c_n(x') dx'.$$

If periodicity is greater than 2 the behavior to the left of the origin and to the right of the origin are not necessarily opposite and ξ_n does not vanish. However, if solutions are period- p , then the average of ξ_n will vanish over a whole p -cycle. Thus, an argument can be made that $c_{0\pm}$ will probably behave in a similar way as c in the uncoupled map (equation (1)). It's likely, however, to display some noise.

B. Bifurcation Diagrams

Next we simulate the system numerically and show the bifurcation diagrams for $c_{\pm\infty}$ and $c_{0\pm}$. Figure 4 gives the bifurcation diagrams using $\eta = -0.2$ ($\alpha = -\sqrt{0.2}$, $\gamma = \sqrt{0.2}$) and figure 5 gives the bifurcation diagrams using $\eta = 0.2$ ($\alpha = -\sqrt{0.2}$, $\gamma = -\sqrt{0.2}$). (Note that switching both signs of α and γ yields the same results, since η is their product.)

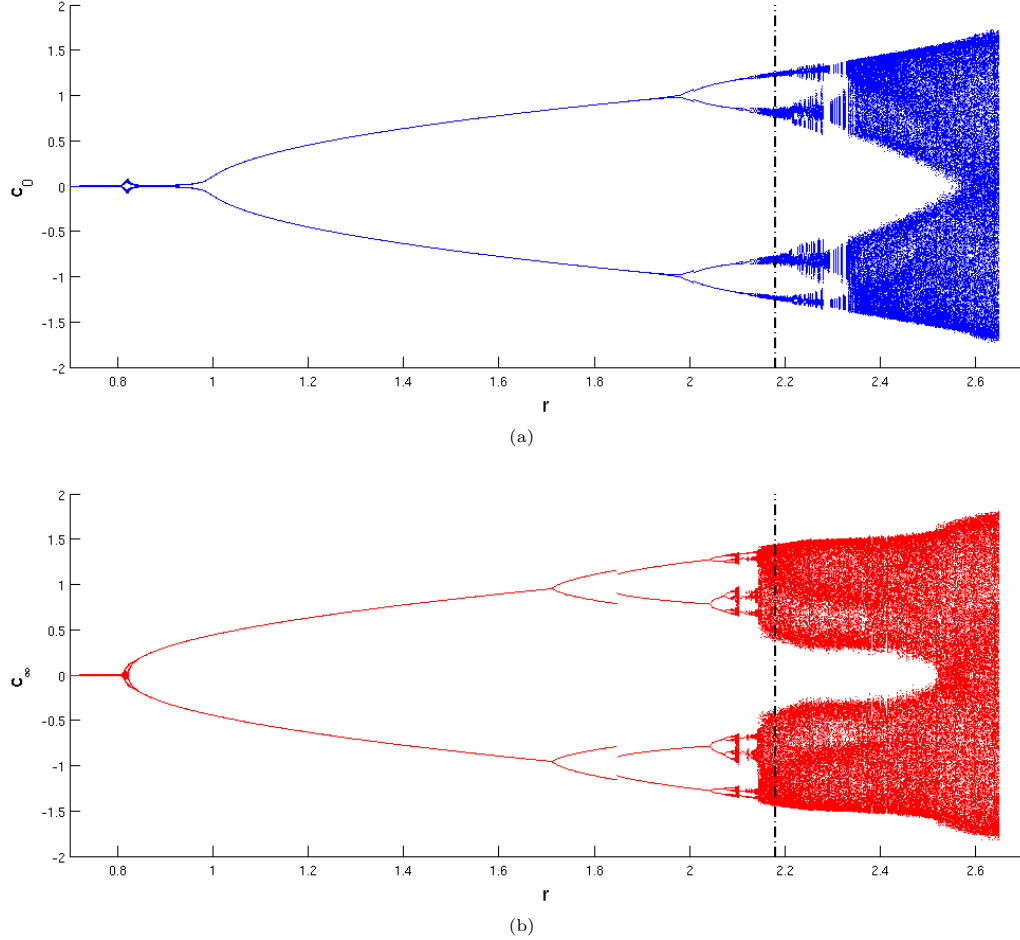


FIG. 4: Bifurcation diagrams for $c_{0\pm}$ (a) and $c_{\pm\infty}$ (b) using $\eta = -0.2$.

First we note that there is a strange behavior in the bifurcation diagram for $c_{\pm\infty}$ for $r > 0$ for r values slightly larger than one. It turns out that this is a modal instability, which will be shown later.

Other than this modal instability the bifurcation diagrams look similar to what we predicted with our analytical results. The bifurcation diagrams for $c_{\pm\infty}$ are shifted by η and the bifurcation diagram for $c_{0\pm}$ looks very similar to

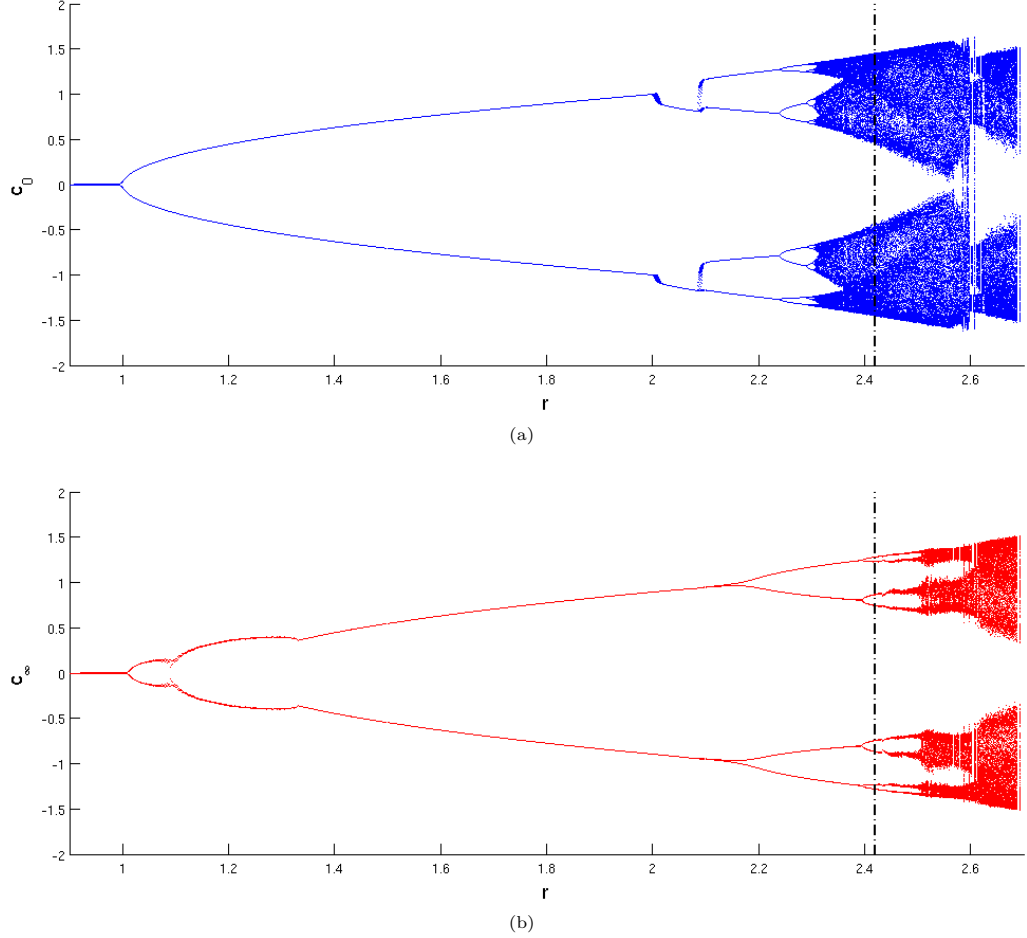


FIG. 5: Bifurcation diagrams for $c_{0\pm}$ (a) and $c_{\pm\infty}$ (b) using $\eta = 0.2$.

that for the uncoupled map. The simulations show some noise that doesn't exist in the uncoupled map. However, since numerical simulation required discretization of the spatial domain we should expect the bifurcation diagrams to look a little "fuzzy".

Finally, we see that in both cases $\eta > 0$ and $\eta < 0$ there are ranges of r in which $c_{\pm\infty}$ behaves chaotically and $c_{0\pm}$ doesn't move chaotically or vice-versa. This coexistence of chaotic and non-chaotic behavior is an interesting result, since it means that even though the behavior at points x and x^* are coupled by the smoothing integral their behavior can be *fundamentally* different. For instance, $r = 2.18$ and $\eta = -0.2$ gives chaotic behavior for $c_{\pm\infty}$ but not for $c_{0\pm}$ (illustrated by the dashed line in figure 4). Also, $r = 2.42$ and $\eta = 0.2$ gives chaotic behavior for $c_{0\pm}$ but not for $c_{\pm\infty}$ (illustrated by the dashed line in figure 5).

C. Bifurcation diagrams for $\beta \neq 0$

Although our analytical analysis is only valid for $\beta = 0$, we can run numerical simulations to explore the behavior of the system for $\beta \neq 0$. Given our analysis fro the period-two solutions, we guess that β will have no effect of $c_{0\pm}$ and will shift bifurcations even further if $\beta < 0$ and shift bifurcations less if $\beta > 0$. In fact, this is what we see.

Figure 6 gives the bifurcation diagrams for $c_{0\pm}$ and $c_{\pm\infty}$ for negative β and positive η ($\beta = -0.2$ and $\eta = 0.2$). As predicted, the bifurcation diagram for $c_{0\pm}$ remains unchanged and the bifurcation diagram for $c_{\pm\infty}$ is shifted even further (note that the bifurcation point between period two and four is $r_{c,\pm\infty}$ less than 2.2 for $\beta = 0$ but greater than 2.2 for $\beta = -0.2$). The other three sets of bifurcation diagrams are given in the appendix.

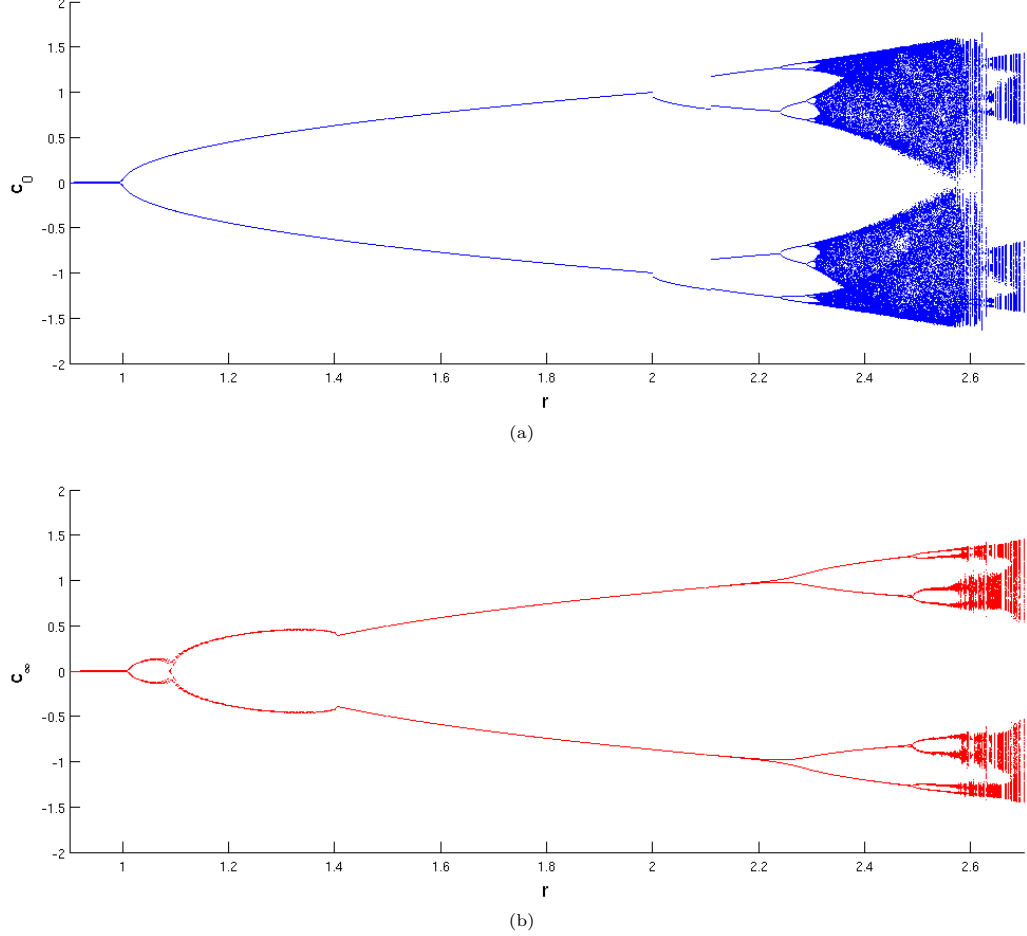


FIG. 6: Bifurcation diagrams for $c_{0\pm}$ (a) and $c_{\pm\infty}$ (b) using $\eta = 0.2$ and $\beta = -0.2$.

D. Mode analysis

To show that the discrepancy in figure 5(b) is truly a modal instability, we will need to do two things. First, instead of the system in equation (2), we will consider the system given by

$$\begin{aligned} c_{n+1}(x) &= \int G(x, x', \sigma_1^2) [-rc_n(x') + c_n^3(x') + \alpha a_n(x')] dx', \\ a_{n+1}(x) &= \int G(x, x', \sigma_2^2) [\beta a_n(x') + \gamma c_{n+1}(x')] dx', \end{aligned} \quad (3)$$

where $\sigma_1 \ll \sigma_2$ (i.e. $\sigma_2 = \mathcal{O}(1)$ and $\sigma_1 = \mathcal{O}(\epsilon)$). This map give qualitatively equivalent behavior as the system in equation (2). Second, we will assume stable solutions for $c_n(x)$ and $a_n(x)$ and perturb them by the modes $c_n e^{2\pi i k x}$ and $a_n e^{2\pi i k x}$, where $c_n, a_n \ll 1$, and see how the perturbations evolve. Since the onset of discrepancy occurs when the dynamically stable solutions are $c_n(x) = a_n(x) = 0$, the perturbations will be

$$\begin{aligned} c_n(x) &\rightarrow 0 + c_n e^{2\pi i k x}, \\ a_n(x) &\rightarrow 0 + a_n e^{2\pi i k x}. \end{aligned}$$

First note that the characteristic function of a gaussian distribution with standard deviation σ^2 is $e^{-\frac{4\pi^2 k^2 \sigma^2}{2}}$.

Dropping nonlinear terms, we get the system

$$\begin{aligned} c_{n+1} e^{2\pi i k x} &= e^{2\pi i k x} e^{-\frac{4\pi^2 \sigma_1^2 k^2}{2}} [-r c_n + \alpha a_n] \\ a_{n+1} e^{2\pi i k x} &= e^{2\pi i k x} e^{-\frac{4\pi^2 \sigma_2^2 k^2}{2}} [-\gamma(r+1) c_n + (\beta + \alpha\gamma) a_n], \end{aligned}$$

which we can write as the following matrix equation (after cancelling the $e^{2\pi i k x}$ terms):

$$\begin{bmatrix} c_{n+1} \\ a_{n+1} \end{bmatrix} = \underbrace{\begin{bmatrix} -r e^{-\frac{4\pi^2 \sigma_1^2 k^2}{2}} & \alpha e^{-\frac{4\pi^2 \sigma_1^2 k^2}{2}} \\ -\gamma(r+1) e^{-\frac{4\pi^2 \sigma_2^2 k^2}{2}} & (\beta + \alpha\gamma) e^{-\frac{4\pi^2 \sigma_2^2 k^2}{2}} \end{bmatrix}}_{M(k)} \begin{bmatrix} c_n \\ a_n \end{bmatrix}.$$

It follows that if the dominant eigenvalue $\lambda(k)$ of $M(k)$ is greater than one in absolute value, then mode k is unstable. Furthermore, if the dominant mode (i.e. k^* such that $|\lambda(k)|$ is maximum at $k = k^*$) is not equal to zero, then the functions $c_n(x)$ and $a_n(x)$ will have a modal instability and oscillations will occur.

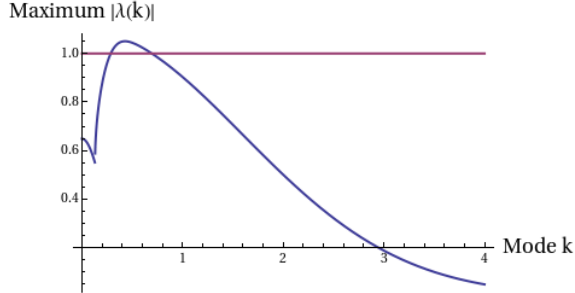


FIG. 7: $|\lambda(k)|$ vs k for $\alpha = -\sqrt{0.2}$, $\beta = -0.2$, $\gamma = -\sqrt{0.2}$, $\sigma_1 = 0.1$ and $\sigma_2 = 1$.

Figure 7 plots $|\lambda(k)|$ vs k for the $\eta > 0$ case. Clearly the dominant mode is both greater than one in magnitude and away from zero. We can further check our analysis by simulating $c_n(x)$, computing the FFT and checking that the dominant frequency matches up with the dominant mode. This comparison is given in figure 8(a). An example of oscillations propagated by a modal instability is given in figure 8(b).

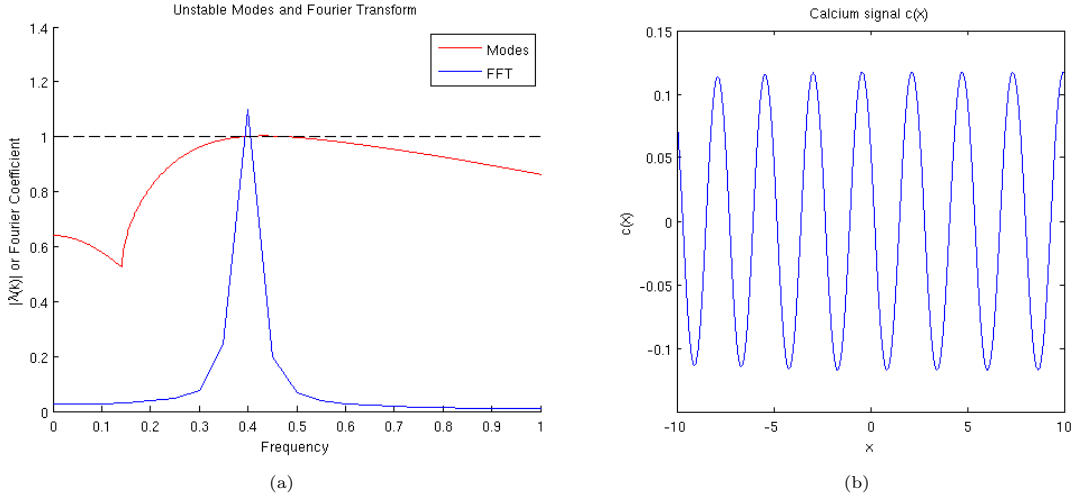


FIG. 8: Comparison of modal analysis to the FFT(a). Example of oscillations propagated by a modal instability(b).

The range of parameters that give rise to modal instability is that in which we see a discrepancy in figure 5(b). Because of the propagation of oscillations, the function $c(x)$ does not subdivide into different in-phase regions. Therefore, no “boundaries” exist and neither do $c_{\pm\infty}$ or $c_{0\pm}$.

IV. GENERALIZATION TO OTHER MAPS

So far we have analyzed the system given by

$$\begin{aligned} c_{n+1} &= f(c_n(x); r) + \alpha a_n(x), & \text{where } f(\xi; r) = -r\xi + \xi^3, \\ a_{n+1} &= \int G(x, x')[\beta a_n(x') + \gamma c_n(x')]dx'. \end{aligned}$$

We chose this form of f because its inherent symmetry made several features analytically tractable.

A natural question that arises at this point is the following: If we generalize $f(\xi; r)$ to another map that displays period-doubling cascades and chaos, do we see similar behavior? Given similar definitions $c_{\pm\infty}$ and $c_{0\pm}$, do the choices of the parameters α , β , and γ shift the bifurcation diagram in a similar way? Also, is it possible to have a coexistence of chaotic and non-chaotic behavior at different points in space?

To investigate these questions, suppose f is the logistic map: $f(\xi; r) = r\xi(1-\xi)$ (which also displays period-doubling cascades and chaotic regions in parameter-space). For the quantities $c_{\pm\infty}$ and $c_{0\pm}$ defined as they are above, figure 9 gives the bifurcation diagrams for $\eta < 0$ and figure 10 gives the bifurcation diagram for $\eta > 0$.

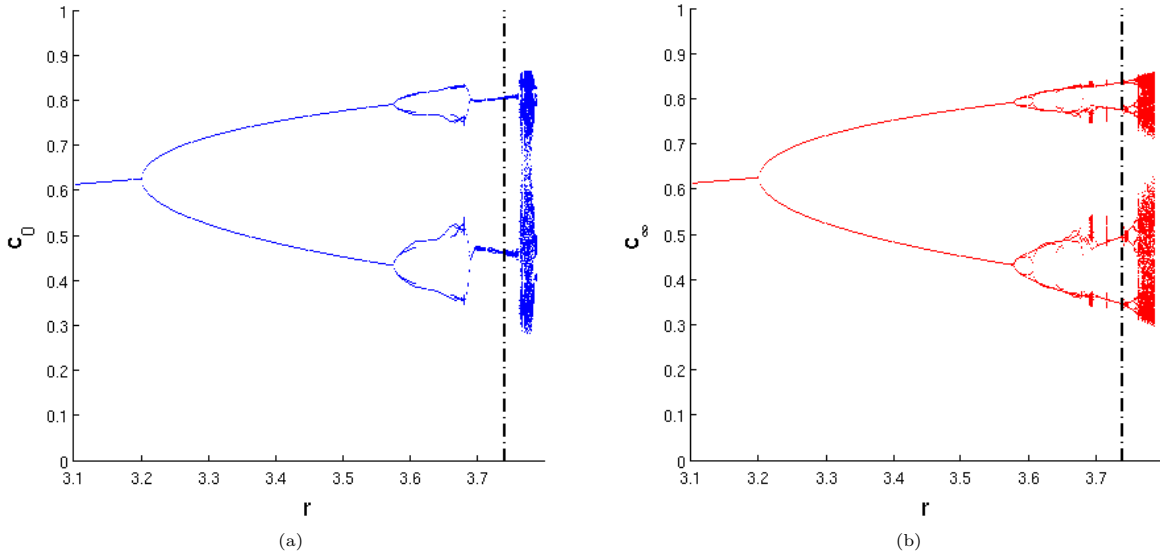


FIG. 9: Bifurcation diagrams for $c_{0\pm}$ (a) and $c_{\pm\infty}$ (b) using $\eta = -0.2$ ($f(\xi; r) = r\xi(1 - \xi)$).

We observe that for both η positive and negative the bifurcation diagrams are affected differently. First, in both cases the bifurcation diagrams for both $c_{\pm\infty}$ and $c_{0\pm}$ are shifted. For $\eta < 0$ it seems that there is no coexistence of chaotic and non-chaotic behavior, although there are values of r for which $c_{\pm\infty}$ and $c_{0\pm}$ have different periodicity (for instance $r = 3.74$). For $\eta > 0$, on the other hand we can find r values for which $c_{0\pm}$ is chaotic but $c_{\pm\infty}$ is not.

For example, as $x \rightarrow \pm\infty$ we have

$$c_{n+1, \pm\infty} = (r + \eta)c_{n, \pm\infty} - rc_{n, \pm\infty}.$$

As long as $\eta \neq 0$ this map is fundamentally different from the standard logistic map. In other words, we cannot shift parameters to obtain the same map. This is because in the logistic map the parameter r is also a coefficient of the nonlinear terms. In general, any map whose nonlinear terms are also affected by the parameters will be fundamentally changed by the coupling parameters because it becomes function with two parameters instead of one combined parameter. We should not expect the coupling scheme to shift the bifurcation diagrams of these maps in a uniform way.

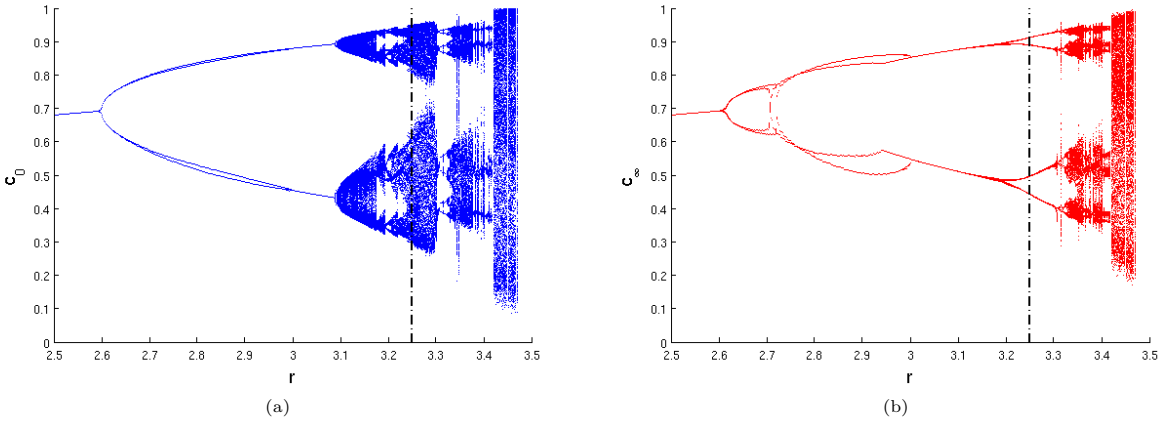


FIG. 10: Bifurcation diagrams for $c_{0\pm}$ (a) and $c_{\pm\infty}$ (b) using $\eta = 0.2$ ($f(\xi; r) = r\xi(1 - \xi)$).

V. CONCLUSION

The effects that a spatial component can have on a dynamical system come from a wide spectrum of possibilities depending on both the spatial and dynamical behavior of a system. In fact, spatiotemporal dynamics can be applied to a huge range of systems in physics, biology, etc., but the nature of solutions are very problem specific due to their complexity.

In this paper we've explored the behavior of one of the simplest spatiotemporal systems one can write down (equation (2)). The dynamical component is driven by a simple discrete-time map that exhibits period-doubling bifurcations and chaotic behavior and the spatial component consists of a simple smoothing operator. These aspects are combined in a system consisting of two functions on one spatial dimension that are coupled by a few parameters.

With a conveniently chosen map and smoothing kernel ($f(\xi; r) = -r\xi + \xi^3$ and the Gaussian kernel $G(x, x', \sigma^2)$) several qualities of the system can be understood through analytical computation. Much of this analysis is obtained by exploring the time series of the functions at a fixed point in space, \vec{x}^* . In this paper we've used the quantities $c_{n,\pm\infty} = \lim_{x \rightarrow \pm\infty} c_n(x)$ and $c_{n,0\pm} = \lim_{x \rightarrow 0\pm} c_n(x)$ to describe the dynamic behavior of the function $c_n(x)$.

Solutions ($c_{\pm\infty}$ and $c_{0\pm}$) of low-order periodicity are attainable analytically. However, since the map displays both and infinite number of period-doubling cascades as well as regimes of chaotic behavior, the use of numerical exploration is necessary. In general, finding the exact form of the function $c_n(x)$ (and $a_n(x)$) is very difficult if not impossible. Most likely the use of asymptotics and perturbation theory would be a more fruitful approach.

One interesting feature to observe is the competition between the parameter r and the smoothing operator and how the coupling parameters affect it. Depending on the coupling parameters we observe a coexistence of different behavior at different points in space. For instance, steady state $c_{\pm\infty}$ can have a periodicity of four while steady-state $c_{0\pm}$ can have periodicity two. Furthermore, if we increase r enough then one of these quantities can be chaotic while the other is not.

In summary the class of spatiotemporal dynamical systems is a huge family of dynamical systems that are usually difficult to solve. This has been an analysis of *one* such system. Using both analytical and numerical tools we can begin to understand how the dynamic and spatial components coexist in solutions and affect bifurcation and chaotic behavior. Albeit simple, systems like this one are in some sense solvable and easy to understand, which is useful in trying to understand more complicated spatiotemporal problems.

Special thanks to Professor Juan G. Restrepo (Department of Applied Mathematics, University of Colorado at Boulder), Professor Alain Karma (Department of Physics and Center for Interdisciplinary Research on Complex Systems, Northeastern University), and Professor Elizabeth Bradley (Department of Computer Science, University of Colorado at Boulder).

Appendix A: Computation of $\tilde{G}(x, x', \sigma^2)$ (for $-1 < \beta < 0$)

Starting from the equation

$$c_{n+1}(x) = -rc_n(x) + c_n^3(x) + \eta \sum_{k=1}^{\infty} \beta^{k-1} \underbrace{\int \dots \int}_{k} \left[\prod_{j=1}^k G(x^{(j-1)}, x^{(j)}, \sigma^2) \right] c_{n-k+1}(x^{(k)}) dx^{(k)} \dots dx^{(1)},$$

we seek to simplify the k integrals into a term with just one integral. Since everything inside the integrals are absolutely and uniformly convergent we can use Funini's theorem¹¹ to switch the order of integration:

$$\begin{aligned} & \underbrace{\int \dots \int}_{k} \left[\prod_{j=1}^k G(x^{(j-1)}, x^{(j)}, \sigma^2) \right] c_{n-k+1}(x^{(k)}) dx^{(k)} \dots dx^{(1)} \\ &= \int \left[\underbrace{\int \dots \int}_{k-1} \prod_{j=1}^k G(x^{(j-1)}, x^{(j)}, \sigma^2) dx^{(k-1)} \dots dx^{(1)} \right] c_{n-k+1}(x^{(k)}) dx^{(k)}. \end{aligned}$$

Inside the brackets we have the convolution of k Gaussian distributions. Next we will use the property that the convolution of a Gaussian with standard deviation μ^2 and ν^2 is a Gaussian with standard deviation $\mu^2 + \nu^2$ (this is an easy property to check, for instance with Mathematica). Formally, if $G_{\sigma^2} = G(x, x', \sigma^2)$, then

$$(G_{\mu^2} * G_{\nu^2}) = G_{\mu^2 + \nu^2} = G(x, x', \mu^2 + \nu^2).$$

It follows that the convolution of two identical Gaussian distributions with standard deviation σ^2 is a Gaussian distribution with standard deviation $2\sigma^2$. Applying this k times means that after k convolutions we are left with a Gaussian distribution with standard deviation $k\sigma^2$, or

$$\underbrace{\int \dots \int}_{k-1} \prod_{j=1}^k G(x^{(j-1)}, x^{(j)}, \sigma^2) dx^{(k-1)} \dots dx^{(1)} = G(x, x', k\sigma^2).$$

Thus, the k -integral term reduces to the single integral

$$\int G(x, x', k\sigma^2) c_{n-k+1}(x') dx'.$$

Finally, we use the absolute and uniform convergence of both the integral and the sum to interchange the two. The equation we are left with is

$$\begin{aligned} c_{n+1}(x) &= -rc_n(x) + c_n^3(x) + \eta \int \sum_{k=1}^{\infty} |\beta|^{k-1} G(x, x', k\sigma^2) c_{n-k+1}(x') dx' \\ &= -rc_n(x) + c_n^3(x) + \eta \int \tilde{G}(x, x', \sigma^2) c_{n-k+1}(x') dx'. \end{aligned}$$

Appendix B: Remaining Bifurcation Diagrams for $\beta \neq 0$

Figures 11, 12, and 13 give the remaining bifurcation diagrams from $\beta \neq 0$: $\beta = -0.2$ and $\eta = -0.2$, $\beta = 0.2$ and $\eta = -0.2$, and $\beta = 0.2$ and $\eta = 0.2$, respectively.

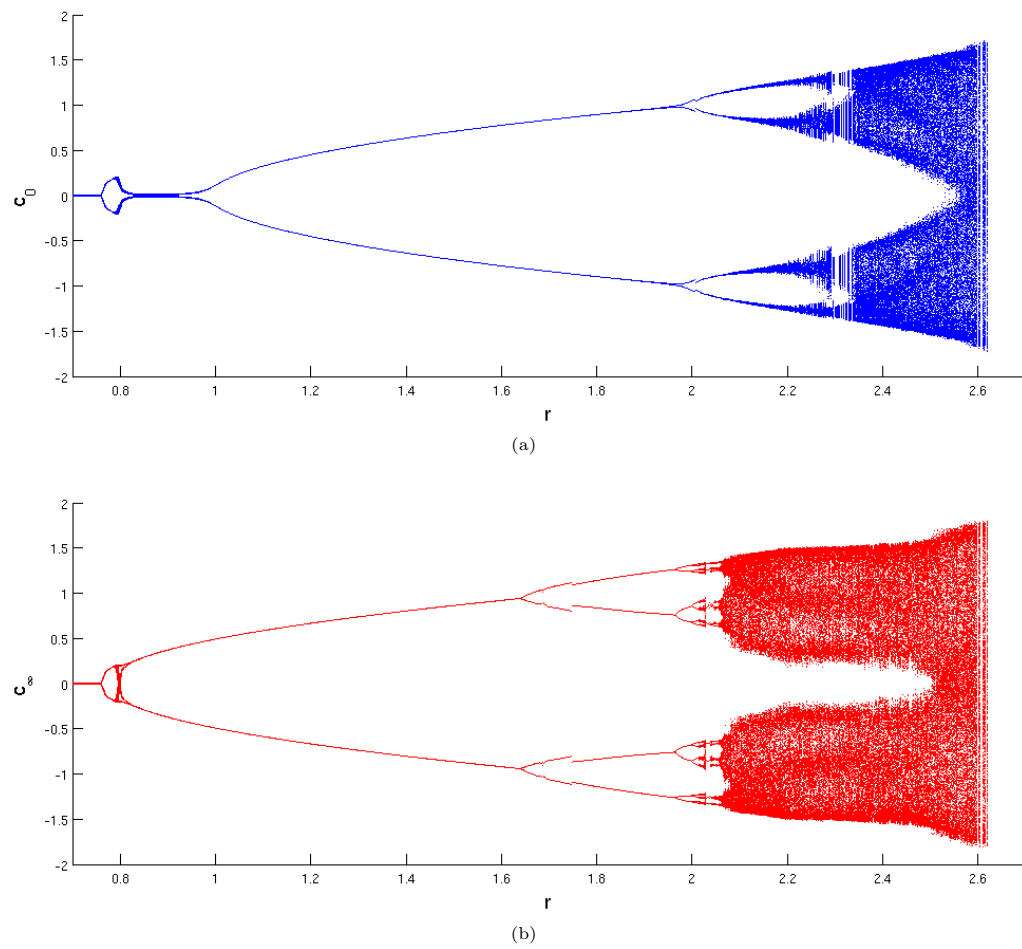


FIG. 11: Bifurcation diagrams for $c_{0\pm}$ (a) and $c_{\pm\infty}$ (b) using $\eta = -0.2$ and $\beta = -0.2$.

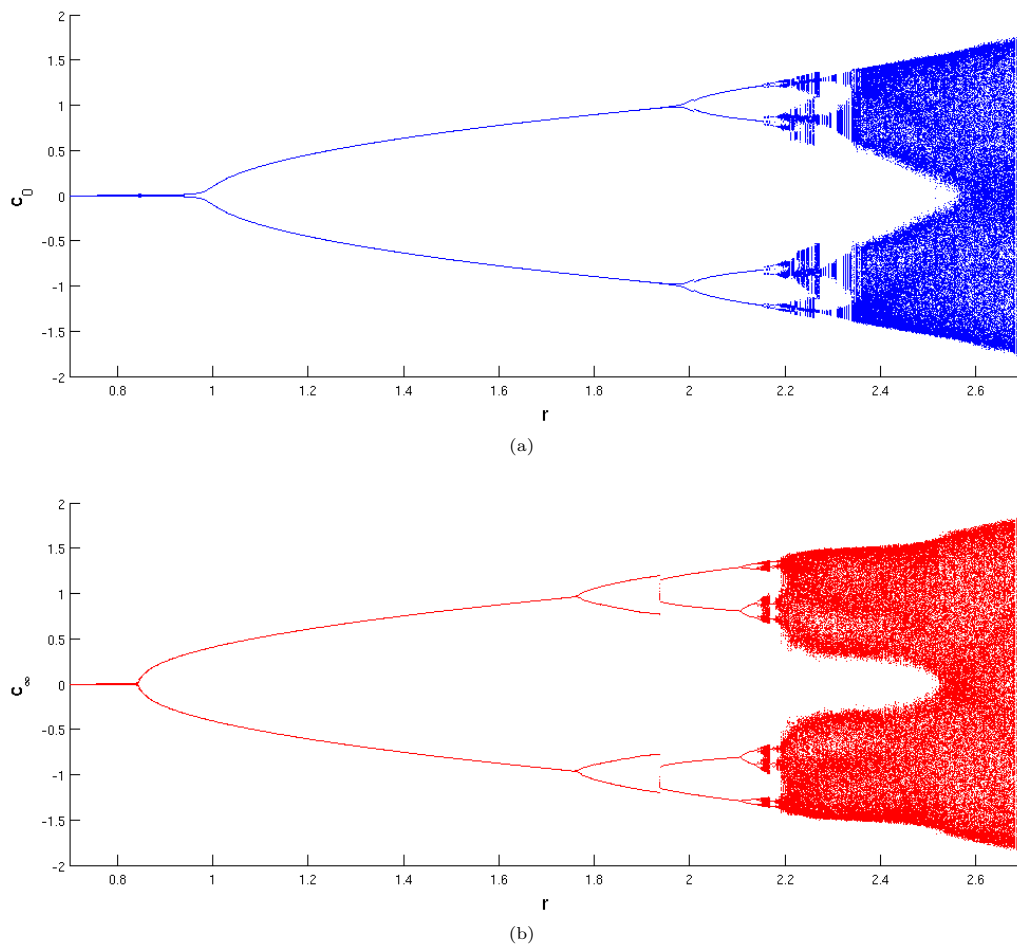


FIG. 12: Bifurcation diagrams for $c_{0\pm}$ (a) and $c_{\pm\infty}$ (b) using $\eta = -0.2$ and $\beta = 0.2$.

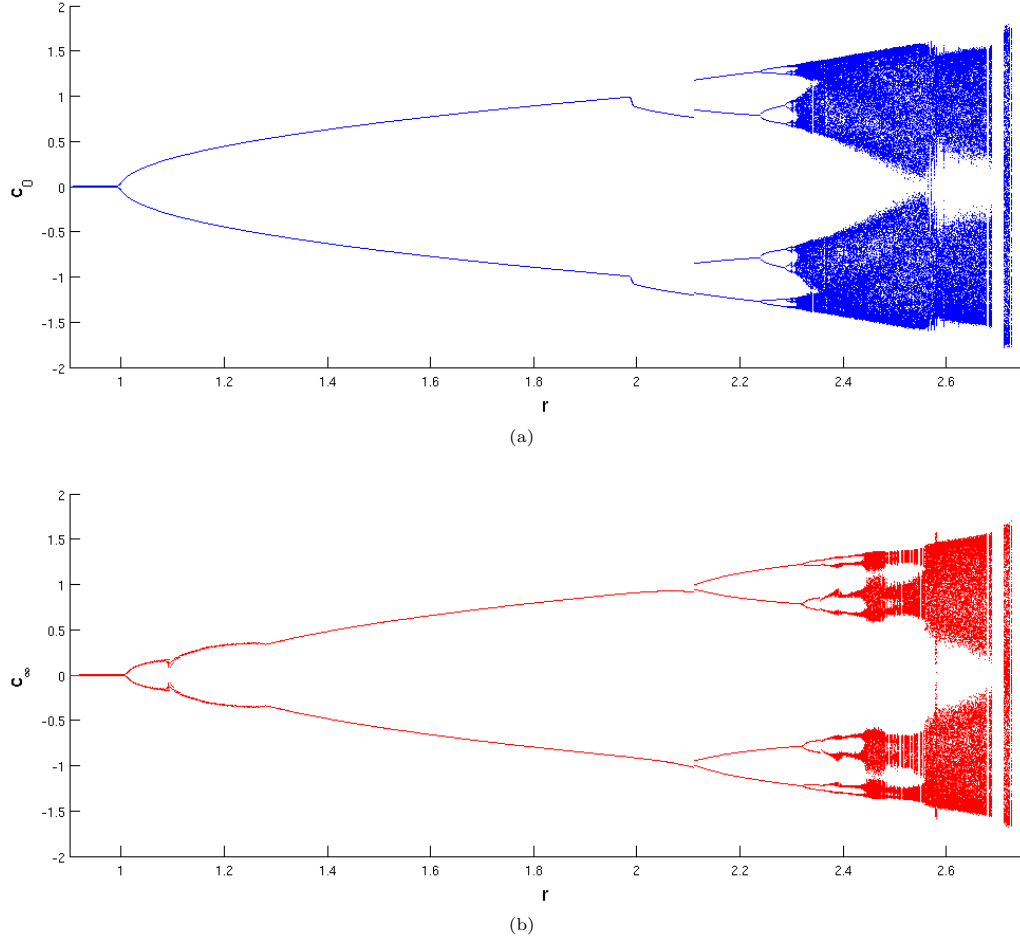


FIG. 13: Bifurcation diagrams for $c_{0\pm}$ (a) and $c_{\pm\infty}$ (b) using $\eta = 0.2$ and $\beta = 0.2$.

- ¹ Donald S. Cohen, John C. Neu, and Rodolfo R. Rosales. Rotating spiral wave solutions of reaction-diffusion equations. *SIAM Journal on Applied Mathematics*, 35:536–547, 1978.
- ² Y. Kuramoto and D. Battogtokh. Coexistence of coherence and incoherence in nonlocally coupled phase oscillators. *Nonlinear Phenomena in Complex Systems*, 5:380–385, 2002.
- ³ Daniel M. Abrams and Steven H. Strogatz. Chimera states for coupled oscillators. *Physics Review Letters*, 93:174102:1–4, 2004.
- ⁴ Erik A. Martins, Carlo R. Laing, and Steven H. Strogatz. Solvable model of spiral wave chimeras. *Physics Review Letters*, 104:044101:1–4, 2010.
- ⁵ Blas Echebarria and Alain Karma. Amplitude equation approach to spatiotemporal dynamics of cardiac alternans. *Physics Review E*, 76:051911:1–23, 2007.
- ⁶ Mark Kot and William M. Schaffer. Discrete-time growth dispersal models. *Mathematical Biosciences*, 80:109–136, 1986.
- ⁷ Shankar C. Venkataramani and Edward Ott. Spatiotemporal bifurcation phenomena with temporal period doubling: Patterns in vibrated sand. *Physical Review Letters*, 80:3495–3498, 1998.
- ⁸ M.R. Guevara, G. Ward, A. Shrier, and L. Glass. Electrical alternans and period-doubling bifurcations. *IEEE Computers in Cardiology*, pages 167–170, 1984.
- ⁹ Alain Karma. Electrical alternans and spiral wave breakup in cardiac tissue. *Chaos*, 4:461–472, 1994.
- ¹⁰ Evelyn Sander and James A. Yorke. Connecting period-doubling cascades to chaos. *Unpublished Manuscript, University of Maryland, College Park, MD*, 2010.
- ¹¹ John K. Hunter and Bruno Nachtergael. *Applied Analysis*. World Scientific Publishing Company, 2001.

Are Chaotic Variations ‘Superior’ to Random Variations on a Drum Rhythm

Laura Stiles

April 30 2010

Abstract

Chaotic and random variations of an original drum rhythm are created with music software then studied with the aim of discerning which is superior. Samples of the two types of variations were presented without knowledge of the project and a survey was used to collect opinions. It was found that chaotic variations were more pleasing to the audience. Though iterations of creating music, however, it was found that the differences in each resulting production of a chaotic or random variation can vary significantly, thus survey results should not be widely generalized.

1 Introduction

A chaotic system is a deterministic system which shows sensitive dependence on initial conditions.¹ A wide variety of disciplines can employ chaos theory, such as engineering, economics, and communications. Chaotic dynamics have also been used in a variety of artistic and creative applications. In the work of Diana Dabby, a chaotic attractor is used as a means to create variations in pitch sequences of classical music.² This work inspired other similar applications, such as dance sequence variations³ and route-setting for rock climbing.⁴ Using a chaotic dynamical system for variations ensures each new sequence of music or dance will be varied from the original due to the system’s sensitive dependence on initial conditions, but theoretically maintains the structure of the original piece.

In this project, the question was addressed whether the variations in a drum sequence created using a chaotic attractor maintain enough of the structure of the original piece to sound more pleasing than a random variation. Previous work has investigated the similarities and differences between stochastic and chaotic data and how they can often appear similar and even indistinguishable.⁵ Drum rhythms were chosen as the subject of this study on random vs. chaotic variations due to the relative simplicity of the instrument and repetitiveness of a drum pattern. Results and interpretations come from surveying individuals about samples of the musical variations.

1.1 Previous Work

In Reference 2, Dabby describes a procedure that was created for a chaotic mapping to generate musical variations on an original work. The purpose of using a chaotic attractor was for ‘linking and tracking’ the original and varied piece of music.² Using a chaotic attractor as a reference trajectory, x-values of this reference were paired with pitch sequences in a musical piece. A new trajectory from a perturbed initial condition was then generated



Figure 1: Original dance sequence (top); Chaotic variation on the sequence(middle); Interpolated chaotic variation (bottom)³

and a nearest neighbor-type procedure was used to create a new ordering of the pitches. The procedure produced some variations that retained the ‘flavor of the original’ and other variations which were not recognizable from the original, depending on parameters of the method.²

Similar to Dabby’s procedure, Bradley et. al. used a ‘chaotic symbol-sequence reordering technique’ to create a variation on a dance sequence.³ Variations on a dance sequence required careful techniques for interpolating between body positions and smoothing transitions, as shown in Figure 1.

Another interesting application was explored by Phillips and Bradley to use a chaotic system to aid in setting rock climbing routes.⁴ The procedure for the variations is similar to those for the dance sequences and a survey was used as a tool to evaluate the resulting climbing routes. Surveying techniques for the climbing project inspired the approach for analysis in this project.

2 Project Approach

To address the question of the superiority of chaotic variations over random variations, an original 1-measure drum rhythm was created. A method to map the original rhythm onto a chaotic attractor and onto a random number sequence then back into a drum sequence was devised, as described in the following sections. Samples of each type of variation were presented in a survey to aid in drawing a conclusion on the superiority of the variations.

2.1 Music Generation

The music software Fruity Loops (FL) Studio⁶ was used to create the original rhythm and the chaotic and random variations. FL Studio allows users to choose from a large variety of musical interface digital instruments (MIDI) to create measures of music. As shown in Figure 2, the measure is divided into sixteenth notes (using 4/4 time). On each sixteenth note, the user can choose any MIDI instrument to play a note. For this project, a cymbal (called the hi-hat, or simply hat) and a bass drum (called a kick) were used. To give variety



Figure 2: Screenshot

to the music, the original rhythm included the four possible combinations of these drums: no hit notes, only kick notes, only hat notes, and both drums together, as can be seen in Figure 2. Effects of different drums and different combinations will be discussed in the results section.

2.2 Chaotic Variations

To generate chaotic variations on the original rhythm, a mapping was established between the sixteenth notes of the rhythm and data points along a trajectory. The chosen trajectory was the Lorenz attractor, described by Equation 1, with the parameters $a = 16$, $r = 45$, and $b = 4$. A fixed-step fourth-order Runge Kutta integrator was used to generate the trajectory.

$$\begin{aligned}\dot{x} &= a(y - x) \\ \dot{y} &= rx - y - xz \\ \dot{z} &= xy - bz\end{aligned}\tag{1}$$

The sixteen notes of measure of kick and hat hit combinations were mapped to sequential data points starting with the initial condition of the trajectory and repeating continually along the trajectory's length every 16 notes. With a chaotic system, a slight variation in initial condition will yield a very different trajectory. This property was taken advantage of to create a new trajectory from a slightly different initial set of coordinates in the state space, as seen in Figure 3.

A nearest neighbor function was used on each point of the new trajectory to find the closest data point on the original trajectory (as defined by the smallest Euclidean norm). The note that had been mapped onto the original trajectory was now mapped back to the new trajectory. This mapping back to the new trajectory provided a variation on the original rhythm that was input into the FL Studio software to create measures of music.

Different methods for compiling the variations were explored. First, a single measure of a chaotic drum pattern was created, then repeated for several measures. This will be referred to as the ‘short variation.’ With many trials of this method, it was found that there was a wide range in the qualities of the variation, such as maintaining the structure of the original, maintaining a good beat, or listening pleasure. It is important to remember that these interpretations were subjective to the author. A second approach to creating a drum sequence was to follow the new trajectory for 8×16 data points, then use the inverse mapping to create eight different measures of a chaotic variation. This sequence will be referred to as the ‘long variation.’

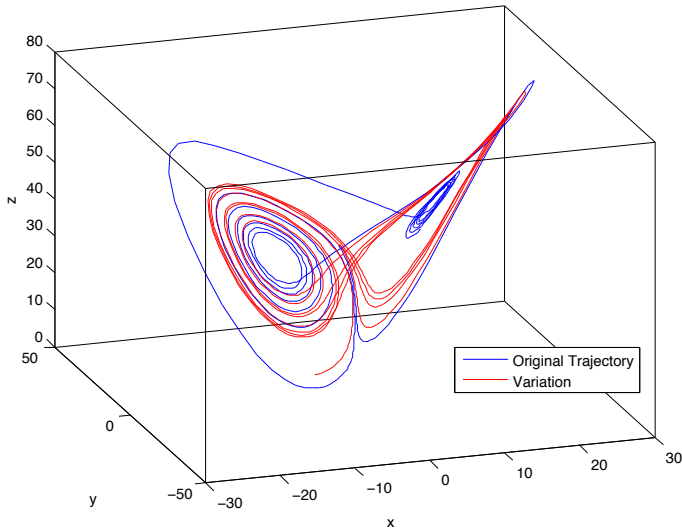


Figure 3: Lorenz Attractor and Perturbed Trajectory

2.3 Random Variations

Random variations on the original drum rhythm were created with a mapping between the original notes and random numbers generated with the MATLAB program. The rand function was modified to randomly output numbers between 1 and 16. The 1/16th notes of the original trajectory, assigned numbers in order from 1 through 16 as before, were mapped onto these random numbers. The new sequence of notes was input manually into the FL Studio program to produce the random variation.

Similar to the method for creating short and long variations of the chaotic rhythms, short and long variation of the random variations were chosen. For the short variation, one set of 16 random numbers were generated, then the sequence mapped to the sixteenth notes. This measure was then repeated multiple times. The repetition of the one measure added structure to the variation that countered the randomness. The long variation was created by generating 8 x 16 random numbers, then creating eight different measures of random rhythms to be played together.

3 Survey and Results

Two short, repeating variations of both chaotic and random rhythms were chosen to be presented, as well as two long variations of each. The rhythms selected were the first created for each type, as to avoid bias in selection. A Likert scale survey was designed and presented to the students of the CSCI 5446 to optionally provide opinions on the drum variations. 18 students provided responses about the drum rhythms presented.

3.1 Survey Design

The Likert scale is a surveying approach that has been used since 1932 in measuring attitudes of survey respondents.⁷ The traditional Likert-type survey has five responses, which was

chosen for this project. The scale is ordinal, and the 5 possible responses were assigned the values shown in Table 1. It is important to recognize that the scale is not interval, and it cannot be assumed that the difference in attitude between response choices are the same.⁸ For example, the difference in attitude between strongly disagree and agree is not necessarily the same in attitude difference between disagree and neutral.

Table 1: Likert Scale Values

Criteria	Value
Strongly Disagree	1
Disagree	2
Neutral	3
Agree	4
Strongly Agree	5

The survey participants were presented with short and long variations of the music without being informed of the nature of the project. For the short variations, three questions were presented, each a comparison between a short chaotic variation and a short random variation. Two of the questions, which has better rhythm and which is more pleasant to listen to, were presumed to receive similar responses. It has been suggested that rhythm in music can be nearly synonymous to aesthetic appeal.⁹ For the long variations, five questions were presented relating only to the variation and the original, with no direct comparison between the chaotic rhythm and the random rhythm. Survey participants did not know that some rhythms were chaotic and some were random. A copy of the survey is included in the Appendix.

3.2 Survey Results

In this section, the results of the survey will be discussed, with focus on the responses concerning the long variations. As mentioned in the section ‘Music Generation’ the random short variations gained structure from the repetition, suppressing the random nature. Also, the repetition with the chaotic short variations nearly extinguished the structure that resembled the original. These issues were also made apparent by the inconclusive results for this part of the survey.

Table 2 and Table 3 display a basic statistical analysis of the survey data for the long drum variations. Reference 7 describes, however, that the mean is often not a representative quantity for Likert-scale analysis. Calculating the mean with this ordinal scale is more of a function of audience size than attitude.⁷ For each question, the median and mode were found to be the same value, reenforcing the significance of these statistics.

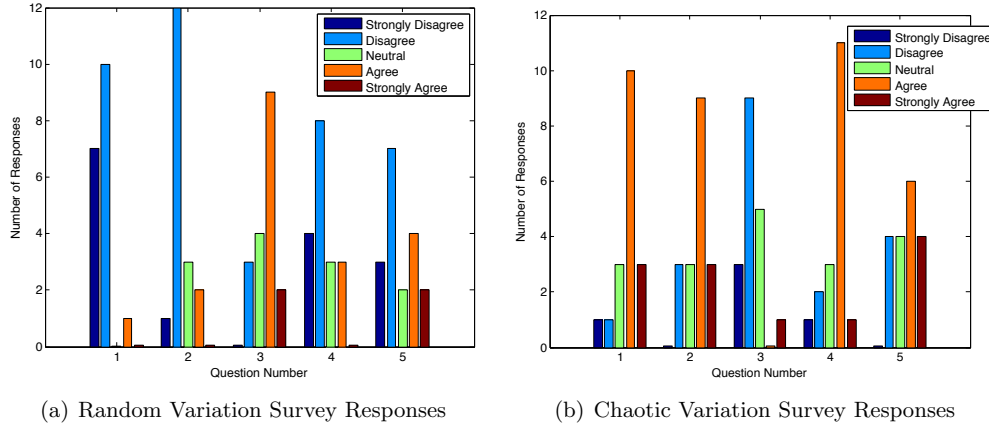
The plots shown in Figure 3.2 display the raw numbers from responses of the survey participants for the long variations of drum rhythms. It is interesting to note that the responses are nearly mirrored for the random and chaotic variations, as was seen in the statistics tables. Clearly, the chaotic variations were given better scores than the random variations in every category.

Table 2: Random Variation Survey Results

Question	Mean	Median	Mode
Sounds like the Original	1.7	2	2
Has Good Beat	2.3	2	2
Sounds Random	3.6	4	4
Maintains Flow	2.3	2	2
Enjoyable for Listening	2.7	2	2

Table 3: Chaotic Variation Survey Results

Question	Mean	Median	Mode
Sounds like the Original	3.7	4	4
Has Good Beat	3.7	4	4
Sounds Random	2.3	2	2
Maintains Flow	3.5	4	4
Enjoyable for Listening	3.6	4	4



(a) Random Variation Survey Responses

(b) Chaotic Variation Survey Responses

Figure 4: Survey Responses for Drum Variations (a) Random and (b) Chaotic

3.3 Interpretation of Results and Recommendations

From the survey response, it was clear that more of audience considers that chaotic variations are superior to random variation for the musical pieces presented. However, during the exploration of methods to create variations of drum rhythms, it was discovered that there are numerous parameters that greatly effect the resulting music. Some of these include: initial conditions, trajectory length for the mapping, number of drums, complexity of the original rhythm, and how the measures are combined.

Of the parameters effecting the mapping, length of the trajectory was the most significant. This effect can be visualized by considering the extreme cases of a very short and very long trajectory. If the trajectory were very short, it is likely that execution of the

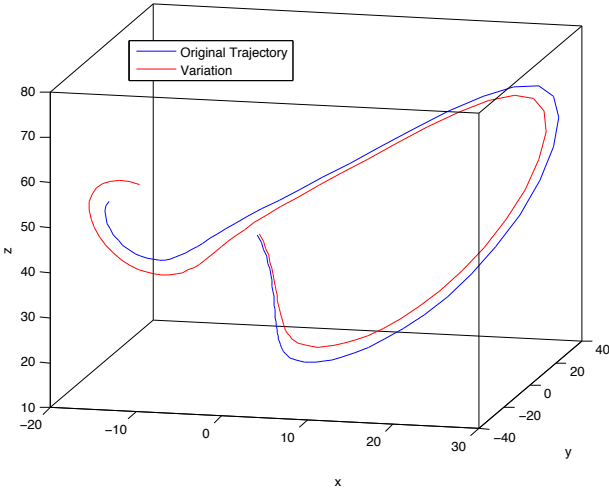


Figure 5: Short Trajectory Length: Mapping Reproduces the Original Rhythm

nearest neighbor procedure would simply reproduce the original trajectory. This concept is shown in Figure 5. If the trajectory is generated from a very large number of integration steps, it is simple to imagine the nearest neighbor function would produce data points which continually ‘jumped’ between different parts of the chaotic attractor.

Regarding the original composition, a first approach to this project was to take several measures of an existing song as the original piece. It was found that the complicated pieces that were investigated were not suited for this project, as it was difficult for any variation to match a complex structure. The original piece was therefore simplified to one repeating measure with only two types of drums. Interesting future work would be investigating a different number of drums, or adding other instruments to the original piece.

4 Conclusions

A project was proposed and executed for the CSCI 5446 Chaotic Dynamics course to study the superiority of chaotic versus random variations of a drum rhythm. A method was devised to map an original drum rhythm onto a chaotic attractor. A new trajectory of the chaotic system was created with a perturbed initial condition, and a nearest neighbor procedure was used to link back to the original attractor and invert the mapping to create new rhythm sequences. A random number generator was used to create random variations on the original measure of drum beats. Different variations were presented to participants of a survey created for this project, and opinions were provided about different characteristics of the music. Results show that in all categories judged, the chaotic variation was superior to the random variation. It was noted, however, that many different parameters chosen in creating the variations effect the quality and these results cannot be widely generalized.

References

- [1] S. Strogatz. *Nonlinear Dynamics and Chaos*. Perseus Books Publishing, LLC, 1994.
- [2] Diana S. Dabby. *Musical Variations from a Chaotic Mapping*. PhD thesis, Massachusetts Institute of Technology, September 1995.
- [3] Elizabeth Bradley and Joshua Stuart. Using chaos to generate choreographic variations. *Chaos*, 8(4):800–807, 1998.
- [4] Caleb Phillips and Elizabeth Bradley. Strange beta: Chaotic variations for indoor rock climbing route setting. Technical Report CU-CS-1057-09, University of Colorado at Boulder, December 2009.
- [5] O. A. Rosso et. al. Distinguishing noise from chaos. *Physical Review Letters*, 99(154102), October 2007.
- [6] Fruity Loops Studio 8. *Software*. <http://flstudio.image-line.com>, 2010.
- [7] Dennis L. Clason and Thomas J. Dormody. Analyzing data measured by individual likert-type items. *Journal of Agricultural Education*, 35(4):31–35, 1994.
- [8] Susan Jamieson. Likert scales: How to (ab)use them. *Medical Education*, 38:1212–1218, 2004.
- [9] Ben Neill. Pleasure beats: Rhythm and the aesthetics of current electronic music. *Leonardo Music Journal*, 12:3–6, 2002.

Appendix

Figure 6 shows the survey that was presented to the CSCI 5446 class to optionally provide opinions.

Survey on Chaotic and Random Variations of Drum Beats

Background Questions

- i. Do you/have you seriously played an instrument before?
- ii. Do you/have you seriously played the drums before?

SHORT SETS

BEAT 1	Strongly Disagree	Disagree	Neutral	Agree	Strongly Agree
1.1 Song A has better rhythm than Song B					
1.2 Song A sounds more like the original than Song B					
1.3 Song B is more pleasant to listen to than Song A					

BEAT 2	Strongly Disagree	Disagree	Neutral	Agree	Strongly Agree
2.1 Song A has better rhythm than Song B					
2.2 Song A sounds more like the original than Song B					
2.3 Song B is more pleasant to listen to than Song A					

LONG SETS

BEAT 3	Strongly Disagree	Disagree	Neutral	Agree	Strongly Agree
3.1 This song sounds like the original					
3.2 This song has a good beat					
3.3 This song sounds random					
3.4 This song maintains flow					
3.5 I enjoy listening to this song					

BEAT 3	Strongly Disagree	Disagree	Neutral	Agree	Strongly Agree
4.1 This song sounds like the original					
4.2 This song has a good beat					
4.3 This song sounds random					
4.4 This song maintains flow					
4.5 I enjoy listening to this song					

Figure 6: Survey